Structural analysis of particulate systems using X-ray tomography

Strukturanalyse partikulärer Systeme mittels Röntgentomographie

Der Naturwissenschaftlichen Fakultät
der Friedrich-Alexander-Universität
Erlangen-Nürnberg

zur

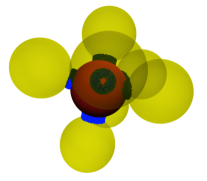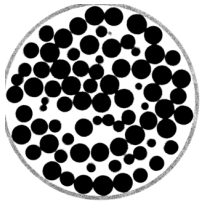Erlangung des Doktorgrades Dr. rer. nat.

vorgelegt von

Simon J.A. Weis

aus Fürth

Als Dissertation genehmigt
von der Naturwissenschaftlichen Fakultät
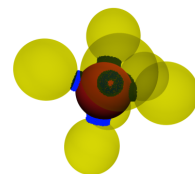der Universität Erlangen-Nürnberg

Tag der mündlichen Prüfung:
Vorsitzender der Promotionskommission:
Erstberichterstatter: PD. Dr. Gerd Schröder-Turk
Zweitberichterstatter: Prof Dr. Alexander Schneider

List of publications

- Simon Weis, Philipp W. A. Schönhöfer, Fabian Schaller, Matthias Schröter, and Gerd E. Schröder-Turk. "Pomelo, a tool for computing Generic Set Voronoi Diagrams of Aspherical Particles of Arbitrary Shape". In: *EPJ Web of Conferences* 140 (2017), p. 06007. DOI: `10.1051/epjconf/201714006007`

- Simon Weis and Matthias Schröter. "Analyzing X-ray tomographies of granular packings". In: *Review of Scientific Instruments* 88.5 (May 2017), p. 051809. ISSN: 1089-7623. DOI: `10.1063/1.4983051`

- Simon Weis, Gerd E. Schröder-Turk, and Matthias Schröter. "Structural similarity between dry and wet sphere packings". In: *(In preparation for peer review)* XX (Aug. 2018). URL: `https://arxiv.org/abs/1808.04342`

- André Schella, Simon Weis, and Matthias Schröter. "Charging changes contact composition in binary sphere packings". In: *Physical Review E* 95.6 (June 2017). ISSN: 2470-0053. DOI: `10.1103/physreve.95.062903`

- Anais Giustiniani, Simon Weis, Christophe Poulard, Paul Kamm, Francisco García-Moreno, Matthias Schröter, and Wiebke Drenckhan. "Skinny emulsions take on granular matter". In: *Soft Matter* (2018). ISSN: 1744-6848. DOI: `10.1039/c8sm00830b`

- N. Thyagu, M. Neudecker, Simon Weis, Fabian Schaller, and Matthias Schröter. "Local analysis of the history dependence in tetrahedra packings". In: *Physical Review E. (in review)* (2018). URL: `http://arxiv.org/abs/1501.04472`

The flicker book images in the top corner on even pages show XY-slices through a tomogram of a dry sphere packing. The spheres are aqualino gel spheres with a mean diameter of $d = 3$ mm. The spatial resolution of the tomogram is 37 μm. In order to obtain a clearer image the gray values of the tomogram have been inverted and the brightness has been adjusted.

The images in the top corner on odd pages show a subset of particles and liquid clusters from a wet sphere packing. All liquid clusters around the central (red) sphere as well as all particles connected via liquid clusters are shown. Liquid bridges occur between particles in contact (the liquid cluster is a ring, e.g. on page 5) as well as between particles which are close but not in contact (in which case the liquid cluster has no hole, e.g. on page 115).
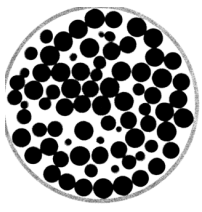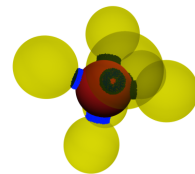
Abstract

Particulate and granular materials are ubiquitous in nature, industry and science. In such systems the spatial structure plays a central, often dominant, role in determining physical properties. In this thesis, I develop X-ray tomography methods and quantitative structure measures to examine various experimental particulate systems, such as dry and wet monodisperse sphere packings, bidisperse sphere packings, packings of frictional emulsion droplets or tetrahedral packings.

The properties of particulate systems depend strongly on the local environment of each particle, as interactions between particles are local in most cases, e.g. repulsive contact forces or cohesive liquid bridges. Therefore geometric approaches to characterize the local environment are needed. This local environment is characterized by the Set-Voronoi tessellation. While a Voronoi cell of a particle is the volume that is closer to the center of this particle than to any other particle, the Set-Voronoi cell is the volume that is closer to the boundary of the particle than to any other particle surface. Set-Voronoi tessellations can be used on arbitrary particle shapes and configurations. The Set-Voronoi tessellation allows for a local description by geometric measures, mainly the local packing fraction and different shape measures based on Minkowski functionals and Minkowski tensors. Independent of the Set-Voronoi tessellations the contact number is measured. As contacts are a key mechanism of transmitting forces through the system, the contact number is an important measure for the mechanical stability. In this work four different physical systems are investigated using structure measures:

Tribo-charging in bidisperse sphere packings   Tribo-charging describes the generation of electrical charge on particles by collisions. It can lead to either repulsive or attractive forces within a packing. Packings of bidisperse spheres made of polytetrafluorethylene are analyzed in order to determine the influence of tribocharging on segregation, packing fraction and contact numbers. By controlling the humidity while shaking the beads the tribocharging can be controlled. For such systems, we here show that the contact numbers are charge dependent: With increasing charge density the same-type contact numbers decrease while the opposite-type contact numbers increase.

Tetrahedral packings   When compared to sphere packings, tetrahedral particles show an increased complexity due to the fact that different contact types (face-to-face, edge-to-face, edge-to-edge, vertex-to-face contacts) impose a different number of mechanical constraints. History dependence is defined as the fact that apparently identical granular samples will differ depending on their history of preparation. The effect of history dependence is visible in the investigated packings of plastic, injection-moulded tetrahedral particles. We perform a local analysis of the contact distribution by grouping the par-

ticles together according to their individual local packing fractions, as obtained by the Set-Voronoi tessellation. We then show that for sufficiently tapped packings the number of face-to-face contacts becomes a universal function of the global packing fraction, while the edge-to-face and point contacts vary with the applied packing protocol.

"Skinny" emulsions Frictional emulsions are a new, interesting type of soft and deformable particulate system. We present a first systematic analysis of the structural features of such systems using X-ray tomography on polyethylene glycol drops. While in normal granular systems the particles are assumed to be ideally hard, the droplets in emulsions are deformable. Systems with different drop sizes are investigated with respect to the pair correlation function and packing fraction distributions. The local structural properties of these system are quite interesting as some aspects are similar to packings of hard, frictional particles, like the local packing fraction distributions and the constant global packing fraction with emulsion height (Janssen effect). Other properties are quite different from hard frictional particles, for example the flat pair correlation function. When compared to other emulsion systems it becomes obvious that friction and adhesion have a major impact on the local structure of the packing.

Liquid-stabilized sphere packings The mechanical properties of granular systems change significantly when small amounts of liquid are present in the packing due to the formation of capillary bridges. The structural differences between dry and wet sphere packings are examined using a model system of monodisperse polyoxymethylene beads and bromodecane as a wetting liquid. Our analysis demonstrates that no visible structural differences are found with respect to the contact numbers and packing anisotropy. Additionally the bridge number, the average amount of bridges per particle, is reported to be higher by a value of 2 than the contact number, independent of packing fraction, preparation method and liquid content.

All systems investigated in this thesis have in common that the structural properties play a governing role for the physical properties. Thus gaining insight into the internal structure by using X-ray tomography will help to get a better understanding for granular and particulate systems. The importance of Set-Voronoi tessellations as a description of the local environment and their general applicability is demonstrated in the investigated systems. Our investigations focus on granular and particulate systems. Other disciplines, for example in soft matter physics, are likely to benefit from the methods and results, which are discussed in this thesis as X-ray tomography and Set-Voronoi cells are easily applicable to those systems.
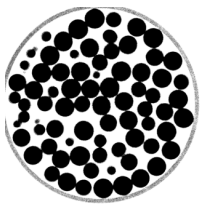
Zusammenfassung

Partikelförmige und granulare Systeme sind allgegenwärtig und nehmen eine wichtige Rolle in Natur, Industrie und Wissenschaft ein. Die räumliche Anordnung der einzelnen Teilchen spielt in solchen Systemen eine zentrale Rolle für die physikalische Eigenschaften des Gesamtsystems. In dieser Arbeit werden Methoden der Röntgentomographie und quantitative Strukturmaße weiterentwickelt, um verschiedene experimentelle Systeme zu untersuchen, wie zum Beispiel trockene und nasse monodisperse Kugelpackungen, bidisperse Kugelpackungen, reibungsbehaftete Emulsionen oder Packungen von tetraederförmigen Teilchen.

Die Eigenschaften korpuskularer Systeme sind insbesondere von der lokalen Umgebung jedes einzelnen Teilchens abhängig, da die Interaktionen zwischen Teilchen meistens lokal sind. Beispiele für lokale Interaktionen sind repulsive Kontaktkräfte oder kohäsive Kräfte durch Flüssigkeitsbrücken. Deshalb werden geometrische Ansätze benötigt, um die lokale Umgebung der Teilchen zu charakterisieren. Diese lokale Umgebung eines Teilchens wird über die Set-Voronoi-Tessellierung beschrieben. Die Voronoi-Zelle eines Teilchens ist das Volumen, welches näher am Zentrum dieses Teilchens ist als an den Zentren aller anderen Teilchen. Im Gegensatz dazu beschreibt die Set-Voronoi Zelle eines Teilchens das Volumen, welches näher an der Oberfläche dieses Teilchens ist als an allen anderen Teilchenoberflächen. Set-Voronoi-Tessellierungen können auf beliebige Teilchenformen angewendet werden. Die Zerlegung einer kompletten Packung in einzelne Set-Voronoi Zellen ermöglicht eine lokale Beschreibung mittels geometrischer Strukturmaßen, wie zum Beispiel der lokalen Packungsdichte und verschiedenen Maßen basierend auf Minkowski Funktionalen und Minkowski Tensoren. Die Kontaktzahl kann unabhängig von der Set-Voronoi-Tessellierung gemessen werden. Da Kräfte durch das System über Kontakte vermittelt werden, ist die Kontaktzahl eine wichtige Größe für die mechanische Stabilität von Packungen. In dieser Arbeit werden vier verschiedene physikalische Systeme mit Hilfe von diesen Strukturmaßen untersucht:

Aufladung durch Reibungselektrizität in bidispersen Kugelpackungen Reibungselektrizität (Tribo-charging) beschreibt die elektrische Aufladung von Teilchen durch Kollisionen zwischen Teilchen. Diese Ladungen können zu anziehenden oder abstoßenden Wechselwirkungen innerhalb einer Packung führen. Bidisperse Kugelpackungen bestehend aus Kugeln aus Polytetrafluorethylen werden im Hinblick auf den Einfluss von Tribo-charging auf Segregation, Packungsdichte und Kontaktzahlen untersucht. Durch die Luftfeuchtigkeit während der Präparation der Packung kann Tribo-charging gezielt kontrolliert werden. Für solche Systeme wird hier gezeigt, dass die Kontaktzahlen ladungsabhängig sind: Mit steigender Ladungsdichte nehmen den Kontakte zwischen Teilchen der gleichen
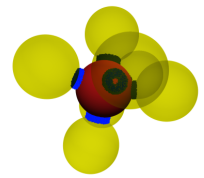
Größe ab, während die Kontakte zwischen Teilchen unterschiedlicher Größe steigen, ohne dass es zu Segregation kommt.

Tetraederpackungen   Im Vergleich zu Kugelpackungen können bei tetraederförmigen Teilchen verschiedene Kontakttypen (Fläche-zu-Fläche, Kante-zu-Fläche, Kante-zu-Kante und Punkt-zu-Fläche) auftreten. Diese unterscheiden sich in der Anzahl der fixierten mechanischen Freiheitsgrade. Das Stichwort *History dependence* beschreibt die Tatsache, dass augenscheinlich identische granulare Packungen sich abhängig von ihrer Vorgeschichte durch die Präparation unterscheiden. History dependence zeigt sich in den hier untersuchten Packungen von Tetraedern aus Spritzgussverfahren. Es wird eine lokale Analyse der Kontakttypen durchgeführt, welche nach den jeweiligen lokalen Packungsdichten aufgelöst ist. Dabei zeigt sich, dass die Anzahl der Fläche-zu-Fläche Kontakte eine universelle Funktion der globalen Packungsdichte ist, während die Kante-zu-Fläche und Punktkontakte von der jeweiligen Entstehungsgeschichte abhängen.
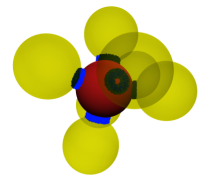
Reibungsbehaftete Emulsionen   Reibungsbehaftete Emulsionen sind ein neuer, interessanter Typ weicher und deformierbarer korpuskularer Systeme. Während in den bisher betrachteten Systemen die Teilchen als ideal hart angenommen werden, sind die Tropfen in Emulsionen deformierbar. Verschiedene Emulsionen mit unterschiedlichen Teilchengrößen werden im Bezug auf die Paarkorrelation und die Verteilung der lokalen Packungsdichten untersucht. Wir präsentieren eine erste systematische Analyse der strukturellen Eigenschaften solcher Systeme mittels Röntgentomographie. Die lokale Struktur der Emulsionen sind interessant, da einige Aspekte, zum Beispiel die Verteilung der lokalen Packungsdichten oder der Janssen Effekt, mit Packungen von harten, reibungsbehafteten Teilchen verglichen werden können. Andere Eigenschaften unterscheiden sich hingegen fundamental von Packungen harter Teilchen unterscheiden, wie beispielsweise die flache Paarkorrelationsfunktion. Vergleicht man die Ergebnisse mit denen anderer reibungsfreien Emulsionen, ist es offensichtlich, dass die Reibung einen großen Einfluss auf die lokale Struktur der Packungen hat.

Feuchte Kugelpackungen   Die mechanischen Eigenschaften granularer Systeme ändern sich grundlegend, wenn kleine Mengen Flüssigkeit in der Packung vorhanden sind und sich so Flüssigkeitsbrücken bilden. Die strukturellen Unterschiede zwischen trocken und nassen Kugelpackungen werden mit einem Modellsystem aus monodispersen Kugeln aus Polyoxymethylen untersucht. Als benetzende Flüssigkeit wird Bromodekan verwendet. Die Analyse zeigt keine strukturellen Unterschiede im Bezug auf Kontaktzahl und Anisotropiemaß zwischen nassen und trockenen Packungen. Außerdem wird gezeigt, dass die sogenannte Brückenzahl, die mittlere Anzahl von Flüssigkeitsbrücken pro Teilchen,
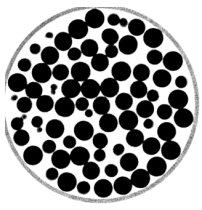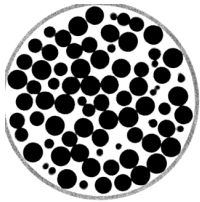
unabhängig von der Packungsdichte, Präparationsmethode und Flüssigkeitsgehalt um einen Wert von zwei höher liegt als die Kontaktzahl der gleichen Packung.

Alle in dieser Arbeit untersuchten Systeme haben gemeinsam, dass die strukturellen Eigenschaften eine bestimmende Rolle für die Physik der Systeme spielt. Durch den Einblick, den Röntgentomographie in die innere Struktur ermöglicht, kann ein besseres Verständnis für granulare Systeme entwickelt werden. Die wichtige Rolle von Set-Voronoi Tessellierungen als eine Beschreibung der lokalen Umgebung, sowie deren breite Anwendbarkeit wird an den vorgestellten Systemen gezeigt. Die Untersuchungen dieser Arbeit fokussieren sich auf granulare Systeme. Andere Forschungsgebiete, wie zum Beispiel die Physik der weichen Materie, können ebenfalls von den Methoden und Ergebnissen dieser Arbeit profitieren, da Röntgentomographie und Set-Voronoi Zellen leicht auf andere Systeme angewendet werden können.
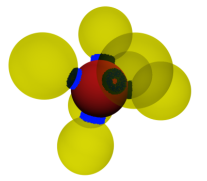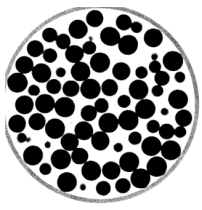
Contents

13

Introduction

Figure 0.1.: Examples of particulate systems. (a) Pharmaceutical pills come in different shapes and sizes. (b) Sand of a Baltic Sea beach. (c) A random, unordered packing of pistachios in a bowl. (d) A packing of spheres as a model system for particulate matter.

Particular systems play an important role in our modern society. More than half of the world production of raw materials for the pharmaceutical and chemical industry is provided in form of granulates [SGH04]. Processing granulates in industrial applications consumes roughly 10 % of the total energy production of our planet [Dur99]. Particular systems
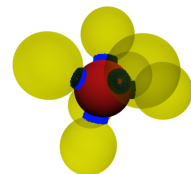
are also important in geophysics: Sand covers up to 10 % of the land surface of the globe [Bag53; Tso94]. Massive landslides, avalanches in snowy regions and dunes in the desert are some of the geophysical phenomena, which are based on sand and soil[Bag53; JN92; PH07]. Even something as delicious as a bag of pistachios comes as a random, unordered packing of irregularly formed particles.

The physics of granular matter is based on simple interactions between particles, and interesting effects that result from collective phenomena. A large variety of physical effects can occur in particulate systems. This includes different angles of repose [Car70; JLN89], flow and clogging of particles [Zur+05; TD15; Rub+15; TB16; Bör+17], segregation [Kud04; Sch+06; Poh+06; USS07; DS13; Liu+13; SHS17]. Many other effects exist and have been described in books and review articles [AFP13; WA08; CS99; Dur99; HW04; AT06].

The geometric structure of particulate systems is the key to understanding all other physical properties[KT14]. Although intensively studied, the structure of random particulate systems is still not fully understood, not even for simple model systems like packings of spheres. In this work, X-ray tomography (chapter 1) is used to obtain structural information about particulate systems. One of the main aspects of this work is the use of Voronoi and Set-Voronoi cells for a local description of structural properties (chapter 2), which are put to use in different physical systems (chapter 3). In dry particulate systems, the structure is governed by particle properties, like particle shape or inter-particle friction. In wet particulate systems, liquid bridges introduce a new way of transmitting forces (chapter 4).

A brief history of particulate systems   Working on particulate systems has a long history and some well-known physicists have worked on this topic. Analyzing particulate systems dates back to the roman poet and natural philosopher Lucretius. In 55 B.C. he was the first to mention granular flow in assemblies of poppy seeds [Dur99]. Interestingly, poppy seeds are still used in granular experiments today.

Leonardo da Vinci investigated piles of sand in the Renaissance but did not publish his results [Mel11]. In 1611, the advance of modern granular physics was born with Kepler's conjecture (see below). Among many other fields, C.A. Coulomb also worked on granular systems, especially on the geometry of stone structures, which is one of the foundations of the physics of particulate systems [Cou73]. In 1776 he presented a study of granular materials to the "Academic Royale" in Paris [HW04]. At roughly the same time, Hales investigated how a set of (irregularly shaped) particles assembles into a mechanical stable packing [Hal27] regarding vegetables. Faraday conducted experiments to find out how vibrations induce the formation of sand piles in 1831 [Dur99]. In 1895 Janssen worked on the saturation of pressure in granular media inside silo cells and derived the equivalent of the barometric formula for granular materials [Spe05].
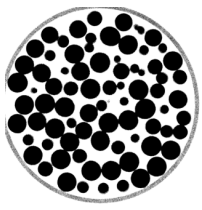
Figure 0.2.: (a) Lucretius, Roman poet and philosopher [Com16b]. (b) Leonardo da Vinci, Italian natural philosopher [Com18b]. (c) Charles de Coulomb, French physicist [Com18a]. All images public domain ☺.

With the beginning of the twentieth century the number of contributions from various scientists and engineers has grown quite tremendously. One of the earliest experiments regarding random sphere packings have been performed by Smith and Westman around 1930 [SFB29; WH30] and were followed by Scott and Bernal around 1960 [SCO60; BM60; Rut62; Ber64; BF67; Fin70] who started the ascend of modern granular physics.

Crystalline and disordered particulate systems   In static particulate systems the local structure is key to understanding the macroscopic mechanical properties of the complete system. This is due to the fact that forces can only be transmitted through contacts between particles in most particulate systems. The structure encountered in particulate systems is quite different from crystalline structures, which are normally taught in most solid state physics lectures. Crystalline structures (figure 0.3 (a)) show a distinct short and long range translational order in a way that a clear mapping from one particle (atom) to it's nearest neighbors is possible as well as to neighbors at larger distances. That is the reason why crystals can be described with powerful symmetries [Kit17]. While defects in (ideal) solid state physics are the exception, the structure of a particulate packing can be described as "one large defect itself" [Gas91]. To some extent Descartes' dream of a purely geometrical physics [DC96; des] comes true in particulate systems.
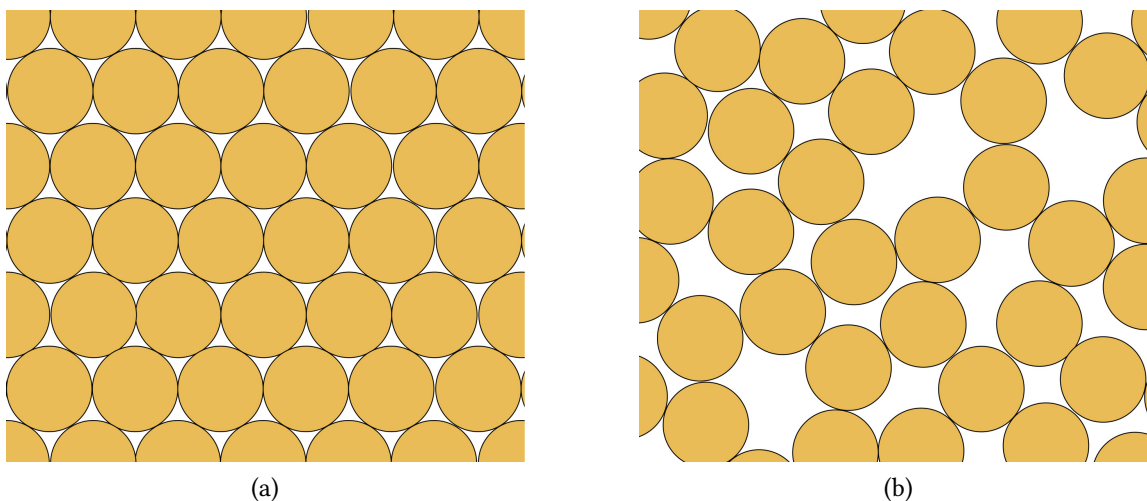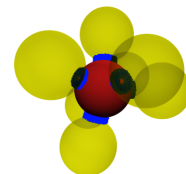
Figure 0.3.: Crystals (a) show a distinct short and long range translational order. Each particle has the same local packing fraction and number of contacts. In the random packing (b) no order can be found and each particle has a unique environment.

Structural properties of particulate systems have been intensively studied starting with one of the key aspects, the Kepler conjecture (1611) [WA08]. Kepler was asked about the densest packing of cannon balls (spheres) and conjectured the face centered cubic lattice (FCC) to be the optimal packing. Gauß showed in 1831 that the FCC lattice is the densest possible packing based on Bravais-lattices [TS10]. Only very recently (and around 400 years after the initial question) it has been proven that the FCC structure is in fact the densest crystalline packing of spheres [Hal05].

In contrast to these findings, this work will focus on random, disordered packings (figure 0.3 (b)). The question "What is a random packing?" is still not answered completely and discussions about that question are sill held today [Our72; TTD00]. While early publications focus on a phenomenological list of experimental and numerical results for the packing fraction, Torquato argues that the definition of *random close packing* is mathematically not precise and introduces the *maximally random jammed* state, which can be defined precisely using an order parameter. The second publication lays the mathematical foundation for studying the randomness of particulate packings. In this question entropy [EO89; ME89; Bau+18] plays an important role[1]. For a statistical description of random particulate systems, the question is not only "are there packings more dense or more loose?" but also "What is the probability of those packings to occur?".

---

[1]However, entropy does not imply temperature as known from statistical physics. In fact, a granular temperature can be defined in granular systems [Ipp+95; TB17], but granular systems are athermal nevertheless (see next paragraph in main text)
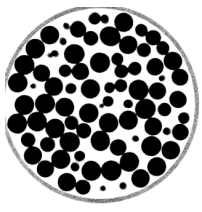
Granular systems   Two properties are common in granular systems: they are athermal and dissipative. Combined, both athermal effects as well as dissipative effects require some influx of external energy to the system for particles to be agitated. To illustrate, the nuts and flakes in muesli do not mix spontaneously, but require shaking or bumping on the kitchen bench to rearrange.

The athermal property describes the fact that the thermal energy of the environment is way too small to agitate the macroscopic particles of the packing. In contrast, in colloidal systems, where the particle size is in the range of nm to μm, thermal agitation of particles is possible [Jon02; Doi13]. In granular systems, this imposes a lower bound for the particle size. However, there is no upper bound for the particle size. Geophysicists as well as astrophysicists use granular descriptions across a broad range of scales, ranging from dust and sand particles with the size of some hundreds of μm over icy particles in the rings of Saturn of a size of around a cm up to ice floes drifting on the oceans.

In a dissipative system, interactions between two particles or between a particle and the container will lead to the dissipation of energy. This dissipation leads to the conversion of kinetic velocity, to deformation energy and can be quantified by the coefficient of restitution e [TM15]. This coefficient describes the ratio of final relative velocity to initial relative velocity before and after a collision. For a super ball made of rubber, which collides with a hard surface the coefficient of restitution is $e \approx 1$, while for a medicine ball a value of $e \approx 0$ is found.

Jammed systems   All packings investigated in this thesis are mechanically stable, which is related to the onset of finite shear-stress at the so-called *jamming transition* [LN98; LN01; SWM08]. In many-body systems the jamming transition describes the transition from a flowing state to a static, clogged or *jammed* state which is far from thermal equilibrium [HW04]. Jammed systems are the counterpart to low density systems such as a granular gas with respect to packing fraction. Jamming occurs in various system, e.g. in *traffic jams*, when the traffic flow becomes unstable and changes phase into a traffic jam [Tad+13] or in foams [LN01; KTH13]. Jamming in granular systems has been extensively studied in the last two decades [LN98; OHe+01; OHe+03; Zur+05; ZM05; Som+07; Hec09; HHS10; Sil10; Cia+11].

X-ray tomography of particulate systems   Obtaining structural information from three-dimensional particulate systems is hard, especially for bulk properties of large systems. As most particulate systems are opaque for visible light, normal optical methods can not be used to access the internal structure. First experiments regarding the structure of granular systems were performed around 1930 by Smith and Westman [SFB29; WH30] and were continued by Bernal and Scott around 1960 [SCO60; BM60]. However, they had to focus on tricks and indirect methods to gain access to the structural information.
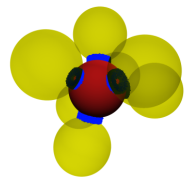
The increased availability of X-ray tomography in the last decades enables scientists to take an non-invasive look inside three-dimensional materials [Amo+17]. This is a major improvement, as not only surface effects, but also bulk properties can be accessed and analyzed. The use of X-ray tomography began with the discovery of "a new kind of rays" (German title: "Über eine neue Art von Strahlen") by Wilhelm Conrad Röntgen [Rön98]. He notes that those previously unknown rays, which were thus coined with the letter "X" are different from visible light and can not be blocked by otherwise opaque materials. First applications for everyday life were created shortly after the discovery: The so-called *Pedoscope* or *X-ray Shoe Fitter* (see figure 0.4 (b)) was used to check how much space is left when trying a new pair of shoes [Bus15]. However, it was found that X-rays impose a serious thread to health[2]

(a)   (b)

Figure 0.4.: (a) One of the first medical X-ray images: The hand of Wilhelm Conrad Rönt-
gen's Wife Anna Bertha [Com16a]. (b) The *Pedoscope*, a machine to check
whether a new pair of shoes is fitting. Both images are public domain [wik18].☉

X-rays soon made their appearance in medical applications. However, with the increased availability of computational power and new mathematical methods, like the Radon Transform or the Feldkamp algorithm [GBH70; FDK84; Rad86] a new way of measuring introduced the possibility to gain access to three-dimensional information [Kal06; Buz10]. This lead to what we know as X-ray tomography today. Most medical facilities nowadays

---

[2]Although it is known, that Röntgen did not know this when performing his early experiments, he nevertheless used the hand of his wife (instead of his own) for the first medical X-ray scan, see figure 0.4 (a).
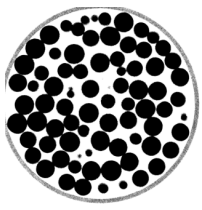
have at least one of such machines. The other big application of X-ray tomography nowadays is in non-destructive testing of materials [ezr18].

The implications for the scientific analysis of particulate systems are that the internal structure of granular materials is now accessible. This has been used in countless publications in general, but especially in the field of granular physics [Sei+00; Ric+03; AlA+05; Hal+10; Liu+13; Bar+17; Bör+17; Kar+18; Mik+18].

Local structural analysis using (Set-)Voronoi cells   Physical interactions in particulate systems are local, as forces can only be transmitted via contacts between particles or over a short distance, e.g. through capillary bridges. Each particle only *knows* about it's close local environment [Sch17].

The use of Voronoi cells [Vor09] for systems of spherical monodisperse particles allows the analysis of those local environments by dividing a system into non-overlapping cells, each of them belonging to a particle. Each cell is defined by the volume that is closer to the particle's center than to any other particle's center. The concept was originally introduced by Descartes, see references in [Oka+00], and has found countless applications [Joh06; FS01; Rah66; Ric+99; Sta+02].

However, the (point-)Voronoi construction requires a generalization when particles are not equally sized spheres. Set-Voronoi cells [Sch+13a] (also called *navigational map* [Luc+99] or *tessellation by zone of influence* [Pre92]) are a generalization of Voronoi cells and are applicable to generic particle shapes and sizes. The particles do not need to be convex or even simply-connected. In contrast to (point-)Voronoi cells, Set-Voronoi cells contain the volume that is closer to the boundary of the particle than to any other particle boundary. Details on the (Set-)Voronoi construction, numerical implementation and physical results obtained by (Set-)Voronoi cells can be found in chapter 2.

The (Set-)Voronoi cells are then used as for local description of physical properties. The volume of the cell leads to the definition of packing fraction (see next paragraph), while the shape of the objects is characterized using Minkowski tensors (see section 2.2.2).

Packing fractions in particulate systems   The definition of a local environment for each particle allows the definition of a local packing fraction Φ_l. By averaging, using the harmonic mean, a global packing fraction Φ_g can be defined as the ratio between total particle volume and total cell volume and thus measures how dense a system is packed. A detailed introduction on global and local packing fractions is given in section 2.2.1.

The global packing fraction Φ_g is a key parameter in particulate systems and granular packings in particulate and has been studied intensively. The bounds of the global packing fraction Φ_g in random systems have been tested. For spherical monodisperse particles

20
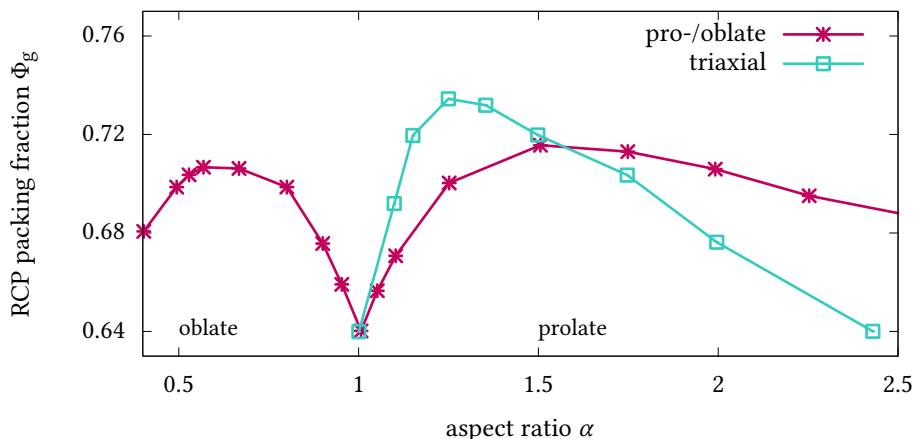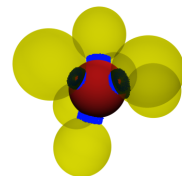
Figure 0.5.: Densest found global packing fraction Φ_g as a function of particle aspect ratio α for pro and oblate ellipsoids (pink) as well as for triaxial ellipsoids (turquoise). Data is extracted from [Don+04].

global packing fractions are in the range of $\Phi_g = 0.55$ to $\Phi_g = 0.64$. Those limits are the so-called *Random Loose Packing* (RLP) and the so-called *Random Close Packing* (RCP). A comprehensive overview of the history of RLP and RCP is given by Schröter [Sch14].

RLP is a phenomenological definition and describes the sphere packing with lowest packing fraction which is still mechanically stable [Sil10]. The first reported measurement of RLP was performed in 1962 [Rut62] and was followed by other publications [OL90; Jer+08; F3M10]. The value for the packing fraction at RLP is given as $\Phi_g^{\text{RLP}} = 0.60$ for glass spheres under gravity. However, all named publications deal with simple spheres without any further interactions. When the effect of gravity can be neglected (e.g. when sedimenting in density matched liquids [Don+06]) lower values down to $\Phi_g^{\text{RLP}} = 0.55$ [OL90] can be achieved. When introducing adhesive forces, e.g. through electrostatic or cohesive interactions between the particles, even lower values of packing fractions can be found, e.g. down to $\Phi_g^{\text{RLP}} = 0.275$ in a granular system of toner powder as commonly used in printers [VC06].

RCP is referred to as the densest state uniform spheres can achieve when randomly packed and is found at a value of $\Phi_g = 0.6366$ [SCO60; SK69]. It is found to be at $\Phi_g = 0.64$, see [Ric44; BM60; NDP00]. The absolute value given in literature depends on material properties as well as on the protocol used for preparing the system. With the increased used of simulation techniques more studies were published. One of the first studies to use Monte Carlo Simulations on RCP sphere systems was performed by [Fin70]. Multiple definitions for RCP are given, linking RCP either to the point pressure divergence in a hard sphere gas, which avoids crystallization [RT98; KL07] or to the onset of jamming [Sil+02;
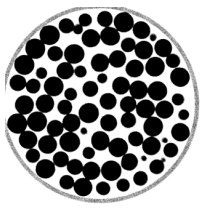
ZM05]. However, RCP is still an empirical definition, lacking a mathematical foundation. That is why Torquato introduced the *Maximally Random Jammed* (MRJ) state [TTD00].

Shape dependence in granular systems A simple generalization of monodisperse sphere packings are bidisperse sphere packings, which have been explored in detail [EY62; Pin+98; DRE98; KHH08; Bia+09; Hop+11; CT15; Kum+16; SHS17; SWS17; Sch+17a]. As already shown in figure 0.5, the shape of the particles beyond spheres is an important factor [ML03; BS13].
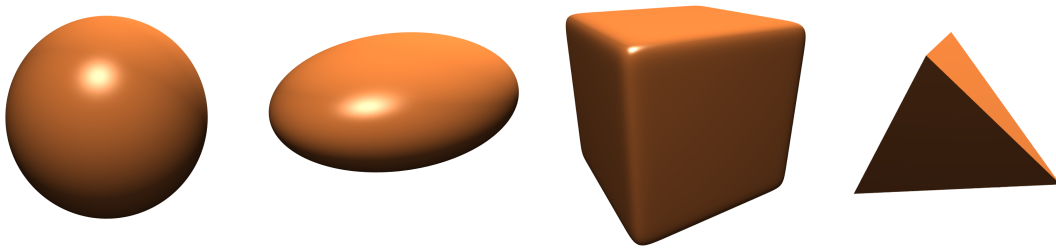
Figure 0.6.: Generalization of particle shape. Spheres (left) are the most simple model system. Ellipsoids (middle left) can be pro- or oblate or triaxial. Superellipsoids (middle right) introduce another parameter, while tetrahedra (right) have flat faces and sharp edges.

The simplest model system consists of spherical particles[3]. A typical generalization of spherical particles are pro- and oblate particles [Don+04; Sch12; Sch+15b] and triaxial ellipsoids, which have three independent axis lengths [Wei15]. Other types of particle shapes have been researched, such as super-ellipsoids [DC10], rod-shaped particles [Bör+12; Bör+17] or tetrahedra and octahedra [Neu+13; Thy+18], see also figure 0.6.

Forces in particulate systems The structure of a particulate system controls the forces. In two-dimensional systems forces between particles in contact can be directly measured using the photoelastic method [Wak50; MB05; Hur+14; Pap+16; DKP17; BKD18]. In three-dimensional systems there is yet no well developed experimental method, to conduct such measurements [HHS10; Saa+12; Hur+14; BDB15; Hur+16]. However theories exist, which describe the influence and distribution of forces in jammed systems based on numerical simulations [MJN98; OHe+01; Don+06; SHS07].

---

[3]For two-dimensional packings there is a particularly interesting app available for mobile phones which investigates the issue of shape in packings [gey18]. It allows the user to draw arbitrary two-dimensional convex shapes. Then a packing process under gravity is simulated and the packing fraction is measured. Users can compete for the densest packing fraction.
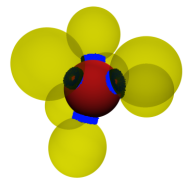
Figure 0.7.: Sculptures of sand are only possible due to the increased mechanical stability of wet granular systems. Image from [Com17]. ☉

Wet granular systems   Up to now only contact forces have been introduced. In wet packings (see flicker book images on the top right corner, figure 0.8 and chapter 4) another type of force can be observed: the cohesive force originating from liquid bridges. Cohesive forces act with a force of their own (created by the surface tension of the liquid bridge) on the connected particles. Additionally, liquid bridges also increase the frictional tangential force between the particles due to the liquid bridge pushing the particles harder together [Her13]. This leads to increased mechanical stability, which enables the building of sand sculptures, see figure 0.7.
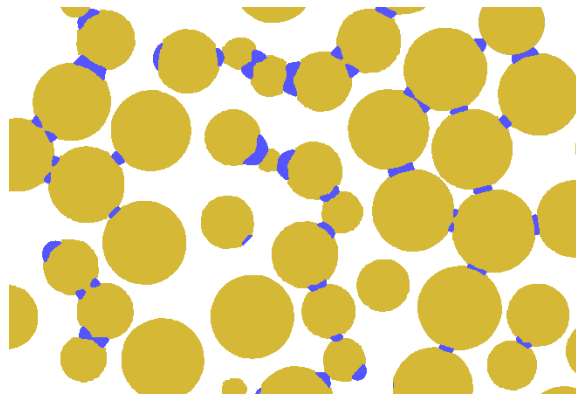
Figure 0.8.: Slice through a tomogram of a wet packing (POM particles at global packing fraction $\Phi_g = 0.596$, Bromodecane liquid content $\eta = 2.1\,\%$). Yellow corresponds to particles, blue to liquid and white to air.

Wet granular matter is clearly different from dry systems: wet systems are stable at lower packing fractions Φ_g [Her13]. The effect of liquid on the dynamical behavior of a system has been studied [Alb+97; Hor+97; Boc+98; HL97; FTP99; Mas+99; Ive+01; Ger+03b; Koh+04;
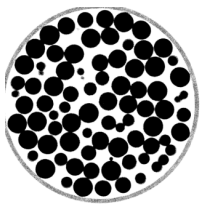
SGH04; Fou+05; Sch05a; Sch+08; LYY11; Van+12; Her13; KTH13; Fal+14]. The morphology of the liquid clusters inside wet systems has been investigated lately [Koh+04; Sch+08; LYY11]. This thesis investigates, amongst others, structural properties of dry and wet particulate systems and how they are governed by liquid bridges.
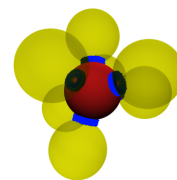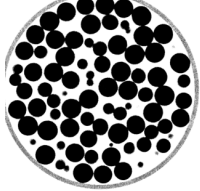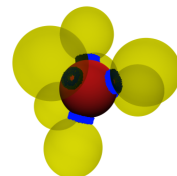
1. Measuring and analyzing granular packings using X-ray tomography[4]

Accessing bulk properties of granular materials is not an easy task. Granular materials are opaque to visible light [Amo+17]. Thus, with visible light mainly surface properties can be analyzed. It is an inherent drawback that bulk and surface of a granular packing can differ quite drastically in their physical properties [DW09].

The scientific examination of granular materials dates back to experiments performed by Smith in 1929 [SFB29] and Westman [WH30] in 1930. In those early experiments bulk properties like the contact number were accessed indirectly. By adding ink to a granular packing, letting the ink dry and disassemble the packing particle by particle it was made possible to count the number of contacts per particle. Other, quite integral measures, like the global packing fraction Φ_g of a packing can be obtained by measuring the height of a granular packing in a container of known volume. This leads to the definition of Random Close Packing (RCP, [SCO60; Ber64; NDP00; TTD00]) and Random Loose Packing (RLP, [Rut62; OL90; Jer+08; SWM08; F3M10]), see also section 2.2.1 and [Sch14].

In two-dimensional systems the variables of state are a lot easier to access than in three dimensions. A lot of experiments were performed in two-dimensional systems using the photoelastic method which was introduced in the 1950s [Wak50] and put to use by the Behringer group [HBV99; MB05] around 2000. As the photoelastic method allows to directly measure the forces in a two-dimensional granular material as well as the structure of the packing, a wide variety of variables are directly accessible. For example it has been possible to access the contact network, force anisotropy [MB05], particle scale anisotropy of the contact force networks [PD13; BDB15; Pap+16], the fabric and stress tensors [Bi+15] and lately *angoricity* [BKD18], a state variable in the Force-Moment Ensemble. Furthermore it was possible to test the validity of statistical ensembles for granular media, to identify dilatancy softening, to observe effects of fluid flow and to investigate the evolution of network architecture under compression [Pap+16; DKP17].

---

[4]The content of this chapter is partially based on the publication: Simon Weis and Matthias Schröter. "Analyzing X-ray tomographies of granular packings". In: *Review of Scientific Instruments* 88.5 (May 2017), p. 051809. ISSN: 1089-7623. DOI: 10.1063/1.4983051. Verbatim quotes of this paper are not necessarily labeled as such.
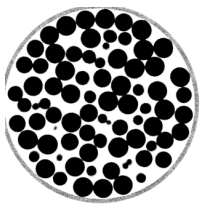
The increased availability of X-ray tomography setups enables scientists for the first time to take a non-invasive look inside three-dimensional granular materials [Amo+17]. This is a major improvement as not only surface effects but bulk effects can be accessed and analyzed on a (sub-)particle level. Structural properties like the position and orientation of each particle in a packing, the contacts per particle, the local packing fraction Φ_l or other local measures are accessible using X-ray tomography. Previous work using X-ray computed tomography has been performed for example in [Sei+00; AA06], by T. Aste [ASS05; ASS06; Ast06], by M. Saadatfar and A. Sheppard [Jer+08; DDA10; Saa+12; Saa+13; Rob+16; Kar+17; Sch+17a], by G. Viggiani, especially on non-monoschematic particles [Hal+10; And+11; Kar+18], and furthermore by [Cao+13; OTT04]. In [Saa+12] and [AA06; HA10] the forces in a three-dimensional packing of spheres and the strain field are analyzed, while in [Rob+16] structural properties of various porous materials (including porous rocks, sandstone and limestone as well as sphere packings and Swiss cheese) are investigated. A detailed description of previous work using X-ray tomography on particulate systems can be found in section 1.2.

This chapter starts with a description and introduction of X-ray setups in section 1.1. The X-ray setup used in this thesis is described in detail. It gives an introduction to the process of taking images and *reconstructing* tomograms. A review of the current state of scientific research of granular systems using X-ray tomography follows in section 1.2. Common techniques for particle detection are also discussed there. In section 1.3 the method used in this thesis is described in detail. Before the summary and outlook in section 1.6 closes this chapter, the data analysis will be discussed. This includes an analysis on how different parameters of the image processing and data analysis process will influence the quality of the image and of the resulting physical measures.

1.1. X-ray tomography

This section is an introduction to X-ray tomography, parameters and typical problems which can occur. For a comprehensive introduction on X-ray tomography, the interested reader can have a look at standard textbooks e.g. [Kal06], [Buz10] or [Sch16]. A detailed introduction on X-ray techniques on granular media is given in section 1.2.

1.1.1. Alternatives to X-ray microtomography

Most measurements presented in this work have been performed using X-ray microtomography (also called μm computed tomography). Before describing the method in detail, a brief overview of other alternative measurement setups is given.
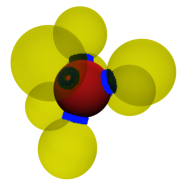
Medical X-ray scanners Most medical X-ray and X-ray CT scanners measure at lower X-ray energies, normally in the range of 30 keV for living tissue. This reduces the radiation exposure for humans. The second difference is only true for tomography setups: Here, not the (object) patient but the tube and the detector are rotated. While it is feasible to perform X-ray measurements for granular physics on medical scanners [Bör+17], the X-ray energies are typically too low for scientific applications.

Synchrotron radiation Another way of creating X-ray radiation is used at synchrotrons and has also been used for imaging granular systems [Ric+03; And+11; Kar+18; Bar+17]. A beam of electrons is created in a linear accelerator or kept in an storage ring. By deflecting the electrons using strong magnets, a monochromatic X-ray beam of high brilliance can be created. The intensities at synchrotrons are quite high, which allows for short acquisition times. However, the specimen size accessible in synchrotrons is limited to diameters in the range of mm. As this thesis investigates static structural properties of large scale systems with no time dependence, applying for beamtime at a synchrotron is not required for the experiments described here.

X-ray phase contrast X-ray phase contrast measurements rely on coherent X-ray sources and refractive optics. In this setup, the phaseshift of the X-rays when passing through the object is measured, allowing for improved soft tissue contrast. As a drawback phase contrast measurements require a complex setup. The improved contrast is not required for measurements of granular samples in most cases, as typical particle materials have sufficient X-ray contrast with the surrounding air.

Magnetic resonance imaging It is possible to access internal structural information via *Magnetic Resonance Imaging* (MRI) [Sta17]. If only one-dimensional scans are required MRI offers very fast acquisition times (around 100 ms). However, two- or three-dimensional scans take much longer. The spatial resolution when using MRI is in the sub-millimeter range which is not sufficient for the particles used in this study.

Laser sheet scanning When the particles of interest are transparent, it is possible to use laser sheet scanning [Jos17; Rie+18]. However, as most particles are opaque, this is not possible for this study.

Confocal microscopy Mostly applied to biological or colloidal systems [WW02; Mic+08], confocal microscopy [Paw06] allows to study particle positions and particle motion in three-dimensional systems. This is possible by using optical sectioning: A pin hole is used to block out-of-focus light, which allows to capture images at different depths in a sample. Those images can be combined to a three-dimensional image.

For this work X-ray μm computed tomography is chosen, because it offers very good spatial resolution and decent image quality. As only static spatial structures are of interest, the measurement time is not a critical parameter for this work.
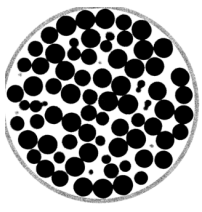
1.1.2. General X-ray setup

Every X-ray setup for real space measurements[5] consists of three parts, as depicted in figure 1.1 (a) and (b): The X-ray source (where a cone beam of X-rays is created) the sample holder (with object and manipulators) and finally the X-ray detector.

X-rays are created in the tube and pass through the object. The intensity of the X-rays after passing through the object (where they are attenuated) is measured at the detector, which produces a two-dimensional image, called *(transmission) radiogram* or *projection (image)*. X-ray Tomography combines a large number of radiograms, which are collected while the sample is rotated around an axis perpendicular to the beam direction. These radiograms are used to create a three-dimensional representation of the sample with the inverse radon transformation algorithm. The resulting three-dimensional image, also called *tomogram*, contains information about the X-ray attenuation at each voxel. A voxel is the three-dimensional equivalent of a pixel – *volume pixel*.

| (a) | (b) |
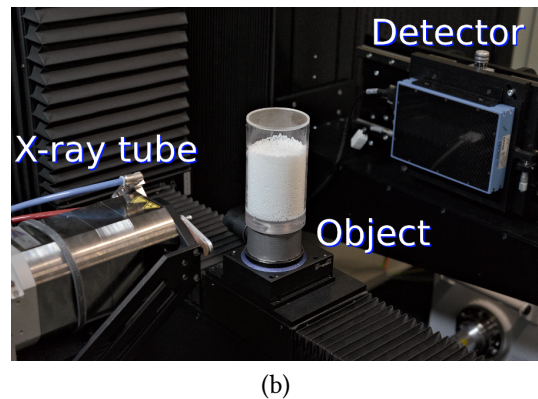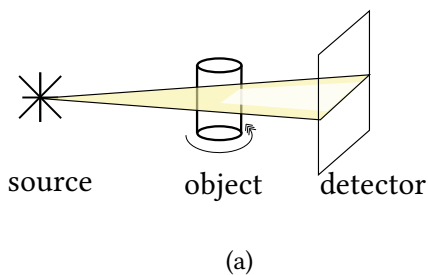
Figure 1.1.: (a) Generalized X-ray setup. X-rays are created in the tube and are attenuated when passing through the object. The detector measures the X-ray attenuation. (b) Photo of the CT-Rex Setup, showing the X-ray tube, the object and the detector.

X-ray source The X-ray source is a vacuum tube in which free electrons are produced using a heating current I_{heat} through a coiled filament. A schematic is displayed in figure 1.2 (a). Applying an acceleration voltage U_{acc} between the filament (kathode) and a target (anode) accelerates the electrons towards the target. The electrons enter the target material,

---

[5] Scattering methods, common in crystallography, work in the frequency domain (in contrast to the methods described in this section), are not covered here. However, they can also be used to investigate granular materials [Hur+14; Hur+16].
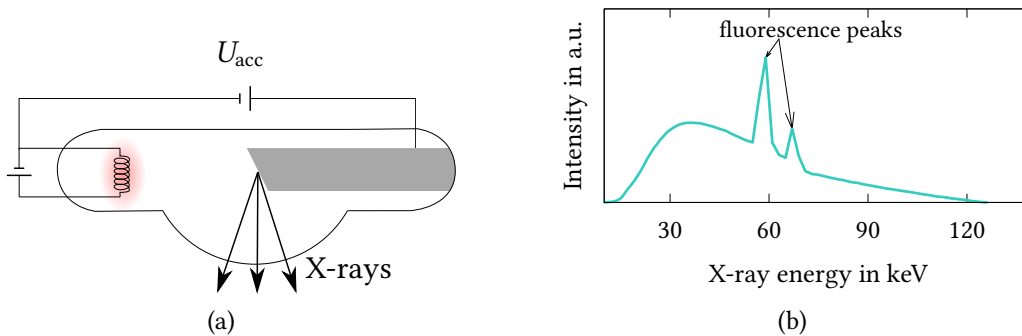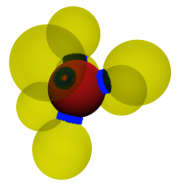
Figure 1.2.: (a) Schematics of an X-ray tube. (b) Exemplary X-ray spectrum from a tungsten X-ray tube operated at 125 keV. Data obtained from [Sie18].

often tungsten or molybdenum, creating two types of photon radiation: Further details on X-ray tubes can be found in textbooks [Kal06; Buz10].

Bremsstrahlung When charged particles decelerate, e.g. by being deflected in close vicinity to a positively charged atomic nucleus or negative electrons in an atomic shell, the moving particle loses kinetic energy, which is converted into photons. The energy spectrum of Bremsstrahlung is continuous with the highest energy given by the accelerating voltage U_{acc} as this is the maximum amount of energy the particle can loose.

X-ray fluorescence If the energy of incoming electrons is high enough to ionize an atom in the anode, this leads to an unstable atom for a very short time. The removal of an electron from one of the inner shells leads to electrons of higher shells *falling* down to the empty shell. This process corresponds to emission of photons of discrete energies, which leads to fluorescence peaks of characteristic energies.

Combined, both effects lead to the typical energy spectrum of an X-ray tube as shown in figure 1.2 (b). The created photon radiation can exit through a window typically made of beryllium glass. The passing through the tube window as well as the fact that X-rays are not only created directly on the surface of the anode, but also within a certain (small) penetration depth and thus have to pass through some anode material, leads to the so-called *self-filtering* of the energy spectrum of the X-rays. This self-filtering leads to a roll-off at low energies in the X-ray spectrum.

Despite the tube setup described above, there are other types of X-ray tubes like the transmission tube. In this transmission setup, the target is also the window of the tube and photons are created while being transmitted through the target. One benefit of transmission targets is that they in general allow for a smaller focal spot.
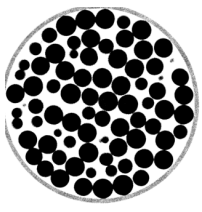
The parameters available to the user of an X-ray machine are the heating current I_{heat} as well as the acceleration voltage U_{acc}. The number of free electrons at the coiled filament scales linearly with I_{heat} and thus the number of photons is also linearly dependent on the heating current. While I_{heat} does not change the energy spectrum of the created X-rays (only its intensity), the acceleration voltage U_{acc} will change the energy spectrum as well as the photon count. Most tubes are limited by power P, which is calculated by $P = I_{heat} \cdot U_{acc}$.

Sample holder and manipulator   The sample holder is a set of translational stages and at least one rotational stage (manipulators) and allows the user to position the object within the X-ray beam as well as to rotate the object to different angles to create the two-dimensional images for the reconstruction algorithm. Stepper motors, piezo elements or linear stages are commonly used for the manipulators.

The X-rays passing through the object interact with the matter of the object via three relevant physical processes: The photo electric effect, Compton scattering and Rayleigh scattering. All three effects can be combined in a single variable, the *mass attenuation coefficient μ*, which is a material specific value. The attenuation of X-rays while passing through the object is described via the Lambert-Beer-law:

$$I = I_0 \cdot \exp(-\mu d) \tag{1.1}$$

Here I_0 and I are the intensity of the X-rays before and after passing through the object. d is the length of material which is passed by the X-rays. Note that the Lambert-Beer law is only valid for monochromatic X-rays (all photons have the same energy). For polychromatic X-rays (photons have multiple energies leading to a broad spectrum) the intensity after passing through the object can be calculated by the integral over different energies. Note that the mass attenuation coefficient is also a function of energy: $\mu = \mu(E)$ [NIS18].

Detector   Most X-ray tomography systems have a two-dimensional flat panel detector, which uses indirect detection of the incoming X-ray photons. Although there are many materials for the scintillator layer available, the basic principle is the same: The high energy X-ray photons are converted to photons in the energy range of visible light. Those low energy photons are then converted to electrons which are read by a TFT array.

Most common flat panel detectors can not resolve the energy of incoming photons. Their detection probability is strongly depending on the energy of the incoming photon. In typical use cases this is never a problem as all measurements are normally performed using the same detector and therefore can be compared directly.
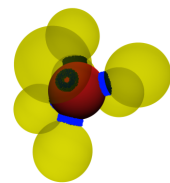
The main parameter for taking images is the integration time T_i. The number of detected photons scales linearly with T_i. Changing T_i is equivalent to changing the current I_{heat} of the X-ray source.

Image corrections   X-ray tomography software allows to correct the detected image with multiple correction images. The first correction is the *dark image*, also called *offset image*. The *dark image* is taken without any radiation, measuring the self-noise of the detector. In the correction, the *dark image* is subtracted from the actual image to be taken.

After that a *bright image* or *gain image* can be taken for a flat field correction with the X-rays switched to the desired X-ray tube parameters for the measurement. This will correct multiple effects. Different conversions of different pixels (black lines in figure 1.3 (a)) which are due to detector construction are normalized to same gain using the *bright image*. The fact that the detector is flat (and not spherical) leads to the issue that the center of the detector is exposed to a higher photon count than the edges of the detector, due to geometrical reasons. This decline can be seen in the plot profile of figure 1.3 (a) in the air region. Those corrections will significantly increase the image quality, as shown in figure 1.3 (b).

Note that while searching for the optimal X-ray tube parameters (U, I_{heat}), the detector image corrections need to be disabled. Otherwise, the corrections will change the resulting gray values, which might lead to wrong decisions when picking parameters. Furthermore multiple images can be averaged, which can help to get a good signal to noise ratio while not clipping the analog to digital converter of the detector.

1.1.3. Acquisition and reconstruction of tomograms

Using the setup described in section 1.1.2 it is now possible to take a projection image (also called *shadow image* in [Buz10]) of the object. The term *shadow image* originates from the fact that the detector measures the attenuation of the X-rays when passing through the object. So the detector "sees" the shadows the object casts.

The rotation stage below the object holder allows to take multiple images of the object at different rotation angles. For a full CT scan the full 360° are divided in equidistant angular steps and a sufficiently large number of those steps, normally 1800, should be performed[6]. Those projection images will now be used to calculate the *reconstruction* volume, which will from now on be called *tomogram* or *volume*.

---

[6]The required number of steps depends on the desired resolution of the resulting tomogram. A too low value will yield a bad quality image, too many steps will increase measurement time and bring no significant improvement of image quality except for a better signal to noise ratio.
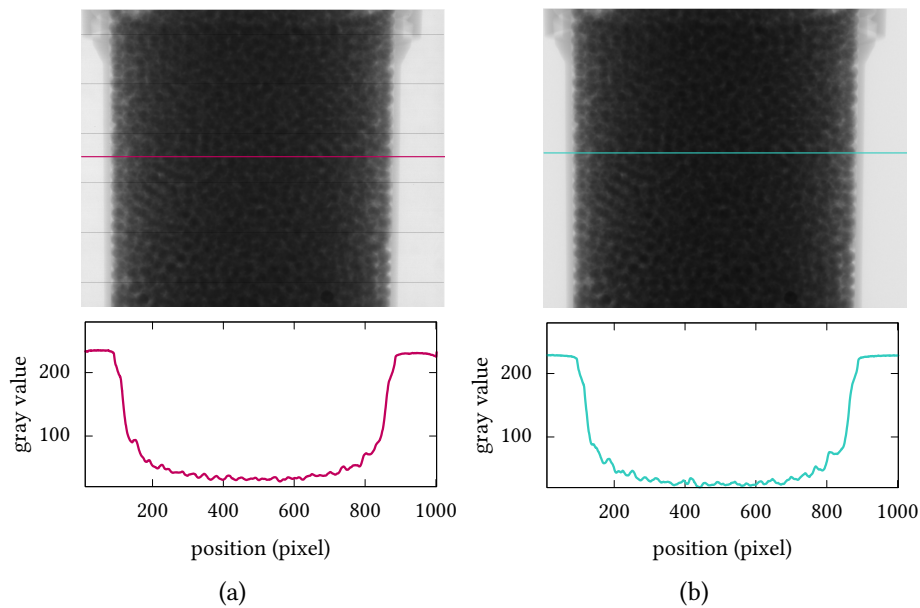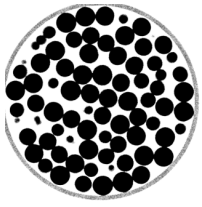
Figure 1.3.: Projection of a container with approximately 5000 glass beads with size 2.0 mm. The colored lines show the position of the line profile in the plots below each image. The profile has been averaged over a height of 10 pixels. (a) Uncorrected Projection. The black lines are due to detector construction. Note the decline in gray values near the edges of the profile plot. (b) Projection of the same sample with dark and bright correction applied. The black lines are corrected and the background is homogeneous.

The reconstruction of tomograms from the projections is a classic inverse problem. The mathematical foundation for solving this problem has already been created by Radon in 1917 [Buz10; Rad86]. The *filtered backprojection* [Her80; FDK84; Nat86] is the most common algorithm to be used for reconstruction. Yet other methods, for example the *algebraic reconstruction Technique* [GBH70], are also available.

Details of the specific reconstruction methods are of no further interest to this work as ready-to-use algorithms and programs are shipped with every X-ray machine. Furthermore there is a variety of free reconstruction software, e.g. [con18], [ast18] or [rtk18].

Each of the projections consists of pixels, which corresponds to the individual pixels on the detector. The reconstructed volume consists of so-called *voxels* (volume pixels). The volume will be a three-dimensional image, where each voxel can be addressed by three coordinates and represents the X-ray absorption coefficient at that coordinates. In this work slices through the volume will be shown in most of the cases e.g. figure 1.4 or 1.6.
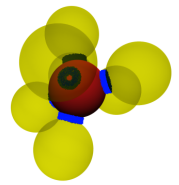
1.1.4. Influence of image parameters on image quality

Image quality itself, here just for the case of single images (in contrast to section 1.5), can be defined as the resolution (the image should resolve interesting details) and the contrast (gray values at regions with and without objects should be large enough). Noise – inherent to every imaging system – can be quantified by the *signal to noise ratio* (SNR) and has a detrimental effect on contrast as well as resolution. The resolution is limited by the size of the pixels of the detector, the size of the X-ray focus spot and the typical length scales of the system (in this granular case the size of the particles and the size of the whole container). A trade-off between resolution, number of particles in the sample and the particle size has to be made to find a reasonable compromise. For this work, the resolution is about 40 to 60 voxels per particle diameter (depending on the system under investigation) has been found as a reasonable resolution.

The contrast is based on the material properties (the mass attenuation coefficient of the particles) as well as the used X-ray settings. Generally speaking, X-ray contrast is better for low X-ray energies. This means a lower acceleration voltage U_{acc} will yield better contrast. However, for lower acceleration voltage U_{acc} the overall intensity will also be lower. To compensate this lack of intensity, a higher heating current is required. If the tube is already at the power limit, an increase in the number of images to average over or the exposure time can solve this problem, as this will increase the signal to noise ratio.

Furthermore, due to X-ray absorption large samples are harder to measure, as most of the X-rays get attenuated within the sample, resulting in a poor SNR. In this work the contrast was chosen to be as high as possible while a good signal to noise ratio is ensured.

The limiting factor for taking images in our lab is the measurement time. If the setup has an intrinsic time scale, the measurement has to be performed fast enough to be well below that time scale. Luckily this is not the case. However, for a reasonable amount of measurements[7] measurement time does play an important role and has to be balanced with the parameters mentioned right above. For this work the usual time for one complete CT scan varied between 0.5 and 9 hours depending on the system.

1.2. Tomography of granular systems

In the last two decades X-ray tomography has been used to investigate a lot of properties of granular media. This section gives an overview on the literature of this topic. It is ordered by the shape of the particles under investigation. At first studies of packings of spherical particles are summarized, followed by more complex particle shapes, like ellipsoids or spherocylinders. The section closes with packings of non-monoschematic systems. While

---

[7]e.g. to probe the system at various parameter combinations or to allow for sufficient statistics
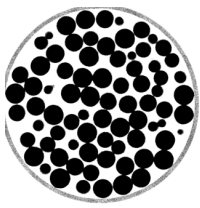
the previously investigated systems share a common particle shape, non-monoschematic systems feature particles over a broad range of shapes within one packing, for example real grains of sand, where each grain has a unique shape.

1.2.1. Previous work on spherical particles

In 2000 it was shown [Sei+00] that synchrotron X-ray microtomography with a remarkable resolution of 3.5 µm can be used to obtain structural information on monodisperse glass beads. Structural properties like the position of each particle as well as the local connectivity (based on a simple distance criterion) can directly be obtained from the date. This allows the calculation of the global packing fraction Φ_g, the pair correlation function $g(r)$ (see section 1.4.1), the nematic order parameter of the *bonds* and the fabric anisotropy introduced by the boundary walls.

Structural properties, contacts and local arrangements of random sphere packings were examined using X-ray tomography in a broad range of global packing fractions (0.58 to 0.64) [Ast05]. Some conclusions can be drawn from the experiments: The average number of contacts increases with the global packing fraction Φ_g, the packings have a compact force network and sphere packings can locally pack more efficient (denser) than crystalline packings[8]. More work has been performed on the topic of local configurations of spheres [Ric+03; ASS05]. The local configurations of particles, their relative occurrences and their correlations have been investigated in systems with global packing fractions Φ_g in the range of 0.58 to 0.64. Additionally, Voronoi volumes and their distributions are analyzed and it was concluded that the distributions decay exponentially for large volumes. The analysis of Voronoi volumes finally lead to the introduction of a rescaling for Voronoi volume distributions [Ast+07], resulting in an invariant distribution for granular media, similar to the Maxwell-Boltzmann distribution for a molecular gas. The rescaling resulted in a theory based on so-called *k-gamma* distributions. They require the minimal possible volume of a Voronoi cell, which relates to the maximal possible packing fraction, as well as the average volume of all Voronoi cells. The same method has been adapted to uniaxial ellipsoids in [SWK16]. This local approach has applications in a variety of other systems [Sta+02].

Further investigations on local motives, such as bridges (arches) in dry sphere packings, have been performed [Cao+13]. X-ray tomographies and simulations of glass beads are analyzed for bridge-like structures, which can be linked to the contact network of the packing. It has been shown that linear bridges are predominant for bridges with less than 10 particles, which follow an exponential size distribution. Larger bridges show a complex behavior and follow a power-law size distribution.

---

[8]The topic of the densest local arrangement has been further investigated and generalized for rotational symmetric ellipsoids in [SWK16].
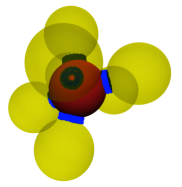
The first analysis of contact networks in three-dimensional sphere packings have been performed by [ASS06], see also section 1.4.2. It has been shown that the number of contacts Z increases from 5.5 to 7.5 when the global packing fraction Φ_g is increased from 0.58 to 0.64. A local analysis in the same publication leads to a positive correlation between the local number of contacts and the local density. An interesting combination of X-ray tomography and DEM simulations [DDA10] compares different structural properties of granular sphere packings, like the first peaks of the pair correlation function, contact numbers (using an early version of the contact number scaling introduced in section 1.4.2), contact number distributions, as well as global and local packing fractions with respect to contact numbers.

1.2.2. Previous work on non-spherical particles

However, spheres are just the most simple particles to look at. A detailed analysis using X-ray tomography on the structural properties of pro- and oblate ellipsoids has been performed in [Sch12; Sch+13b; Sch+15b; Sch+15a; SWK16]. [Sch+13b] is a technical publication on how to perform and analyze tomographic experiments of jammed ellipsoid packings. It shows how to perform image analysis and particle detection and explains an early version of the *Contact Number Scaling* (CNS) method, introduced in section 1.4.2 in this work.

[Sch+15b] has analyzed global and local packing fractions and contact numbers on a global and local level. It was shown that the global contact number of packings of frictional spheres and ellipsoids can be explained by an ansatz, which uses the local packing fraction Φ_l and the aspect ratio α of the particles.

The local arrangement of particles in ellipsoid packings has been investigated using Set-Voronoi cells and Minkowski tensors, see sections 2 and 2.2.2. It was shown that jammed ellipsoid packings obtained by X-ray experiments and by DEM simulations follow an universal local packing fraction distribution when rescaled properly (see section 2.2.1). Furthermore the shape and anisotropy of the Set-Voronoi cells is quantified using Minkowski tensors. The Average cell shape for a given local packing fraction Φ_l does not differ between dense and loose sphere packings. However in ellipsoid packings the local structure of dense and loose ellipsoid packings differs substantially [Sch+15a].

For soft, compressible spheres under compression, forces inside a granular packing due to particle deformations under have been identified [Saa+12].

Other groups have investigated other particle shapes than spheres and ellipsoids with X-ray tomography, like spherocylinders, tetrahedra or octahedra. Structural properties like the alignment, ordering and rotation of elongated spherocylinders was studied in
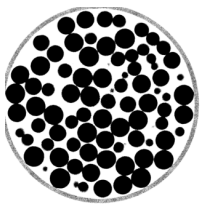
shear flow [Bör+12]. Using X-ray tomography allowed the access of dynamical structural properties through particle tracking.

Flow and clogging of granular materials of elongated grains in a hopper have been intensively studied by the Stannarius group [Bör+17] with respect to the particle's aspect ratio for spheres and spherocylinders. Subjects of interest are structural features like the local packing fraction, the alignment and orientations of the particles in the flow zone as well as clogging statistics and the number of particles included in the clogging dome at the orifice.

1.2.3. Non-monoschematic particles

It has been shown that using microfocus X-ray CT allows to construct clear images of microscopic sand particles [OTT04]. While this first approach to non monoschematic particles just used the tomograms to draw conclusions about the microstructure of the packing (no in depth image analysis was performed), it clearly was shown, that tracking of non-monoschematic particles is also possible [Hal+10]. Three-dimensional displacements and rotations of sand-grain particles have been measured using digital image correlation (DIC) techniques and are used to observe the evolution of localized deformation, which leads to the calculation of displacement- and strain-fields with a sub grain-scale resolution. A similar technique has been applied to analyze the deformation and breakage of individual sand particles [Kar+18]. A different approach has been used by [And+11] by using *ID-Tracking*, which can be compared to DIC-methods but without a use of an template particle for tracking.

Another collection of studies falls in this category, namely the analysis of porous media as performed e.g. in [Rob+16], who investigated structural properties of various materials, including porous rocks, sandstone and limestone as well as sphere packings and Swiss cheese. Other studies worked on consolidated and porous rocks [Pet09].

1.3. Particle detection

This section aims to describe the particle detection process. This process dramatically decreases the amount of data by converting the three-dimensional image, the reconstructed tomogram, which can easily have a size of multiple gigabytes (see section 1.1.3) to a list of particle positions, usually in the size of some kilobytes. All steps required in the process are described in this section including the multiple steps of image preprocessing and the particle detection algorithms based on an Euclidean Distance Map (EDM) Watershed approach. The code required to run the particle detection as well as the following data analysis (see section 1.4) can be found in [WS17], including a sample dataset. The method is based on [WS17], extending the work of [Sch+13b].
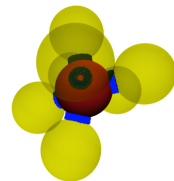
1.3.1. Image preprocessing

This section will cover all the steps of image preprocessing [RD76; Pra78; G79; Lee81; Das91; B02] in detail. The starting point is the tomogram of the packing with the mass attenuation coefficient μ encoded in the gray value of each voxel. Image preprocessing will take care of experimental noise, correct for beam hardening artifacts, binarize the volume and close internal voids. The result is a binary tomogram in which each voxel can have one of two values: one (white) if it is a voxel inside one of the particles, and zero (black) if it is an air voxel.

Like all imaging systems X-ray tomography is subject to noise. Noise can be caused by various physical, electronical or numerical reasons, like fluctuations of the photon flux created by the X-ray tube, electronic noise in the detector, or noise introduced by the reconstruction algorithm. The decision about "What is noise?" and "What is signal?" is a core question in all image analysis. If possible in any way, noise should be reduced to a minimum by choosing optimal imaging parameters. However no imaging systems will be completely free of noise. Treating noise afterwards during image processing is no easy task and highly subjective. Therefore all results obtained from image processing have to be checked for systematic dependence on the image analysis parameters used in image processing. This is done in section 1.5.

Bilateral Filter

Noisy gray values in the tomogram lead to problems in the upcoming image processing steps, and should be taken care of as early as possible. Some of the reasons for noise can be overcome by changing parameters of the measurement (see section 1.1), but often noise has to be dealt with as the first step[9] of image processing.

A lot of different filtering methods can be used for denoising [GW07]. The most common method to reduce noise is to use a low pass Gaussian filter [Das91; Par10]. The filter iterates over all voxel positions $\vec{x}$ in the tomogram and computes for each voxel:

$$f_{\text{Gaussian}}(\vec{x}) = k \sum_{\vec{\eta}} o(\vec{\eta}) \cdot g(\vec{x} - \vec{\eta}) \tag{1.2}$$

---

[9] It can be favorable to switch the filtering and the homogenization step, depending on the image material at hand. The homogenization step can *shift* the noise to different gray value ranges, so a bilateral filter afterwards will be fully efficient only in some regions of the image. If the noise is distributed equally over the image and not depending on the position, the filtering should be performed first. If the noise is depending on the *underlying* gray value, which means the noise in bright regions is stronger, the homogenization should be performed first.
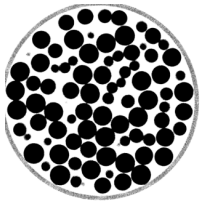
where $f_{\text{Gaussian}}(\vec{x})$ and $o(\vec{x})$ are the gray value of the filtered and the original image at position $\vec{x}$. k is a normalization factor. The sum runs over all voxel positions $\vec{\eta}$ in a predefined neighborhood of $\vec{x}$ and g is a Gaussian function. The parameter of g is the geometric distance between the voxels at $\vec{x}$ and $\vec{\eta}$. The mean value of g is always zero and its standard deviation σ_g can be used to control the extent to which the gray values at $f_{\text{Gaussian}}(\vec{x})$ are blurred. The effect of an Gaussian filter can be seen in figure 1.4 (a).

(a) (b)
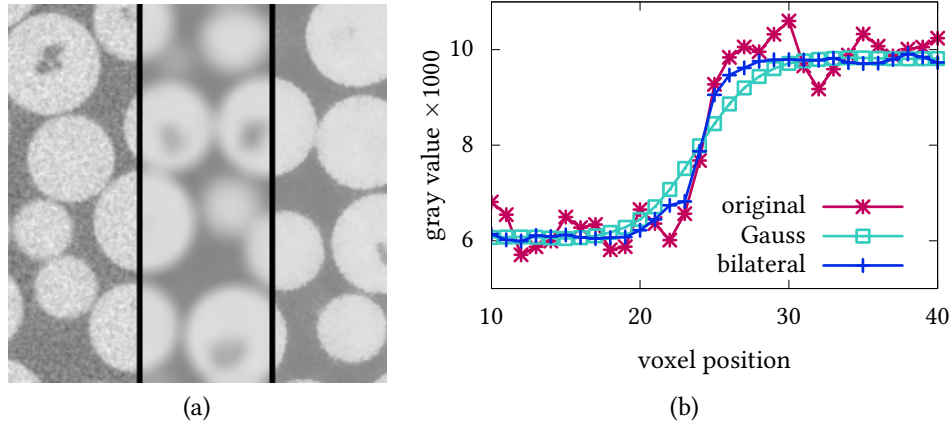
Figure 1.4.: (a) Tomogram before (left), after the Gaussian filter ($\sigma_g = 4$, center) and after the bilateral filter ($\sigma_g = 4$, $\sigma_p = 1000$, right). The Gaussian filter reduces noise but blurres the edges, while the bilateral filter keeps the edges sharp. (b) Gray values through an edge for the original image, the Gauss filter image and the bilateral filter ($\sigma_g = 4$, $\sigma_p = 1000$) image. The line profile after the Gaussian filter is broadened, while the profile of the bilateral filter is as steep as in the original image.

A major drawback of the Gaussian filter is that edges are blurred by the filtering process. This can be seen when looking at the line profile through an edge, as it is plotted in figure 1.4 (b). To suppress this effect, a bilateral filter [TM98] is used. This type of filter has found countless applications in science and image processing [Ela02; Jia+03; PD06].

A bilateral filter can reduce noise and simultaneously keep the edges sharp. This is done by introducing a second Gaussian function $p(o(\vec{x}) - o(\vec{\eta}))$. The term p works on the photometric distance, which is the difference between the gray values of the voxels at x and at η.

$$f_{\text{bilateral}}(\vec{x}) = k(\vec{x}) \sum_{\vec{\eta}} o(\vec{\eta}) \cdot g(\vec{x} - \vec{\eta}) \cdot p(o(\vec{x}) - o(\vec{\eta})) \qquad (1.3)$$
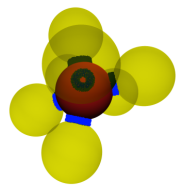
The Gaussian function p also has a mean of 0 and its standard deviation σ_p can be used to determine in which gray value range the filter is working[10]. Thus the parameters for the bilateral filter are the standard deviations of the two Gaussian functions σ_g and σ_p. In general they have to be adapted to the data at hand and a parameter scan must be performed to find the optimal combination of values[11]. The effect of different parameter pairs can be seen in figure 1.5, which shows the same region of a tomogram for different combinations of values of σ_g, σ_p and figure 1.4 (a), which shows the tomogram before and after the bilateral filter step.
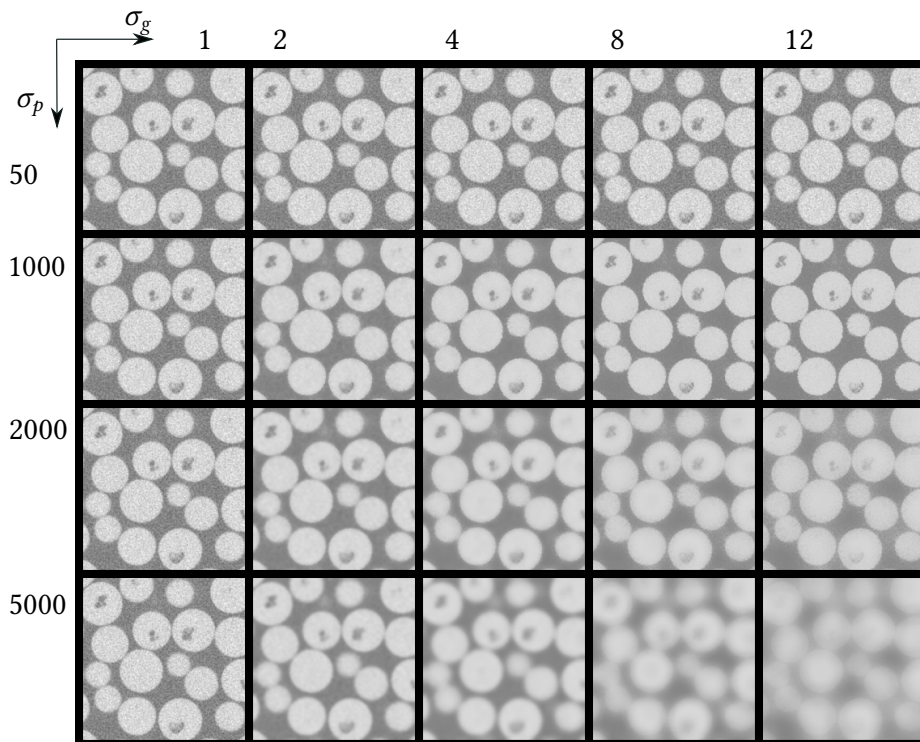
Figure 1.5.: Systematic parameter scan of the bilateral filter parameters: Bilateral filter results for different σ_g, σ_p pairs.

The parameters σ_g, σ_p have to be chosen in a way that the noise is reduced while simultaneously the edges of particles remain sharp. This can be done by eye with the tomograms or via line plots through edges of the particles. To verify the chosen parameters in a more robust manner, see section 1.5.1.

---

[10]In fact, the Gaussian filter is a special case of the bilateral filter with the parameter $\sigma_p = \infty$, $p = 1 =$ const. For those parameters the bilateral filter ignores gray value differences and acts as a normal Gaussian filter.

[11]It is sufficient to perform this parameter scan for a small region of the tomogram.
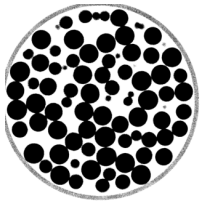
Radial intensity correction

Most X-ray sources create photons with a broad energy spectrum as shown in figure 1.2 (b). As the mass attenuation coefficient μ of the object depends in a non-linear way on the energy of the incoming photon, the decay of X-ray intensity with thickness is a complicated function [Kle99]. Unless complex algorithms are used to correct for beam hardening [Fuc98], most reconstruction algorithms [Her80; Nat86; Buz10] assume a simple, exponential decay. So-called *beam hardening* artifacts are the result. In the samples under investigation beam hardening leads to a radial gradient in gray values throughout a (actually homogeneous) sample. This results in lower gray values at the center of the sample and brighter voxels at larger radii. Figure 1.6 shows the average gray value in radial bins (azimuthal average). As the next step (called *binarization*) will use a single threshold value for the entire tomogram. This inhomogeneity has to be corrected beforehand.

| (a) | (b) |
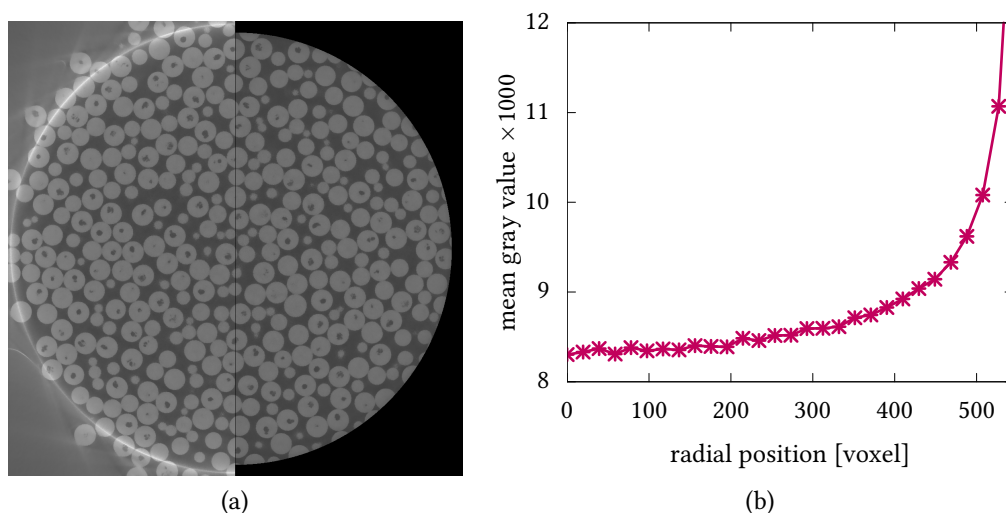
Figure 1.6.: Radial intensity correction. (a) slice through the filtered (left) and homogenized (right) tomogram. (b) radial mean gray value (azimuthally averaged).

This is done by normalizing each voxel using a correction factor. The correction factor is determined by the radial position of the voxel from the azimuthally averaged gray values. Between the sampling points a linear interpolation is used to obtain a smooth transition between the discrete values of the bin. This is shown in figure 1.6 (b).

The reconstruction algorithm can not reproduce sufficient information on the outmost parts of the tomogram due to the lack of information from the original projections, see section 1.1.3. Therefore the corresponding radial outer area in the tomogram is set to black and thus excluded from further image processing and particle detection. The resulting tomogram after the homogenization step can be seen in figure 1.6 (a) on the right side.
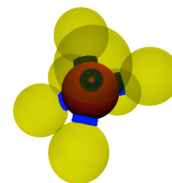
Binarization

The next step is to create a binarized volume. In this binarized volume, all voxels which belong to particles are assigned a value of 1 (white) while all voxels which belong to the air are assigned to a value of 0 (black). To determine which voxel belongs to particle or air, a gray value threshold is used. Every voxel value is compared with the threshold and then put into the respective class. This is justified as the grayvalue of each voxel is correlated to the mass attenuation coefficient μ in this point[12] and air has a very low value of μ (around $10\,\mathrm{cm^2\,g^{-1}}$), while the μ of common particle materials is orders of magnitudes larger[13].
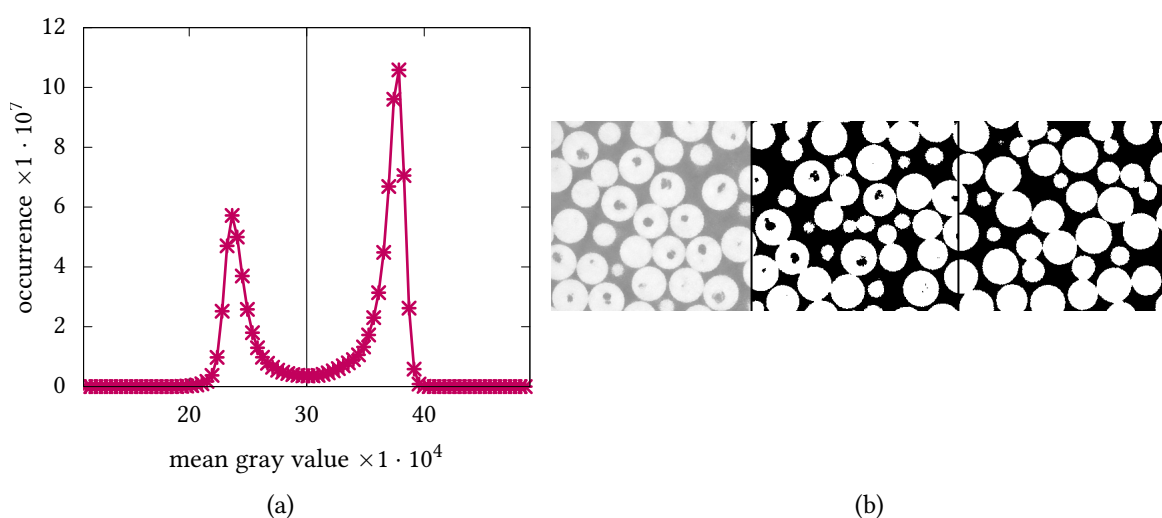
Figure 1.7.: Data for a dry system of monodisperse spheres (material: Polyoxymethylene, diameter $d = 3.5\,\mathrm{mm}$) at packing fraction $\Phi_g = 0.639$. (a) Gray value histogram used for binarization. The vertical black line is the selected threshold value. (b) homogenized (left), binary (center) and filled binary (right) tomogram.

The threshold to separate air and particle voxels can be determined using the histogram of gray values, see figure 1.7 (a). In this histogram two peaks are present. The left peak represents all the voxels which are air, while the right peak represents the particle voxels. The optimal threshold, which is between those two peaks, can be determined using Otsu's method [Ots75]. This method minimizes the weighted sum of the standard deviations of the two phases (air and particles) created by this threshold.

---

[12]Actually with beam hardening this correlation is a complicated function. As the beam hardening has been resolved in the homogenization, the assumption can still be made.

[13]Mass attenuation values for almost all materials are provided by NIST [NIS18].
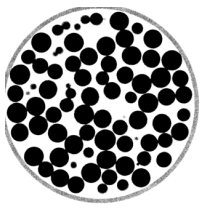
After the threshold is determined from the histogram each voxel can easily be assigned to one of the two classes. The resulting binary tomogram can be seen in figure 1.7 (b).

Otsu's method is not limited to separating two classes but can be extended to distinguish between any number ($\geqslant$ 2) of classes. This will be used in chapter 4 to determine between three classes: Air, particles and liquid. The result will not be one binary image with the particles in white and the air in black but two binary images. In both images air will be black. One image contains the particles as white clusters. The other image contains the identified water voxels as white clusters. This is called *three phase segmentation* and has, quite generally, applications beyond granular systems [SGH04; Sch+08]. For example, image processing comparable to the three phase segmentation has been applied to flow problems in porous media [AlA+05; Ber+13; Mur+15; GO16; Mik+18].

Filling internal voids

Particles can have internal voids or cavities (also called *lunker*) due to their manufacturing process. Those voids have to be removed so the calculation of the centroid of each particle is not influenced by the empty space. As the voids are completely encapsulated inside the particle, they are not connected to the exterior air. To remove the internal voids a simple algorithm can be used: At first the Hoshen-Kopelman algorithm, see appendix A.1, is run on the binarized image to identify all individual clusters of black voxels. The largest of those clusters is the surrounding air while all other clusters have to be internal voids. The cavities are filled by setting the voxels of all but the largest cluster to 1 (white). The result can be seen in figure 1.7(b, right). If the voids are connected to the air cluster, it is still possible to fill them by applying the above algorithm to individual slices in x, y, and z direction [Zha14].

1.3.2. Particle detection

This section starts from the binarized tomogram, in which each voxel is either belonging to a particle (white) or to the air (black) as shown in figure 1.8 (1). The result will be a list of particle coordinates. At first, each white voxel from the binary image has to be assigned a label (a particle ID), which uniquely identifies to which particle this voxel belongs. After this labelling step the positions of a particle can be calculated as the centroid of all of its voxels.

Euclidean Distance Map (EDM)

The first step for finding particles is to calculate the *Euclidean Distance Map* (short EDM) [RD76], which is also called *Euclidean Distance Transformation* (short EDT) [Saa+12]. It was
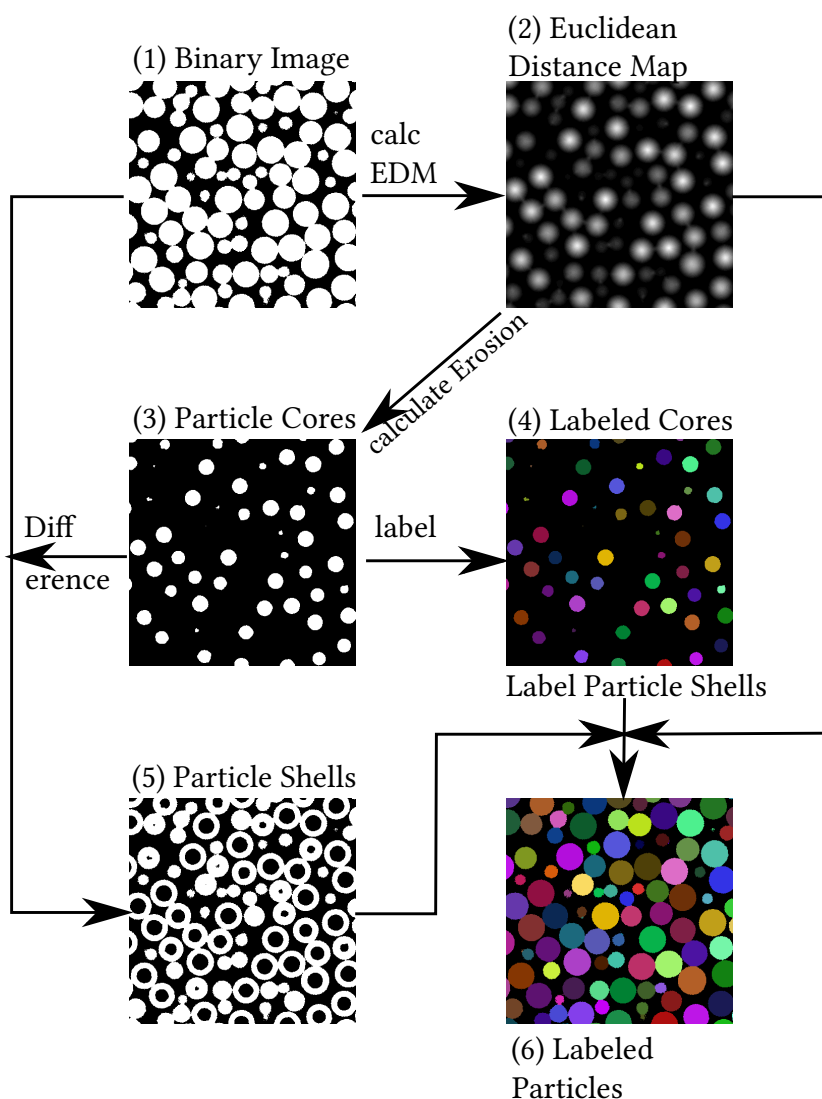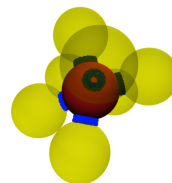
Figure 1.8.: Flow diagram for the detection of particles: The algorithm starts with the binary image (1) and calculates the Euclidean Distance Map (2) or *EDM*. The EDM can be used to obtain the particle cores (3) by performing an erosion. The particle cores are then labeled (4) using the *Hoshen-Kopelman algorithm*, see appendix A.1. The differences between (1) and (3) are the particle shells (5). Combining the information from (2), (4), (5) allows to obtain the completely labeled particles (6).
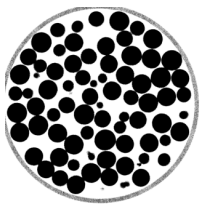
originally introduced by Danielsson in 1980 [Dan80]. The EDM is a distance transformation from the binarized tomogram ($b(\vec{x})$) to a grayvalue tomogram ($\text{EDM}(\vec{x})$). In the EDM, each white voxel is assigned the Euclidean distance d (stored as the gray value in units of voxels) to the closest black voxel.

$$\text{EDM}(\vec{x}) = \min\left(d(\vec{x}, \vec{\eta})\right) \quad \forall \vec{\eta} \quad |b(\vec{\eta}) = 0$$
$$\text{with} \quad d(\vec{x}, \vec{\eta}) = \sqrt{\sum(x_i - \eta_i)^2}$$

(1.4)

All black (air) voxels in the binary image are assigned a distance of 0. The central voxels of a particle are assigned the highest values as they are farthest away from any black voxel. The closer a voxel inside a particle is to the border of the particle the lower the assigned value is. Figure 1.8 (1) and (2) show a region from a binarized image as well as EDM of the same region. Different algorithms for the implementation of EDMs exist and yield different computational complexities [Dan80; PG87; Rag92]. In this work an algorithm comparable to [Rag92] is used.

Erosion

In the binary tomogram individual particles are connected due to their contacts and the limited resolution of the tomogram, aliasing artifacts, noise or a suboptimal threshold value. The erosion step [RD76] described in this section separates this cluster of particles into the individual particles by removing an outer layer. The thickness of this layer is called the *erosion depth* λ.

There are multiple versions of the erosion algorithm [You+81; GF84; VV88]. However, as the previously calculated EDM can easily be used for speeding up the erosion of the binary tomogram, we perform a simple thresholding of the EDM as proposed in [Rag92]. Thresholding the EDM with a threshold value T will erode the binary tomogram by a distance of exactly T voxels. All voxels with a gray value smaller than T are set to black, while all other voxels (their gray value is larger or equal to T) are set to white.

The optimal choice of the value of the erosion depth λ depends on the image material at hand. While a starting value for λ can be obtained by eye, a detailed analysis of the effect of this parameter to the (physical) results of the image processing should be performed and is described in section 1.5.2. Eroding the binary tomogram will result in a tomogram of separated particle cores, as displayed in figure 1.8 (3).
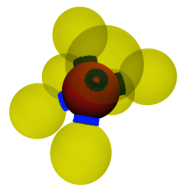
Labeling the particle cores

The separated particle cores can now be labeled[14] using the *Hoshen-Kopelman-*Algorithm (HK) [HK76], which is described in detail in appendix A.1 . The result of the HK step on the cores is a labeled tomogram of the particle cores, in which all voxels of each particle have been assigned the particle's label. The result of this step is shown in figure 1.8 (4).

Labeling the particle shells

The particle cores are now labeled, but a lot of voxels are missing due to the previous erosion step. To identify the correct label for the particle shells (see figure 1.8 (5)) the EDM is used again. For each voxel of a particle shell (those are the voxels which are white in the binary tomogram and black in the eroded particle core tomogram) an uphill search in the EDM is performed until an already labeled voxel from the labeled cores tomogram is found.

If a particle is touching the previously "cleaned" area outside of the tomogram (see radial intensity correction) or touches the first or the last slice in the tomogram, this particle has to be removed. This is due to the fact, that the particle is not completely contained in the tomogram. Thus the next step, the centroid calculation, would yield wrong results for this particle. The result is the full labeled particle image, see figure 1.8 (6).

Obtaining Particle information

Obtaining the particle information from the labeled tomogram is now easily done by calculating the volume of each particle (sum of voxels with the particle id) and position (centroid by averaging the positions of all voxels with the particle id). The result is a list of particle positions and volumes, which can be used for further analysis.

A detailed look at detection accuracy will be given in section 1.5. However, the quality of the centroid calculation once the labeled tomogram is computed, is not the limiting factor. This is due to the fact that all voxels of a particle are used for the centroid calculation, so the amount of voxels to average over is high compared to the size of one single voxel.

---

[14]Labeling the binary tomogram directly would not work as the particles are touching at their contacts, which would result in one large particle cluster.
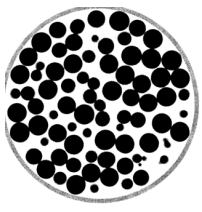
1.4. Data analysis

1.4.1. Pair correlation function

A widely used geometrical measure for the structure of particle configurations is the *pair correlation function* $g(r)$, or *radial distribution function* [Yar+73; HM06; Rap04], which has been used extensively in the structural analysis of random and crystalline packings [Rah66; Fin70; JT85; CW87; CJ93; Sei+00; OHe+01; WW02; Ric+03; DTS05; Ast05; ASS05; ZM05; HM06; TJ10; DDA10; JST11; Saa+12; Zha14; Pal+13; KT14; Bar+16; Sch17; SWS17; WS17]. $g(r)$ describes how the average number density changes while moving away a distance r from an arbitrary reference particle. In a system with N particles, $g(r)$ is defined as

$$g(r) = \frac{1}{N^2} \sum_i \sum_{i \neq j} \frac{\delta(r - r_{ij})}{\pi r \, dr} \tag{1.5}$$

where r_{ij} is the inter-particle spacing between particle i and j [HW04].

For systems accessible to radiation-scattering methods like atomic crystals, powders or liquids, $g(r)$ can be calculated by the Fourier transform of the static structure factor $S(\vec{k})$[Yar+73]:

$$\rho g(\vec{r}) = (2\pi)^{-3} \int [S(\vec{k}) - 1] \exp(i\vec{k} \cdot \vec{r}) d\vec{k} \tag{1.6}$$

When all the particle coordinates are known (as in our case for particulate systems), the direct calculation of the pair correlation function $g(r)$ without the use of the Fourier transform is possible, see equation 1.7. This makes $g(r)$ easily accessible in granular systems, however no analytic expression for $g(r)$ is known yet for random granular systems [HM06; OHe+01]. Quite generally $g(r)$ consists of a pattern of peaks and troughs. For large values of r, the pair correlation tends to unity $\lim_{r \to \infty} g(r) = 1$ and for short distances the pair correlation function vanishes $\lim_{r \to 0} g(r) = 0$.

The pair correlation function $g(r)$ can be related to various physical properties. In this thesis it will mainly be used to determine the particle size (figure 1.9 inset) and the contacts between particles (see section 1.4.2). It can furthermore be related to pressure, which allows to derive the equation of state for granular liquids [SDP02; MGG06].

In practice $g(r)$ is computed in shells of finite thickness Δr. This discretized version [Rap04] of the pair correlation function can be calculated by counting the number of particle clusters in a spherical shell around a reference particle:

$$g(r, \Delta r) = \frac{\langle N(r + \Delta r) - N(r) \rangle}{V_{\text{shell}} \rho} \tag{1.7}$$

$N(r)$ is the number of particles within a sphere of radius r around a given particle. $N(r + \Delta r) - N(r)$ corresponds to the number of particles in a spherical shell of radius r and
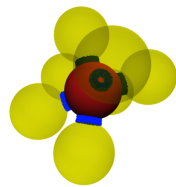
thickness Δr (Δr is assumed to be small compared to r). The average $\langle ... \rangle$ is taken over all particles in the sample. In practice, the numerator is computed by calculating the center to center distance of all pairs of particles and then storing this information in a histogram with binsize Δr.

The normalization in the denominator consists of two parts. Firstly, the volume of the spherical shell V_{shell} does depend on r: $V_{shell} = 4\pi r^2 \Delta r$. Secondly, dividing by the number density $\rho = \frac{N_{tot}}{V_{tot}}$ a totally uncorrelated system will have $g(r) = 1$.

When analyzing experimental data, Δr has to be chosen small enough, so important features are not smeared out, but large enough to have good statistics in each bin. Another effect to be taken into account is the finite size of all experimental samples. For increasing r, the number of particles for which at least a part of the spherical shell will be outside the sample volume (and thus resulting in less counts for those particles) will also increase. As $g(r)$ is required to be 1 for $r \to \infty$ by definition, the $g(r)$ calculated in this way is only valid[15] for approximately half the smallest box length [FS01; Rap04].
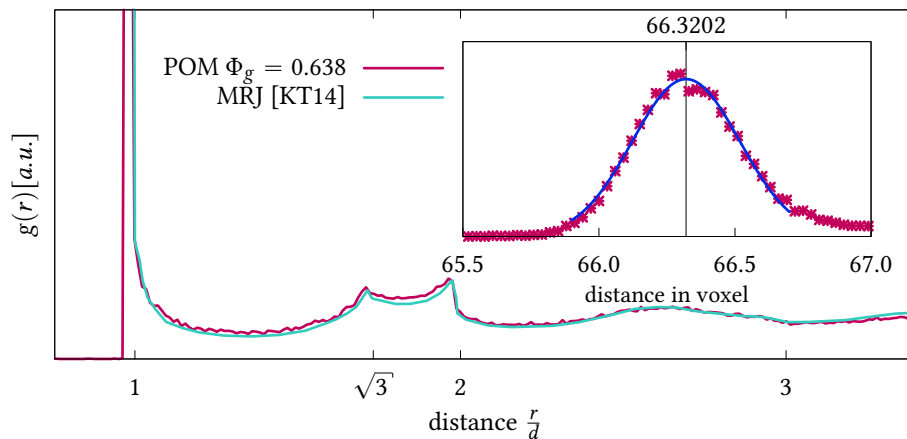
Figure 1.9.: The inset shows the first peak of the pair correlation function $g(r)$ and a Gauss fit to determine the particle diameter (radius in voxel). Fitting parameters are mean and standard deviation of the Gauss function as well as a multiplicative factor. Main panel: $g(r)$ for a system of monodisperse polyoxymethylene spheres with $\Phi_g = 0.638$ and a maximally random jammed (MRJ) sphere system as reference [KT14]. After the particle diameter has been calculated, r can be displayed in units of the particle diameter. The first peak is strongly pronounced, while decreasingly smaller features at larger r show the absence of long range order.

---

[15][Hie15] proposes a different approach: By normalizing to the autocorrelation of the homogeneous sample volume a very good fit even for distances larger than half of the box length. However, as in random systems order vanishes after some particle diameters, this is not required here.
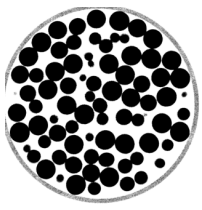
In an ideal gas (without any spatial correlations), $g(r)$ is a constant and set to 1 by definition. $g(r)$ is displayed for an amorphous packing of monodisperse spheres at $\Phi_g = 0.638$ and for an MRJ Packing [KT14] in figure 1.9. For distances shorter than a particle diameter d the value of $g(r)$ is zero because the spheres cannot overlap. Finite values in this range point to either the presence of additional smaller particles or accuracy problems during image processing. At the distance of one particle diameter there is a strong peak formed by all the pairs of particles in contact. Due to both the polydispersity of the particles and noise in the experimental data, this peaks will be broadened. This effect can be seen in the inset of figure 1.9. In amorphous systems without far-reaching order there are just a few other less prominent peaks of $g(r)$ for the values of $\sqrt{3}\,d$ and $2d$, which is shown in figure 1.9. But for larger distances $g(r)$ approaches the value of one, which is characteristic for disordered systems (aside from the finite size effects discussed above).

In an ideal world of absolutely monodisperse, hard spheres and zero error in the coordinate detection, the left shoulder of the first peak of the pair correlation function would be a step function. The shape of the right shoulder reflects the extent to which particles have almost formed contacts (also called spurious contacts [WS17]). For frictional particles the exact analytic form of this decay is not known, but the results discussed below indicate that it will also be a steep decay. Any broadening of the first peak can therefore be traced back to the polydispersity of the spheres and/or experimental noise[16]. The latter is well modeled by a Gaussian distribution [Bar+16], the former can often be approximated by a Gaussian.

The inset of figure 1.9 shows a Gaussian fit to the first peak [WW02] in the $g(r)$ in a system of monodisperse spheres. The two fit parameters are the mean and the standard deviation of the Gauss. The mean value corresponds to the interpolated maximum of $g(r)$, which is the most frequent separation two sphere centers will have. It is therefore our best estimate for the mean diameter of the spheres d_{mean}. The quality of this method to determine average particle diameters is demonstrated in a study of segregation in a polydisperse system [FSS15] where d_{mean} changes of fractions of a percent can be detected in a reliable way.

The standard deviation σ of the Gaussian fit expresses a convolution of the effects of polydispersity, experimental noise and particle detection. Thus it can be used as an indicator for the quality of the image processing, see section 1.5.1.

---

[16]In a system of soft particles, this broadening might also be due to deformations of the particles, see [Jos17; Giu+18].
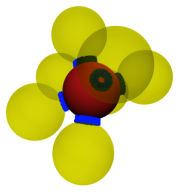
1.4.2. Contact numbers

Contacts are the points or areas between two neighboring particles, where those particles interact with forces [Sch14]. In a packing Z_i is the number of contacts of particle i. To form a mechanically stable packing, the translational and rotational degrees of freedom of each particle need to be fixed by the forces acting in the contact points [SW62; DTS05; Sch14]. The number of degrees of freedom a contact satisfies depends on the dimension of the problem as well as the shape of the particle and the friction.

In the case of a three-dimensional system, spherical particles and finite inter-particle friction, each contact has three individual force components (one normal component and two tangential components). As a contact is shared between two particles, one contact fixes 1.5 degrees of freedom. The number of degrees of freedom to be fixed is 6 (three translational and three rotational degrees of freedom). This leads to the requirement of $Z_i \geqslant 4 = Z^{\text{iso}}$ for mechanical stability. In general Z^{iso} is called the *isostatic* contact number required for mechanical stability. Z^{iso} can also be seen as a minimal number of contacts below which the system looses rigidity [Hec09]. Thus the mechanical stability of a particle packing is directly related to the contacts formed by the particles because those contacts block translational or rotational degrees of freedom.

The average contact number Z (also $\langle Z \rangle$ or Z_g) of a packing with N particles in total is defined as

$$Z = \frac{1}{N} \sum_{i}^{N} Z_i \qquad (1.8)$$

The average number of contacts Z is a very important ingredient of most theories dealing with static granular matter. The number of contacts is required for statistical mechanics approaches (for spherical [ZM05; SWM08] and non-spherical particles [Bau+13]), in granocentric models [Clu+09; Cor+10] or in other theories [Mou98]. It can also be linked to other physical properties of the system, like tensile strength [CS79] or heat transfer [WK82].

Contacts are easy to determine in simulations as all forces between particles are known to the algorithm [SW62; CJ93; RT98; OHe+01; Sil+02; ZM05; Som+07; SHS07; DTS05; HHS10; JST11]. Some numerical publications which investigate particulate systems without gravity distinguish contacts by the force acting on this contact F_z, see [SWM08]. Purely *geometrical* contacts bear no force $F_z = 0$, while *mechanical* contacts have a finite force $F_z > 0$. However, in experiments it is not possible to distinguish between those two types as individual forces cannot be accessed. As this work is based on experiments (including gravity), both contact types will be treated equally.

Contacts have also been measured in various experiments. Before the advent of tomographic imaging, researchers had mixed particles with small amounts of paint which was
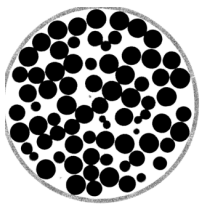
then attracted to the contact points by capillary forces. After the paint had dried, the packing could be disassembled and the analysis of the paint marks at the surface allowed to estimate Z for packings of spheres [SFB29; BM60; Pin+98]. The *Contact Number Scaling* (CNS) method [ASS05; ASS06; Sch+13b; Sch+15b; SWS17] is a robust method to measure contacts based on the particle positions and the shape of the particles.

Measuring contacts and contact number scaling

The availability of tomographic images seems to allow the direct observation of contacts in form of connected pathways of voxels between particle centers. However, in practice this idea is hard to realize [Saa+12; Hur+16]. The actual contact between two particles is a point contact and is formed in a small area only, corresponding to a small number of voxels. Even a minor error in the choice of the binarization threshold can erase or fill erroneous voxels and therefore lead to substantial errors for the detected number of contacts. Thus detecting contacts based on tomography data on a particle level is a hard task.

An alternative approach is a) to not consider contacts between individual particles but to compute Z from the whole ensemble of particles at once using their center of mass coordinates. And b) to rely on the information contained in the whole surface of the particles, not only at the position of potential contacts. The second point is already used in the particle finding algorithm, as small mistakes in the binarization threshold will influence all voxels in the same way. The resulting error for the detection of surface voxels is radially symmetric (as all voxels on the surface of the particle are treated equally) and will therefore have only a small influence on the determined center of mass.

Point a) is exploited by using the information from the ensemble of all particles to first determine the best estimate for the particle diameter itself (as discussed in section 1.4.1) and then to fit a model to the data which allows to identify both Z and the strength of experimental noise and polydispersity. This so-called *ensemble-based fitting method* is depicted in figure 1.10. The idea for this approach has first been suggested and applied by [Ast05; ASS05]. In the last years the method has then been used to determine Z for packings of spheres and ellipsoids [Sch+15b], tetrahedra [Neu+13], and cylinders [ZS14].

The ensemble based fitting approach to determine the global contact number Z works on the basis of the information contained in the first peak of $g(r)$. The first step is to endow all particle centers in the packing with a virtual diameter x and then determine the average contact number $I(x)$ of this packing by counting the number of intersections between these virtual spheres. For monodisperse spheres, $I(x)$ is equal to an integral over $g(r)$ up to the value x.
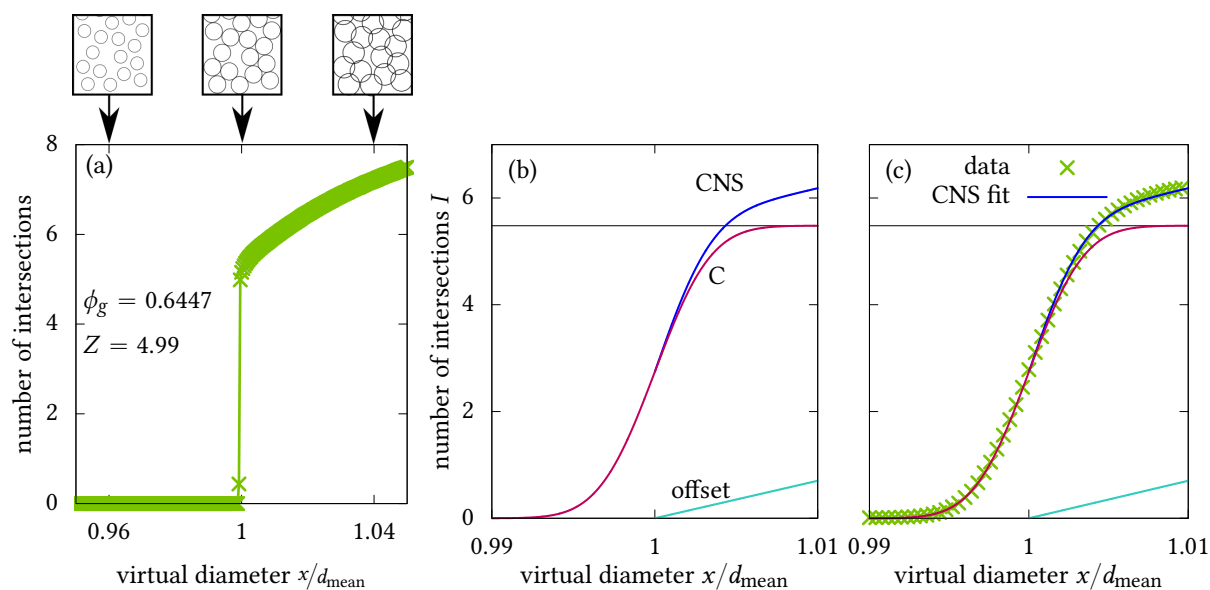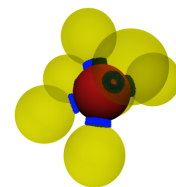
Figure 1.10.: Determining contact numbers by using ensemble based fitting. (a) Number of intersections between perfectly monodisperse spheres $I(x)$ from a simulation [Mak13]. The three images at the top show two-dimensional sketches for different virtual side lengths x. (b) the Contact Number Scaling function (equation 1.9) separated in its components: CNS, C, offset. (c) A fit of the CNS function (equation 1.9) to experimental data.

Figure 1.10 (a) depicts $I(x)$ for an idealized dataset of monodisperse spheres and in the absence of experimental noise[17]. The data in figure 1.10 (a) has been extracted from a packing created by simulation [Mak13]. This means the beads are perfectly monodisperse and there is only a neglectable numeric error on the particle positions. For $x < d_{\mathrm{mean}}$ there are no intersections between particles at all, thus $I(x)$ is zero. At the actual sphere diameter d_{mean}, I jumps to the global contact number Z. For values of $x > d_{\mathrm{mean}}$, $I(x)$ keeps increasing due to the formation of spurious contacts. Modeling this behavior results in a function $Z \cdot \theta(x - d_{\mathrm{mean}}) + \mathrm{off}^{\mathrm{ideal}}(x)$ with θ being the Heaviside step function and $\mathrm{off}^{\mathrm{ideal}}(x)$ modeling the a priori unknown increase of Z above d_{mean}.

In any experimental system, the particles are not ideally monodisperse and there will be experimental noise in the imaging system. These effects are similar to convoluting the above described ideal model with a Gaussian function centered around d_{mean} and with a standard deviation σ. The resulting model is called *Contact Number Scaling* (CNS) and introduces the CNS function:

---

[17]A comparable plot for numerical data was already shown in [RT98] (Fig. 9) in 1998 for a numerical hard sphere system.
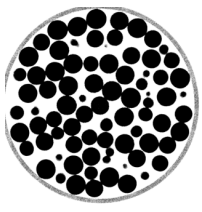
$$\text{CNS}(x) = C(x) + \text{off}^{\text{real}}(x)$$
$$C(x) = Z/2 \cdot (\text{erf}(\sigma \cdot (x - d_{\text{mean}})) + 1) \tag{1.9}$$

with σ being the width of the error function. Examples of $\text{CNS}(x)$, $C(x)$, and $\text{off}^{\text{real}}(x)$ are shown in figure 1.10(b). [18]

By fitting equation 1.9 to the experimental $I(x)$ data points (as shown in figure 1.10(c)), the global contact number Z can be determined as a fit parameter. The free fit parameters are Z, d_{mean} and σ. Here d_{mean} is not a fit parameter as it has already been determined from the Gaussian fit to $g(r)$ discussed in section 1.4.1.

One open parameter is the fitting range. The left border has no influence on the result (as no contacts can be formed for $x \ll d_{\text{mean}}$). On the other hand the right border has an influence on the result. The fitting range can be described by the value ϵ which is expressed in units of the width of the error function. A systematic analysis of the influence of ϵ on the contact number Z is performed in section 1.5.3.

If Z is determined for a larger series of tomographic datasets, all taken with identical imaging conditions, the number of effective fit parameters can be reduced further as neither the polydispersity nor the experimental noise will depend on the individual experiment. Consequentially, σ should also be the same for all experiments. We can therefore perform a second round of fits where σ is held constant at a value which is the mean of the first round of fits [Neu+13].

Once the global contact number Z has been measured, a local contact number Z_l can be identified. Therefore all particles are dilated to their actual size (d_{mean} in the fit of equation 1.9). After that the overlaps between each individual particles and its neighbors is calculated. Especially for frictional particles, Z_l shows a strong dependence on the local packing fraction Φ_l [Sch+15b; Thy+18]. Note that the local contact number of each single particle still is flawed as mentioned above. Only when averaged over a sufficiently large number of particles, the local contact number may be trusted.

For particles with different types of contacts, such as tetrahedra, a further step of image processing is required to determine the type of contact from the angle between the surface normals of the involved faces, see section 3.2 and [Neu+13].

---

[18]Note that the functional form of off^{real} is subject to lively discussions in the community. For our experimental data it can be shown, that any sufficiently good function can be used and that the result of Z does not depend on the functional form of off^{real}.
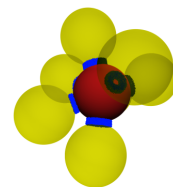
1.5. Image quality

Image quality is influenced by various factors (parameters for the X-ray setup and the reconstruction, particle size and mass attenuation coefficient, contrast between multiple materials in the sample, . . .) and it always depends on the application at hand.

The result of image processing and data analysis is a list of positions of particles. Those results are used as the measure for the image quality in this work. The particle positions will always have some uncertainty. However, the uncertainty can be minimized by performing a systematic analysis of the parameters used in the process. This systematic analysis is presented in this section.

Every setup is unique and imaging methods and results will vary between different setups. Thus the values for "optimal" image quality presented here will not be directly applicable to other setups. However, the methods to determine optimal parameters are applicable to other setups.

1.5.1. Bilateral filter

The bilateral filtering step (section 1.3.1) is one of the first steps in image processing and has a large influence on the particle detection and on the quality of the physical results. The two open parameters are σ_g and σ_p. If the values are chosen too small, noise will remain in the image, making the task of binarization and particle detection hard. If the values are chosen too large, edges will be blurred and particles are impossible to separate in the erosion step, resulting in one big particle in the packing. This will result in a decrease in the number of detected particles. Also larger values of σ_g drastically increase the computation time as the number of voxels to include in the calculation of one filtered voxel scales with $\mathcal{O}(\sigma_g^3)$.

One measure to quantify the quality of particle detection is the width of the first peak of the pair correlation function $g(r)$, see section 1.4.1. This value is easy to calculate and directly reflects the quality of the particle detection. The dependence of the width of the first peak of $g(r)$ on the σ_g, σ_p values is shown in figure 1.11 for one exemplary measurement of glass beads with diameter (2.0 ± 0.2) mm.

As it can be seen in figure 1.11, a too small value of σ_g leads to a large width of the peak and should therefore not be chosen. When σ_g is increased, the width decreases and an optimal value is found at $\sigma_p = 400$. This value can already be estimated by looking at the grayvalue histogram and estimating the width of each bin.

Finally a value of $\sigma_g = 6$, $\sigma_p = 400$ is chosen, as the value for $\sigma_g = 8$, $\sigma_p = 400$ differ by just 0.2 % (0.1807 and 0.1810). However the computations are faster with $\sigma_g = 6$. If larger
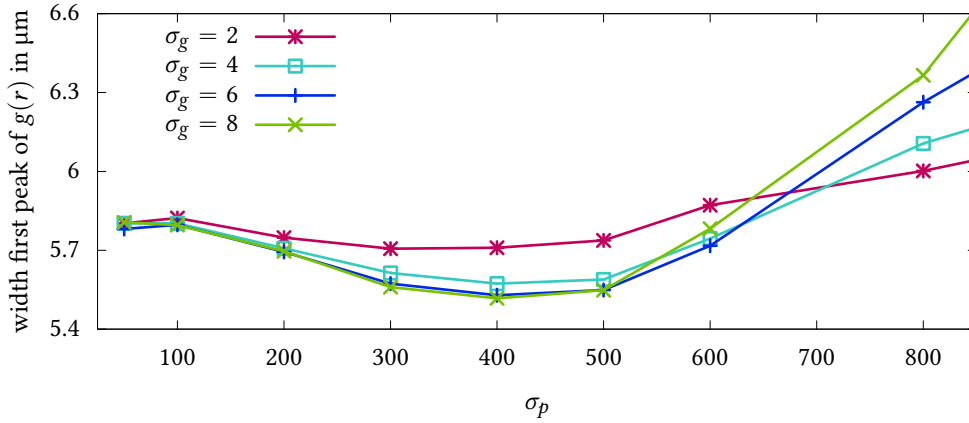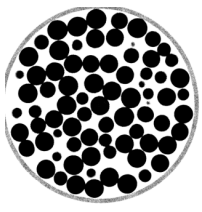
Figure 1.11.: Dependence of the width of the first peak of $g(r)$ on the bilateral filter parameters σ_g, σ_p. σ_g is given in voxels, σ_p is given in gray values. Lower values for the width of the first peak of $g(r)$ indicate a better image quality. Here the analysis is performed for a measurement of glass beads with diameter (2.0 ± 0.2) mm at a global packing fraction of $\Phi_g = 0.622$.

values for σ_g are chosen, particles blur and can not be separated from each other, which leads to a decrease in detected particles.

1.5.2. Erosion depth

The erosion depth λ is a central parameter for particle detection, see section 1.3.2. A first guess of λ can be obtained by eye. However for a systematic analysis, different values of λ have to be tested and the results have to be compared. If the value of λ is too small, particles will not be separated completely, and can thus not be identified as separate particles. If the value of λ is too large, it can happen that particles get eroded completely and are then missing for the following centroid calculation.

A nice way of checking for the correct value of λ (for sufficiently small particle polydispersity) is by looking at the volume of the resulting particles as a function of particle label (or z coordinate). If, for a specific value of λ, there are particle volumes with the double or triple average value, λ should be increased as particles are not separated from another. If volumes occur which are significantly lower than the average value, a smaller λ should be chosen as particles are split during the erosion process.
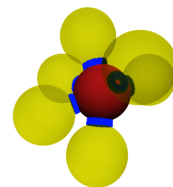
1.5.3. Contact number scaling fitting range

Another free parameter that has to be controlled is the fit range ϵ for the CNS function fitting. This is an important value as the CNS fitting does not only determine the contact number Z but also the actual size of the particles to be used later for example in the Set-Voronoi calculation (chapter 2).

In figure 1.12 the dependence of the global contact number Z of a packing as a function of the CNS fitrange ϵ is shown. For small values of ϵ the CNS fit is over a very short range and therefore the CNS function can diverge from the actual value. This results in crossing curves in figure 1.12. For large values of ϵ a large portion of the spurious contacts is taken into account for fitting, which could have a detrimental effect on the contact number.

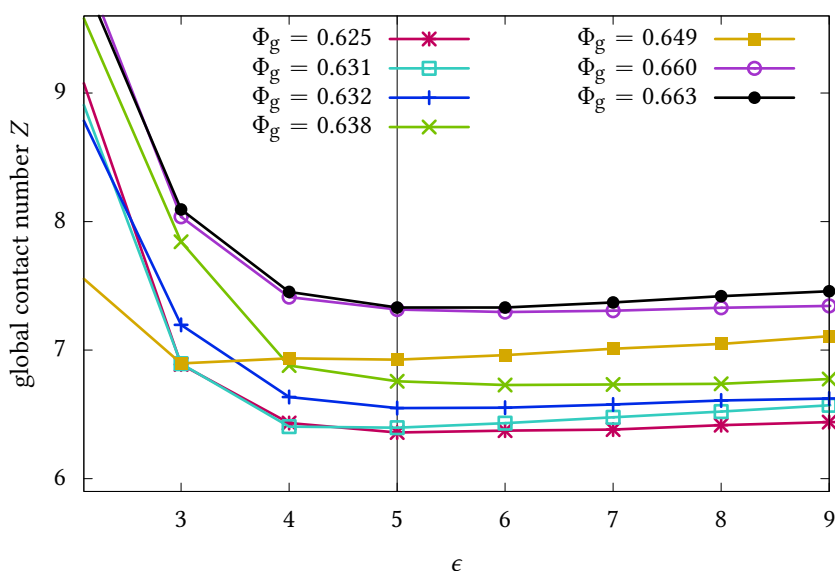Figure 1.12.: Global contact number Z as a function of the CNS fitrange ϵ. The process works for spherical and ellipsoidal particles. The vertical line distinguishes the chosen value of ϵ which is the point where the curves do not cross anymore. There is no clear distinction between the curves and they cross each other for small values of ϵ. For larger values of ϵ the curves do not cross anymore and the progression is clear.

The ideal value for ϵ is the lowest value at which the curves do no longer cross, therefore yielding a good trade-off between statistics and the inclusion of spurious contacts. It is however important to use one value for all measurements so the calculated contact numbers are comparable to each other.
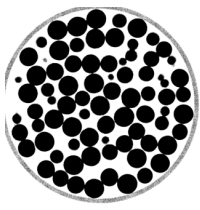
For the wet systems described in chapter 4 no crossing of curves occurs, but the contact number is monotonically increasing with ϵ. To enable comparability for the different systems, the same value is chosen as for the dry systems.

1.6. Summary and outlook

X-ray tomography has developed into a powerful tool to investigate the structural properties of objects and can be applied from the nano-scale up to the macro scale [ezr18]. As a method it proves to be especially helpful for granular physics, because structural bulk properties are otherwise hard to access. Using the techniques and methods introduced in this chapter it is possible to obtain the particle positions and orientations with sub-pixel accuracy as well as physical properties of the granular system. The current availability of X-ray tomography setups provides access to those machines for an increasingly larger group of scientists.

While the method is powerful, the "devil is in the detail". Acquiring nice looking images is great, but a quantitative analysis based on X-ray data has to be based on a sound understanding of all parameters and especially the pitfalls of image acquisition and processing up to particle detection and data analysis. Thus obtaining X-ray data and using that data for research, requires a sound knowledge – from obtaining the tomography over image processing to physical analysis.

The analysis described in this chapter is limited to static structural properties of the system under investigation. With increasingly powerful and fast X-ray tomography machines (a scan can be done as quick as 30 seconds) or when using synchrotron radiation, which is orders of magnitudes brighter than a normal X-ray tube, it is possible to resolve dynamical processes in granular media on smaller and smaller timescales [HA10].

The image preprocessing described in this chapter is widely applicable to various two-dimensional or three-dimensional tomograms of spheres and ellipsoids. While the particle detection described here is tailored to those specific particles, it can easily be applied to non-monoschematic, anisotropic particles (see section 3.3).

However, if non-spherical particles should be detected, further information has to be obtained as the centroid position, orientations and axis lengths are not enough to capture the details of most more complex particles. Some examples of more complex particle detection algorithms are listed here and described in the following chapters:

- For the identification of pro- and oblate or triaxial ellipsoids in a packing the three individual axis lengths and their orientations have to be calculated [Sch+13b]. This has also been applied in section 2.4.1.
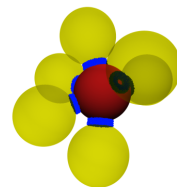
- For tetrahedral particles the four vertices of the tetrahedra have to be obtained. This can be done for example by fitting a tetrahedra to the two-dimensional projections of the label. Additional information about the size of the tetrahedra has to be applied here, as the erosion will not work due to flat face to face contacts between neighboring tetrahedra, see section 3.2 and [Neu+13; Thy+18].

- For the description of a root growing in a sphere packing the surface voxels of the root are identified to be used for a Set-Voronoi calculation, see section 2.4.2 and [Zol17].

60
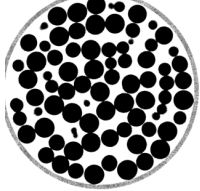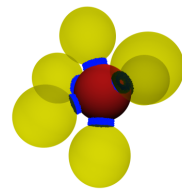
2. Structural analysis of granular systems using Set-Voronoi diagrams[19]

(a)   (b)
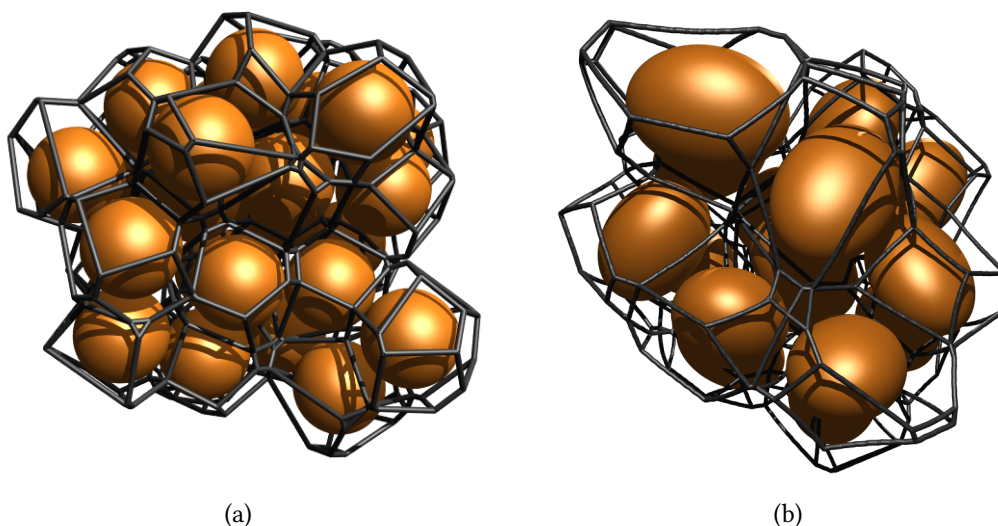
Figure 2.1.: Renderings of particles with their (Set-)Voronoi cells. Videos available online at [Vor18]. (a) Cluster of 47 particles from the central region of a sphere packing with the corresponding Voronoi cells as a wireframe. (b) One ellipsoidal particle (aspect ratio $\langle \alpha \rangle = 1.4$, shrinked by 10 %) and its Voronoi neighbors as well as their Set-Voronoi cells as a wireframe.

The analysis of the geometries and structures based on the local geometry around each particle is an important tool in granular and soft matter physics to gain insights on many features. Taking a close look at the local environment of each particle is a well established method [Sta+02; SK05; ASS06; Kap+10; Zha+12; KT14; Sch+15b; Sch+15a;
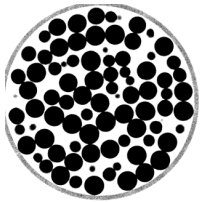
SWK16; Sch17; Thy+18; ZEZ18]. This environment can be defined using the so-called *(Set-)Voronoi tessellation*, which will be described in detail in this chapter.

<table>
<tr><td>(a)</td><td>(b)</td></tr>
</table>

Figure 2.2.: Point Voronoi diagrams in two dimensions for (a) a system of monodisperse disks and (b) a system of bidisperse disks. The red striped regions in the right image show the areas inside particles, which are not part of the Voronoi cell of the respective particle.
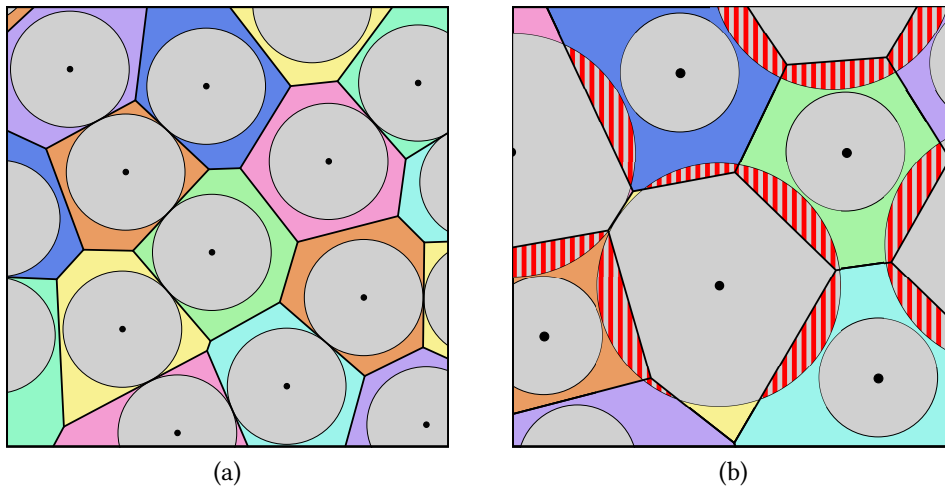
The intuitive idea of assigning each particle the volume which is closer to this particle center than to any other particle can be dated back to Georgy Voronoi [Vor09], Dirichlet and even Descartes [Oka+00] in 1644. The definition is based on dividing the system into individual, non overlapping *Voronoi cells*.

The Voronoi cell V of particle K_i is mathematically defined as

$$V(K_i) = \{x \in \mathrm{E}^3 | D(\vec{x}, \vec{c}_i) \leqslant D(\vec{x}, \vec{c}_j) \forall j \neq i\} \tag{2.1}$$

Where the distance $D(\vec{x}, \vec{c}_i)$ between a point $\vec{x}$ and the center $\vec{c}_i$ of particle i is given by the (Euclidean) distance $D(\vec{x}, \vec{c}_i) = |\vec{x} - \vec{c}_i|$. Similar definitions can be given for other dimensions E^2, E^4 …

The Voronoi tessellation of a system is the combination of all cells of the points in the system. It is evident, that the Voronoi tessellation is space filling and it is relying on the Euclidean distance to the particle's center points. Voronoi diagrams (shown in figure 2.2 (a)), also called *Point Voronoi* diagrams, have found countless applications for granular materials [Fin70; CW87; Oge+96; Luc+99; SK05] and in other topics, e.g. in solid state physics (the Wigner-Seitz cell is actually a Voronoi construction), engineering (material science uses Voronoi cells as grains for atomistic simulations [FS01], or to study segregation [Hou+18] or for the growth of cellular materials [Pit99]), or health and civics (finding the nearest school or hospital, correlating cholera outbreaks with water pumps in 1854, see
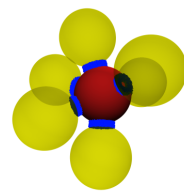
[Joh06]). Rahman suggested Voronoi cells in 1966 as a valuable measure for the analysis of local structures and molecular environments in liquids [Rah66]. Glotzer and coworkers [Sta+02] have applied Voronoi volumes as free volume estimates.

In granular media, the basic Voronoi diagram is only applicable to monodisperse spheres [Oge+96; Sch+13a; Wei+17]. In a system of more complex particles, like polydisperse spheres or arbitrarily shaped particles, the above method fails to work for two reasons: The concept of a particle center is not well defined for complex particle shapes. More importantly, it can happen that parts of particles are not part of the cell, that was generated by the respective particle (see the red areas in figure 2.2 (b)). This contradicts the intuitive idea of spatial segmentation of the system with respect to the particles and can be seen in figure 2.2 (b).

The *weighted Voronoi diagram*, which is also called *Laguerre tessellation* [Eva+13] or *Voronoi S-net* [Ric+99], can be used for systems of polydisperse spheres, but will also break down for systems of aspherical particles [Oka+00]. A generalization of the Voronoi diagram to aspherical particles is the *Set-Voronoi diagram*, see [Sch+13a], which is also called *navigational map* [Luc+99] or *tessellation by zone of influence* [Pre92].

The Set-Voronoi diagram is still space filling, but now based on the Euclidean distance to the particle's surface. This new definition extends the range of accessible particle shapes from monodisperse spheres to almost arbitrary particles. The particles are neither required to be convex nor simply connected any more.

The Set-Voronoi cell V_s of particle K_i is defined as

$$V_s(K_i) = \{x \in \mathrm{E}^3 | D(\vec{x}, \vec{K}_i) \leqslant D(\vec{x}, \vec{K}_j) \forall j \neq i\} \tag{2.2}$$

where the distance $D(\vec{x}, K)$ between a point $\vec{x}$ and a body K is is given by the minimal (Euclidean) distance $D(\vec{x}, K) = \min_{\vec{p} \in K} |\vec{x} - \vec{p}|$. If the point x is inside the body K, so $\vec{x} \in K$, the distance will automatically be $D(\vec{x}, K) = 0$ and thus the point will belong to cell V_i for body K_i. For the more relevant case where $\vec{x}$ is outside K, so $x \notin K$, the point $\vec{p}$ of K nearest to $\vec{x}$ is always on the bounding surface $S = \delta K$.

Nowadays *Set-Voronoi diagrams* and *Set-Voronoi cells* are well-established concepts. The definition of a local environment sheds light on many aspects of geometrical systems [Oka+00; SK05; Ast+07; Kap+12; SWK16; Sch+10b; Sch+15b; Sch+17b], which are described in detail in section 2.2. Set-Voronoi tessellations can also be applied outside granular media due to the relation to the Level-Set methods and the medial axis theorem [Set85; OS88; AB99; Set99; SP08; SS11; SAM12; Rob+16; GFO17]

Despite the success of local descriptions and although the importance of local properties of granular packings is known, existing software only covers specific problems. A widely applicable software for calculating Set-Voronoi diagrams of particles with arbitrary shape was missing. To address this issue the program `Pomelo` was developed [Wei+17]. The
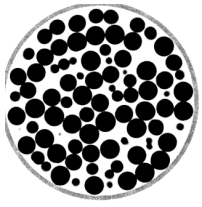
program is capable of calculating Set-Voronoi tessellations of systems of generic particles and thus is applicable to a wide variety of problems, which will be shown in the sections 2.4 and 3. Details about `Pomelo` and important parameters for the calculation are described in section 2.3, as well as an convergence analysis for the number of surface points.

At the end of this chapter, in section 2.4, various systems are listed, showing the applicability of Set-Voronoi tessellations to different geometrical problems.
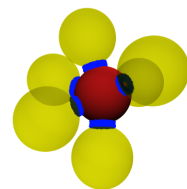
2.1. The computation of the Set-Voronoi diagram
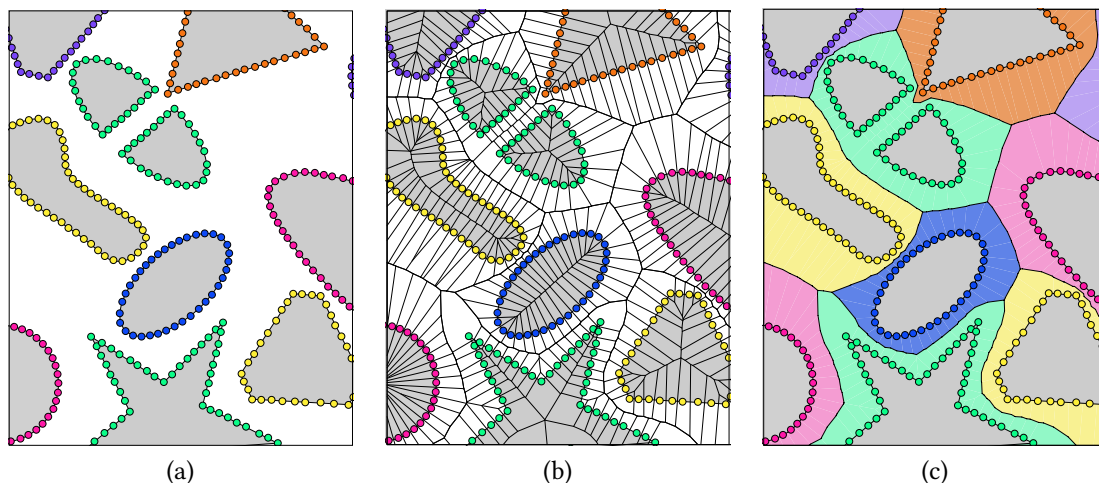

| (a) | (b) | (c) |

Figure 2.3.: The algorithm to calculate the Set-Voronoi diagram of arbitrary particles schemed for a two-dimensional system. (a) Creating points on the particles' bounding surface. (b) The Point Voronoi diagram for all surface points. (c) The resulting Set-Voronoi diagram after merging the Point Voronoi cells. Note that the particles are not required to be convex nor simply connected, which can be seen at the star shaped particle or the spliced ellipse.

Consider a system which consists of N Particles $K = \{K_i\}$ with $i = 0 \cdots N - 1$. The computation of the Set-Voronoi diagram is based on [Sch+13a] and can be split in three steps:

1. Discretize the particle's surface with a number of M *surface points*. Fig 2.3 (a).

2. Calculate the Point Voronoi diagram for all those surface points. Fig 2.3 (b).

3. All the Point Voronoi cells belonging to the same particle are merged. Fig 2.3 (c).

For a dense discretization of the particles' bounding surface, the Set-Voronoi cell of particle i is thus the union of all the Point Voronoi cells, which belong to surface points of particle i. See section 2.3.2 for further details on the discretization.

In the first step, the particles bounding surface is discretized by creating surface points. The bounding surface's features are required to be sampled in a sensible way. This means that the positions of the surface points are accessible, either with a mathematical equation (discretize the surface of a sphere) or that the surface points are known in another way (e.g. the surface voxels can be determined from a three-dimensional image). Another requirement is that the sampling can reproduce the important features (like sharp edges, kinks or corners) of the surface completely. This, for example, would not be possible for
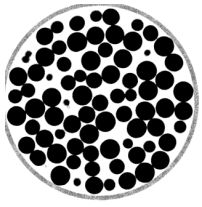
the surface of a fractal, as a finite number of surface points can never reproduce all features of the surface.

Afterwards the Point Voronoi diagram for all the surface points is calculated in the second step. After that, in the third step, all cells that belong to the same particle are merged. This is done by removing faces from the Point Voronoi diagram with the following scheme: Each face of a Voronoi cell can be associated with two surface points r and s. A Voronoi face corresponds to a Voronoi line in figure 2.3 (b). A check is performed for each face f of all Voronoi cells: If the two surface points r and s of the face f belong to the same particle i, the face is discarded. Otherwise the Voronoi face is part of the boundary of the Set-Voronoi cells and needs to be kept. An example for this check can be given using figure 2.3 (b): When looking at the orange triangle, the faces (lines in figure 2.3 (b)) that are between two orange surface points (surface points of the same particle) are discarded, while faces (lines) between an orange point and a point of any other color (e.g. green or pink) have to be kept, as those are the faces that define the Set-Voronoi cell of the particle. The result after merging all cells is the Set-Voronoi diagram of the packing, which is shown in figure 2.3 (c).
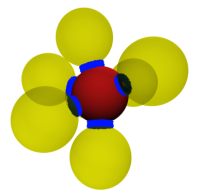
2.2. Physical properties extracted from (Set-) Voronoi cells

Defining a local environment yields insights into particulate systems of arbitrarily shaped particles, like the definition of a local packing fraction, see section 2.2.1, the shape of the Voronoi cells (section 2.2.2) and can be extended to the correlation of the volume of the cell with other spatial properties [Sch+17b]. The measures introduced in this section are used to determine the quality of Set-Voronoi tessellations in section 2.3 and in the analysis of most systems investigated in this work, see section 2.4 and chapter 3.

This is by far not a complete list of physical measures based on (Set-)Voronoi cells, but rather a summary of the ones used in this work. Other measures include vertex, edge or face distributions [BM60; KRS03], or correlation between any of those measures [KT14; KSM17b].

2.2.1. Local and global packing fractions

Knowing the volume of all particles ($V_{\text{particles}} = \sum_i^N V_i$, where V_i is the volume of particle i) and the volume of the container ($V_{\text{container}}$) of a system allows to define the global packing fraction (also called *volume fraction*) Φ_g of the system:

$$\Phi_g = \frac{V_{\text{particles}}}{V_{\text{container}}} \tag{2.3}$$

which is a key parameter for the statistical physics description of granular media [WH30; BF67; SK69; OL90; Kni+95; RT98; Pin+98; Ric+99; TTD00; Sil+02; ZM05; Rib+05; Rib+07; ASS06; Ast06; Don+06; Ast+07; KL07; SHS07; DW09; Clu+09; Hec09; Cor+10; Sil10; DDA10; DC10; Sch+10b; Wan+10; Cia+11; Kap+12; Saa+12; Bau+13; Mae+13; ZS14; BDB15; Che+16; SWK16; Sch+17a; Sch17; Wei+17; Thy+18; Bau+18].

Local packing fractions

Using the Set-Voronoi tessellation of a system, the analogy of equation 2.3 can be formulated on a local – per particle – level. The following equation is applicable to any particle i of a system containing N particles in total. The particles are not required to be monodisperse or even monoschematic, as long as the particle's volume and the volume of its Set-Voronoi cell can be calculated. The relation between Φ_l (equation 2.4) and Φ_g (equation 2.3) is given in equation 2.5.
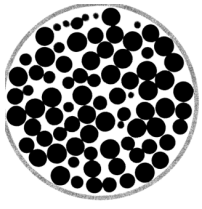
$$\Phi_l^i = \frac{V_{\text{particle}}^i}{V_{\text{cell}}^i} \tag{2.4}$$

where Φ_l^i is the local packing fraction of particle i, V_{particle}^i is the volume of the particle and V_{cell}^i is the volume of the corresponding Set-Voronoi cell. This equation shows vividly that the Set-Voronoi cell of a particle represents exactly the volume associated with this specific particle, while its neighborhood is defined by the other particles around particle i.

The global packing fraction can be obtained by calculating the harmonic mean of all local packing fractions Φ_l, see equation 2.5. Note that packing fractions are not additive (but volumes are), which is the reason why the arithmetic mean does not yield the exact result[20].

$$\Phi_g = \frac{V_{\text{particles}}}{\sum\limits_i^N V_{\text{cell}}^i} = \frac{N}{\sum\limits_i^N \frac{V_{\text{cell}}^i}{V_{\text{particle}}^i}} = \frac{N}{\sum\limits_i^N \frac{1}{\Phi_l^i}} \tag{2.5}$$

The definition of *Random Loose Packing* (RLP), *Random Close Packing* (RCP) and the *Maximally Random Jammed* (MRJ) state are given in the introduction chapter, see page 14.

As an advantage, this local formulation allows for the precise treatment of boundaries, because a particle and its Set-Voronoi cell is either included in the calculation or completely excluded from the harmonic mean. Thus the global packing fraction calculation based on the local packing fractions of equation 2.5 should be preferred to equation 2.3.

Local packing fraction distributions

The distributions of (Set-)Voronoi cell volumes in physical systems has been studied in particulate systems [SK05; Ast+07; SWM08; New+11; ZS14; Sch+15b]. Efforts are being made to establish links to statistical mechanics [Sha80; Kan81], granular entropy and the Edwards ensemble [EO89; PD13; Ast+07; ZS14]. An example of the (Set-)Voronoi volume distribution (see also [CW87; Oge+96]) of two systems consisting of monodisperse spheres at different global packing fractions Φ_g is shown in figure 2.4 (a).

It has been shown that the distribution of Voronoi volumes of random jammed sphere packings is universal [Sta+02; Ast+07]. The universality holds for random ellipsoid packings [Sch+15b] and, as recently shown, for tetrahedra and pear shaped particles [Wei+17]. The rescaling subtracts the global packing fraction and divides by the width ($\sigma(\Phi_l)$ of the local distribution:

$$\Phi_l' = \frac{\Phi_l - \Phi_g}{\sigma(\Phi_l)}. \tag{2.6}$$

---

[20]For the distributions of local packing fractions of the systems under investigation in this work, the deviation between the arithmetic and harmonic mean are not exceedingly large, though.
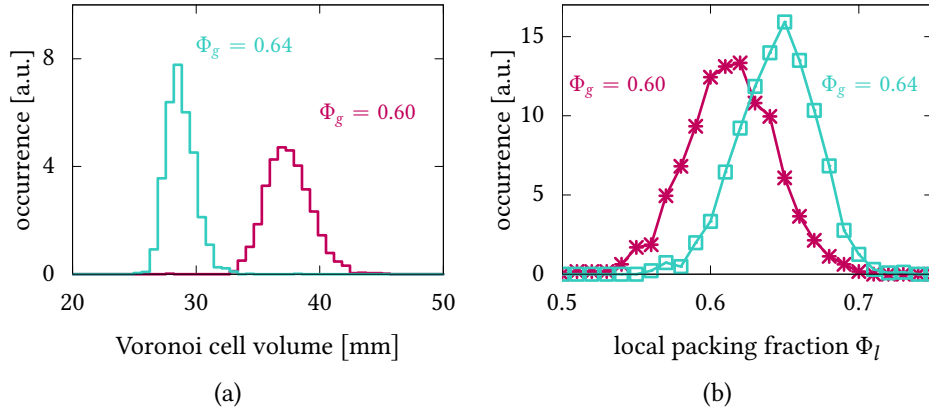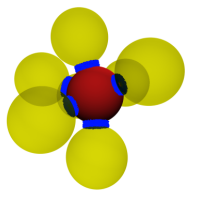
Figure 2.4.: (a) (Set-)Voronoi volume distribution for two mechanically stable sphere packings at different global packing fractions. (b) Local packing fraction distribution for the same two sphere systems. See equation 2.4. The distribution is normalized to unit area.

It is beneficial to look at the local packing fraction distributions $P(\Phi_l)$, which is plotted in figure 2.4 (b) (see also [ASS06; Cor+10]). Performing the rescaling from equation 2.6, the rescaled packing fraction distribution can be obtained, which is shown in figure 2.5 (a). The same universal distribution can be obtained for systems of triaxial ellipsoids 2.4.1, which is shown in figure 2.5 (b).

Figure 2.5.: (a) The same data as in figure 2.4 (b) but after rescaling by equation 2.6. The rescaling leads to a collapse on a universal curve. (b) rescaled local packing fraction distributions for three systems of triaxial ellipsoids with aspect ratio $\langle \alpha \rangle = 1.4$ at different global packing fractions ranging from 0.61 to 0.64. All distributions are normalized to unit area.

2.2.2. Cell shape anisotropy using Minkowski tensors

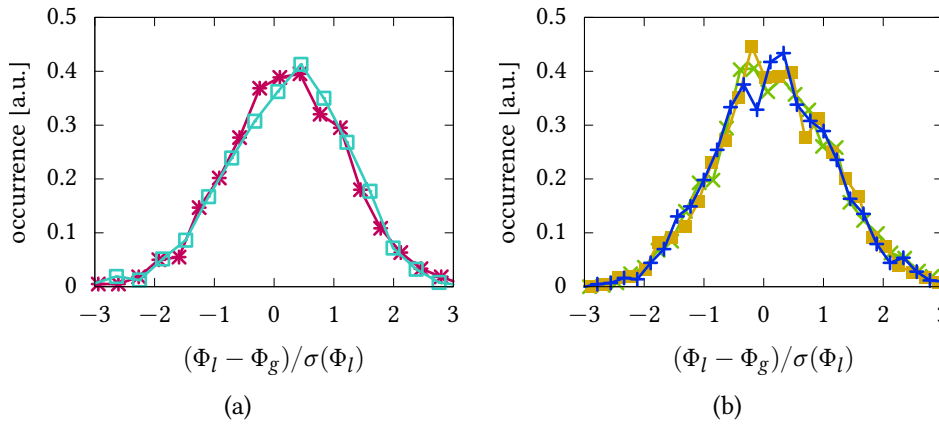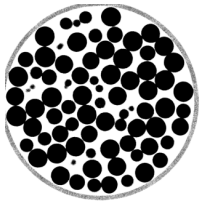As the volume of a Set-Voronoi cell is one of the most basic morphological measures to characterize the local structure, the next generalization relates to the shape of the cells. In this work, the shape of objects will be described using *Minkowski tensors*. The measures described in this section will be calculated on the Set-Voronoi cells of the packing in most cases. But Minkowski tensors are a more general concept, which is not limited to Set-Voronoi cells, and can be applied to any spatial structure. For example, the Minkowski tensors can be calculated for the particles as it has been done in section 3.3.

Minkowski tensors are the next generalization of scalar-valued Minkowski functionals [Sch78; Sch93; MBW94; LMW95; Mec96; MS97; Mec98; Mec00; KMS01; San04; MA05; MS05; RMM08; MJM08; AKM10; SW08; Sch+10a; Gör+13; BFZ15; KSM17a]. The Minkowski functionals are an established method for the description of the morphology and structure of various physical processes [Mec00]. Their mathematical definition has been developed in the context of integral and convex geometry [Had57; San04] and have found applications, e.g. in image analysis [Ser83]. Minkowski functionals are – being a scalar measure – not sensitive to properties like orientation or anisotropy. That is why the generalization to tensor valued measures is useful [Ale99; HSS08b; HSS08a; Sch+10a; Kap+10; Nac+11; Sch+11; MSM12; Sch+13d; Hör+14; KSM17b; Kla+17].

In this work the focus is upon Minkowski functionals and Minkowski tensors of rank two. Minkowski tensors with higher rank can be defined [Kap+12; Mic+13] but will not be covered here.

Minkowski functionals

The four Minkowski functionals (also called *intrinsic volumes*) W_ν with $\nu = 0, 1, 2, 3$ give scalar measures characterizing a geometrical object K and are described in table 2.1. They are based on integrals over the volume and surface of an object K. The integrals are weighted by the mean and Gaussian curvature depending on the functional of interest. Both curvatures can be calculated by the local principal curvatures k_1 and k_2.

The Minkowski functionals can be related to the volume $V(K)$ of the object, surface area $A(K)$ and the[21] Euler characteristic $\chi(K)$. The surface to volume ratio can be used to distinguish different types of morphological clusters. A similar technique has been used in [Sch+08]. W_2 represents the surface area, weighted with the mean curvature and W_3 represents the surface area weighted with the Gaussian curvature. The Euler characteristic

---

[21]There are two rivaling formulae of the Euler characteristic. The one used in this document is based on the bodies. The other one is based on the surface of the bodies and treats surfaces double-sided, which leads to a factor of 2 between the different formulae.
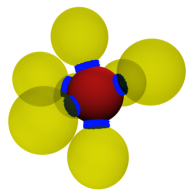
$$W_0 = \int_K \mathrm{d}V = V(K) \qquad\qquad\qquad \text{Volume}$$

$$W_1 = \tfrac{1}{3}\int_{\partial K} \mathrm{d}A = \tfrac{1}{3}A(K) \qquad\qquad \text{Surface area}$$

$$W_2 = \tfrac{1}{3}\int_{\partial K} \tfrac{k_1+k_2}{2}\, \mathrm{d}A \qquad\qquad \text{Surface area weighted with mean curvature}$$

$$W_3 = \tfrac{1}{3}\int_{\partial K} k_1 \cdot k_2\, \mathrm{d}A = \tfrac{4\pi}{3}\chi(K) \quad \text{Euler characteristic}$$

Table 2.1.: Minkowski functionals $W_\nu(K)$ for a body K. Here $V(K)$ is the volume of the body, $A(K)$ is its bounding surface and $\chi(K)$ is the body's Euler characteristic. The integrals are calculated over the volume of K for W_0 and over the body's bounding surface ∂K for the other functionals. $\mathrm{d}V$ and $\mathrm{d}A$ are the infinitesimal volume and surface elements, respectively.

$\chi(K)$, well-known in many other contexts [HZ86; MW91; Wor94; Mec98; Arn+01; Bit04; NMW08; Sch+12; Eva+13], is a topological quantity of the object K and defined[21] as

$$\chi(K) = \#\text{components} - \#\text{handles} + \#\text{cavities}.$$

Thus, a sphere has a value of $\chi = 1$ and an object with the topology of a torus (e.g. a doughnut or coffee cup) has a value of $\chi = 0$. A hollow sphere has a value of $\chi = 2$.
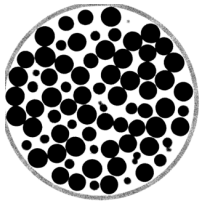
The Euler characteristic can be used to determine the shrink value for the Set-Voronoi calculation, see section 2.3.3.

Looking at the four scalar Minkowski functionals is sufficient in three dimensions, as Hadwiger's theorem [Had57] states that all other scalar measures of an object can be described as a linear combination of the four Minkowski functionals.

Minkowski tensors

The six linearly independent[22] Minkowski tensors of rank two $\left(\mathbf{W}_\nu^{\mathbf{r},\mathbf{s}}\right)_{ij}$ of a body K in three dimensional space $\mathbb{E}^3$ are given in equation 2.7, where ν, r, s name the type of the tensors and i, j enumerate its elements [Sch+13c]. ν defines the type of the integral ($\nu = 0$ volume integral, $\nu = 1$ surface integral and $\nu = 2$ and $\nu = 3$ integral over the curvature weighted surface), r and s the power of position or surface normal vectors, respectively. According to ALESKER's theorem all other additive structural tensor-valued properties of K can be obtained by a linear combination of the $\left(\mathbf{W}_\nu^{\mathbf{r},\mathbf{s}}\right)_{ij}$.

---

[22]Note that the four "scalar" tensors $W_i \times \mathbb{I}$ from table 2.1 also have to be included in this "basis".

$$\mathbf{W}_0^{2,0}(K) := \int_K \mathbf{r} \otimes \mathbf{r} \, \mathbf{dV}$$

$$\mathbf{W}_1^{2,0}(K) := \frac{1}{3} \int_{\partial K} \mathbf{r} \otimes \mathbf{r} \, \mathbf{dA}$$

$$\mathbf{W}_2^{2,0}(K) := \frac{1}{3} \int_{\partial K} H(\mathbf{r}) \, \mathbf{r} \otimes \mathbf{r} \, \mathbf{dA}$$

$$\mathbf{W}_3^{2,0}(K) := \frac{1}{3} \int_{\partial K} G(\mathbf{r}) \, \mathbf{r} \otimes \mathbf{r} \, \mathbf{dA} \qquad (2.7)$$

$$\mathbf{W}_1^{0,2}(K) := \frac{1}{3} \int_{\partial K} \mathbf{n} \otimes \mathbf{n} \, \mathbf{dA}$$

$$\mathbf{W}_2^{0,2}(K) := \frac{1}{3} \int_{\partial K} H(\mathbf{r}) \, \mathbf{n} \otimes \mathbf{n} \, \mathbf{dA}$$

The Minkowski tensors bear a resemblance to the moment of inertia tensor for different mass distributions [Sch12; Sch+13c] or the "interface tensor" [KRS03; Eva+12; Eva+13]. $\mathbf{W}_0^{2,0}(K)$ is related to the moment of inertia tensor for an object, which is filled with constant volume density. The $\mathbf{W}_1^{2,0}(K)$ tensor can be interpreted as the moment of inertia tensor of a hollow object with the mass distributed on the surface of the object and the $\mathbf{W}_2^{2,0}(K)$ and $\mathbf{W}_3^{2,0}(K)$ tensors can be interpreted as the moment of inertia tensors with the mass distributed on the edges or vertices respectively. The remaining tensors $\mathbf{W}_1^{0,2}(K)$ and $\mathbf{W}_2^{0,2}(K)$ are related to surface normal distributions.

Choosing a different reference frame (or *choice of origin*) for the calculation of the Minkowski tensors changes the results, as only some of the Minkowski tensors – namely $\mathbf{W}_1^{0,2}(K)$ and $\mathbf{W}_2^{0,2}(K)$ – are translation-invariant [Sch12]. Only for those two tensors the choice of origin does not matter. If not otherwise stated, the origin in this work will be the centroid of the object, the Minkowski tensor is calculated for (in most cases the Set-Voronoi cell)[23].

To measure the (an-)isotropy of an object, the anisotropy indices $\beta_\nu^{r,s}$ are introduced, which can be defined for every Minkowski tensor of rank two. The anisotropy index

$$\beta_\nu^{r,s} = \frac{|\mu_{\min}|}{|\mu_{\max}|} \qquad (2.8)$$

is calculated by computing the ratio of the smallest to the largest eigenvalues μ of the respective tensor. An alternative would be the use of *tensor invariants*, see [Eva+13]. Isotropy in this analysis means, that the respective Minkowski tensor is the unit matrix. A body can be isotropic, due to certain symmetries of the object[24] [Nye57]. In three

---

[23]Another option would be to use the centroid of the particle as an origin for the Set-Voronoi cell. This type of origin has been used for example in [Sch+10b].

[24]This includes, but is not limited to, all cubic symmetries.

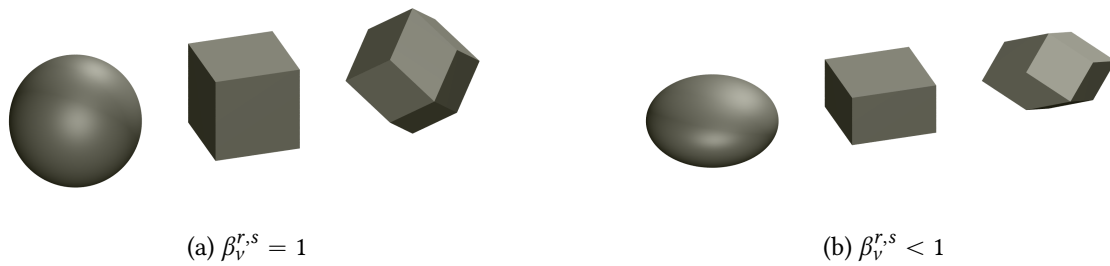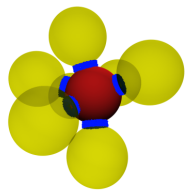(a) $\beta_\nu^{r,s} = 1$ (b) $\beta_\nu^{r,s} < 1$

Figure 2.6.: The anisotropy index $\beta_\nu^{r,s}$ will be equal to one for any isotropic object, like a sphere, an cube or a rhombic dodecahedron (a). Values of $\beta_\nu^{r,s}$ smaller than one will occur for any anisotropic object (b).

dimensions examples for bodies with Minkowski tensor $\mathbf{W}_\nu^{r,s}$ equals $\mathbf{1}$ are the sphere, the cube or the FCC unit cell (rhombic dodecahedron) [Kap11]. For a perfectly isotropic object like a sphere or cube, see figure 2.6 (a) all the eigenvalues of a specific tensor have the same value. Thus $\beta_\nu^{r,s} = 1$ for an isotropic object. If the object is anisotropic, the tensor $\mathbf{W}_\nu^{r,s}$ will have different eigenvalues μ, which will result in a $\beta_\nu^{r,s}$ smaller than one, which is shown in figure 2.6 (b). As for the functionals it can be seen, that the six Minkowski tensors are sufficient to calculate any other tensor valued measure by a linear combination of the Minkowski tensors [Ale99].
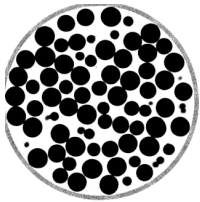
2.3. Details of the Set-Voronoi computation

The concept of how to calculate Set-Voronoi cells of arbitrary particles has been introduced in section 2.1. This section is about how the actual calculation is performed and how the physical results of the Set-Voronoi cells, introduced in section 2.2, depend on two numerical parameters: surface discretization and shrink.

2.3.1. Pomelo – a generic Set-Voronoi tool

The program `Pomelo` is an open source software for Set-Voronoi calculations of generic particles [Wei+17]. It is written in C++11, licensed under GPL3 and can be downloaded at [pom18b]. The package includes a collection of test cases as well as instructions on how to compile and run the program. An even more detailed description on how to run `Pomelo` on a system of mechanically packed monodisperse spheres can be found in [WS17].

The system requirements to run `Pomelo` on a machine are `g++ 4.9.2` or `clang++ 3.5.0-10` or any higher version. `Pomelo` directly supports common particle shapes, like mono- and polydisperse spheres [SWS17], tetrahedra [Neu+13; Thy+18], ellipsoids and spherocylinders. All the predefined particles offer parameters for surface discretization, see section 2.3.2, and a convergence enhancing pre-processing step related to particle erosion, see section 2.3.3. Additionally `Pomelo` provides a `generic` mode. This mode works for any shape which surface can be described mathematically. To use `Pomelo` in `generic` mode, `lib-lua 5.2` or higher is required. The Point Voronoi diagram is calculated using the library `Voro++` [Ryc09; Ryc+06], which is included in the `Pomelo` source code and is published under a modified BSD license.

`Pomelo` performs the calculations described in section 2.1 and encapsulates them in an easy-to-use interface. At the beginning the input file is parsed. This file can either be in a predefined format for one of the implemented particle shapes or a configuration file for the `generic` mode. Examples for all file formats can be found in [pom18a].

`Pomelo`'s output is fully customizable. As the file size for a Set-Voronoi diagram can easily be multiple GiB of data, it is important to save only the required files. Output can be written in a `gnuplot` readable format [WK17] for easy visualization of particle surfaces and Set-Voronoi cells. The Set-Voronoi cells can also be written in `poly` [wikb] or `off` [wika] format, which allows the output to be directly used for Minkowski tensor calculations with the program `karambola`, see section 2.2.2, or for further analysis and visualization using the program `geomview` [geo18] (which has been used for the images in table 2.2 and 2.3. Further output (e.g. for a stereoscopic visualization) or for the use with the program `surface evolver` [evo18] can be performed using the tools [pol18] described in appendix A.2
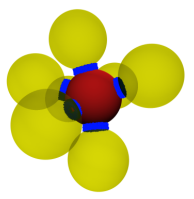
Further outputs are the *Set-Voronoi neighbor list* and the *Set-Voronoi volume list*. The first list names the identifiers of all Set-Voronoi neighbors of each particle. For a Set-Voronoi cell, the Set-Voronoi neighbors are all the cells, that share at least one common face. Note that the particles of two neighboring Set-Voronoi cells are generally not in mechanical contact. This is why the number of Set-Voronoi neighbors is equal or larger than the number of contacts Z. The second list gives the volume of each Set-Voronoi cell. This is the basic building block for the local packing fraction calculation, see section 2.2.1.

2.3.2. Surface discretization

The resolution of the surface discretization determines the quality of the calculated Set-Voronoi diagram and is critical for the convergence of the algorithm [AB99; BC00; ACK01; ACR03]. The ideal Set-Voronoi diagram would be obtained for an infinitely dense discretization. This is, however, not possible to calculate due to calculation time and memory limitations. Thus, the surface discretization has to be a compromise between the required quality of the Set-Voronoi diagram and those limitations.

Furthermore, a sufficient resolution of the surface discretization cannot be given in advance as it depends on the particles' shape, their relative arrangement and also on the physical properties of interest. For example, the volume of the Set-Voronoi cell can be considered a robust measure, as small deviations are likely to cancel out, due to shifts in the Set-Voronoi vertices. If, however, other shape measures of the Set-Voronoi cells are of interest, e.g. the surface of the cell or their shape anisotropy, see section 2.2.2, a finer resolution of the surface of the particles might be required to produce sufficiently discretized Set-Voronoi cells and thus robust results.

For monodisperse sphere packings it is obviously enough to use just the spheres' center points and to perform a Point Voronoi calculation. Besides that, a systematic analysis of the resolution of the surface discretization has only been performed for some corner cases, like spheres or ellipsoids [ZEZ18]. In the systems investigated here, it has been shown that a good resolution for mechanical stable packings of monodisperse pro- and oblate ellipsoids can be achieved with 500 surface points [Sch+13a].

A complete guide can not be given here, due to the variety of possible particle shapes and configurations. However, a systematic check on exemplary systems can help to develop a notion of the dependence of physical results on different surface discretizations by comparing physical results for different surface discretization. For a description of the physical properties investigated here, see section 2.2.

Monodisperse triaxial ellipsoids One example system is a mechanical stable packing of monodisperse triaxial ellipsoids with aspect ratio $\langle \alpha \rangle = 1.1$. Details on the particles
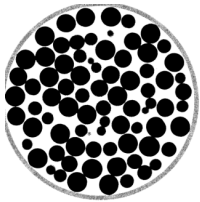
are given in section 2.4.1. Calculations of the Set-Voronoi diagram have been performed for 78, 502 and 1131 surface points per particle and the results are shown in table 2.2. The physical properties[25] of interest are the global packing fraction Φ_g and for one exemplary particle with ID 1010, the local packing fraction, which is denoted by $P_{1010}\Phi_l$ Furthermore, the resulting number of Set-Voronoi vertices and Set-Voronoi faces for the same particle are given (P_{1010} SV vertices and faces).

It can be seen in table 2.2, that increasing the number of surface points increases the resolution of the Set-Voronoi tessellation (SV vertices and SV faces). For the two finest resolutions, the physical properties Φ_g and $P_{1010}\Phi_l$ do not change significantly anymore. This is true on a local scale (Φ_l), as well as for properties, which are averaged over the whole system (Φ_g). Thus, the discretization with 502 surface points is fine enough for these properties.
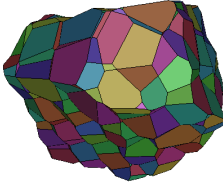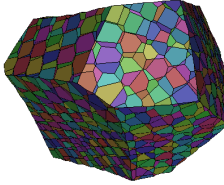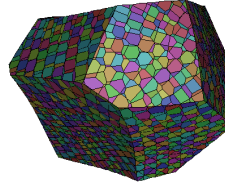
Image			
steps	4	10	15
Surface points	78	502	1131
P_{1010} SV vertices	742	3791	8194
P_{1010} SV faces	497	2578	5562
$P_{1010}\ \Phi_l$	0.5832	0.5829	0.5829
Global packingfraction Φ_g	0.6186	0.6185	0.6185

Table 2.2.: Influence of surface discretization for the Set-Voronoi cells of a mechanical stable packing of triaxial ellipsoids with aspect ratio $\langle\alpha\rangle = 1.1$. The images depict the Set-Voronoi cell of one particle from the central part of the packing and have been created using the program geomview [geo18]. The colors are picked randomly for each Set-Voronoi face. This is the same particle for which the number of Set-Voronoi (SV) vertices and faces are counted and for which the local packing fraction is given.

Monodisperse Tetrahedra   Another example system is a mechanical stable packing of monodisperse tetrahedra, see section 3.2 for details. Calculations of the Set-Voronoi

---

[25] The physical properties have been calculated using the program Pomelo, see [pom18a] and also section 2.2 as well as a program which interlinks with Pomelo's input and output, which is available at [pom18c].
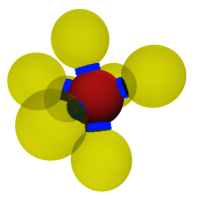
diagram have been performed for 34, 130 and 514 surface points per particle. Details on the system as well as the creation of the surface points by subdividing the tetrahedron's surfaces can be found in section 3.2.

The results for different discretizations are shown in table 2.3. In addition to the physical properties, which have also been investigated for the ellipsoid packing, see table 2.2, the anisotropy of the Set-Voronoi cell has been investigated here. The anisotropy is characterized by the anisotropy index $\beta_0^{2,0}$, which can be calculated from Minkowski tensors. Details on the Minkowski tensors can be found in section 2.2.2.
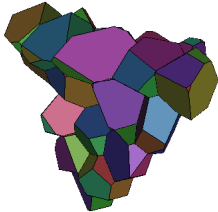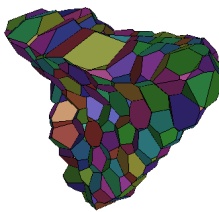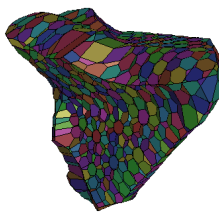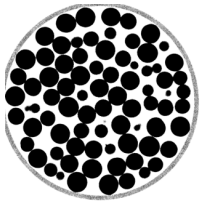
Image			
subdivisions	2	3	4
Surface points	34	130	514
P_{1999} SV vertices	404	1154	3877
P_{1999} SV faces	262	767	2618
P_{1999} Φ_l	0.525	0.520	0.520
P_{1999} $\beta_0^{2,0}$	0.822	0.780	0.779
Global packingfraction Φ_g	0.4814	0.4813	0.4813

Table 2.3.: Influence of surface discretization for a mechanical stable packing of monodisperse tetrahedra. The images show one exemplary particle's cell from the central part of the packing and is rendered using geomview [geo18]. Each face of the Set-Voronoi cell is assigned a random color.

Table 2.2 shows, that the packing fractions on a local and global level are quite insensitive to refinements of the particle's bounding surface above a certain point. The anisotropy index $\beta_0^{2,0}$ is more sensitive and its value changes even between 130 and 514 surface points. As the change between the two values is quite small ($< 1\%$) and the next step in surface subdivision would exceed the memory limits, the surface discretization with 514 vertices is considered fine enough.

2.3.3. Improvement of convergence ("Shrink")

After particle detection it might occur that particles overlap. Possible reasons for particle overlaps are the finite resolution of the tomogram, experimental noise, unwanted artifacts in image processing or aliasing effects, see section 1.5. This imposes a threat for the correctness of the Set-Voronoi calculation and has to be treated, as it can be seen that the resulting Set-Voronoi cells are showing artifacts if particles overlap. See figure 2.7 (a). In this image the Set-Voronoi cell of the top (red) particle "leaks into" the bottom (blue) particle, which will yield a large error for structural measures, as the volume of the cells. Overlaps like this have to be avoided.
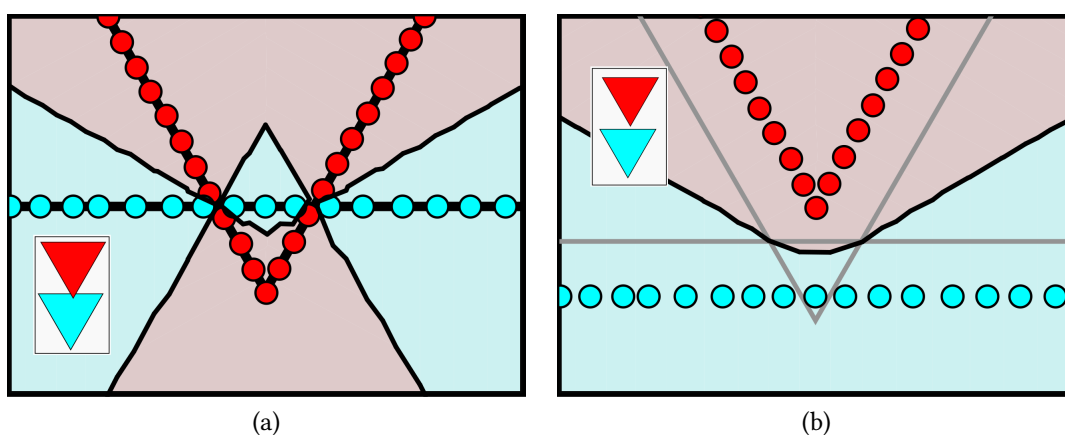

| (a) | (b) |

Figure 2.7.: For overlapping particles it is required to shrink the particles prior to the Set-Voronoi calculation until the overlaps are resolved. (a) Overlapping and non shrunk particles in a two-dimensional example. Due to the overlapping surface points, the Set-Voronoi cells can be arbitrarily wrong as it can be seen with the red area inside the blue particle. (b) Shrinking the particles can resolve that issue and lead to correct Set-Voronoi cells. The gray lines show the particle boundaries prior to shrinking. The insets in both (a) and (b) show the bird's eye view of the configuration of the two particles.

One way to fix this issue is to "shrink" or erode the particles in terms of mathematical morphology [Ser83; Dou92; SHB14]. This will resolve overlaps between particles and is shown in figure 2.7 (b). For smooth particles, the concept of maximal erosion should be applied as described in [Sch+13a]: Examples are monodisperse spheres, which can easily be shrunk down to their center points without any loss of precision in the Set-Voronoi diagram and ellipsoids (with half axes e_1, e_2, e_3), which should be shrunk to $e_c = \frac{e_1^2}{e_3}$ [MAr29]. Shrinking particles which have cusps or sharp edges, can change the shape of Set-Voronoi cells and should be avoided if possible. However, if there are particle overlaps between the particles (e.g. due to errors or a limited resolution in image processing) a compromise
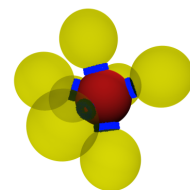
between the errors of overlapping particles (and thus wrong Set-Voronoi cells) and the errors of shrinking of the original particle (and thereby alternating the particle shape the Set-Voronoi cell "sees") has to be found. Special attention has to be payed if the particles are highly polydisperse compared to the actual particle size or if sharp edges occur. In the case of sharp edges, like tetrahedral particles, the reduction in size of the particles will not lead to the same effect as mathematical erosion. In this case the physical results have to be checked carefully for possible errors due to the shrinking of the particles. The convergence of this algorithm has been investigated in different publications [AB99; BC00; ACK01; ACR03].

For example, in a system of bidisperse spheres (with ratio 1:10), it might be tempting to just multiply the radius of each sphere by a shrink factor $f \leqslant 1$. This will lead to incorrect results as the surface of the larger sphere will be moved twice as far as the surface of the small sphere, which will absolutely result in a shift of the Set-Voronoi cell boundaries. This is displayed in figure 2.8 (a). The right way to do the shrinking is by using a parallel surface without self-overlap, which happens to be a subtractive term to the radius for spheres, as it can be seen in figure 2.8 (b).

(a)   (b)
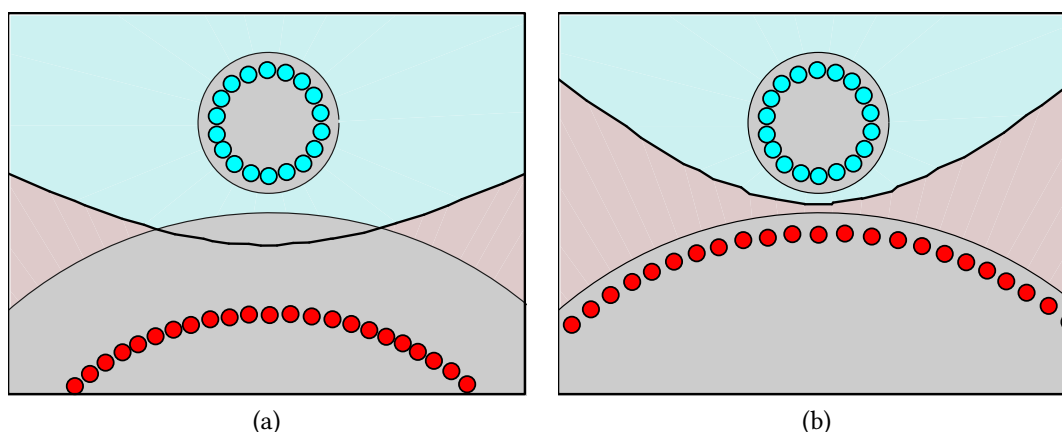
Figure 2.8.: Applying shrink in a polydisperse system of discs with ratio 1:10. (a) applying shrink as a multiplicative factor will yield wrong results, as the surface points of the large disc will be moved further away from the original Set-Voronoi boundary (by a factor of 10) than the surface points of the small disc. (b) in polydisperse systems, shrink has to be applied as a subtractive term of the (corresponding) radius, which will guarantee, that the surface points of both particles will be moved the same distance away from the original Set-Voronoi boundary.

As the particle shape can be complex, it might not be easy to determine a-priori which particles are overlapping (e.g. due to errors in image processing). Tests for ellipsoids (and spheres) can be performed by using the respective axis lengths and particle orientations.
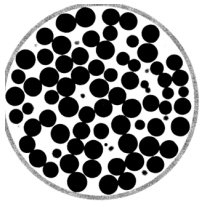
Arbitrary particle shapes can render the issue of overlap testing a complex complex problem. It could be solved e.g. by the separating axis test [Ber97; Huy09] but this can be computationally expensive.

There is, however a simple, yet mathematically robust way of checking if the surface points of two particles are overlapping if the Set-Voronoi cells of those particles have already been calculated: This can be done by checking the Euler characteristic χ (based on the W_3 Minkowski functional) of the resulting Set-Voronoi cell. See section 2.2.2 for further information on Minkowski tensors. If the particles are not overlapping, the Set-Voronoi cells will have Euler characteristic of 1 as it is a closed and solid object (see figure 2.7 (b)). If the Euler characteristic deviates from that value, which could be the case if the cell has internal holes or handles, the surface points from the two particles were overlapping (see figure 2.7 (a)).
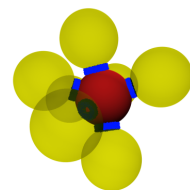
2.4. Applications of Set-Voronoi tessellations to arbitrary particle shapes

This section covers the application of Set-Voronoi diagrams to particles of various shapes. The focus in this section is on the general applicability of Set-Voronoi diagrams and of the program `Pomelo` in detail to different systems and particle shapes. The physical problem is described in detail, including its geometry. After that, the *implementation* for the surface discretization is explained. Physical results are discussed in chapter 3.

The first part describes the application of Set-Voronoi cells on experimental systems of *monoschematic* particles. Monoschematic in this context means that all of the particles in the system have the same shape and size. Examples of such particles are spheres, triaxial ellipsoids (section 2.4.1) and tetrahedra packings (section 3.2), while the second part describes the advantages of Set-Voronoi cells on generic particles, which are not required to be monoschematic. Systems of interest are the root growth of a plant (section 2.4.2), a new system of frictional emulsions (section 3.3), and network structures.

2.4.1. Set-Voronoi diagrams of monoschematic particles

Mono- and Polydisperse sphere packings

Sphere packings can easily be handled by Set-Voronoi diagrams. For monodisperse sphere packings the Set-Voronoi diagram is equal to the Point-Voronoi diagram. Thus, it is sufficient to use the sphere's centroid position as the only "surface point" of a particle. Because of that, the merging step (Step 3. in section 2.1) can be omitted and there is no need for a surface discretization. As the reduction to the centroid is equivalent to the shrinkage (see chapter 2.3.3 of the spheres to on point and merging all points together, there is no need for another shrinkage of the particles.

For bidisperse spheres (see section 3.1), or in general polydisperse spheres, it is necessary to take the complete surface of the particle into account. This means that shrinking the particle to a point is no longer viable. The Set-Voronoi diagram requires the centroid position, the radius for each sphere, as well as the desired discretization and the shrink value. The discretization is given as the steps in both spherical angles N_Θ and N_Φ. As shown in section 2.3.3, the shrink should be an additive term to the radius.

For each particle, the following steps have to be performed to get the surface discretization:

1. Loop over N_Θ and N_Φ and calculate the current pair of (Θ, Φ) values.
2. The effective radius is given by $r_{\text{eff}} = r - r_{\text{erosion}}$.
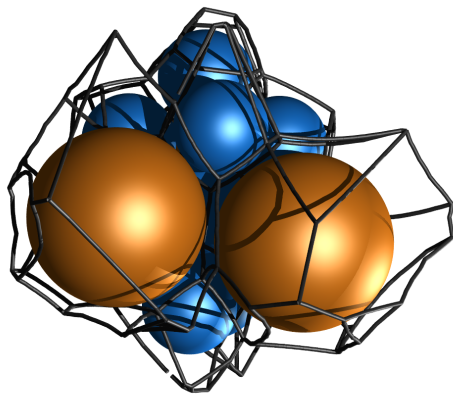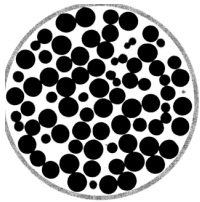
Figure 2.9.: Rendering of the Set-Voronoi cells for a bidisperse sphere packing.

3. Calculate the Cartesian coordinates for each (Θ, Φ) pair using r_{eff} as the radius of a sphere centered at the origin and create a surface point at that coordinates.

4. Translate all points of the surface triangulation by the centroid position of the sphere.

A rendering of the resulting Set-Voronoi cells for a packing of bidisperse spheres (further details on the system are given in section 3.1) can be seen in figure 2.9. Note that the curved faces in this figure are due to the polydispersity of the spheres.

Triaxial ellipsoids
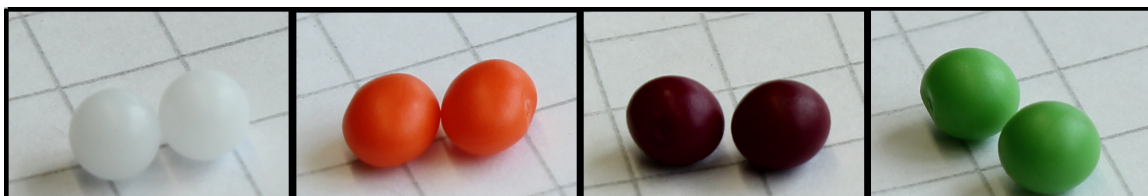
Figure 2.10.: Triaxial ellipsoids. From left to right: Spheres $\langle\alpha\rangle = 1$ (white), triaxial ellipsoids: $\langle\alpha\rangle_{\text{N}} = 1.4$ (orange), $\langle\alpha\rangle_{\text{N}} = 1.1$ (pink) and $\langle\alpha\rangle_{\text{F}} = 1.1$ (green). Image originally created for [Wei15].

Starting from spheres as the most basic shape model of granular materials, the next step in the generalization of particle shapes are ellipsoids. Extensive research has been performed on pro- and oblate ellipsoids [Don+04; DC10; Sch12; Sch+13a; Sch+13b; SWK16; Sch+15a; Sch+15b; ZEZ18], for which two of the three axis lengths $e_{1,2,3}$ are equal. This corresponds to an aspect ratio α. Pro- and oblate ellipsoids are defined by the rule

$$e_1 : e_2 : e_3 = \alpha : 1 : 1$$
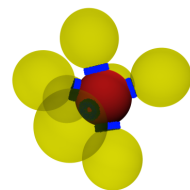
For further generalization the next step is to use triaxial ellipsoids, which have in general three independent axis lengths. The particles of interest are injection molded triaxial ellipsoids, which follow the rule

$$e_1 : e_2 : e_3 = \alpha : 1 : \alpha^{-1}$$

For brevity, the different particle shapes will be labeled by their mean aspect ratio $\langle \alpha \rangle$. Some examples for triaxial ellipsoids used in experiments are shown in figure 2.10.
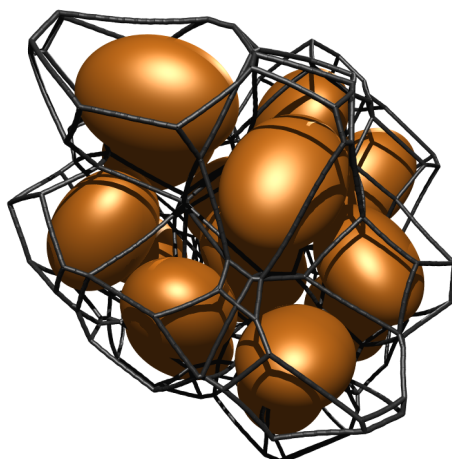

Figure 2.11.: Rendering of the Set-Voronoi tessellation of a cluster of neighboring ellipsoids. See section A.2 for details on the rendering process.

Packings of the triaxial ellipsoids are analyzed using X-ray tomography to detect the ellipsoid's positions and orientations using the methods described in chapter 1. Based on that data, the Set-Voronoi cells for the ellipsoids are calculated using the program `Pomelo`. A total of 502 Surface points per ellipsoid are used using the built in `ELLIP` mode of `Pomelo`. In `ELLIP` mode `Pomelo` creates the surface triangulation of an ellipsoid in a similar way as for spheres (see above). The only difference is, that the surface points of an ellipsoid have to be scaled and rotated due to the ellipsoid's axis length and orientation.

1. Loop over N_Θ and N_Φ and calculate the current pair of (Θ, Φ) values.

2. The effective radius is $r_{\text{eff}} = 1$. The maximal erosion will be applied after spawning all particle surfaces.

3. Calculate the Cartesian coordinates for each (Θ, Φ) pair using r_{eff} as the radius of a sphere centered at the origin and create a surface point at those coordinates.

4. Scale the sphere to an ellipsoid with the axis lengths (given from the particle detection step) oriented on the coordinate system axis.
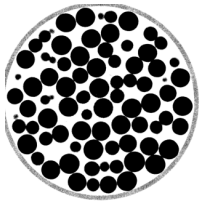
5. Rotate the ellipsoid, so that the orientation of the axis corresponds to the orientation of the particle.

6. Translate all points of the surface triangulation by the centroid position of the sphere.

After all ellipsoids have been created, the erosion value is calculated as described in the maximal erosion step (see section 2.3.3) and the ellipsoids are scaled respectively. A rendering of the Set-Voronoi tessellation of a cluster of neighboring ellipsoids is displayed in figure 2.11.

Note the curved faces of the Set-Voronoi cells in figure 2.11, due to the non-spherical shape of the particles. Thus the Point-Voronoi tessellation is not sufficient and the use of Set-Voronoi cells is required.

Tetrahedra particles

(a)   (b)
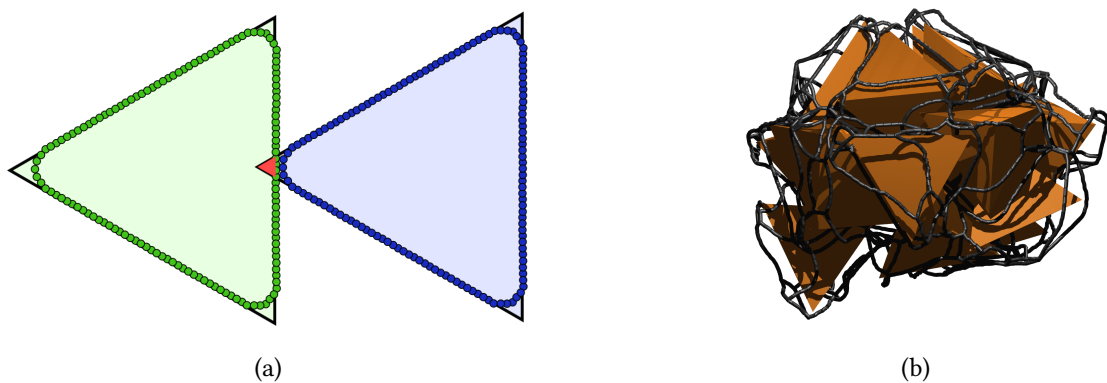
Figure 2.12.: (a) Two-dimensional sketch of the surface discretization of two blunt tetrahedra. The red area depicts overlaps when sharp tetrahedra would be used. (b) Rendering of the Set-Voronoi cells of the same particle as in table 2.3 of section 2.3.2 and it's neighboring particles. The tetrahedra are rendered with ideally sharp edges but the calculation has been performed using the blunt tetrahedral shape.

Tetrahedral particles are quite different from the previously introduced spheres and ellipsoids as they have flat surfaces and sharp edges and corners. The description given here will be used in section 3.2.

In a first approach the ideal tetrahedral shape was used. However, this does not resemble the shape of the tetrahedral particles, which have been used in the experiments. The corners of the particles are not ideally sharp, which leads to a large amount of overlaps between particles at exactly those vertices, see the red area in figure 2.12 (a). These overlaps
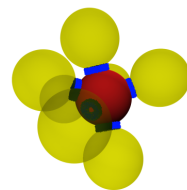
would have to be corrected using a large shrink value for a robust Set-Voronoi calculation, which is unwanted due to the errors introduced by large shrink values, see section 2.3.3.

In order to account for those particle imperfections, the bluntness of the particles is modeled for the Set-Voronoi calculation. Blunt corners are produced on the level of the discretized surface. At first, the center of mass is calculated for all surface points. Then the distance to the tetrahedron's center of mass is calculated for each surface point. This distance is compared to a threshold. If the distance is smaller than the threshold, no change is made to the surface point's position. If,however, the distance is larger than the threshold, the position of the surface point is blended between the original sharp tetrahedral shape and a sphere with corresponding radius. A two-dimensional sketch of the surface points of a blunt tetrahedra is depicted for reference in figure 2.12 (a). Additionally the side lengths of the tetrahedra are shrinked by 1 % to remove remaining overlaps between the particles. This is not equivalent to mathematical erosion, but as only a small shrink value is used, this does not lead to large errors. The Set-Voronoi calculation is then performed using this surface discretization. A total of 514 surface points per tetrahedron is used.

The Set-Voronoi tessellation of one particle (the same as in table 2.3 of section 2.3.2) and it's neighbors is depicted in figure 2.12 (b). Although the lines may look jagged, the discretization of the surface is fine enough, as the physical and structural properties do not vary with significantly with an increase in the number of surface points, as shown in table 2.3 on page 77.

2.4.2. Set-Voronoi diagrams of arbitrary particles

Root growth in sphere packings

This section will not only be an example of different object shapes in one packing, but also of a very irregularly shaped object. The system of interest is the growth of a root, which was planted in a monodisperse spherical bead packing and investigated using X-ray tomography [Zol17]. The long term goal of this project is to answer the question "How smart is a root?" [MV15; Cha17]. It is not known, how the local environment around the root tip influences the growth process and direction of the root. On the other hand this growth leads to a local increase in packing density of the surrounding granular system. Combined, both effects lead to a interaction between the granular system and the root. This results in a complex system, which is yet not fully understood. Here we present one of the first steps, mainly the methods and tools to analyze such systems. A systematic analysis has yet to be performed.

While the spherical particles (diameter $d = (1.5 \pm 0.2)$ mm) are monoschematic, the root has a very irregular form and will be unique for each measurement. Thus, Set-Voronoi cells are mandatory to resemble the shape of the root.
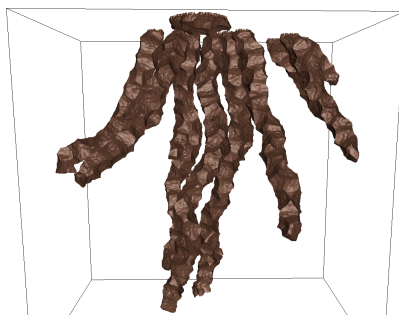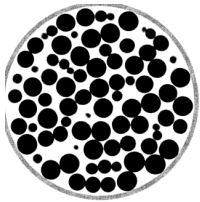
Figure 2.13.: Three-dimensional rendering of the Set-Voronoi cell of the complete root. The image was created using [geo18].

Starting from the tomogram of the system, the particles and the root are identified on the voxel grid. The result is a labeled tomogram, in which air voxels are zero, particle voxels are labeled with the identifier of the particle and the root voxels are labeled with a unique label. On that labeled tomogram, the surface voxels are identified by determining the voxels, which have at least one neighbor (neighborhood of 26) that belongs to a different object or no particle at all. The positions of the surface voxels are then used as the surface points for the Set-Voronoi calculation.

The voxel grid of the tomography measurement is quite dense when compared to the size pf the particles. Thus calculation times can be optimized by discarding voxels for the Set-Voronoi calculation. For this, only every n-th voxel is used. This is equicalent to the check, if the result of each coordinate (x, y, z) of a surface voxel modulo the required resolution is zero. In this case every second voxel has been used. If the results for all coordinate values of a surface voxel are zero, this voxel is used in the Set-Voronoi tessellation. Figure 2.13 shows the Set-Voronoi cell of the complete root[26].

Close observation of the rendering of the Set-Voronoi cell of the root shows a lot of concave areas. Those are the borders of the Set-Voronoi cells of the particles, thus showing that the root can indeed grow around the particles and fills the volume of the cells of the particles. Details on the pysical properties of the system can be found in [Zol17].

Network structures

The application of Set-Voronoi cells is not limited to particulate systems, as already shown in the introduction of this chapter and in the root example. The applications of Set-Voronoi

---

[26]The actual structure of the root could be investigated for example by calculating the skeletal graph[Sch05b; Sch+13a] of the root. However, this study does not focus on the structure of the root itself, but on the structure of the packing and how this structure changes with the root growing inside.
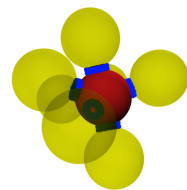
diagrams described here are closely related to the Medial axis transform [AB99; ACK01; ACR03] and the skeletal graph [Sch05b].

This section will show the application of Set-Voronoi tessellations to a periodic network structure, the Gyroid (see fig 2.15 (a) for a 3d printed gyroid object). As the Gyroid is ubiquitous in Nature, e.g. it appears on the micro to nanoscale in butterfly wing scales, like in the Green Hairstreak butterfly (*Callophrys rubi*) [MDS09], it is an interesting system to study.

Schoen [Sch70] described the Gyroid as a remarkable member of the family of *minimal surfaces*. Minimal surfaces are surfaces which is a symmetric saddle surface with the principal curvatures $\kappa_1 = -\kappa_2$ and hence vanishing mean curvature. The Gyroid is a triply-periodic minimal surface with BCC cubic symmetry and divides space into two not interconnected channels. The *network graph* of the Gyroid was introduced by Laves [Lav32] and is topologically equivalent to one of the Gyroid's channels. This network graph is similar to the skeletal graph [Sch05b]. An image of the network can be found in figure 2.14.
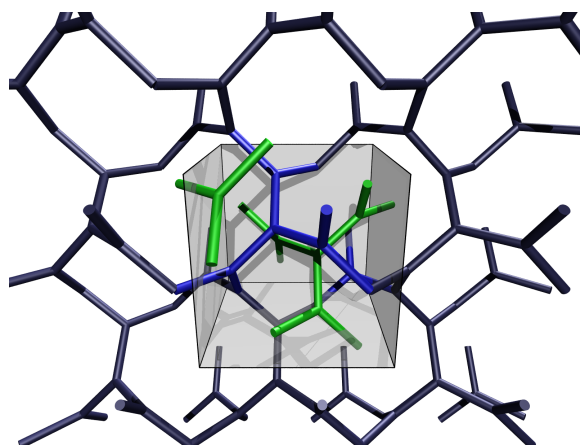
Figure 2.14.: Network graph of the double Gyroid. The blue and green network correspond to the two channels of the Gyroid. For easy viewing only one channel is plotted outside of the unit cell (box). For the Set-Voronoi calculation each of the lines is discretized with 22 points.

The "surface triangulation" of the Set-Voronoi cells will be performed on a discretized version of the Gyroid network graphs, by creating 22 points on each line segment of both skeletal graph. This results in a total of 528 surface points. Periodic boundary conditions are used. Figure 2.15 (b) shows the isosurface of the Gyroid, which was created based on the Enneper-Weierstrass representation of the Gyroid minimal surface. Next to that, figure 2.15 (c) shows the Set-Voronoi tessellation of the network graph of the Gyroid. Each of the line segments of the network graph is sampled with 15 points, resulting in a total of 45 568 points for the "surface triangulation". Note that Hyde and coworkers have used a closely
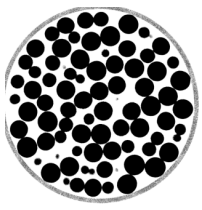
related method to create initial interface configurations for polycontinuous intergrowth of nets for more than two nets [HCO09]. This is also related to Schoen's concept of inflating tubular graphs [Sch70].

(a)   (b)   (c)
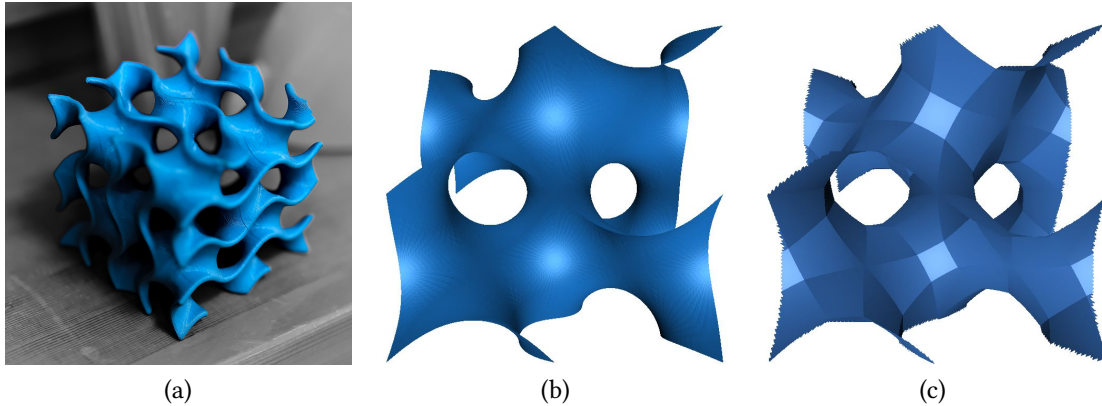
Figure 2.15.: (a) Photo of a 3d printed gyroid with sidelength 4 cm. (b) The Enneper-Weierstrass representation of the Gyroid minimal surface. (c) Set-Voronoi tessellation of the network graph of the Gyroid. The jagged edges appear due to the cropping of the surfaces out of a periodic system.

As it can be seen in figure 2.15, the isosurface of the Gyroid and the Set-Voronoi tessellation of the Gyroid network are quite similar. Both show an equal distribution of volume in the two channels of the Gyroid, which is at the expected value of 0.5. The topological features, as well as the symmetries are reproduced by both representations. However, the straight lines of the network graph result in flat Set-Voronoi faces. While the original Gyroid exhibits curved surfaces, this feature can not be reproduced by the Set-Voronoi tessellation of the Gyroid network.

While further work has to be performed on this topic, it could be shown, that the Set-Voronoi tessellation is not limited to particulate systems, but also applicable to network-like, periodic structures. This example mainly shows the general applicability of the Set-Voronoi tessellation beyond the use on particulate systems.
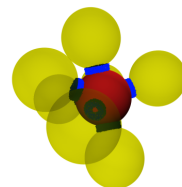
2.5. Outlook

The Set-Voronoi calculation is based on the discretization of the surface. The question how dense the discretization has to be, can in most cases only be answered after the calculation of the Set-Voronoi cells and correlated physical properties, as it has been shown in section 2.3.2. An adaptive discretization process could give a robust and automated procedure on this drawback of the Set-Voronoi calculation. This relates to the analysis of the convergence of the medial axis algorithms [AB99; BC00; ACK01; ACR03; Sch+13a].
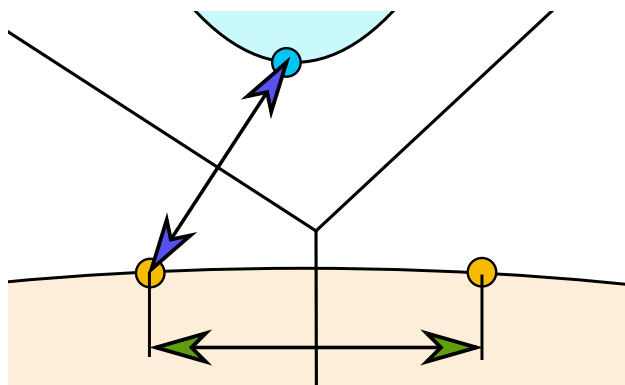

Figure 2.16.: Check for the adaptive Set-Voronoi process. By comparing the ratio between the length of the green arrow and the length of the blue arrow with a user defined threshold a decision can be made whether the local discretization has to be refined.

The adaptive Set-Voronoi calculation performs a simple geometrical check on a local environment, which is displayed in figure 2.16.

At first a coarse discretization of the surface of all particles is calculated. After that for each surface point a check is performed. Two values have to be computed: The distance between two neighboring surface points on the same particle d_{same} (green arrow in figure 2.16), as well as the distance from the surface point to the neighboring surface point on another particle d_{other} (blue arrow in figure 2.16). If the ratio $r = \frac{d_{same}}{d_{other}}$ is larger than a given threshold, another surface point has to be created between the two neighboring surface points on this particle. The position of the new surface point is determined by the position of the two surface points on this particle. The result is a refined surface discretization and the checks can be performed again, until all points have a sufficiently small value of r.

Thus, the adaptive Set-Voronoi calculation could improve the Set-Voronoi calculation based on two aspects: The precision of the calculation will be better, as regions, where a high density of surface points is required to produce an accurate result for the Set-Voronoi calculation, are sampled with enough points. Furthermore the calculation time can be reduced as regions, where a low density of surface points is sufficient, can be calculated quickly.
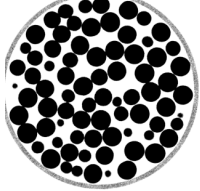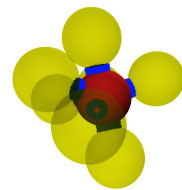
# 3. Physical applications of Set-Voronoi diagrams

While section 2.4 described the mathematical foundation, technical aspects, and the general applicability of Set-Voronoi diagrams for different systems, this section will focus on physical questions. Three experimental systems are investigated using the Set-Voronoi tessellation. In section 3.1 a bidisperse sphere packing is analyzed with respect to tribo-charging (generation of electrical charge on a particle by collision. Section 3.2 analyzes the effects of history-dependence in tetrahedra packings and section 3.3 investigates packings of deformable emulsion droplets.

3.1. Tribo-charging in bidisperse sphere packings[27]

Besides gravity and radial contact forces, there is a variety of other forces in granular materials, e.g. tangential forces due to friction [Wei15; Sch17], electrostatic forces [KL09; Mat+10; Qin+16; HXZ12; Xie+13; Wai+14], or capillary forces [Her13]. Understanding the effects of these forces is an interesting scientific problem, as the dynamics and structure of granular media is controlled by those forces.

The easiest way to avoid crystallization in sphere packings is to use a binary distribution of spheres. Structural properties [DRE98; KHH08] of binary sphere packings, their jamming behavior [CT15] and their binary contact numbers [Kum+16] have been thoroughly studied along with other structural properties [EY62; Pin+98; Bia+09; Hop+11; Kum+16]. Depending on the dominating segregation principle [Sch+06], the larger beads either rise to the top (called the *Brazil Nut effect*) or sink to the bottom (called *Reverse Brazil Nut effect*). Segregation is a common issue in the manufacturing industry and for chemical or pharmaceutical processes [Kár+98; HK04; Poh+06; Pla+06; Sch+06; Cia+06; USS07; Liu+13; DS13; GSB17].
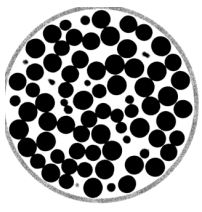
By definition, tribo-charging is the generation of electrical charge on a particle by collision. Tribocharging of granular materials proves to be challenging, because it can lead to both repulsive and attractive interactions between particles [LT86a; KL09; LM11; HXZ12; Xie+13; Wai+14; Lee+15; Qin+16; Che+16; Che+16; Kol+16; Yos+17]. Tribo-charging is pervasive in the handling of granular materials, because every time two particles get in contact, charges are transferred [Har57; MW08]. Tribo-charging itself can influence the structural properties of packings, as it can lead to the formation of clusters [Lee+15], to demixing [MMS07] or to the suppression of segregation [SHS17], or other effects [Qin+16; Che+16; Yos+16; Kol+16; Yos+17]. The amount of tribo-charging is known to depend on the humidity of the air [SHS17], which can be used to control the amount of surface charges on the beads. Despite the broad coverage in literature, the microscopic effects of tribo-charging are not fully understood. Therefore, we cannot give a comprehensive explanation what microscopic effects lead to the observed charging in our systems.

In this work, it is ensured that the charges are large enough to avoid global segregation. As bidisperse spheres are used as particles, the use of Set-Voronoi diagrams is mandatory, as ordinary point Voronoi diagrams can not reproduce an adequate structural tessellation (see section 2).

3.1.1. Experimental setup and data analysis

The bidisperse sphere packings (sphere radii r_s = 0.795 mm, r_L = 1.5 mm) contain polytetrafluorethylene (PTFE) spheres in a cylindrical polyamide container with radius R = 50 mm. Packings are prepared at various global packing fractions Φ_g by vertical vibration (Frequency 100 Hz, critical acceleration $2g$) on an electromagnetic shaker (model number LDS 406). X-ray tomographies (GE Nanotom) of the samples are performed to investigate the structural properties of the packings. Furthermore the contact number Z is analyzed, resolved by the size of the particles in contact: small-small, small-large, large-small and large-large. Further details on the experimental setup as well as the image processing are given in [SHS17; SWS17].

As the surface charge Q scales with the size of the particle, the surface charge density $\sigma = \frac{Q}{4\pi r^2}$ is used in this analysis. The index $_L$ or $_s$ represents the respective value for the large and small beads. The surface charge is measured by averaging over ten particles, which are extracted from the packing once the vibration has stopped. The beads are deposited in a Faraday cup, connected to an electrometer (Keithley 6514)[28]. Figure 3.1 (a) demonstrates that under our shaking conditions, large spheres charge negatively and small spheres charge positively. This observation is the opposite of what has been found in previous granular experiments [HXZ12; Xie+13; Wai+14] and predicted by some models

---

[28]We note that the the sum of all charges on the beads is not necessarily zero, as the walls of the shaking container will also carry some electrostatic charge.
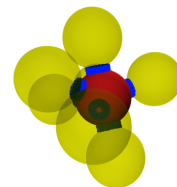
of same-material tribo-charging [KL09; LM11]. Similar systems have been investigated in experiments [SKZ08]. It was shown that simple geometry can lead to the transfer of electrons from larger to smaller particles [KL09]. However it is still an open debate whether electrons, ions or the exchange of surface material is the charge carrier [SHS17; Mat+10]. A result similar to our observation was found in experiments with spheres sliding along a plane made from the same material [LT86a; LT86b].

The X-ray tomographies allow access to both contact number Z as well as the Set-Voronoi tessellation of the packing. Details on the Set-Voronoi calculation process for binary sphere packings can be found in section 2.4.1. Using the radius of the spheres and the Set-Voronoi cells, the local packing fraction Φ_l for each particle as well as the global packing fraction Φ_g can then be calculated using equations 2.4 and 2.5. A binary mixture has four different contact numbers: Z_{LL}, Z_{Ls}, Z_{sL} and Z_{ss}. The contact number scaling method described in section 1.4.2 can be adapted to measure the individual contact types. This is done by not taking all particle pairs into account for the overlap test, but just the particle pairs which are relevant for the current pair. Further details of the contact analysis step can be found in [SWS17].

(a)

(b)
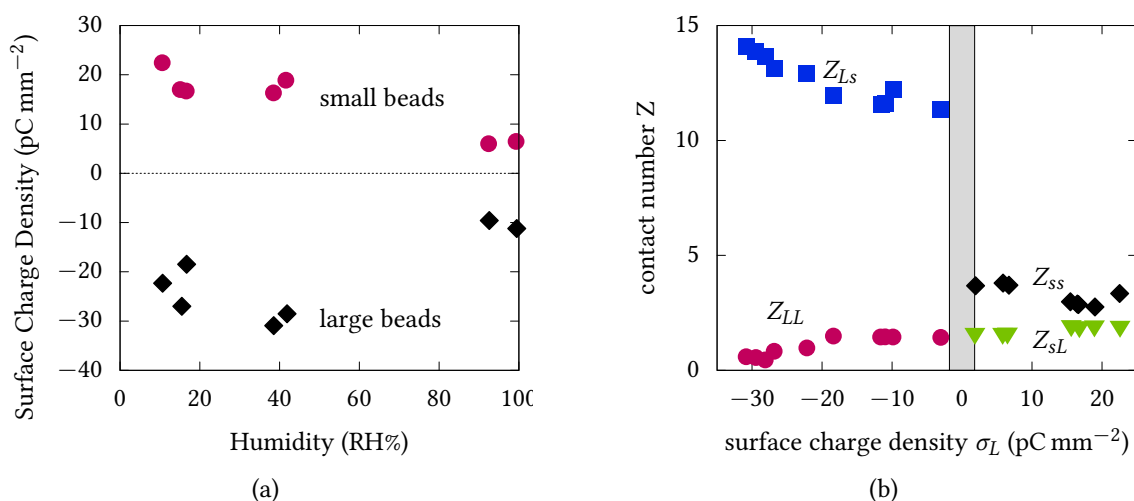
Figure 3.1.: (a) The amount of charge accumulated by shaken PTFE spheres depends on the relative humidity. The sign depends on the size of the particles, with small particles being positively and large particles being negatively charged. Data is taken from samples of equal volumes of small and large PTFE spheres, shaken vertically in a polyamide container. (b)Number of contacts Z per particle (resolved by contact type) as a function of the surface charge density. The shaded area corresponds to the residual charge regime.
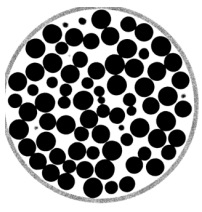
3.1.2. Charge controls the contact numbers

The contact numbers resolved by type, as shown in figure 3.1 (b), are clearly depending on σ_L and σ_s. For example, Z_{Ls} is the average number of small s particles in contact with a large L particle. Note that Z_{Ls} can thus reach values close to 15. This is larger than the contact number for FCC in monodisperse spheres, but as a large sphere can be surrounded by more small than large particles this value is reasonable. When increasing the surface charge density σ, the numbers of large-small Z_{Ls} and small-large Z_{sL} contacts increases as well. Those are contacts between particles of different size.

At the same time, the number of same-particle contact types Z_{LL} and Z_{ss} decreases with increasing surface charge density. This dependence of contact numbers on the surface charge density σ is in good agreement with a simple model assuming that like-charged large beads repel each other, whereas oppositely charged particles attract each other.

None of the investigated packings show macroscopic segregation, though the local structure differs, as the large particles form more string-like structures in the highly charged sample. Similar structures have been identified in simulations and experiments of monodisperse charged grains [Che+16; Cao+13].

3.1.3. The effect of surface charge density on packing fractions and contacts

As shown in figure 3.2, tribo-charging affects global properties of binary sphere packings. The packing fraction Φ_g decreases approximately 1 % with increasing surface charge density σ, which has also been seen in simulations of monodisperse particles [Che+16].

When looking at the average contact numbers (calculated as described in section 1.4.2), it can be seen that Z also decreases with increasing surface charge density. This means, the packing expands and gets looser. This correlation of Z and Φ_g is expected, as shown in section 1.4.2 for monodisperse spheres.

Qualitatively, increasing the charge density on the beads will also increase attractive interactions between large and small particles. Thus, a decreasing packing fraction with increasing charge density seems counterintuitive at first glance. However, attractive interactions also alter the mechanical stability of granular packings since these have a stabilizing effect, causing the formation of chain-like, porous structures [Che+16].
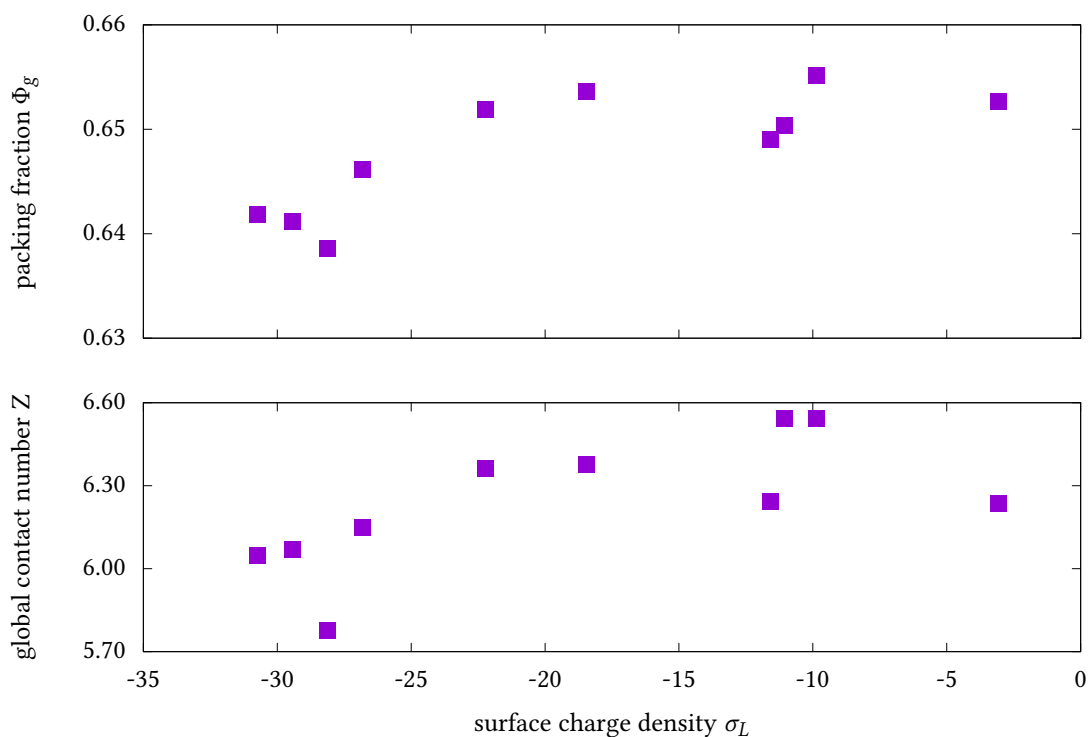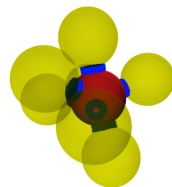
Figure 3.2.: Global packing fraction Φ_g and the global contact number per packing Z depend weakly on the surface charge density σ.

3.1.4. Conclusion

Binary systems of dielectric particles have been shaken vertically at different humidity levels, which allows to control the tribo-charging of the beads. While the microscopic processes of tribo-charging are not fully understood, we report that small and large beads differ in the sign of the their charge. Previous granular experiments and theories of tribo-charging show a different effect[KL09; LM11; HXZ12; Xie+13; Wai+14], where same-material particles of different sizes carry charges with the same signs and thus lead to repulsive forces. Thus, the resulting attractive interactions inhibit macroscopic segregation of the sample. At the same time, the electrostatic interactions due to tribo-charging change the local structure of the packing: The stronger the charge carried by the individual particle is, the more likely becomes the formation of contacts between small and large beads at the expense of same bead type contacts. Furthermore, it could be shown that global properties of the packings also depend on the surface charge density. These findings have various applications for chemical and industrial processes, as tribo-charging can occur at any time two particles collide.
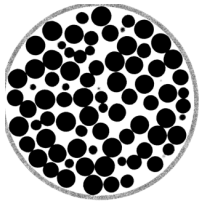
While this work gives a better understanding of the structural effects caused by tribo-charging, we did not investigate the dynamics of the formation of those structures. Once a phenomenological model of the effect of tribo-charging, as observed in our experiments, is known, simulations of the dynamics of the vibration process could help to understand the fundamental processes in the dynamics of the formation of the observed structures. Furthermore a systematic analysis based on different particle size ratios could shed light on further structural properties.
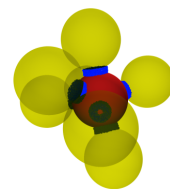
3.2. History dependence in random packings of tetrahedral particles[29]

In contrast to most of the particle shapes described in previous sections (see section 3.1 and 2.4), which have solely point contacts, the tetrahedra particles described in this section allow for a variety of contact types due to their flat faces. Furthermore they show an interesting history dependence based on their preparation protocol. As tetrahedra are non-spherical particles, the use of Set-Voronoi diagrams is mandatory to calculate packing fractions.

Packings of mould casted polypropylene tetrahedral particles with a sidelength of 7 mm and static friction coefficient 0.8 are prepared using different preparation protocols and are investigated using X-ray tomography. Preparation is performed on an electromagnetic shaker (shaker model: LDS-V555) by tapping the particles with a frequency of 3 taps per second. Starting from a loose initial packing in a cylindrical container (diameter $D = 10.4$ cm) the amount of taps as well as the critical acceleration ($\Gamma = 2g$, $5g$ or $7g$) vary between the different preparations, see section 3.2.4. X-ray tomographies are recorded on the GE Nanotom machine with a resolution of 100 µm per voxel. Particles are detected by a two-step algorithm [Neu+13], involving a cross-correlation and a steepest-ascent gradient search. After the particles are found, the number and type of contacts is computed for each particle. Further information about particles, image analysis and particle detection is given in detail in [Neu+13].

3.2.1. History dependence in granular matter

Various granular experiments have shown, that mechanical and structural properties of apparently identical samples will differ based on their preparation history. Examples include the response to shear [HW04] or the pressure distribution below a pile of sand [Van+99]. Another term for history dependence is also *memory effect* [Van+99; Jos+00]. However, there is no clear definition of the term "history dependence" and different authors use it with slightly other meanings [HW04; Jos+00; Pug+10; Pug+11; Ard+14].

The term history dependence describes the fact, that the global packing fraction Φ_g (see section 2.2.1) of a granular packing is not sufficient to provide a complete description of the state of the packing of tetrahedra[30].

---

[29]This section is based on the publication N. Thyagu, M. Neudecker, Simon Weis, Fabian Schaller, and Matthias Schröter. "Local analysis of the history dependence in tetrahedra packings". In: *Physical Review E. (in review)* (2018). URL: http://arxiv.org/abs/1501.04472. Verbatim quotes of this paper may not be labeled as such.

[30]For the case of spherical and ellipsoidal particles, which do not show history dependence, the global packing fraction Φ_g is a sufficient descriptor.
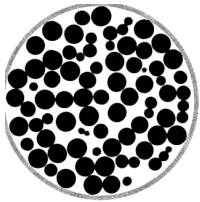
3.2.2. Contact types between tetrahedral particles

(a) Face-to-face, F2F

(b) Edge-to-face, E2F

(c) Vertex-to-face, V2F

(d) Edge-to-edge, E2E
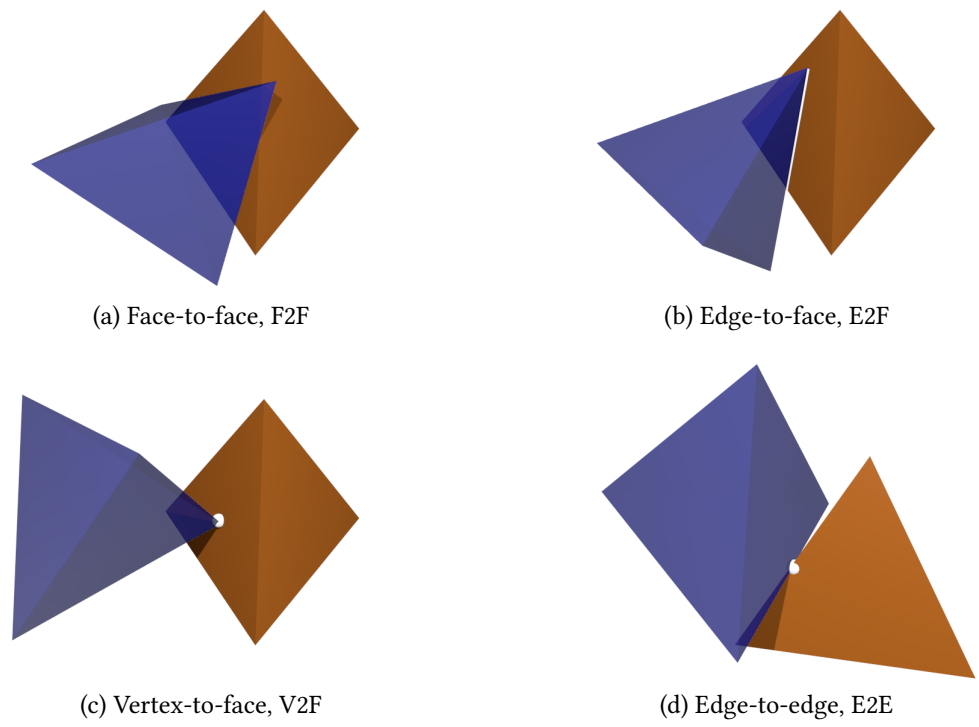
Figure 3.3.: Different contact types for tetrahedral particles.

Due to the tetrahedron's flat surfaces and edges, tetrahedra have four different contact types. The differentiation between the individual contact types is important, as each type fixes a different number of degrees of freedom. Face-to-face (F2F, figure 3.3 (a)) contacts are mechanically equivalent to three individual point point contacts, while edge-to-face (E2F, figure 3.3 (b)) contacts are equivalent to two point contacts. The two contact points labeled with *point contacts* here are vertex-to-face (V2F figure 3.3 (c)) contacts and edge-to-edge contacts (E2E, figure 3.3 (d)), that both represent the mechanical equivalent of one individual point contact.

The total number of constraints per particle C is given by the sum of the number of contacts Z_i of contact type i multiplied with the number of constraints of that type m_i:

$$C = \sum_i m_i \cdot Z_i \tag{3.1}$$

. In this equation the value of m_i depends on the contact type. While all contact types impose three translational constraints. E2F contacts add two rotational constraints (5
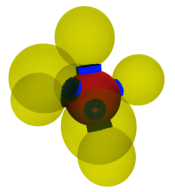
constraints in total). F2F impose three rotational constraints (6 constraints in total). All constraints are shared between two tetrahedra.

3.2.3. Set-Voronoi calculations on tetrahedra packings

To calculate the local packing fractions Φ_l, the Set-Voronoi cells of the particles are required. The details of the Set-Voronoi calculation can be found in section 3.2. The result is the Set-Voronoi tessellation of the tetrahedra packing.

Using the size of the particles and the volume of the cells, the local packing fraction Φ_l can be calculated. Note that although the particles are shrinked and blunt edges are used, the volume of the un-shrinked, ideally sharp tetrahedra is used for the local packing fraction calculation. Furthermore, the shape of the Set-Voronoi cells is analyzed using Minkowski tensors of rank two, as introduced in section 2.2.2. Here, the focus is set on the anisotropy index $\beta_0^{2,0}$.

3.2.4. A local view on tetrahedral packings

As already shown in [Neu+13], the average number of constraints in a tetrahedra packing does not only depend on Φ_g, but also on the preparation protocol. The preparation in this case is a number of taps on a vertically mounted electromagnetic shaker. This history dependence allows to prepare six packings in total, with three pairs of packings, each having approximately identical Φ_g, but different values in C, which are depicted in figure 3.4. Φ_g has been calculated using equation 2.5. The naming will be [*Number of Taps*]G[*shaker peak acceleration*]. The files for all six systems containing the particle positions are available with the original publication [Thy+18]. The fact that packings with the same global packing fraction Φ_g, but different constraint number C can be reached using different preparation protocols, shows the presence of history dependence in the systems under investigation.

A global model, i.e. understanding C as a function of Φ_g, is only appropriate for compressible particles where pressure acts as a hidden variable controlling both C and Φ_{global} [Sch17]. Hard and frictional particles have no mechanism how Φ_{global} could control the number of contacts they form. And even if we assume the existence of a particle scale demon, this demon would be unable to compute Φ_{global} by averaging the Φ_{local} values of the surrounding particles, because these values are spatially correlated [Lec+06; Zha+12].

Because the formation of contacts in granular materials is a local process, we need to describe it with locally defined variables. The most important one is Φ_l, see equation 2.4. The most likely contact number of a particle depends only on Φ_l and *not* on Φ_g. In a first approximation, this locality of the contact formation also holds true for ellipsoid packings
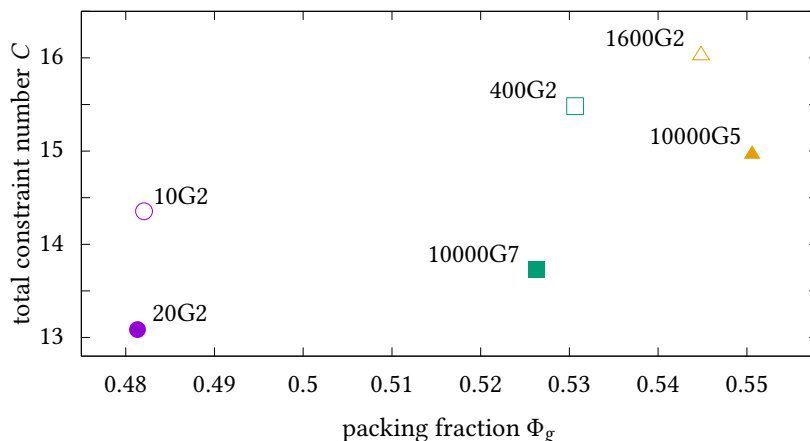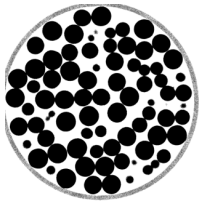
Figure 3.4.: Six packings (three pairs, indicated by open and filled symbols) are prepared at approximately the same Φ_g but different values of the constraint number C (see equation 3.1). The fact that the same packing fraction, but different constraint number can be reached with different preparation protocols, shows the presence of history dependence of the systems under investigation. The data is the same as in [Thy+18] and was originally obtained by [Neu+13].

where next to Φ_l only the aspect ratio α of the particles is required to know for predicting the average contact number [Sch+15b].

For the highly non-spherical tetrahedra, it can be expected that both the shape of the free volume surrounding them, and their relative orientation with respect to the neighboring particles might influence the number of contacts they form. We will describe the former with the isotropy index $\beta_0^{2,0}$ of the Voronoi cells and the latter by the contribution of the individual contact types Z_i (where we acknowledge that the latter choice blurs the line between control parameter and result).

Distributions of local packing fractions

The harmonic mean of Φ_l (which is how Φ_g is defined) is roughly the same within each pair of tetrahedra packings shown in figure 3.4 and 3.5. For spheres [Sch+15b] one could therefore expect, that their contact numbers Z are also identical.

A possible explanation for their different values of Z would be the following idea: As in the case of spheres and ellipsoids, there exist some universal, nonlinear functions for $Z_i(\Phi_l)$. If at the same time the local packing fraction distributions $P(\Phi_l)$ for the two different samples would be skewed in different directions, this could result in different mean values of Z. However, Figure 3.5 (j), (k) and (l) show that this is not the case: There is a small
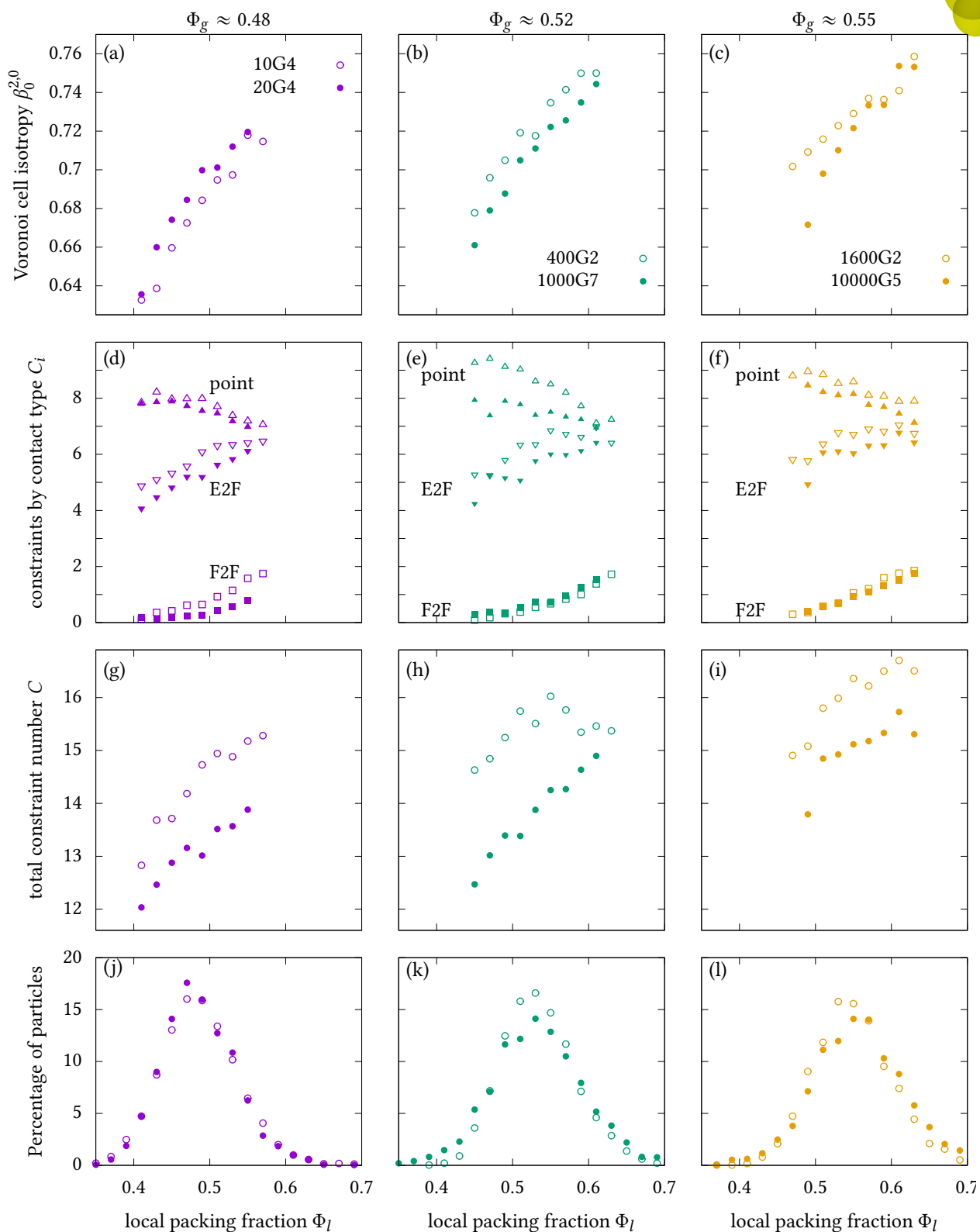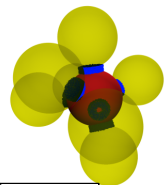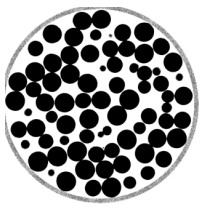
Figure 3.5.: Comparing pairs of packings at average $\Phi_g = 0.48$ (left), 0.53 (center) and 0.55 (right). Colors are chosen as in figure 3.4. Bins with less than 3 % of particles are only displayed in the lowest row, subfigure (j) to (l).

shift corresponding to the slightly different mean values and a small change in the width of the distribution (quantified below), but no pronounced asymmetry in $P(\Phi_l)$.

When comparing the pairs of packings created with different accelerations, the less constrained packings have the broader distributions; The width of the distribution w (relative to its mean value) for the `10000G7` system is 25%, while w for the `10000G5` system is 14 % larger than their counterparts. We note, however, that such a global analysis is susceptible to spatial gradients within the sample. While for all other samples the fluctuations of Φ_{local} as a function of height are smaller than $\pm$ 0.01, Φ_{local} of `10000G7` changes ≈ 0.03. This explains the larger values of w to some extent. In summary, the differences in w seem to be rather small between the samples.
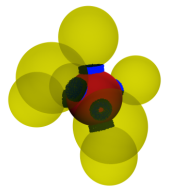
Contact probabilities depend on local packing fraction

A more detailed analysis on how C depends on Φ_l is shown in figure 3.5 (d) to (i) . In all three pairs of experiments the values of $C(\Phi_l)$ are consistently larger for the higher constrained packing. However, the functional form of the $C(\Phi_l)$ curves is not identical. $C(\Phi_l)$ increases monotonically for both marginally tapped samples in figure 3.5 (g); the two curves are only shifted vertically against each other. The situation is more complex for the two pairs tapped with different strengths (figure 3.5 (c) and (d)): for the packings `400G2` $C(\Phi_l)$ seems to approach a plateau, for the other three packings $C(\Phi_l)$ increases monotonically but with different slopes.

Subfigures 3.5 (d) to (f) display how the contribution of the three different contact types changes with Φ_l for the different packings. Point contacts provide the largest contribution to C for all six systems, which holds true for all individual values of Φ_l. Interestingly however, the slope $dC_{point}/d\Phi_l$ is negative while it is positive for the E2F and F2F contacts (see figure 3.3 for the contact types), as it is for contacts between spheres or ellipsoids [Sch+15b]. This agrees with the intuitive notion that the closer two tetrahedra get to each other, the more likely it is that their flat faces or straight edges align with each other. Thus, for close distances the probability of point contacts is lower than of the higher constrained contact types.

For all pairs of packings the difference in preparation is visible in the E2F and point contacts: in a first approximation the $C_{E2F}(\Phi_l)$ and $C_{point}(\Phi_l)$ curves are shifted vertically while their average slope is preserved.

The situation is different for the F2F contacts: for the pairs tapped at different accelerations the $C_{F2F}(\Phi_l)$ curves fall on top of each other. Figure 3.6 demonstrates that this agreement goes even further: with the exception of the loose `10G2` sample all other $C_{F2F}(\Phi_l)$ curves coincide within experimental errors. This points to the existence of a preparation-

independent master function controlling the number of F2F contacts in samples that have been sufficiently tapped.
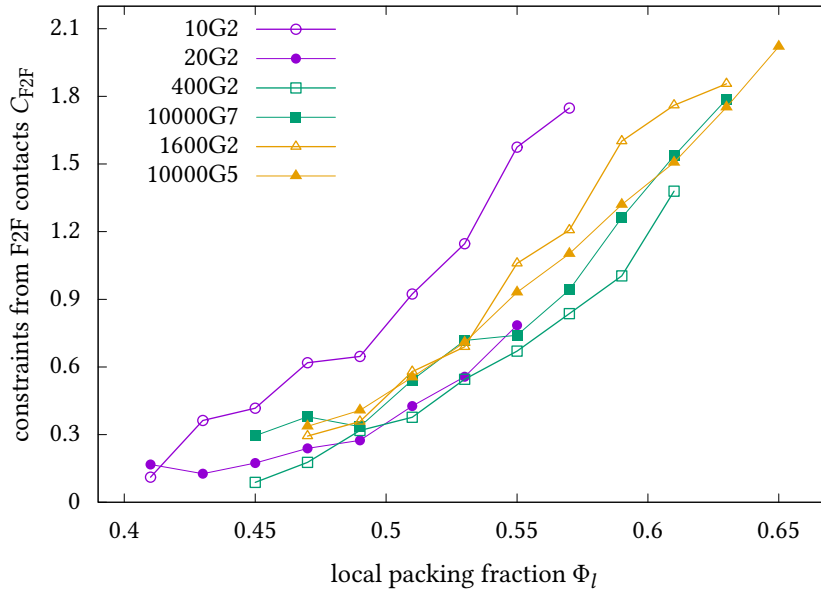
Figure 3.6.: Constraints due to F2F contacts seem to fall on a universal curve for samples which have been sufficiently tapped (in this study: all samples except for 10G2). Bins with less than 3 % of the total number of particles are discarded.

Some motivation for this different behavior of the F2F contacts can be derived from the high value of their constraint multiplier m_{F2F}: Once a particle has formed an F2F contact with another particle, all three rotational degrees of freedom are completely blocked for both particles. Any additional F2F contact (i.e. increase in C_{F2F}) depends therefore solely on the capability of another incoming particle to align itself in such a way, that there is a 180 degree angle between the face normal vectors. The probability that such a rotation is possible will depend strongly on the available space (i.e. Φ_l).

In contrast, pairs of particles, that have established an E2F or point contact between themselves, retain one or even three rotational degrees of freedom to facilitate another contact. This means that geometrical factors, other than Φ_l, will play a role in determining the probability if another contact of the same type can be formed.

Voronoi cell isotropy

Figures 3.5 (a), (b) and (c) display the monotonic increase of the isotropy index $\beta_0^{2,0}$ with Φ_l in all our experiments. While such an increase is in agreement with the results for sphere
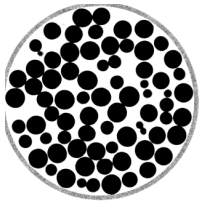
packings [Sch+10b], the fact that there is no universal curve for $\beta_0^{2,0}(\Phi_l)$ differs from the behavior of spheres but is compatible with packings of ellipsoids [Sch+15a].

For the only marginally tapped samples the lower constrained packing contains the more isotropic Voronoi cells, for the samples tapped at different levels of g, the higher constrained packings are more isotropic. This implies that $\beta_0^{2,0}$ is *not* likely to be the hidden parameter connecting the preparation history with the constraint number of the packing.

3.2.5. Conclusion and outlook

Tetrahedra have four flat faces and four edges. Thus, they can not only create point contacts similar to sphere packings, but also edge-to-face and face-to-face contacts, which fix a higher number of mechanical constraints. It is not possible to predict the number of contacts of a special type based on the local packing fraction Φ_l or global packing fraction Φ_g. This is due to the preparation history, that seems to be encoded in another (yet to be identified) parameter. On the other hand, the number of face-to-face contacts in sufficiently tapped samples seems to be a function of the local packing fraction Φ_g alone.

From a physical viewpoint, history dependence poses a lot of interesting questions. The mechanisms behind the dynamics of the packing process are not yet fully understood. This means that packings of tetrahedra are inherently more complicated to describe than sphere packings. While for sphere packings the global packing fraction Φ_g is a sufficient description of the state of the system, this is not the case for packings of tetrahedral particles and yet another *hidden* variable has to be found.

Neither of the isotropy of the Set-Voronoi cells $\beta_0^{2,0}$ nor the width of the local packing fraction distribution $w(\Phi_l)$ seems to qualify as the missing hidden parameter to quantify history dependence and to allow for a comprehensive description of tetrahedra packings. Thus, another measure has to be found. Possible candidates are for example the fabric tensor [Cow85] or spherical Minkowski tensors [Kap+12], which have yet to be probed in further studies. Simulations of packings of tetrahedral particles could give access to the internal forces, thus allowing for additional measures to be tested, e.g. the force-moment tensor [PD13].
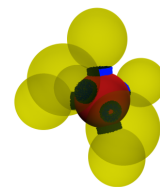
3.3. Frictional emulsions[31]

The main difference between emulsions and most other systems[32] discussed in this work, is the fact that the drops ("particles") in an emulsion are not hard, but deformable and compressible. More specifically, liquid dispersions consist of discrete liquid drops which are tightly packed within a continuous liquid phase. Coalescence between these soft drops is avoided by the addition of interfacially active agents, which create a protective monolayer at the drop surface.

Due to the deformability of the drops, the limiting maximum global packing fraction for emulsions is much higher than in hard systems and can reach up to $\Phi_g^{max} \approx 1$. At this point the particles become completely polyhedral. As for granular packings of hard particles, those emulsions are a-thermal, out-of-equilibrium systems and normally do not show frictional forces between the particles. Foams and emulsions are therefore often described as *soft granular media* [Wea+07; Hec09; KTH13].

Most emulsions that have been considered in the past [WH99] are stabilized by interfacially active agents which create fluid-like drop surfaces with constant interfacial tension and negligible solid friction/adhesion. The structural features of this kind of systems close to jamming and at very high packing fractions may now be considered well understood [DH15; WH99]. Usually the deformation of a drop caused by one of its neighbors is only depending on the relative positions of the drop and the neighbor. However, the influence of multi-particle interactions can not be neglected and leads to a so-called *non-locality* [HC17].

A number of recent developments in the search for super-stable emulsions [Rio+14; Hei+15] has led to an increased use of stabilizing strategies which create solid-like drop surfaces. Such interfaces are obtained in numerous ways, either by using specifically designed agents (certain particles, proteins or polymers) or by creating gels of agents at the interface via chemical or physical cross-linking [Giu+16]. The resulting *skin-like interfaces* have a finite, solid-like interfacial elasticity (i.e. the surface tension varies with deformation). Thus, such systems are also called *skinny emulsions*. They also lead to solid friction between the soft drops, and in some cases, they render the drops adhesive. The resulting normal and tangential forces lead to complex interactions between drops and additional mechanical constraints that influence strongly how the soft drops pack and deform around and beyond jamming.

---

[31]The content of this section is based on Anais Giustiniani, Simon Weis, Christophe Poulard, Paul Kamm, Francisco García-Moreno, Matthias Schröter, and Wiebke Drenckhan. "Skinny emulsions take on granular matter". In: *Soft Matter* (2018). ISSN: 1744-6848. DOI: 10.1039/c8sm00830b. Verbatim quotes of this paper are not necessarily labeled as such.

[32]except for the root growth from section 2.4.2.
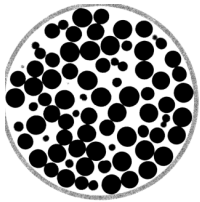
Sample name	%Dod	$\langle R \rangle$ (μm)	σ_R (μm)	PI	Φ_g	$\sigma(\Phi_l)$	$\langle \beta_0^{20} \rangle$	σ_β
5%-S	5%	915.0	19.1	2.1%	0.48	0.08	0.68	0.16
10%-S	10%	904.4	63.3	7.0%	0.34	0.10	0.57	0.25
5%-L	5%	1121.0	75.3	6.7%	0.50	0.10	0.60	0.17
10%-L	10%	1071.1	118.4	11.1%	0.40	0.16	0.39	0.22

Table 3.1.: Summary of the main parameters of the emulsions under investigation. *%Dod* is the dodecane percentage in the continuous phase. $\langle R \rangle$ is the average equivalent radius of the drops (see text) and σ_R the width of the distribution from figure 3.8. *PI* is the polydispersity index, Φ_g the global packing fraction and σ_{Φ_l} the width of the distributions of the local packing fraction Φ_l obtained by fitting the distributions with Gaussian functions, and $\langle \beta_0^{20} \rangle$ the average value and σ_β the width of the distributions of the parameter β_0^{20} characterizing the drop deformations.

3.3.1. Characteristics of skinny emulsions

In order to advance with the experimental investigations of soft drops forming a super-stable emulsion, a model system is used that consists of monodisperse polyethylene glycol drops (PEG) that are dispersed in a liquid (PDMS) continuous phase composed of Sylgard 184® base, D_4 and dodecane (5 % or 10 % in weight, leading to a change in friction and adhesion between the drops). The emulsions are generated by letting the PEG drops settle one by one through the PDMS phase. Details on the sample preparation can be found in [Giu+16; Giu+18]. A plane cut through the 5%-S sample[33] is shown in figure 3.7

Two different drop sizes are investigated for each dodecane concentration. X-ray tomographies are recorded on a micro-focus Hamamatsu machine with a tungsten target, an acceleration voltage of 60 kV and a voxel size of 20 μm. The image analysis is based on section 1.3 with bilateral filter parameters of $\sigma_g = 40$ and $\sigma_p = 4$ and applies an additional median filtering step (kernel size 5 × 5 × 5) to reduce image noise. The position of the centroid as well as the volume V of each particle is calculated from the labeled tomogram. Additionally, the surface of the particles based on a voxel grid will be used for the Set-Voronoi calculation, see below.

The average equivalent radius $\langle R \rangle$ and the associated standard deviation σ_R for each sample is calculated from the tomography results and is given in Table 3.1. Both are obtained from the distribution of the equivalent radius. The equivalent radius is obtained by calculating the radius R of a sphere with the same Volume V as the drop (which is not spherical, see the anisotropy $\langle \beta_0^{2,0} \rangle$ of the drops, figure 3.12). The equivalent radius of each particle can

---

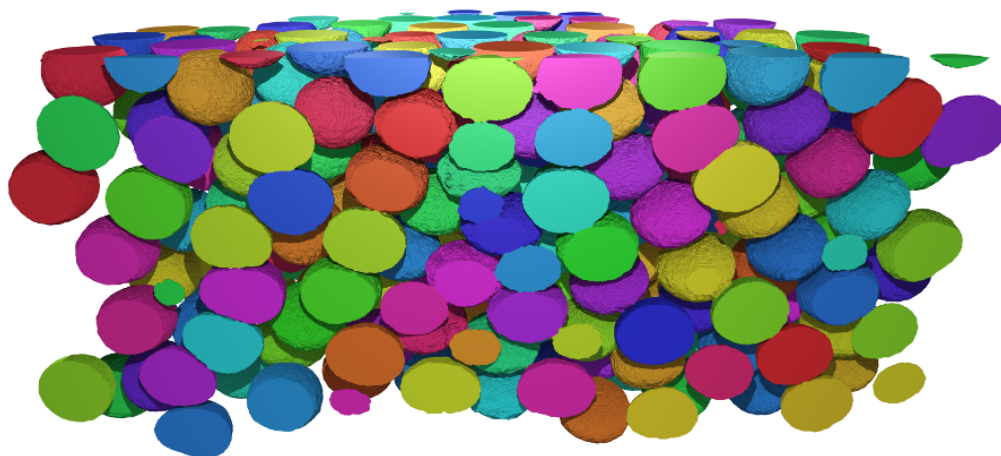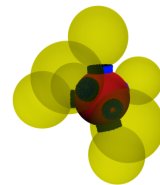[33]rendered in povray [pov18] using the voxel data of the tomogram

Figure 3.7.: Rendering of a plane cut through the tomogram of the 5%-S sample. The labels of the individual droplets are depicted by the (randomly assigned) colors.

be calculated based on the Volume as obtained from the tomography data by the relation [BSM12]

$$V = \frac{4}{3}\pi R^3 \qquad (3.2)$$

For this equation the drop is assumed to be spherical, which is in fact not the case[34]. Table 3.1 also lists the polydispersity index $PI = \sigma_R/\langle R \rangle$ of the drops and the amount of dodecane added in the continuous phase $\%DOD$ (in weight %). For simplicity, in the remainder of the study the drop size will be referred as either S (small, $R \approx 930\,\mu m$) or L (large, $R \approx 1150\,\mu m$).

Figure 3.8 shows the distributions of the equivalent radius R for all four samples (see Table 3.1). The samples 5%-S, 5%-L and 10%-S have a low polydispersity index PI. However, the sample 10%-L has a high PI due to the presence of smaller drops in the emulsions, which might have been created during the generation. The results given for this sample are therefore to be interpreted with caution.

3.3.2. Structural analysis of the emulsions

In the following, the structural properties of the emulsions are studied in detail based on the 3D tomography data. The distribution of the local packing fraction Φ_l and the global packing fraction Φ_g of the emulsions are calculated and analyzed, as well as the organization and deformation of the drops within the emulsions.

---

[34]That is the reason for the naming "equivalent" radius.
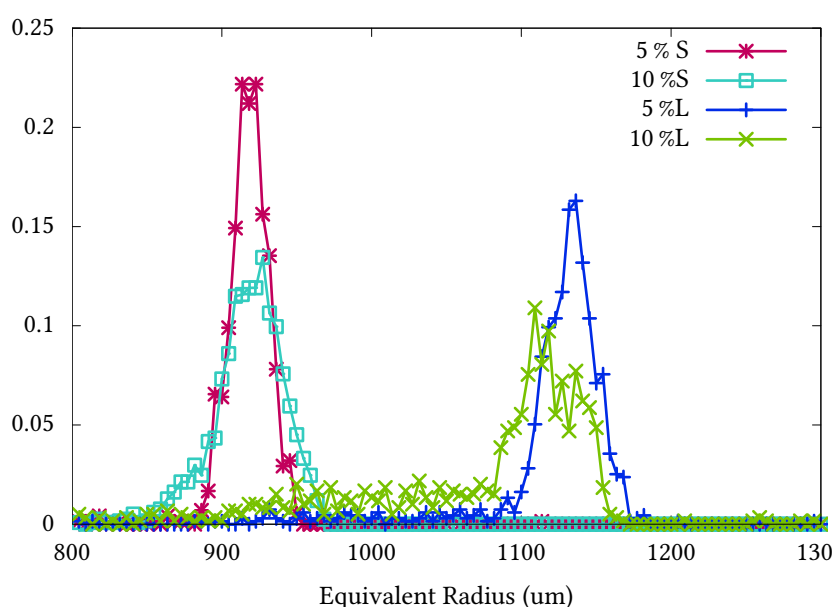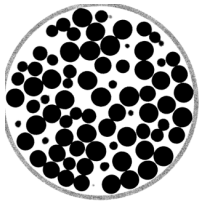
Figure 3.8.: Equivalent radius distributions for all four samples. The equivalent radius is calculated according to equation 3.2.

(a)

(b)
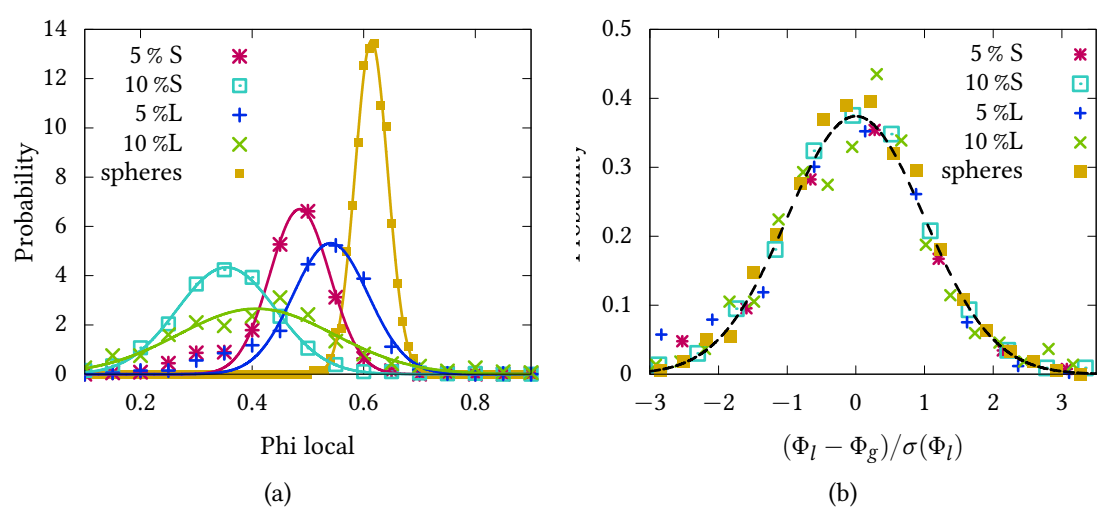
Figure 3.9.: (a) Local packing fraction distribution for the emulsions as well as for a reference system of hard spheres. Fits are Gaussian functions. The systems are labeled according to table 3.1. (b) Rescaled local packing fraction distributions according to equation 2.6 for the same systems as in (a). The dashed black line is the average rescaled Gaussian distribution of all systems.

The local packing fraction Φ_l of the emulsions is used as defined in equation 2.4. The volume of the drop is directly obtained from the X-ray analysis by counting the voxels of each drop, the volume of the cell is computed using the *Set-Voronoi tessellation* [Sch+13a; Wei+17] based on the voxelized surface of the drops with the same method as described in section 2.4.2. The outmost layer of drops is excluded to avoid boundary effects.

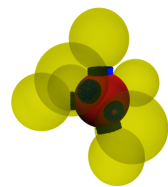Figure 3.9 (a) shows the distributions of the local packing fraction Φ_l obtained for the four emulsions presented in Table 3.1 together with distributions of local packing fractions obtained for hard frictional spheres [WS17]. It can be seen that all distributions can be fitted by Gaussian functions, though in the case of the samples 5%-S and 5%-L an overpopulation of loosely packed drops (tail-like structure) on the left side of the distribution appears[35]. These low Φ_l tails means that the 5% packings have some interesting geometrical feature, which has not been identified yet. The distribution of the 10%-L sample is noisy - probably due to the large *PI* - but can still be described with a Gaussian function.

### 3.3.3. Local packing fraction distributions

The global packing fraction Φ_g of the whole packing is calculated using the harmonic mean of the local packing fractions as described in equation 2.5. Φ_g and the standard deviation $\sigma(\Phi_l)$ of the local packing fraction distributions are listed in Table 3.1. The value of Φ_g seems to decrease with increasing dodecane percentage for a given drop radius, being an indication of a looser packing.

In order to compare these distributions independently of the value of Φ_g, the rescaling as described in equation 2.6. The result is shown in figure 3.9 (b). It can be seen that within the data scatter, all distributions collapse on a single common master curve (black dashed line). This means that the rescaled distribution of the local packing fraction of our system is not distinguishable from a packing of hard frictional spheres or soft frictionless drops, whether they show adhesive surfaces or not. This representation of the local packing fraction thus seems to be independent of the interactions between the spheres and of the global packing fraction of the packings within the error bars of our experiments.

3.3.4. Locally resolved global packing fraction $\Phi_g(h)$

Based on the local packing fraction and the position of a droplet, the global packing fraction can also be calculated within different bins at an emulsion height h, where $h = 0$

---

[35]There is no systematic dependence of local packing fraction Φ_l and the position of the drop. This means that (a) the packing is rather homogeneous and (b) boundary effects ranging inside the packing are not responsible for the loosely packed drops. However, it was found that the radius of the drop is depending very weakly on the z position of the drop, which could be caused by the deposition process of the drops.
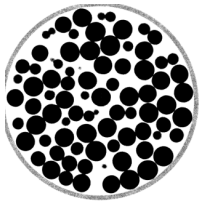
corresponds to the bottom of the emulsion. The variation of the global packing fraction with height $\Phi_g(h)$ is shown in figure 3.10. $\Phi_g(h)$ does not follow the model provided by Maestro *et al.* [Mae+13] for surfactant-stabilized, frictionless emulsions with the same drop size, density difference and interfacial tension. On the contrary, the profiles for the skinny emulsions presented here are constant, and do not depend on h. For their model, Maestro *et al.* only took surface tension effects into account and neglected any surface elasticity of the drops. In our system, however, the surface elasticity of the drops is not negligible and will strongly resist the drop deformations. Nevertheless, the drops are significantly deformed and cannot be approximated by non-deformable spheres.

The constant packing fraction of soft spheres may instead be explained by the Janssen effect[36] [Spe05]: in the presence of friction, the contact forces between the spheres redirect the weight, i.e. the pressure, towards the walls of the container, and therefore the pressure in the bulk is independent of the height. Since a non-negligible friction is existing in the system [Giu+18], it can therefore be assumed that the elasticity of the drops together with the tangential forces between them act simultaneously to explain the constant packing fraction $\Phi_g(h)$ with the emulsion height h.
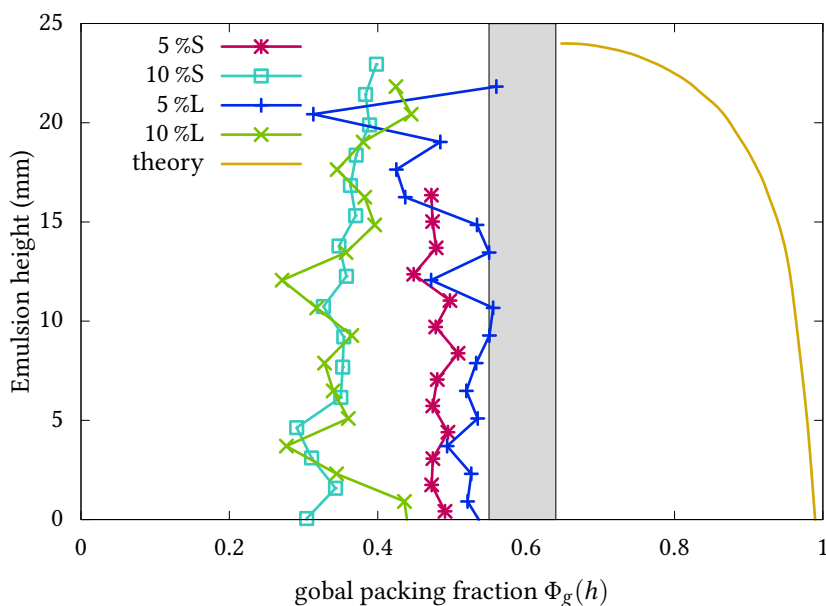
Figure 3.10.: Evolution of global packing fraction as a function of emulsion height $\Phi_g(h)$, measured for the emulsions presented in table 3.1. The theory for soft, frictionless emulsion drops [Mae+13] is shown along with the accessible range of packing fractions for hard frictional spheres (gray shaded area).

---

[36]This effect is also visible in the hourglass: The pressure does not vary with height, which leads to a constant flow of sand.
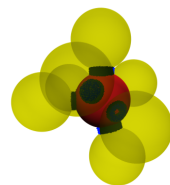
Additionally to the invariance of the packing fraction with height, surprisingly low values of Φ_g are found compared to the lowest values of the global fraction $\Phi_{\mathrm{RLP}} \approx 0.55$ known for hard spheres with friction. A slight underestimation of the packing fraction may come from the fact that the thickness of the skin around the drops is not known precisely, i.e. their effective size is unknown. However, closer analysis of the thickness of the flat "films" between neighboring drops in the tomography images estimates the thickness of the skin to be $< 50 \ \mu$m. This makes a correction of 0.08 to add to the values of Φ_g in figure 3.10 which can therefore not explain the very low values observed for 10% of dodecane. Values of Φ_g below the loose-packing density of hard, frictional spheres were observed for spheres connected by liquid bridges [LYY11], i.e. in the presence of adhesive forces between the spheres. The presence of the polymeric skin around the droplets in the emulsions induces both normal attractive and tangential forces between the drops in the presence of dodecane [Giu+18]. The low values of Φ_g are in that sense consistent with previous findings for hard sphere packings.

Figure 3.10 also seems to show that the amount of dodecane has an impact on the global packing fraction of drops in the emulsion. Indeed, the values of Φ_g for 10% of dodecane are lower than the values for 5% of dodecane, with a difference of $\Phi_g(5\%) - \Phi_g(10\%) \approx 0.15$ for a given drop radius. The decrease of Φ_g with %DOD in this system may be explained by the increasing interaction between the drops with dodecane concentration. The width of the distributions of Φ_l also increases with the strength of the adhesion between emulsion droplets [Jor+11], which correlates well with the findings presented here.

3.3.5. Pair correlation function

The local fluctuations in density in the emulsions can be probed by calculating the pair correlation function $g(r)$ as introduced in section 1.4.1. Figure 3.11 shows $g(r)$ for the emulsions, compared with the $g(r)$ obtained for a packing of hard frictional spheres. In the case of the frictional hard spheres, the expected sharp peak at $r/r_0 = 1$ can be clearly observed, as well as the two peaks at $r/r_0 = \sqrt{3}$ and $r/r_0 = 2$, which are characteristic of amorphous packings of monodisperse spheres.

In the case of the emulsion drops, two important observations can be drawn. Firstly, the peak at $r/r_0 = 1$ is broad, with a width $\sigma_g \approx 0.45$ which is independent of the dodecane concentration %DOD. This cannot be explained by the polydispersity of the drops since - as shown in Table 3.1 - the PI are low for the samples represented in figure 3.11. However it can be seen that the peak at $r/r_0 = 1$ for the soft, frictionless and non adhesive emulsions from [ZM05] is broader than the one for the hard frictional spheres, which is due to the deformability of the emulsion drops. The large peak calculated for these emulsions could be the result of the deformation of the drops. Secondly, it is also noticeable that there is a complete absence of any further characteristic peaks in $g(r)$ of our emulsions. This
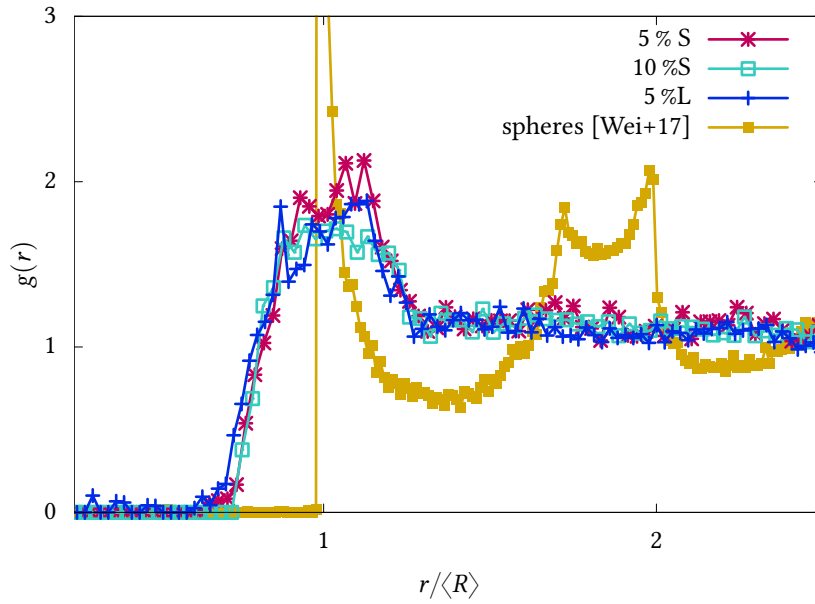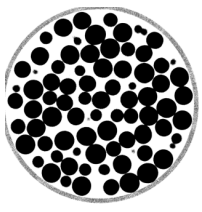
Figure 3.11.: Pair correlation function $g(r)$ according to section 1.4.1 for frictional emulsion drops and a monodisperse sphere packing at $\Phi_g = 0.638$ (also shown in figure 1.9).

indicates no correlations in the positional order of the drops with respect to each other in the packing. The flat $g(r)$ may also be explained by the deformation of the drops, which is why a close analysis of the drop shapes is required.

3.3.6. Particle anisotropy

Anisotropy in the shape of objects are characterized by Minkowski tensors as introduced in section 2.2.2.

The distributions of the particle anisotropy β_0^{20} for the drops of the four emulsions of Table 3.1 are shown in figure 3.12 (a). The distributions are indeed systematically large and centered on relatively low values of β_0^{20}, when hard spheres have a constant value of $\beta_0^{20} = 1$ (as indicated by an arrow in figure 3.12 (a)). Table 3.1 gives the average value $\langle \beta_0^{20} \rangle$ and the width σ_β of each distribution fitted with a Gaussian function. The amount of dodecane in the continuous phase does not seem to have a significant impact on $\langle \beta_0^{20} \rangle$. Except for the sample 10%-L, for which the average value $\langle \beta_0^{20} \rangle = 0.39$, the other samples exhibit similar values of $\langle \beta_0^{20} \rangle = 0.7$. The highly deformed drops of the sample 10%-L are probably due to another mechanism which would also be responsible for the high polydispersity of this drop packing. These high deformations of the drops can explain the broad peak at
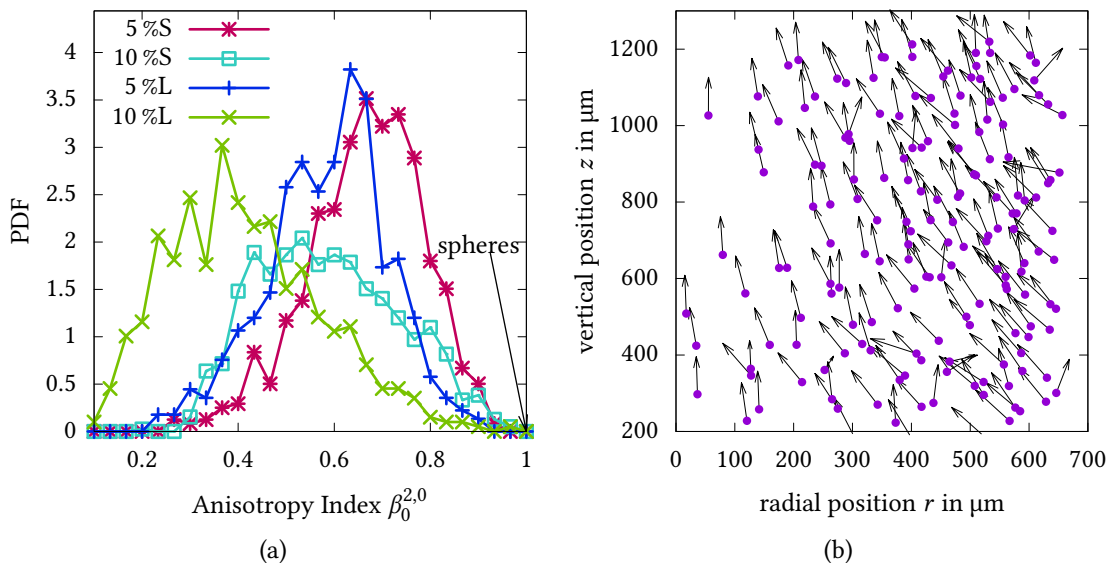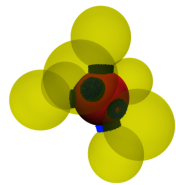
Figure 3.12.: (a) Distribution of $\beta_0^{2,0}$ values of the particles. (b) Azimuthally averaged particle positions of a 45° wedge. The arrows indicate the axis of the strongest particle deformations. Aligned particles/arrows indicate chains of particles.

$r/\langle R \rangle = 1$ and the missing structure peaks for $r/r_0 > 1$ of the pair correlation function in figure 3.11.

To understand where such strong deformations may come from, figure 3.12 (b) shows azimuthally averaged particle positions and the directions of strongest particle deformations. The $W_0^{2,0}$ Minkowski tensor is calculated for the spheres (not for the Set-Voronoi cells). In figure 3.12 (b) the eigenvector to the smallest eigenvalue is depicted in the arrows, when projected to the radial direction. This arrow depicts the direction of the strongest deformation of each drop. As it can be seen, in the central part for small values of r the deformation is almost vertical, while for increasingly larger values of r the deformation direction of the drops rotates towards a 45 degree direction, which can qualitatively be compared to results from [Van+99].

It can be seen, that figure 3.12 (b) distinguishes lines of drops whose deformations follow a single direction (indicated by successive arrows), which are similar to force chains observed in packings of hard granular spheres [AM05; BDB15] or disks [DKP17]. Figure 3.12 (a) and (b) show that the drops are strongly deformed by pairwise or multi-particle interactions. This indicates that the adhesive and frictional forces between our drops might be responsible for the creation of force-chain like structures during the emulsion generation.
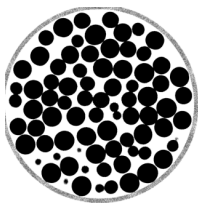
Finally, the average contact number C (see section 1.4.2) of the drops was not accessible because of the inability of the X-ray tomography technique to differentiate between the polymeric skin and the continuous phase, as well as the irregular shape of the drops, which renders the contact number scaling method 1.4.2 inapplicable.

3.3.7. Conclusion

With the *skinny emulsions* presented in this section, a new model system for frictional and adhesive emulsions has been introduced. The local structural properties (which are mostly only accessible because of the use of Set-Voronoi tessellations) of these system are quite interesting, as some aspects are similar to packings of hard, frictional particles (like the local packing fraction distributions and the constant global packing fraction with emulsion height), while other aspects are quite different from hard frictional particles. Especially the flat pair correlation function $g(r)$ in the skinny emulsion system poses some interesting questions, as such a result can not be seen in other granular systems.

When compared to other emulsion systems it can be seen that the skin changes the interaction of the droplets by introducing friction and adhesion. Both (yet indistinguishable in our analysis) have a major impact on the local structure of the system. Thus, interesting facts are to be expected from further analysis.

While our work is a first study of the structural properties of such systems, further experiments are needed to acquire a complete understanding of skinny emulsions and their structure. Further research should perform experiments to distinguish between tangential friction and radial adhesion forces inside the packing. Furthermore, using a dye in the continuous phase could allow to differentiate between the polymeric skin of the droplets and the surrounding continuous phase, which could then be used to calculate contact numbers of those systems. Simulations of skinny emulsion droplets can shed light on the forces inside the packing and thus give a more detailed explanation for the deformation mechanism of the droplets, as well as for the question of force chains.

116
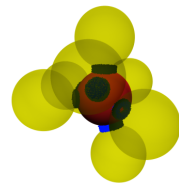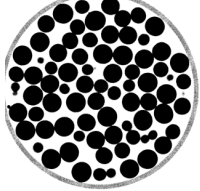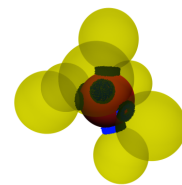
# 4. The effect of friction and cohesion in monodisperse sphere packings[37]

In dry packings of hard particles forces at the contact points (see section 1.4.2) are the main interactions between particles and mainly governed by the friction between particles [Sch14; OHe+01]. This leads to a variety of physical effects, influencing the structure of packings [OHe+02; Poh+06; Ute+11; Utt12; Neu+13; Sch+15b], jamming [SHS07; Som+07; Sil10; HHS10], on segregation [USS07] and other topics [AM05; Bar+16; Wei15]. The force at the contact point splits into a normal component and a tangential component, which are depending on the friction coefficient μ of the particles.

In wet particulate systems cohesion due to the liquid bridges acts as an additional force on the particles [Her13]. This is a very interesting system to study, as dry systems consist of only repulsive interactions, while wet systems inhibit repulsive and attractive forces between particles [Sch05a]. Wet packings show fundamentally different mechanical properties when compared to dry packings [SGH04; Fou+05; Sch+08; Ger+03b; Ger+03a; Sch05a; Van+12], however little is known about the structure and local geometry in dry packings [Sch+08].

4.1. Friction and cohesion in granular packings – a literature overview

Friction in dry granular packings is responsible for converting radial contact forces into tangential forces at the contact points. In wet packings liquid bridges can create another type of force, namely attractive interactions due to surface tension. This section lists the results of for both topics from previous publications.

---

[37]This section is partially based on Simon Weis, Gerd E. Schröder-Turk, and Matthias Schröter. "Structural similarity between dry and wet sphere packings". In: *(In preparation for peer review)* XX (Aug. 2018). URL: https://arxiv.org/abs/1808.04342. Verbatim quotes are not necessarily labeled as such.
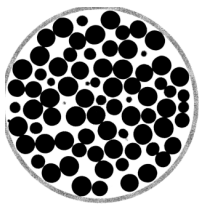
4.1.1. Friction in granular packings

Structural properties of packings strongly rely on inter-particle friction [Utt12; Wei15; Sch17]. This can be described by the friction coefficient μ. μ describes the ratio between the force of friction between two particles and the force pushing them together. Friction can not be neglected in experimental packings as $\mu > 0$ for all experimental particles[38].

Friction is the main difference between granular packings and emulsions (see section 3.3) or foams (see e.g. [HC17]) as it can lead to tangential forces at contact points. Those tangential forces add additional constraints for the mechanical stability (see figure 4.1), by providing additional ways to satisfy force and torque balance.

Experiments on frictional particles have revealed various effects, mainly studied for granular segregation [HK04; Sch+06; Pla+06; USS07; DS13; Liu+13; LHW14; GSB17], but also for the angle of repose [Car70; JLN89; Poh+06] and other interesting effects [SCH16]. The effect of friction has also been investigated analytically and in simulations [TG91; Kár+98; Sil+02; Cia+06; HSP09; GSB17]. Little is known about the influence of friction on static structural properties of a packing, but recent publications point out the large importance of friction in experimental granular packings [Sch17].

When looking at individual contacts, a contact between two frictionless spheres provides one normal force component for two particles, thus fixing 0.5 degrees of freedom per particle. To fix all three translational degrees of freedom, the isostatic contact number is required to be at least $Z_{\text{iso}}^{\mu=0} = 6$ for frictionless spheres. For frictional spheres, a contact fixes three force components (two tangential, one normal) for two particles, thus fixing 1.5 degrees of freedom per particle. To fix the three translational degrees of freedom plus the (now important) three rotational degrees of freedom a value of at least $Z_{\text{iso}}^{\mu \neq 0} = 4$ contacts per particle for frictional spheres are required [Sch14].

Many theoretical and numerical publications deal with frictionless packings [OHe+02; Sil+02; Sil10; SWM08; Cor+10; Bau+13]. When compared to experimentally accessible packings, the results from those publications show differences with respect to packing fractions (section 2.2.1), and isostatic numbers (section 1.4.2) and other structural properties. A complete phase diagram (based on discrete element simulations) can be found in [Cia+11]. Further numerical investigations have probed the geometry and jamming properties of frictionless and frictional packings [Sil+02; Sil10]. With decreasing friction, the packing fraction increases [Sil+02]. It was shown that for frictionless spheres, RLP and RCP coexist at $\Phi_g = 0.64$ with a contact number of $Z = 6$.

---

[38]Even for hydrogel spheres, which consist of up to 99.5 % water, the friction coefficient is $\mu = 0.01$ [DZB13; Sch17]
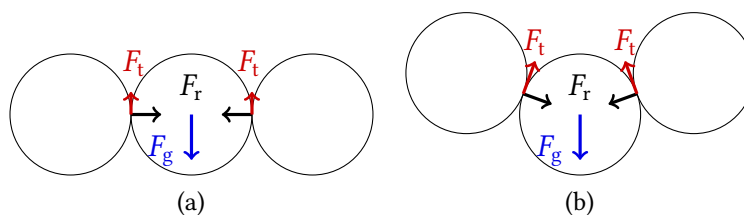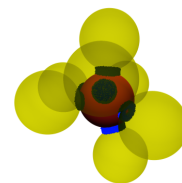
Figure 4.1.: Friction plays an important role for mechanical stability of granular packings. Qualitative two-dimensional image of mechanically stable spheres in a plane. The outer spheres are fixed. Arrows represent the normal (black) and tangential (red) forces as well as the gravitational force (blue). In both systems the central sphere is fixed in position due to tangential forces at the contact points of the outer spheres. Without friction none of the depicted systems would be mechanically stable. Image extracted from [Wei15].

4.1.2. Cohesion in granular packings

The dry case is governed by solid friction. However, when adding liquid to a previously dry granular packing, additional forces (capillary and viscous) can act due to liquid content between the particles, which lead to cohesion and lubrication on a global scale [FTP99]. This has effects on many mechanical properties of wet granular packings, which have been intensively investigated in literature and will be covered in detail this section [Alb+97; Hor+97; Boc+98; HL97; FTP99; Mas+99; Ive+01; Ger+03b; Koh+04; SGH04; Fou+05; Sch05a; Sch+08; LYY11; Van+12; Her13; KTH13; Fal+14].

However, little is known about the structural properties of wet packings besides the fact that liquid in granular packings leads to an improved collective stability [Sch05a] when compared to dry packings and changes in the global packing fraction [Her13]. Even a small amount of liquid content added to a granular packing will lead to the formation of bridges at the contact points due the minimization of the surface energy of the liquid.

The distribution of liquid inside a granular packing is depending on the wetting properties of the liquid and the particles [Her00; OH04; HBS08]. The wetting will depend on the chosen liquid and the material of the particles. A non-wetting liquid will lead to an homogeneous distributions of liquid throughout the packing, which we are not interested in. Thus we focus on the a wetting combination of particles and liquid. Furthermore, the bond number b as the ratio between cohesive forces and gravitational forces [Sch09; Hag12] is an important quantity describing the strength of effects to expect in a wet system. The bond number is influenced by a number of variables, mainly the surface tension of the liquid, the bead size and the contact angle of the liquid with the (particle's) substrate. In the experiments presented here, we will focus on wetting liquids only. For experimental details about the investigated system, see section 4.3.1.
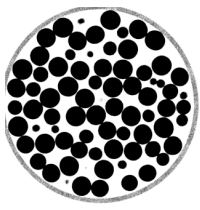
The mechanical stability of wet piles of particles has been investigated in experiments and analytically [Mas+99; Alb+97; FTP99]. Experiments on the effect of adding small quantities of liquid to granular media have shown an dramatic increase in the angle of repose and allow for the formation of large clusters of particles [Hor+97]. Adhesive forces caused by interstitial liquid bridges have been identified to be the main reason for this effect. Experiments were performed using different types of oil on granular systems of polystyrene beads with a roughness of $\approx 1\,\mu m$. The thickness of the liquid skin around the particles is estimated to be in the range $\leqslant 50\,nm$. Surprisingly the estimated amount of liquid in the liquid bridges is very low ($\leqslant 0.1\,\%$).

Theoretical work from the same time investigates the stability of sand piles as a function of liquid volume [HL97]. Assuming rough particles, three regimes for the adhesive forces are identified depending on the liquid volume:

- For small liquid volumes, the liquid is concentrated inside individual aspherities of the particles.

- For intermediate liquid volumes the liquid is wetting a statistically rough region, which is small compared to the macroscopic curvature of the particle.

- For large liquid volumes the macroscopic curvature of the particles is the main contributor which determines the wetted particle surface. It is claimed that surface roughness does not play a role anymore.

Contradicting the estimate of [Hor+97], that only $0.1\,\%$ of the liquid is present in the bridges, a counter argument is made, that the surface wetting has a thickness of only some monolayers, which leads to the conclusion that the majority of liquid has to be in the bridges.

Starting in 2004 the group around M. Scheel and S. Herminghaus started to evaluate the physical properties of wet granular media. First papers were on the mechanical properties of wet granular media, e.g. on mixing and segregation in wet bidisperse sphere systems [Ger+03b] or the influence of liquid content when vertically agitating a sample [SGH04]. On the structural side they investigated both the volume of liquid bridges and the thickness of the liquid film as a function of time as well as the number of liquid bridges per particle (liquid bridge coordination number) as a function of liquid content in two systems containing different sized glass beads [Koh+04]. It was shown that the water volume in individual liquid bridges equilibrates on a timescale of about 5 minutes. Furthermore the geometry (volume to surface ratio) of liquid bridges was used to identify different bridge morphologies (like capially bridge, trimer, …) [Sch+08].

Further structural properties were investigated in [Fou+05]. They examined the average number of bridges per particle by by looking at microscopy images of monodisperse sphere packings at around $\Phi_g \approx 0.62$. The values found are independent of liquid content after exceeding a certain liquid content threshold. It was stated that for liquid content above this
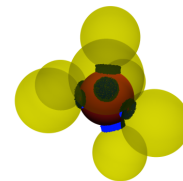
threshold the average number of bridges should be around the number of contacts between particles [Ger+03a]. Furthermore, dynamical properties while shearing the sample were investigated. In [Van+12] the influence of the relative humidity on packing processes of systems of granular spheres was investigated, while [Fal+14] investigated the sliding friction of a sledge on dry and wet sand.

4.2. Friction changes the range of accessible packing fractions

4.2.1. Measuring and changing inter-particle friction

As outlined in section 4.1.1, friction plays an important role in the physics of granular materials. The friction coefficient can be measured using an inclined plane [Wei15; Utt12; Sch+15b]. In this setup three particles of the same type are glued to a sledge (to favor sliding instead of rolling), which is placed on a flat piece of the same material as the particles. This is placed on a plane which is at first in horizontal position and can slowly be raised on any side. The angle of the plane is measured using a digital scale. At the moment the sledge starts to slide the angle is noted as the critical angle γ_{crit}. The friction coefficient is then calculated by using force balance as $\mu = \tan(\gamma_{\mathrm{crit}})$.

The friction coefficient of the original polyoxymethylene particles (see section 2.4.1) is $\mu_{\mathrm{original}} = 0.30 \pm 0.03$. The inter-particle friction coefficient μ can be changed using various methods. Chemical etching can be used to increase the surface roughness (and thereby the friction coefficient) of glass spheres [Utt12]. In this work a "mechanical" approach is used: The particles are grinded using different abrasives for multiple hours. This leads to an increase to 0.53 ± 0.03.

A different batch of particles was used to prepare packings with a dry lubricant, graphite powder. Using graphite powder reduced the friction coefficient in our system to $\mu = 0.23 \pm 0.04$.

It is worth mentioning that for this study the same particles have been used in all systems and only the friction coefficient μ of the particles has been changed.

4.2.2. Results

The friction coefficient μ does not change the structure of the packing. This can be seen in figure 4.2, where for two systems with different friction coefficients μ at the same global packing fraction Φ_g the number of contacts is the same with respect to experimental errors.
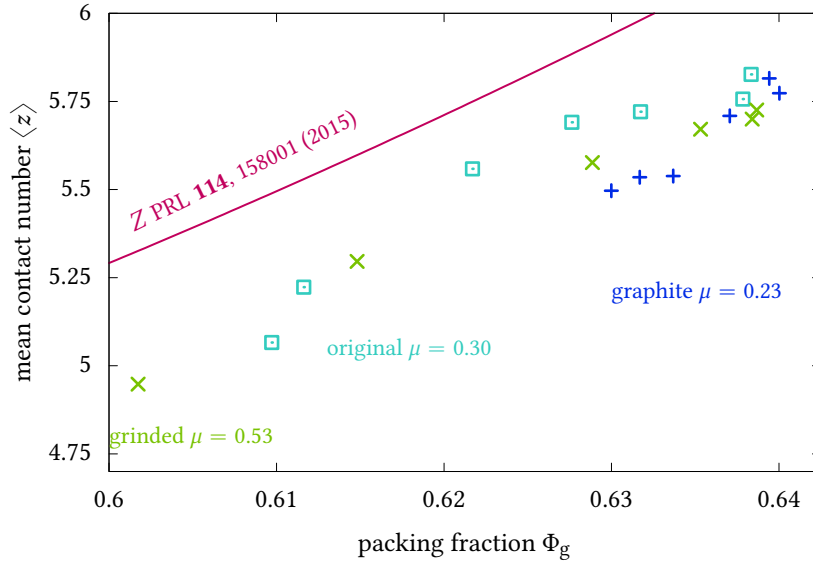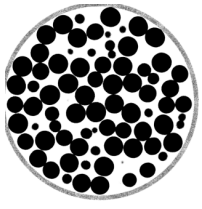
Figure 4.2.: Friction changes the range of accessible packing fractions Φ_g. Packings of spheres with three different friction coefficients μ are prepared at various packings fractions Φ_g. Data points for original and grinded particles are extracted from [Wei15].

However, figure 4.2 shows that the friction coefficient does change the range of accessible packing fractions Φ_g. The original particles with a friction coefficient of $\mu = 0.30$ can be prepared in the range of Φ_g between 0.61 and 0.64. If the friction coefficient is increased to 0.53, the lowest possible packing fraction is closely above $\Phi_g = 0.60$. For the particles with the reduced friction coefficient of $\mu = 0.23$ the lowest possible packing fraction is at $\Phi_g = 0.63$.

This can be explained by the mechanical constraints created by tangential forces. A packing with a low value of μ would not be mechanically stable at a low packing fraction Φ_g. If such a packing would be prepared, it would not be mechanically stable and thus rearrange towards a packing with higher packing fraction Φ_g and higher contact number Z.

Comparing the sphere packings of this study with previous results [Sch+15b] (line in figure 4.2), shows that the contact number of this study are lower than for [Sch+15b]. This is due to improved particle quality. The ratio of the shortest to the longest particle axis can be characterized by the anisotropy index $\beta_0^{2,0}$, see section 2.2.2. For the particles in this study the average particle anisotropy is $\beta_0^{2,0} = 0.99$, while for the particles from [Sch+15b] the average particle anisotropy is around $\beta_0^{2,0} = 0.97$. This can be seen in figure 4.3 (a). It is known that particle asphericity leads to an increase in contact numbers [Sch12; Sch+15b; Sch+15a]. This coincides with the findings of lower contact number Z for our particles than in [Sch+15b].
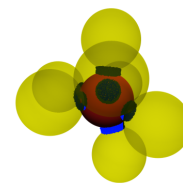
4.3. Structural similarities between dry and wet packings

4.3.1. Measuring wet packings

Wet packings of spherical particles made of polyoxymethylene and a radius of $r = (1.750 \pm 0.011)$ mm (see section 2.4.1) are prepared in a cylindrical container with a diameter of $D = 84$ mm and height $H = 150$ mm with and without additional liquid. Different amounts of bromodecane are used as a wetting liquid: The liquid volume fraction η is defined as the total liquid volume divided by the total sample volume [SGH04; Sch+08]. Measurements at 0 mL, 10 mL and 15 mL are performed, which correspond to liquid volume fractions $\eta = 0\%$, $\eta = 2.1\%$ and $\eta = 3.1\%$, respectively[39] Bromodecane is used as the liquid due to its good wetting properties with the polyoxymethylene particles and the high X-ray contrast.

X-ray tomographies are recorded of the packings. For the dry packings the measurements have been performed at the GE Nanotom, while the dry measurements have been done at a Fraunhofer EZRT CT-Rex. The resolution for the wet packings is 35 µm per voxel which yields a sufficient sampling for the particles as well as for the liquid bridges. For the dry packings the resolution is 64 µm per voxel. Particle center positions are recorded for $N \approx 800$ particles in the central portion of the tomogram ($1300 \times 1300 \times 1000$ voxels) using the methods described in chapter 1. The parameters for the image processing are: Bilateral filter $\sigma_g = 4$ voxels and $\sigma_p = 2700$ in units of greyvalues. An erosion depth of $\lambda = 5$ voxels is used. Furthermore the voxels of liquid bridges are identified.

Figure 4.3 (b) shows the distribution of the bromodecane in a $\eta = 2.1\%$ packing at $\Phi_g = 0.588$ projected onto the XY plane. The liquid is distributed homogeneously throughout the packing. Furthermore there are a lot of small liquid clusters and bridges between particles. The amount of liquid clusters which do not touch two particles is $\leqslant 1\%$.

4.3.2. Contact numbers $\langle Z \rangle$ and bridge numbers $\langle B \rangle$

The local and global packing fractions Φ_l and Φ_g are calculated for the sphere packings (see section 2.2). Φ_g ranges from 0.61 to 0.64 for dry packings and 0.57 to 0.605 for wet packings. For the dry packings an irregular container boundary was used to avoid crystallization [Kap+12; Han+15]. For the wet packings this was not required as the packing fraction is low enough so no crystalline structures occur.

---

[39]The liquid is distributed throughout the spheres by continuously rotating and shaking the container.
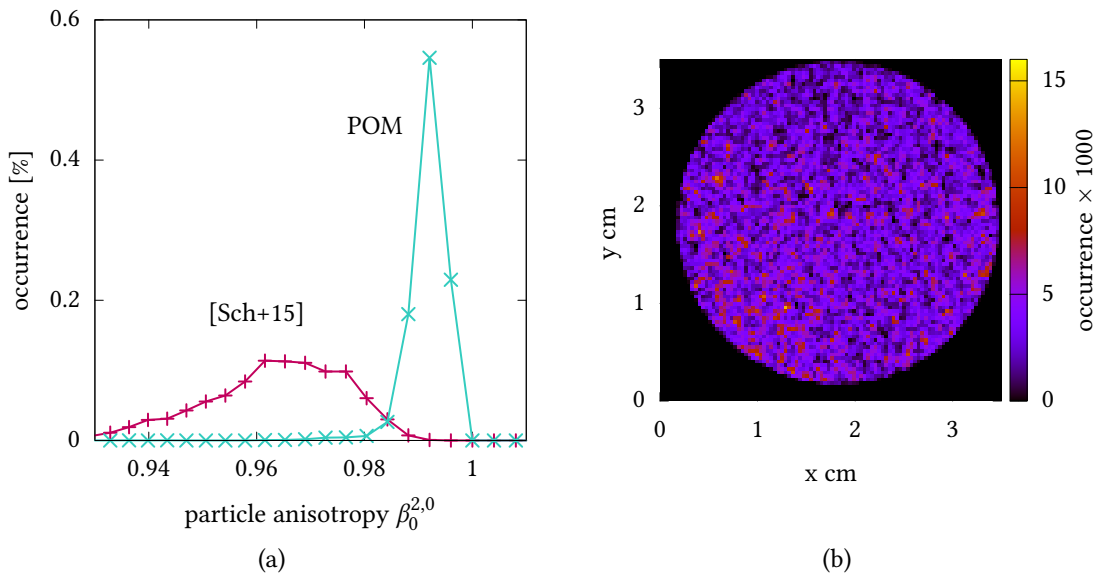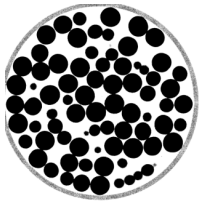
Figure 4.3.: (a) Particle anisotropy for the particles used in this work as well as for the work of [Sch+15b] quantified by the anisotropy index $\beta_0^{2,0}$. The particles used in [Sch+15b] are not as spherical as the ones used for this study. (b) In the central region the bromodecane is homogeneously distributed throughout the packing. This image is from a system with $\eta = 2.1\,\%$ at $\Phi_g = 0.588$.

The average contact number $\langle Z \rangle$ is calculated using the Contact number scaling method as described in section 1.4.2. The brackets $\langle ... \rangle$ denote the average over all particles in a system. For wet packings a similar measure is defined: The *bridge number* $\langle B \rangle$ is the average number of liquid bridges per particle. $\langle B \rangle$ is measured based on the labeled tomogram data for the spheres and the liquid bridges. For each sphere the touching liquid bridges are counted. A bridge i is defined as touching a particle k if at least one voxel of the bridge i is directly adjacent to a voxel of the sphere k. The specific choice of adjacency (straight or diagonal) does not change the results for $\langle B \rangle$.

We define Z_i as the number of spheres that share a contact point with sphere i, B_i^{nc} the number of spheres that are not in contact with sphere i but have a liquid bridge with sphere i, and B_i^c the number of spheres that are in contact with sphere i and where these contacts also correspond to liquid bridges. $B_i = B_i^c + B_i^{nc}$ is the total number of liquid bridges of sphere i. We will denote the averaged properties as $\langle B^{nc} \rangle = \sum_{i=1}^{N} B_i^{nc}/N$, etc where N is the total number of spheres.

The results of our study are

1. In wet packings, the number of force-bearing connections between spheres (including both particle contact points and liquid bridges) is significantly higher than the
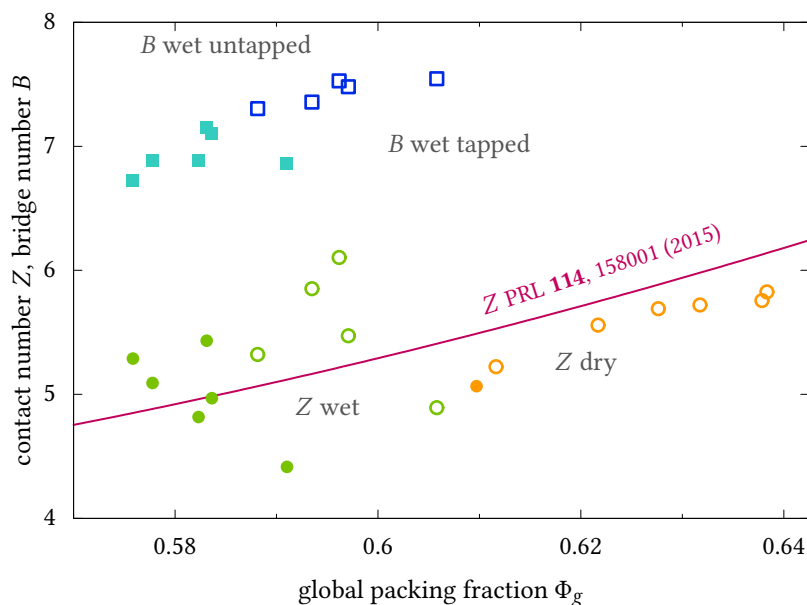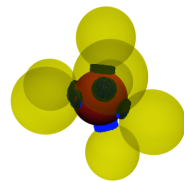
124

Figure 4.4.: Bridge Number $\langle B \rangle$ supersedes contact number $\langle Z \rangle$. Contact numbers $\langle Z \rangle$ are shown in orange (dry) and green (wet) circles, while bridge numbers $\langle B \rangle$ are shown in blue. Open and closed symbols correspond to to tapped and untapped system preparation, respectively

number of contacts alone. In addition to the contact number $\langle Z \rangle$, the particles have on average an additional 2 liquid bridges that do not correspond to contacts, $\langle B^{nc} \rangle \approx 2$. This appears to be largely independent of ϕ_G, see figure 4.4.

2. The structure of the wet and dry sphere packings appears to be largely the same. Neither the contact numbers (figure 4.4) nor the Voronoi cell shape analysis (figure 4.7) reveals any systematic differences. The wet packings can be thought of as dry packings with additional liquid bridges introduced between particles that are not in contact but very close by.

3. As expected for a good wetting liquid, all contacts are surrounded by liquid meniscusses ($\eta(0) = 1$, Fig. 4.6). The fraction $\eta(r)$ of particle pairs at distance r that are not connected through a liquid bridge decays quickly, and in a way that is not dependent on the overall packing fraction ϕ_G of the packing (Fig. 4.6 a). The principal effect of an increase in the liquid content is an increase in the liquid volume per liquid bridge, rather than the creation of additional bridges between more distant particles (Fig. 4.6 b and c).

Both $\langle Z \rangle$ and $\langle B \rangle$ depend on the global packing fraction Φ_g and are displayed in figure 4.4. Due to additional forces and thus mechanical constrains originating from liquid bridges,
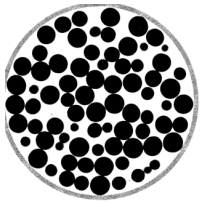
wet packings are stable at lower global packing fractions Φ_g than dry packings. Wet and dry contact numbers coincide with the results from [Sch+15b] (gray line) within experimental noise and particle sphericity. The bridge number $\langle B \rangle$ supersedes the contact number $\langle Z \rangle$ at same packing fractions by on average 37 %.

Contact numbers $\langle Z \rangle$ for wet packings scatter more than contact numbers for dry packings. However, the bridge number $\langle B \rangle$ is quite monotonously.
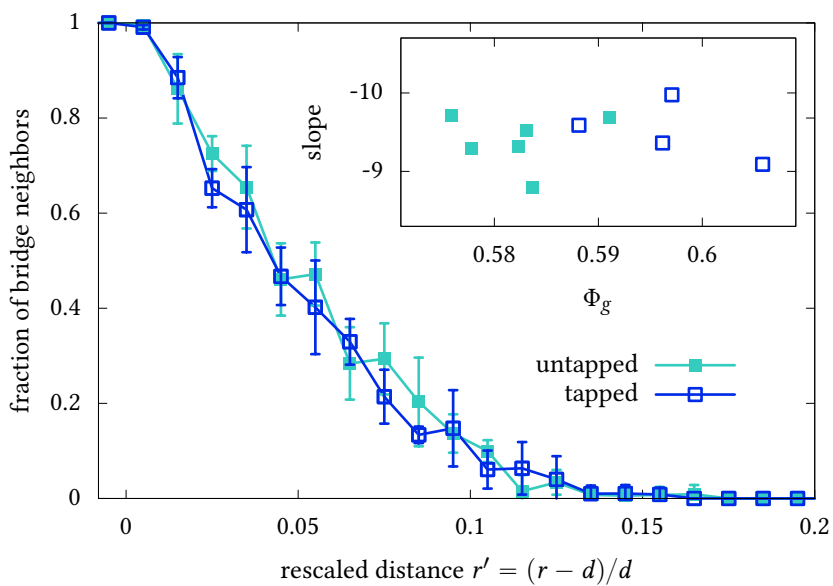

Figure 4.5.: Typical liquid bridges between particles extend up to 0.15 particle diameters regardless of preparation protocol or liquid content. Fraction of liquid bridges between particles in distance $r' = (r - d)/d$ averaged for untapped (dark blue) and tapped (light blue) preparation method. The inset shows the slope of each individual curve fitted in the range of r' between 0 and 0.1.

Another aspect on liquid bridges can be examined by sorting all particle pairs into bins with respect to their center to center distance r between the two particles. The rescaled distance $r' = (r - d)/d$ is used here, with d being the particle diameter. $r' = 0$ corresponds to two particles in contact, while larger values are normalized by the particle diameter d. The fraction η of particle pairs at a certain distance r with a liquid bridge connecting both particles is shown in figure 4.5 for different preparation methods and different liquid content 4.6. In this analysis, we find only $\leqslant 1\,\%$ of liquid clusters not to be dimers (touching only two particles).

For close rescaled distances $r' \approx 0$ the fraction of particle pairs with liquid bridges between them is 1, showing that all contacts are indeed wet contacts. The fact that all particles in contact have liquid bridges, $\eta(0) = 1$, is a strong indication of the Bromodecane being
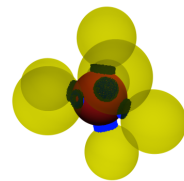
a well-dispersed solvent. We note our earlier failed attempts to use sapphire or glass particles with a solution of CsCl in water due to insufficient X-ray contrast and bad wetting properties. There is a gradual fall-off of the fraction of bridge neighbors for increasing rescaled distances r' until $r' \approx 0.15$ no more liquid bridges are found. As shown in the inset of figure 4.5 the distribution of bridges is not sensitive to the global packing fraction Φ_g, as the slope of the individual curves are independent of Φ_g. This allows to average over packing fractions, as done in figure 4.5. No significant difference between different preparations (tapped and untapped) is reported.

We also probed two different wet percentages $\eta = 2.1\,\%$ and $\eta = 3.1\,\%$. As shown in figure 4.6 (a) the fraction of liquid bridges between particles does not depend significantly on the wet percentage. In this systems varying the wet percentage η does not lead to changes in the bridge length, but rather to an change in the average volume of liquid bridges $\langle L \rangle$ for the same particle pair distances, as shown in figure 4.6 (b).
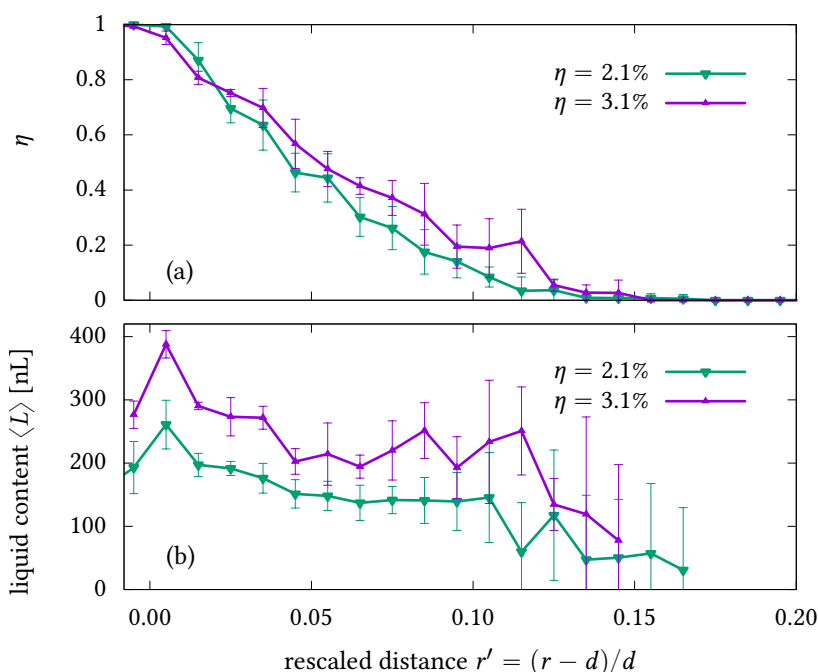
Figure 4.6.: (a): Fraction of liquid bridges averaged over all systems for wet percentage $\eta = 2.1\,\%$ (blue) and $\eta = 3.1\,\%$ (green). (b): Average volume of liquid clusters $\langle L \rangle$ between particles in distance r' for 10 mL (blue) and 15 mL (green) liquid content. If no liquid bridges are present at a distance, no value is plotted in the respective bin.

A important question regarding the structure of wet packings is whether wet packings are just dry packings with added liquid or whether liquid bridges change the structure of packings. Adding liquid to a packing creates liquid bridges between particles, which
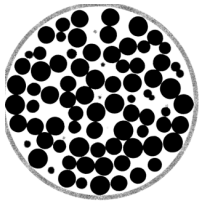
stabilize packings at lower global packing fractions Φ_g than dry packings which would not be stable at that lower Φ_g. However the question remains, whether dry and wet packings differ in structure. Therefore we calculate the Minkowski tensors of rank two of the Voronoi cells of the particles, in this case $W_0^{2,0}$ and the respective anisotropy index $\beta_0^{2,0}$, see section 2.2.

Figure 4.7 reinforces the conclusion that the structure of the wet sphere packings is very similar to the structure of a dry packing at the same packing fraction Φ_G, by the morphometric Minkowski tensor isotropy analysis [Sch+11; Sch+13c]. When applied to the Voronoi partition, these Minkowski structure metrics have become commonly used structure metrics [Sch+10b; Kap+12; Sch+15a], complementary to other metrics such as the pair correlation function $g(r)$, see section 1.4.1.
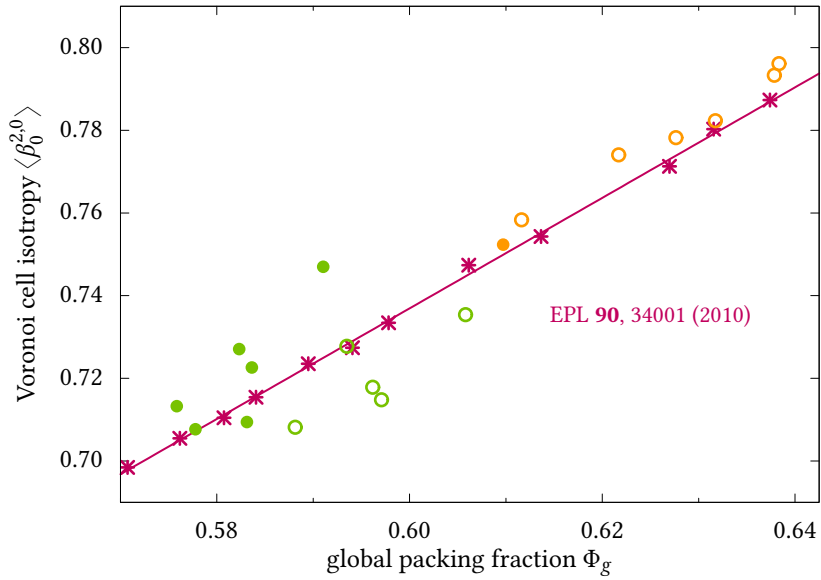
Figure 4.7.: Average Voronoi cell isotropy $\langle\beta_0^{2,0}\rangle$ for the dry (red) and wet (yellow) packings compared to published data (grey) for dry sphere packings [Sch+10b]. Open and closed symbols as in Fig. 4.4.

Figure 4.7 shows the average isotropy index over all particles $\langle\beta_0^{2,0}\rangle$, calculated for all dry and wet packings. The average packing isotropy $\langle\beta_0^{2,0}\rangle$ allows for no identification of a structural difference between dry and wet packings. Both wet and dry systems coincide with earlier independent results [Sch+10b]. For the system and length scale studied here, this supports the conclusion that, structurally, the wet packings are "just dry packings with added liquid bridges", with the presence of the liquid bridges not being accompanied by a significant change in structure of the packing.
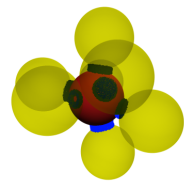
4.3.3. Conclusion and outlook

In conclusion, we have investigated to what extent the structure of a sphere packing changes when it is prepared in the presence of small quantities of a good wetting liquid. We have found that the structure of the wet packings is practically indistinguishable from that of a dry packing at the same packing fraction. This is a surprising result considering that the presence of the wetting liquid has a clear influence on the mechanical properties. These conclusions depend almost certainly on the sphere radius as the intrinsic length scale of the system, as surface tension forces increase when r decreases. Our findings are for beads of diameter around 3mm where the liquid bridges are relevant for the mechanical properties, despite not affecting the structure of the bead pack.

Future research should explore the limit of smaller particles, maybe of size comparable to those of sand grains. In all likelihood, the presence of the wetting liquid then stabilizes packings at substantially lower packing fractions (than what can be reached in dry powders) and will also lead to substantial dependencies on the details of the preparation method. It is well known that the ratio between the cohesive forces and gravitational forces gets larger for smaller particle sizes. Therefore, wet packings with even lower global packing fractions Φ_g are mechanically stable for smaller particle sizes. Preliminary experiments with glass beads with a diameter of $d = 350 \, \mu m$ have shown interesting results. However due to contaminated particle surfaces no liquid with sufficient X-ray contrast was found to be wetting.

Furthermore the morphology of liquid clusters with respect to the liquid content should be investigated. Previous studies [SGH04; Sch+08] only investigated morphology for a fixed liquid volume. It is not known yet, how the cluster morphology changes with liquid content η. Another interesting question is how the bridge number $\langle B \rangle$ changes for large liquid contents $\eta \geqslant 10 \, \%$, which have not been investigated in our study and whether that has effects on the contact number $\langle Z \rangle$ and the isotropy of the packing $\beta_0^{2,0}$.

130
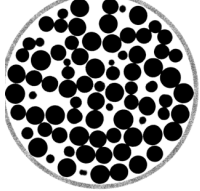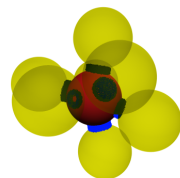
A. Appendix

A.1. Cluster labelling using the Hoshen-Kopelman algorithm

The *Hoshen-Kopelman* algorithm (short HK) [HK76; WS17] is a union-finding algorithm and can be used to identify clusters of voxels in a tomogram. The HK algorithm can be used in any dimensions and can be applied to label either black or white clusters. The following description is strongly oriented at figure A.1 and assumes a two-dimensional image, in which white clusters should be labeled.

The algorithm iterates through all pixels of the input tomogram (depicted in figure A.1 (a)) starting at the top left, coordinates (0,0), and incrementing x, y in that order. Thus it proceeds through the image starting at the top left corner and going left to right, line by line. If the pixel under consideration is a black pixel (which means the pixel has a value of 0 assigned), the output (label) image is assigned a value of 0 at this position and the algorithm proceeds to the next pixel, as only white pixels should be labeled. As nothing of interest happens in this case, this is not depicted in figure A.1.

If however, a white pixel is encountered (figure A.1 (b), the blue pixel is the pixel under investigation in this step), it is assigned a cluster id based on the values of the adjacent pixels which have already been visited (x-1,y), (x, y-1). In three dimensions, neighborhood in three dimensions (top, left and back) has to be checked. Adjacent pixels can be defined as the pixels directly to the left or to the top (x-1,y), (x, y-1) or the previously used pixels and additionally the diagonal voxels[40] (x-1, y-1) and (x+1, y-1).

If all of those previously visited pixels are black pixels, a new cluster id is assigned to this position in the output image. This is shown in figure A.1 (c), (e) and (h). The adjacent pixels (shown as green highlights) contain only black pixels. Thus a new label is assigned, indicated by the number in the respective pixel.

If one of the neighboring pixels is a white one, the cluster label of this pixel is used (figure A.1 (d), (f) and (g)). The same happens if the two adjacent and previously visited voxels

---

[40]Given a sufficient resolution and quality of the binarization, as well a a well-behaved cluster to be labeled, the results should not vary significantly when using different neighboring definitions.
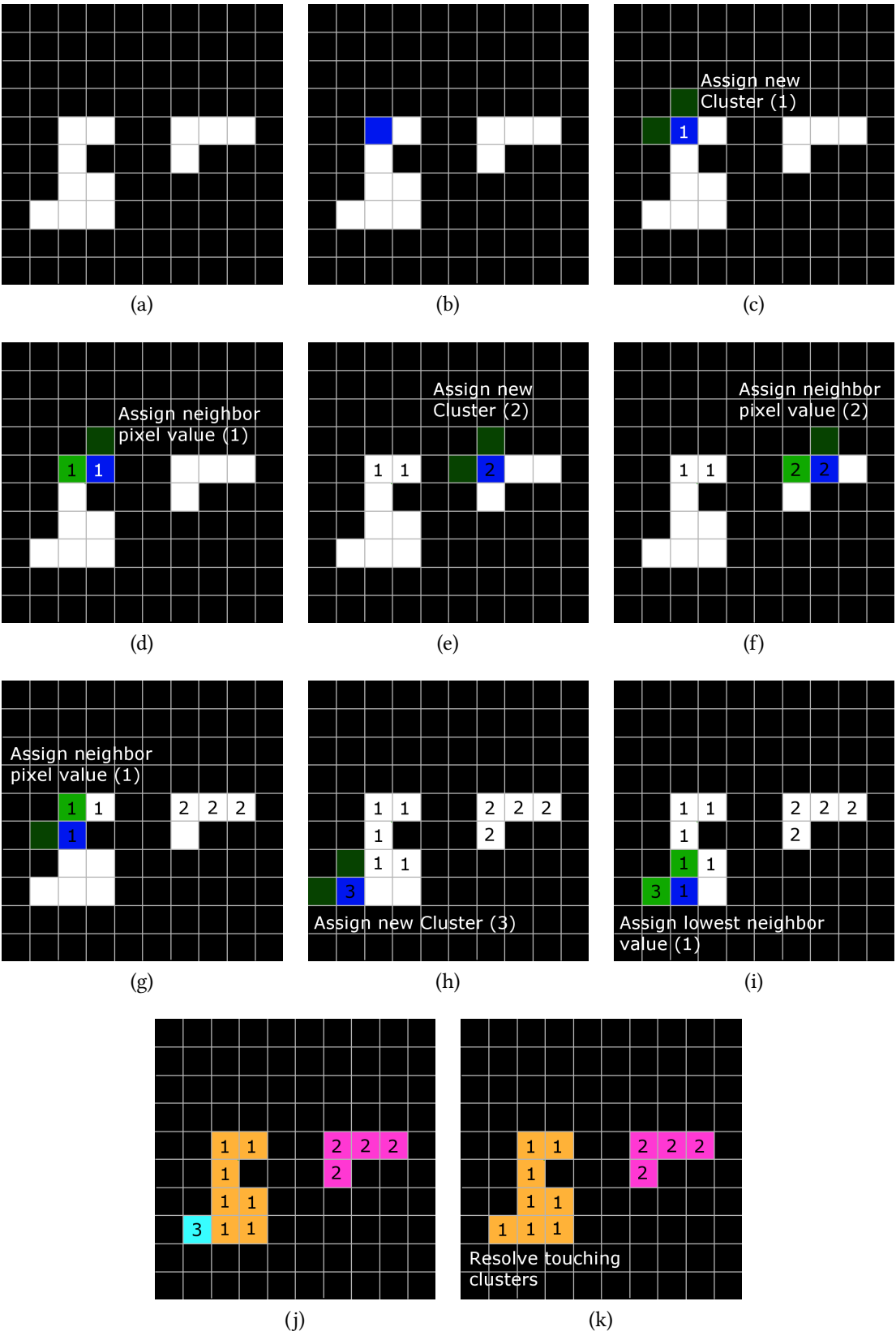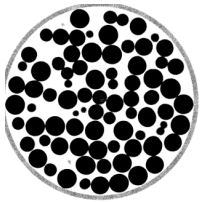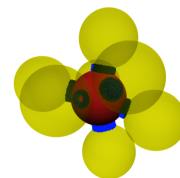
Figure A.1.: Explaining the Hoshen-Kopelman Algorithm using images.

have the same label (not depicted in figure A.1). As only adjacent pixels are checked which have been previously visited, there is always a label available.

If the labels of the two adjacent, previously visited white pixels differ, the lowest cluster id is used and a note is taken in a *connected clusters*- map that the clusters are connected. This is shown in figure A.1 (i)

In a second step, after iterating through all pixels (shown in figure A.1 (j), colors now depend on the assigned labels), the connected clusters are merged using the previously collected information. The final result is shown in figure A.1 (k) where touching clusters have been resolved using the *connected clusters*- map.

A.2. New ways of visualizing granular materials

It is always worth the effort to think about new ways of visualizing scientific data in a smart way [Tuf01]. The topics of this work provide very interesting data for visualization. In recent years, the occurrence of so-called *Virtual Reality* devices, like the Occulus Rift or HTC Vive opened a new way of looking at scientific data. This becomes even more interesting, as even standard consumer smartphones can be used for virtual reality experiences, e.g. using Samsung VR or a Google cardboard.

A.2.1. Visualization in virtual reality

Figure A.2.: Our booth at the "long night of sciences" in October 2017.

133
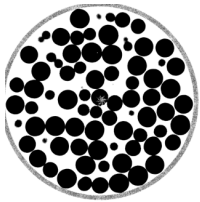
For the "long night of sciences" in October 2017 a presentation of granular materials in virtual reality was prepared in a vivid collaboration with the Startup Cykyria [cyk18]. Using the HTC Vive System, visitors were able to walk inside an experimental sphere packing and their Voronoi cells and pick individual spheres for a detailed analysis, see figure A.2.

The program was implemented by Cykyria using the Unreal engine, which parses the input data is read in the `json` format. For this reason the program `poly2json`, see [pol18], was developed. `poly2json` converts the output of `Pomelo` and `karambola` to a `json` file, which can then be parsed by the Unreal engine. Each object in the json file (currently supported objects are spheres as particles and cylinders for the Voronoi wireframe) can be assigned multiple properties, like object id, particle id, or for the particles/cells also physical properties like local packing fraction, contacts or anisotropy values, see section 2.2.

The particles can then be colored with respect to physical properties chosen by the user, e.g. the local packing fraction Φ_l, contact number Z or the Set-Voronoi cell anisotropy $\beta_0^{2,0}$. Furthermore it is possible to select individual particles and choose different visualization options. It is possible to view all particles, only the selected particle or the selected particles and its direct neighbors. Another feature is to toggle the display for the Set-Voronoi cells.

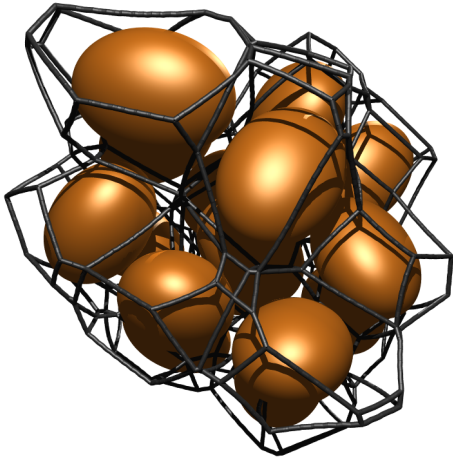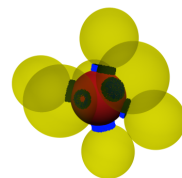### A.2.2. Visualization using PovRay

Figure A.3.: Rendering of one ellipsoidal particle and its neighbors as well as their Set-Voronoi cells as a wireframe using PovRay.

The program described above requires a high end machine and a virtual reality device for rendering. The `PolyRender` tools provided in this section allow to create a images

or videos of any Voronoi or Set-Voronoi tessellation of particles by using the programs provided at [pol18]. A short overview of the rendering process will be given here, while a detailed description as well as instructions on how to run the programs can be found at the reference. The produced pov files can be rendered using the open source tool `PovRay` [pov18]. By creating multiple renderings at different rotation angles[41], a video can be easily composed. As close to no information could be found about stereoscopic rendering, a section about this topic was included.

Rendering (Set-)Voronoi cells

At first, a selection of the particles to be rendered should be performed. Selecting a cluster of particles in the center of the packing is a good starting point. A number of about 50 particles is a good start for a nice image. But rendering is not limited to that number and can be performed for any number of particles. The program (`set-`)`poly2pov` is then used to translate the input files (particle positions, Set-Voronoi tessellation and Minkowski tensors) to a pov file, which can be used with the program `PovRay` [pov18] to create an image.

Normal Voronoi cells are easy to render as each of the facets is flat. To get the rendering of the wireframe of a Voronoi cell, like in image 2.1 (a), it is sufficient to loop over all edges of a Voronoi cell and render a cylinder for each edge.

For Set-Voronoi cells an extra step has to be performed prior to rendering: the Set-Voronoi boundary between two cells can be curved. The Set-Voronoi calculation from chapter 2 approximates this curved surface with a number of flat faces. Rendering all of the edges of all of the faces would just give a very untidy image, especially if the cells edges (the wireframe of the Set-Voronoi tessellation) is rendered. One option to reduce the number of edges to render is to have a look at the number of cells each vertex of the Set-Voronoi diagram is adjacent to. This is displayed in figure A.4.

---

[41]Note that `povray` uses a left handed coordinate system. If you are using the program and notice strangely rotated objects (like the author did), do not hesitate and use the other hand.
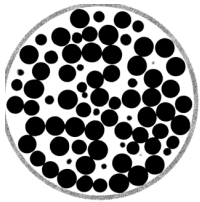
If a vertex exists …

- in two cells, it is a vertex on a facet of a cell.

- in three cells, the vertex is on the edge of a cell.

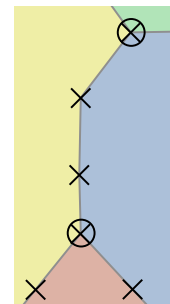- in four or more cells, the vertex is on the corner of a cell.

Figure A.4.

2d example for the description on the left. The symbols $\otimes$ and $\times$ mark vertices of Set-Voronoi cells. The vertices with at least three adjacent cells ($\otimes$ symbol) are the ones to render for the Set-Voronoi wireframe.

Thus the number of cells can be used to dismiss all vertices which exist only in two cells. This will sort out all of the vertices which are on the facets, but not on the edges or corners. After that, all remaining edges can be rendered as the wireframe. The resulting rendering can be seen in figure A.3.

Stereoscopic rendering

For stereoscopic rendering two images are required, one for each eye. They are created by ofsetting the camera position's away from the central axis, while keeping the camera pointed at a focus point. Three parameters have to be chosen[42], which are sketched in figure A.5.

Based on the size of the particles (diameter 60 voxels) and the size of the cluster (50 particles) to render, the following parameters should be chosen:

Interocular distance (red arrow) The first one is the interocular distance (the distance between the two eyes/camera positions, also called offset). This should be set in relation to the characteristic length scale of the sample. For the example system a working interocular distance was found at 10 voxels.

View distance (blue arrow) The viewer's position is the center between the two camera positions. The main parameter is how far away the viewer is from the sample. This will also determine if the complete cluster can be rendered in the image. For the

---

[42]A bad choice of parameters will cause no or a strange stereoscopic effect or even nausea or motion sickness.
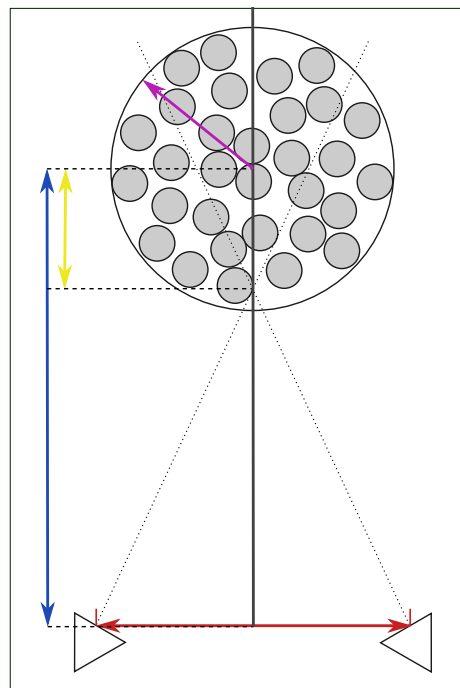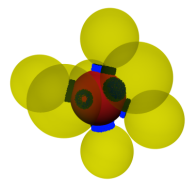
Figure A.5.: Two-dimensional sketch of the stereoscopic rendering parameters. Each of the two cameras renders an image of the object at the top. Based on the radius of the sample (pink arrow), three parameters have to be chosen: the interocular distance (red arrow), the view distance (blue arrow) and the focus position (yellow arrow).

example system the distance from the viewer to the center of the particle cluster was chosen to be 2.1 times the radius of the complete the cluster.

Focus position (yellow arrow) The focus point is the point at which both cameras look at. Shifting the focus spot towards the cameras or away from them can change the perception and feel of depth of the stereoscopic image. A good starting point is to set the focus spot to the center of the cluster. As a rule of thumb, stereoscopic images are easier to visualize if the main part of the object is behind the focus spot. Depending on the required feel of depth of the image, the focus spot can even be shifted towards the camera[43].

---

[43]Shifting the focus spot to the left or right is likely to cause nausea for the viewer as this will change the distances from each camera. If the focus spot is, regardless of the direction of the shift, outside of the cluster a very unpleasant squinting effect can occur.
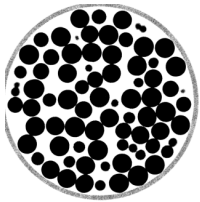
Creation history

Figure A.6.: Development of keywords documenting the progress of this thesis. This plot was created using the power of `git`, `bash` scripting and `gnuplot`.

Acknowledgments

Furthermore, I want to thank the complete group of Theo 1 for providing a pleasant working environment and helpful (and nerdy) discussions in the coffee room. The group at the chair for 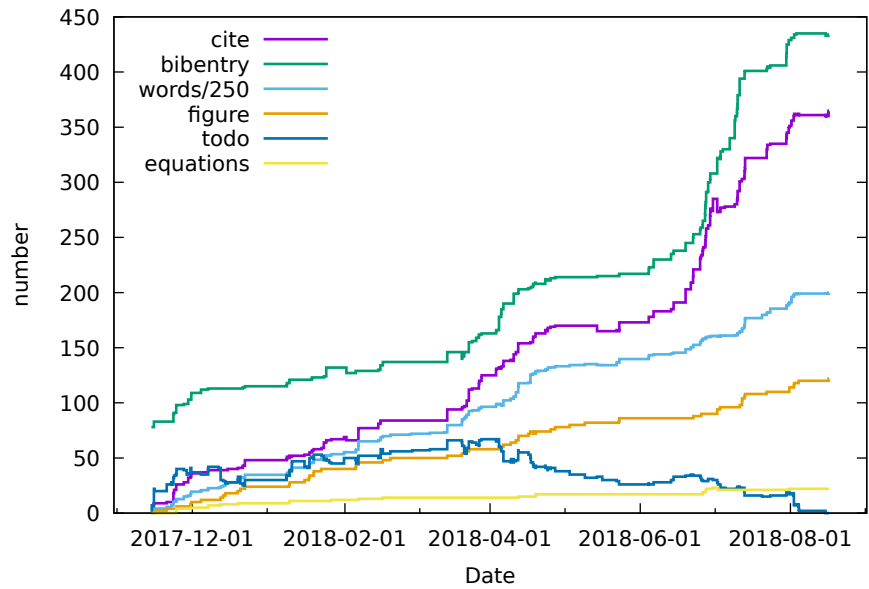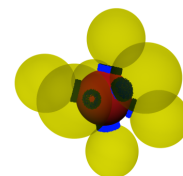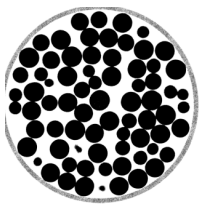Multi-Scale-Simulations had a higher fluctuation of people, who nevertheless shaped various aspects of this thesis and the last three years. Thanks to Doris Zoller, Nora Elhaus, Jan Nicklas and Clemens Hall for using some of my programs or data and thus for providing a use case and valuable feedback. Special thanks to Manuel Baur for sharing a great time in Montpellier and for constant and vivid discussions on scientific topics as well as great music suggestions! Thanks also to Michael Heckel who took care of maintenance for the X-ray machine and Margret Heinen-Krumreich as well as Ingrid Hofmann for keeping bureaucracy at a comfortable minimum. Kudos to Wolf Keiderling at the Max-Planck institute for dynamics and self-organization for building everlasting tools in his workshop and to the Theo 1 admins for keeping the computer infrastructure running at all times.

I also want to thank all the co-authors of joint research articles: Thanks to Philipp Schönhöfer, Fabian Schaller, Andre Schella, Anais Giustiani, Christophe Poulard, Paul Kamm, Francisco Garcia-Moreno, Wiebke Drenckhan and of course Matthias Schröter and Gerd Schröder-Turk.

Writing a thesis is no easy task, but a large group of proof readers supported me. Thanks to: Sebastian, Doris, Manuel, Philipp, Johannes, Gerd, Matthias, Julian, Callum, Dimi and Tanja!

A special word of thanks goes to Benedikt Engelhard and Doris Conrad from Cykyria who ventured with me into the topic of putting granular materials into virtual reality.

Thanks to all the wonderful people who could not be listed here but contributed in one or another way to this work!

Last but not least, I want to thank my family and friends for the support throughout my entire time at university. Thank you Werner for constant interest and support! Thank you Ingrid for a lot of wholeheartedly warm words! Thank you Tanja for continuously asking the important questions! Thanks to the *Nerd Stammtisch* for providing a platform for critical discussions and funny videos, not only but mostly about cats! [44]

---

[44]Special thanks to Johannes for pointing out that the amount of footnotes in this document is "too damn low!"
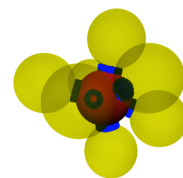
Bibliography

[AA06]   K. Alshibli and B. Alramahi. "Microscopic Evaluation of Strain Distribution in Granular Materials during Shear". In: *Journal of Geotechnical and Geoenvironmental Engineering* 132.1 (Jan. 2006), pp. 80–91. ISSN: 1943-5606. URL: http://dx.doi.org/10.1061/(ASCE)1090-0241(2006)132:1(80).

[AB99]   N. Amenta and M. Bern. "Surface Reconstruction by Voronoi Filtering". In: *Discrete and Computational Geometry* 22.4 (Dec. 1999), pp. 481–504. ISSN: 0179-5376. URL: http://dx.doi.org/10.1007/PL00009475.

[ACK01]   Nina Amenta, Sunghee Choi, and Ravi Krishna Kolluri. "The power crust, unions of balls, and the medial axis transform". In: *Computational Geometry* 19.2-3 (July 2001), pp. 127–153. ISSN: 0925-7721. DOI: 10.1016/s0925-7721(01)00017-7.

[ACR03]   Nina Amenta, Sunghee Choi, and Günter Rote. "Incremental constructions con BRIO". In: *Proceedings of the nineteenth conference on Computational geometry - SCG '03* (2003). DOI: 10.1145/777792.777824.

[AFP13]   B. Andreotti, Y. Forterre, and O. Pouliquen. *Granular Media: Between Fluid and Solid.* Cambridge University Press, 2013. ISBN: 1107034795.

[AKM10]   C.H. ARNS, M.A. KNACKSTEDT, and K. MECKE. "3D structural analysis: sensitivity of Minkowski functionals". In: *Journal of Microscopy* 240.3 (Nov. 2010), pp. 181–196. ISSN: 0022-2720. DOI: 10.1111/j.1365-2818.2010.03395.x.

[AlA+05]   F. A. H. Al-Abduwani, R. Farajzadeh, W. M. G. T. van den Broek, P. K. Currie, and P. L. J. Zitha. "Filtration of micron-sized particles in granular media revealed by x-ray computed tomography". In: *Review of Scientific Instruments* 76.10 (Oct. 2005), p. 103704. ISSN: 1089-7623. DOI: 10.1063/1.2103467.

[Alb+97]   R. Albert, I. Albert, D. Hornbaker, P. Schiffer, and A. Barabasi. "Maximum angle of stability in wet and dry spherical granular media". In: *Physical Review E* 56.6 (Dec. 1997), R6271–R6274. ISSN: 1095-3787. DOI: 10.1103/physreve.56.r6271.

[Ale99]   S. Alesker. In: *Geometriae Dedicata* 74.3 (1999), pp. 241–248. ISSN: 0046-5755. DOI: 10.1023/a:1005035232264.
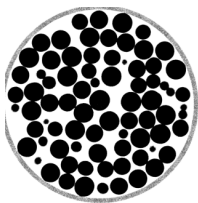
[AM05]   J. Anthony and C. Marone. "Influence of particle characteristics on granular friction". In: *Journal of Geophysical Research* 110.B8 (2005). ISSN: 0148-0227. DOI: 10.1029/2004jb003399.

[Amo+17]   Axelle Amon, Philip Born, Karen E. Daniels, Joshua A. Dijksman, Kai Huang, David Parker, Matthias Schröter, Ralf Stannarius, and Andreas Wierschem. "Preface: Focus on imaging methods in granular physics". In: *Review of Scientific Instruments* 88.5 (May 2017), p. 051701. ISSN: 1089-7623. DOI: 10.1063/1.4983052.

[And+11]   Edward Andò, Stephen A. Hall, Gioacchino Viggiani, Jacques Desrues, and Pierre Bésuelle. "Grain-scale experimental investigation of localised deformation in sand: a discrete particle tracking approach". In: *Acta Geotechnica* 7.1 (Nov. 2011), pp. 1–13. ISSN: 1861-1133. DOI: 10.1007/s11440-011-0151-6.

[Ard+14]   S. Ardanza-Trevijano, Iker Zuriguel, Roberto Arévalo, and Diego Maza. "Topological analysis of tapped granular media using persistent homology". In: *Physical Review E* 89.5 (May 2014). ISSN: 1550-2376. DOI: 10.1103/physreve.89.052212.

[Arn+01]   C. H. Arns, Mark A. Knackstedt, W. V. Pinczewski, and K. R. Mecke. "Euler-Poincaré characteristics of classes of disordered media". In: *Physical Review E* 63.3 (Feb. 2001). ISSN: 1095-3787. DOI: 10.1103/physreve.63.031112.

[ASS05]   T. Aste, M. Saadatfar, and T. Senden. "Geometrical structure of disordered sphere packings". In: *Physical Review E* 71.6 (June 2005). ISSN: 1550-2376. DOI: 10.1103/physreve.71.061302.

[ASS06]   T Aste, M Saadatfar, and T J Senden. "Local and global relations between the number of contacts and density in monodisperse sphere packs". In: *Journal of Statistical Mechanics: Theory and Experiment* 2006.07 (July 2006), P07010–P07010. ISSN: 1742-5468. DOI: 10.1088/1742-5468/2006/07/p07010.

[Ast+07]   T Aste, T. Di Matteo, M Saadatfar, T. J Senden, Matthias Schröter, and H. Swinney. "An invariant distribution in static granular media". In: *Europhysics Letters (EPL)* 79.2 (July 2007), p. 24003. ISSN: 1286-4854. DOI: 10.1209/0295-5075/79/24003. URL: %5Curl%7Bhttp://dx.doi.org/10.1209/0295-5075/79/24003%7D.

[Ast05]   T Aste. "Variations around disordered close packing". In: *Journal of Physics: Condensed Matter* 17.24 (June 2005), S2361–S2390. ISSN: 1361-648X. DOI: 10.1088/0953-8984/17/24/001.

[Ast06]   Tomaso Aste. "Volume Fluctuations and Geometrical Constraints in Granular Packs". In: *Physical Review Letters* 96.1 (Jan. 2006). ISSN: 1079-7114. URL: http://dx.doi.org/10.1103/PhysRevLett.96.018002.

[ast18]   website astra. *http://www.astra-toolbox.com/*. 2018.
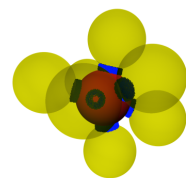
[AT06]   Igor S. Aranson and Lev S. Tsimring. "Patterns and collective behavior in granular media: Theoretical concepts". In: *Reviews of Modern Physics* 78.2 (June 2006), pp. 641–692. ISSN: 1539-0756. DOI: 10.1103/revmodphys.78.641.

[B02]   Jähne B. *Digitale Bildverarbeitung (German Edition)*. Springer, 2002. ISBN: 3540412603.

[Bag53]   R Bagnold. "The Physics of Blown Sand and Desert Dunes". In: *Methuen, London* (1953).

[Bar+16] Vasili Baranau, Song-Chuan Zhao, Mario Scheel, Ulrich Tallarek, and Matthias Schröter. "Upper bound on the Edwards entropy in frictional monodisperse hard-sphere packings". In: *Soft Matter* 12.17 (2016), pp. 3991–4006. ISSN: 1744-6848. URL: http://dx.doi.org/10.1039/c6sm00567e.

[Bar+17] S.M. Barhli, L. Saucedo-Mora, M.S.L. Jordan, A.F. Cinar, C. Reinhard, M. Mostafavi, and T.J. Marrow. "Synchrotron X-ray characterization of crack strain fields in polygranular graphite". In: *Carbon* 124 (Nov. 2017), pp. 357–371. ISSN: 0008-6223. DOI: 10.1016/j.carbon.2017.08.075.

[Bau+13] A. Baule, R. 3i, L. Bo, L. Portal, and H. Makse. "Mean-field theory of random close packings of axisymmetric particles". In: *Nature Communications* 4 (July 2013). ISSN: 2041-1723. DOI: 10.1038/ncomms3194.

[Bau+18] Adrian Baule, Flaviano Morone, Hans J. Herrmann, and Hernán A. Makse. "Edwards statistical mechanics for jammed granular matter". In: *Reviews of Modern Physics* 90.1 (Mar. 2018). ISSN: 1539-0756. DOI: 10.1103/revmodphys.90.015006.

[BC00]   J. Boissonnat and F. Cazals. "Natural Neighbour Coordinates of Points on a Surface". In: *HAL archives FR* (2000).

[BDB15]   Nicolas Brodu, Joshua A. Dijksman, and Robert P. Behringer. "Spanning the scales of granular materials through microscopic force imaging". In: *Nature Communications* 6 (2015), p. 6361. DOI: 10.1038/ncomms7361.

[Ber+13] S. Berg, H. Ott, S. A. Klapp, A. Schwing, R. Neiteler, N. Brussee, A. Makurat, L. Leu, F. Enzmann, J.-O. Schwarz, and et al. "Real-time 3D imaging of Haines jumps in porous media flow". In: *Proceedings of the National Academy of Sciences* 110.10 (Feb. 2013), pp. 3755–3759. ISSN: 1091-6490. DOI: 10.1073/pnas.1221373110.

[Ber64]   J. Bernal. "The Bakerian Lecture, 1962. The Structure of Liquids". In: *Proceedings of the Royal Society of London. Series A, Mathematical and Physical Sciences* 280.1382 (1964), pp. 299–322. ISSN: 00804630. URL: http://www.jstor.org/stable/2415872.

[Ber97]   Gino van den Bergen. "Efficient collision detection of complex deformable models using AABB trees". In: *Journal of graphics tools* 2.4 (1997), pp. 1–13.
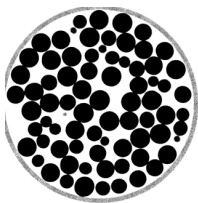
[BF67]   J. Bernal and J. Finney. "Random close-packed hard-sphere model. II. Geometry of random packing of hard spheres". In: *Discussions of the Faraday Society* 43 (1967), p. 62. ISSN: 0366-9033. DOI: 10.1039/df9674300062.

[BFZ15]   C. Bandt, K. Falconer, and M. Zähle. *Fractal Geometry and Stochastics V.* springer, 2015.

[Bi+15]   Dapeng Bi, Silke Henkes, Karen E. Daniels, and Bulbul Chakraborty. "The Statistical Physics of Athermal Materials". In: *Annual Review of Condensed Matter Physics* 6.1 (Mar. 2015), pp. 63–83. ISSN: 1947-5462. DOI: 10.1146/annurev-conmatphys-031214-014336.

[Bia+09] Indaco Biazzo, Francesco Caltagirone, Giorgio Parisi, and Francesco Zamponi. "Theory of Amorphous Packings of Binary Mixtures of Hard Spheres". In: *Physical Review Letters* 102.19 (May 2009). ISSN: 1079-7114. DOI: 10.1103/physrevlett.102.195701.

[Bit04]   F. Bittner. "The universal Euler characteristic for varieties of characteristic zero". In: *Compositio Mathematica* 140.4 (2004), pp. 1011–1032.

[BKD18]   Ephraim Bililign, Jonathan E. Kollmer, and Karen Daniels. "Protocol-Dependence and State Variables in the Force-Moment Ensemble". In: *arxiv preprint server* (2018). URL: https://arxiv.org/abs/1802.09641.

[BM60]   J. Bernal and J. Mason. "Packing of Spheres: Co-ordination of Randomly Packed Spheres". In: *Nature* 188.4754 (Dec. 1960), pp. 910–911. ISSN: 0028-0836. DOI: 10.1038/188910a0.

[Boc+98] L. Bocquet, E. Charlaix, S. Ciliberto, and J. Crassous. "Moisture-induced ageing in granular media and the kinetics of capillary condensation". In: *Nature* 396.6713 (Dec. 1998), pp. 735–737. ISSN: 1476-4687. DOI: 10.1038/25492.

[Bör+12] Tamas Börzsönyi, Balazs Szabo, Sandra Wegner, Kirsten Harth, Janos Török, Ellak Somfai, Tomasz Bien, and Ralf Stannarius. "Shear-induced alignment and dynamics of elongated granular particles". In: *Physical Review E* 86.5 (Nov. 2012). ISSN: 1550-2376. DOI: 10.1103/physreve.86.051304.

[Bör+17] Tamas Börzsönyi, Ellak Somfai, Balazs Szabo, Sandra Wegner, Ahmed Ashour, and Ralf Stannarius. "Elongated grains in a hopper". In: *EPJ Web of Conferences* 140 (2017). Ed. by F. Radjai, S. Nezamabadi, S. Luding, and J.Y.Editors Delenne, p. 06017. ISSN: 2100-014X. DOI: 10.1051/epjconf/201714006017.

[BS13]   Tamas Borzsonyi and Ralf Stannarius. "Granular materials composed of shape-anisotropic grains". In: *Soft Matter* 9.31 (2013), pp. 7401–7418.

[BSM12]   I. Bronstein, K. Semendjajew, and G. Musiol. *Taschenbuch der Mathematik.* Harri, 2012.

[Bus15]   Uwe Busch. "Strahlenexposition bei Schuhdurchleuchtungsapparaten". In: *Zeitschrift für Medizinische Physik* 25.1 (Mar. 2015), pp. 13–18. ISSN: 0939-3889. DOI: 10.1016/j.zemedi.2014.06.007.
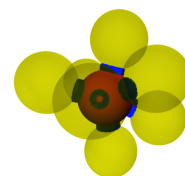
[Buz10]   Thorsten M. Buzug. *Computed Tomography: From Photon Statistics to Modern Cone-Beam CT*. Springer, 2010. ISBN: 3642072577.

[Cao+13]   Y. X. Cao, B. Chakrabortty, G. C. Barker, A. Mehta, and Y. J. Wang. "Bridges in three-dimensional granular packings: Experiments and simulations". In: *EPL (Europhysics Letters)* 102.2 (Apr. 2013), p. 24004. ISSN: 1286-4854. DOI: 10.1209/0295-5075/102/24004.

[Car70]   Maurice a. Carrigy. "experiments on the angles of repose of granular materials". In: *Sedimentology* 14.3-4 (Jan. 1970), pp. 147–158. ISSN: 1365-3091. DOI: 10.1111/j.1365-3091.1970.tb00189.x.

[Cha17]   D. Chamovitz. *What a plant knows: A Field Guide to the senses*. Carl Hanser Verlag GmbH, 2017.

[Che+16]   Sheng Chen, Shuiqing Li, Wenwei Liu, and Hernán A. Makse. "Effect of long-range repulsive Coulomb interactions on packing structure of adhesive particles". In: *Soft Matter* 12.6 (2016), pp. 1836–1846. ISSN: 1744-6848. DOI: 10.1039/c5sm02403j.

[Cia+06]   Massimo Pica Ciamarra, Maria Domenica De Vizia, Annalisa Fierro, Marco Tarzia, Antonio Coniglio, and Mario Nicodemi. "Granular Species Segregation under Vertical Tapping: Effects of Size, Density, Friction, and Shaking Amplitude". In: *Physical Review Letters* 96.5 (Feb. 2006). ISSN: 1079-7114. DOI: 10.1103/physrevlett.96.058001.

[Cia+11]   Massimo Pica Ciamarra, Raffaele Pastore, 3io Nicodemi, and Antonio Coniglio. "Jamming phase diagram for frictional particles". In: *Phys. Rev. E* 84.4 (Oct. 2011). ISSN: 1550-2376. DOI: 10.1103/physreve.84.041308.

[CJ93]   Andrew S. Clarke and Hannes Jónsson. "Structural changes accompanying densification of random hard-sphere packings". In: *Physical Review E* 47.6 (June 1993), pp. 3975–3984. ISSN: 1095-3787. DOI: 10.1103/physreve.47.3975.

[Clu+09]   Maxime Clusel, Eric I. Corwin, Alexander O. N. Siemens, and Jasna Brujić. "A "granocentric" model for random packing of jammed emulsions". In: *Nature* 460.7255 (July 2009), pp. 611–615. ISSN: 1476-4687. DOI: 10.1038/nature08158.

[Com16a]   Wikimedia Commons. *File:First medical X-ray by Wilhelm Röntgen of his wife Anna Bertha Ludwig's hand - 18951222.gif — Wikimedia Commons, the free media repository*. [Online; accessed 16-August-2018]. 2016. URL: %5Curl%7Bhttps://commons.wikimedia.org/w/index.php?title=File:First_medical_X-ray_by_Wilhelm_R%C3%B6ntgen_of_his_wife_Anna_Bertha_Ludwig%27s_hand_-_18951222.gif&oldid=227710495%7D.

[Com16b]   Wikimedia Commons. *File:Lucretius1.png — Wikimedia Commons, the free media repository*. [Online; accessed 16-August-2018]. 2016. URL: https://commons.wikimedia.org/w/index.php?title=File:Lucretius1.png&oldid=218979123.
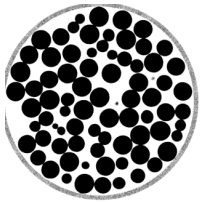
[Com17]   Wikimedia Commons. *File:Flock of Sheep (Jamie Wardley) (22646620750).jpg —
Wikimedia Commons, the free media repository*. [Online; accessed 16-August-
2018]. 2017. URL: https://commons.wikimedia.org/w/index.php?title=
File:Flock_of_Sheep_(Jamie_Wardley)_(22646620750).jpg&oldid=
257393642.

[Com18a]   Wikimedia Commons. *File:Charles de coulomb.jpg — Wikimedia Commons, the
free media repository*. [Online; accessed 16-August-2018]. 2018. URL: https:
//commons.wikimedia.org/w/index.php?title=File:Charles_de_coulomb.
jpg&oldid=312535495.

[Com18b]   Wikimedia Commons. *Leonardo da Vinci — Wikimedia Commons, the free
media repository*. [Online; accessed 16-August-2018]. 2018. URL: https://
commons.wikimedia.org/w/index.php?title=Leonardo_da_Vinci&oldid=
314511627.

[con18]   website conrad. *https://github.com/PhysikerErlangen/CONRAD*. 2018.

[Cor+10]   Eric I. Corwin, Maxime Clusel, Alexander O. N. Siemens, and Jasna Brujić.
"Model for random packing of polydisperse frictionless spheres". In: *Soft Matter*
6.13 (2010), p. 2949. ISSN: 1744-6848. DOI: 10.1039/c000984a.

[Cou73]   CA Coulomb. "Essay on the rules of maximis and minimis applied to some
problems of equilibrium related to architecture". In: *Academy of Royal Science
Memorial Physics* 7 (1773), pp. 343–382.

[Cow85]   Stephen C Cowin. "The relationship between the elasticity tensor and the
fabric tensor". In: *Mechanics of Materials* 4.2 (1985), pp. 137–147.

[CS79]   P. A. Cundall and O.D.L. Strack. In: *Geotechnique* 29.47 (1979). URL: %5Curl%
7Bhttp://websrv.cs.umt.edu/classes/cs477/images/0/0e/Cundall_
Strack.pdf%7D.

[CS99]   J. Conway and N. Sloane. *Sphere Packings, Lattices And Groups*. Springer, 1999.
ISBN: 978-1-4757-6568-7.

[CT15]   D. Chen and S. Torquato. "Confined disordered strictly jammed binary sphere
packings". In: *Physical Review E* 92.6 (Dec. 2015). ISSN: 1550-2376. DOI: 10.
1103/physreve.92.062207.

[CW87]   A. S. Clarke and J. D. Wiley. "Numerical simulation of the dense random
packing of a binary mixture of hard spheres: Amorphous metals". In: *Physical
Review B* 35.14 (May 1987), pp. 7350–7356. ISSN: 0163-1829. DOI: 10.1103/
physrevb.35.7350.

[cyk18]   website cykyria. *https://www.cykyria.de/*. 2018.

[Dan80]   Per-Erik Danielsson. "Euclidean distance mapping". In: *Computer Graphics
and Image Processing* 14.3 (Nov. 1980), pp. 227–248. ISSN: 0146-664X. URL:
http://dx.doi.org/10.1016/0146-664X(80)90054-4.

146
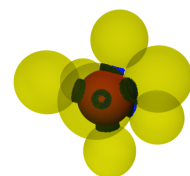
[Das91]   Pankaj K. Das. *Optical Signal Processing: Fundamentals.* Springer, 1991. ISBN: 3540514767.

[DC10]   G. Delaney and P. Cleary. "The packing properties of superellipsoids". In: *EPL (Europhysics Letters)* 89.3 (Feb. 2010), p. 34002. ISSN: 1286-4854. DOI: 10.1209/0295-5075/89/34002.

[DC96]   René Descartes and Ernst Cassirer. *Philosophische Schriften: in einem Band. Und" Descartes' Wahrheitsbegriff".* Meiner, 1996.

[DDA10]   G. Delaney, T. Di Matteo, and T. Aste. "Combining tomographic imaging and DEM simulations to investigate the structure of experimental sphere packings". In: *Soft Matter* 6.13 (2010), p. 2992. ISSN: 1744-6848. DOI: 10.1039/b927490a.

[des]   website descartes. *https://www.iep.utm.edu/descarte/*.

[DH15]   Wiebke Drenckhan and Stefan Hutzler. "Structure and energy of liquid foams". In: *Advances in Colloid and Interface Science* 224 (Oct. 2015), pp. 1–16. ISSN: 0001-8686. DOI: 10.1016/j.cis.2015.05.004.

[DKP17]   Karen E. Daniels, Jonathan E. Kollmer, and James G. Puckett. "Photoelastic force measurements in granular materials". In: *Review of Scientific Instruments* 88.5 (May 2017), p. 051808. ISSN: 1089-7623. DOI: 10.1063/1.4983049.

[Doi13]   Masao Doi. *Soft Matter Physics.* Oxford University Press, 2013. ISBN: 0199652953.

[Don+04]   A. Donev, I. Cisse, D. Sachs, E. Variano, F. Stillinger, R. Connelly, S. Torquato, and P. Chaikin. "Improving the Density of Jammed Disordered Packings Using Ellipsoids". In: *Science* 303.5660 (2004), pp. 990–993. DOI: 10.1126/science.1093010. URL: http://www.sciencemag.org/content/303/5660/990.abstract.

[Don+06]   K. J. Dong, R. Y. Yang, R. P. Zou, and A. B. Yu. "Role of Interparticle Forces in the Formation of Random Loose Packing". In: *Physical Review Letters* 96.14 (Apr. 2006). ISSN: 1079-7114. DOI: 10.1103/physrevlett.96.145505.

[Dou92]   E. Dougherty. *An Introduction to morphological Image Processing.* Tutorial texts in Optical Engineering, 1992. URL: %5Curl%7Bhttps://hqwrg4ntt03.storage.googleapis.com/MDgxOTQwODQ1WA==03.pdf%7D.

[DRE98]   jolein Dijkstra, René van Roij, and Robert Evans. "Phase Behavior and Structure of Binary Hard-Sphere Mixtures". In: *Physical Review Letters* 81.11 (Sept. 1998), pp. 2268–2271. ISSN: 1079-7114. DOI: 10.1103/physrevlett.81.2268.

[DS13]   Karen E Daniels and Matthias Schröter. "Focus on granular segregation". In: *New Journal of Physics* 15.3 (Mar. 2013), p. 035017. ISSN: 1367-2630. DOI: 10.1088/1367-2630/15/3/035017.

[DTS05]   Aleksandar Donev, Salvatore Torquato, and Frank H. Stillinger. "Pair correlation function characteristics of nearly jammed disordered and ordered hard-sphere packings". In: *Physical Review E* 71.1 (Jan. 2005). ISSN: 1550-2376. URL: http://dx.doi.org/10.1103/PhysRevE.71.011105.
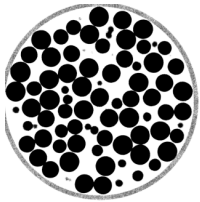
[Dur99]   Jacques Duran. *Sands, Powders, and Grains: An Introduction to the Physics of Granular Materials (Partially Ordered Systems)*. Springer, 1999. ISBN: 0387986561.

[DW09]   Kenneth W. Desmond and Eric R. Weeks. "Random close packing of disks and spheres in confined geometries". In: *Physical Review E* 80.5 (Nov. 2009). ISSN: 1550-2376. DOI: 10.1103/physreve.80.051305.

[DZB13]   Joshua A. Dijksman, Hu Zheng, and Robert P. Behringer. "Imaging soft sphere packings in a novel triaxial shear setup". In: (2013). DOI: 10.1063/1.4811966.

[Ela02]   M. Elad. "On the origin of the bilateral filter and ways to improve it". In: *IEEE Transactions on Image Processing* 11.10 (Oct. 2002), pp. 1141–1151. ISSN: 1057-7149. DOI: 10.1109/tip.2002.801126.

[EO89]   S.F. Edwards and R.B.S. Oakeshott. "Theory of powders". In: *Physica A: Statistical Mechanics and its Applications* 157.3 (June 1989), pp. 1080–1090. ISSN: 0378-4371. DOI: 10.1016/0378-4371(89)90034-4.

[Eva+12]   Myfanwy E. Evans, Johannes Zirkelbach, Gerd E. Schröder-Turk, Andrew M. Kraynik, and Klaus Mecke. "Deformation of Platonic foam cells: Effect on growth rate". In: *Physical Review E* 85.6 (June 2012). ISSN: 1550-2376. DOI: 10.1103/physreve.85.061401.

[Eva+13]   Myfanwy E. Evans, Andrew M. Kraynik, Douglas A. Reinelt, Klaus Mecke, and Gerd E. Schröder-Turk. "Networklike Propagation of Cell-Level Stress in Sheared Random Foams". In: *Physical Review Letters* 111.13 (Sept. 2013). ISSN: 1079-7114. DOI: 10.1103/physrevlett.111.138301.

[evo18]   website surface evolver. *http://facstaff.susqu.edu/brakke/evolver/evolver.html*. 2018.

[EY62]   N Epstein and MJ Young. "Random loose packing of binary mixtures of spheres". In: *Nature* 196.4857 (1962), pp. 885–886.

[ezr18]   website fraunhofer ezrt. *https://www.iis.fraunhofer.de/de/ff/zfp.html*. 2018.

[F3M10]   G. Farrell, K. 3tini, and N. Menon. "Loose packings of frictional spheres". In: *Soft Matter* 6.13 (2010), p. 2925. ISSN: 1744-6848. DOI: 10.1039/c0sm00038h.

[Fal+14]   A. Fall, B. Weber, M. Pakpour, N. Lenoir, N. Shahidzadeh, J. Fiscina, C. Wagner, and D. Bonn. "Sliding Friction on Wet and Dry Sand". In: *Physical Review Letters* 112.17 (Apr. 2014). ISSN: 1079-7114. DOI: 10.1103/physrevlett.112.175502.

[FDK84]   L. A. Feldkamp, L. C. Davis, and J. W. Kress. "Practical cone-beam algorithm". In: *Journal of the Optical Society of America A* 1.6 (June 1984), p. 612. ISSN: 1520-8532. DOI: 10.1364/josaa.1.000612.

[Fin70]   J. L. Finney. "Random Packings and the Structure of Simple Liquids. I. The Geometry of Random Close Packing". In: *Proceedings of the Royal Society A:*
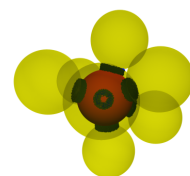
Mathematical, Physical and Engineering Sciences 319.1539 (Nov. 1970), pp. 479–493. ISSN: 1471-2946. DOI: 10.1098/rspa.1970.0189.

[Fou+05] Z Fournier, D Geromichalos, S Herminghaus, M M Kohonen, F Mugele, M Scheel, M Schulz, B Schulz, Ch Schier, R Seemann, and et al. "Mechanical properties of wet granular materials". In: *J. Phys.: Condens. Matter* 17.9 (Feb. 2005), S477–S502. ISSN: 1361-648X. DOI: 10.1088/0953-8984/17/9/013.

[FS01] Daan Frenkel and Berend Smit. *Understanding Molecular Simulation, Second Edition: From Algorithms to Applications (Computational Science Series, Vol 1).* Academic Press, 2001. ISBN: 0122673514.

[FSS15] Tilo Finger, Matthias Schröter, and Ralf Stannarius. "The mechanism of long-term coarsening of granular mixtures in rotating drums". In: *New Journal of Physics* 17.9 (Sept. 2015), p. 093023. ISSN: 1367-2630. DOI: 10.1088/1367-2630/17/9/093023.

[FTP99] N. Fraysse, H. Thome, and L. Petit. "Humidity effects on the stability of a sandpile". In: *The European Physical Journal B-Condensed Matter and Complex Systems* 11.4 (1999), pp. 615–619.

[Fuc98] T. Fuchs. "Strahlaufhärtungskorrekturen in der Computer-Tomographie". In: *Unpublished PhD thesis, Uni Erlangen* (1998).

[G79] Hermann G. *Image Reconstruction from Projections: Implementation and Applications (Topics in Applied Physics).* Springer, 1979. ISBN: 3540094172.

[Gas91] Philip H Gaskell. "Models for the structure of amorphous solids". In: *Materials science and technology* (1991).

[GBH70] Richard Gordon, Robert Bender, and Gabor T. Herman. "Algebraic Reconstruction Techniques (ART) for three-dimensional electron microscopy and X-ray photography". In: *Journal of Theoretical Biology* 29.3 (Dec. 1970), pp. 471–481. ISSN: 0022-5193. DOI: 10.1016/0022-5193(70)90109-8.

[geo18] website geomview. *http://www.geomview.org/*. 2018.

[Ger+03a] D. Geromichalos, M. Kohonen, M. Scheel, and S. Herminghaus. In: *arxiv https://arxiv.org/abs/cond-mat/0307762* (2003).

[Ger+03b] Dimitrios Geromichalos, Mika M. Kohonen, Frieder Mugele, and Stephan Herminghaus. "Mixing and Condensation in a Wet Granular Medium". In: *Physical Review Letters* 90.16 (Apr. 2003). ISSN: 1079-7114. DOI: 10.1103/physrevlett.90.168702.

[gey18] website geyopp. *http://www.maths.qmul.ac.uk/~baule/geyopp.html*. 2018.

[GF84] Frans C.A Groen and Nigel J Foster. "A fast algorithm for cellular logic operations on sequential machines". In: *Pattern Recognition Letters* 2.5 (Sept. 1984), pp. 333–338. ISSN: 0167-8655. URL: http://dx.doi.org/10.1016/0167-8655(84)90021-7.
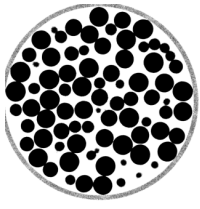
[GFO17]   F. Gibour, R. Fedkiw, and S. Osher. "A Review of Level-Set Methods and Some Recent Applications". In: *Elsevier* (2017).

[Giu+16] Anais Giustiniani, Philippe Guegan, Manon 3chand, Christophe Poulard, and Wiebke Drenckhan. "Generation of Silicone Poly-HIPEs with Controlled Pore Sizes via Reactive Emulsion Stabilization". In: *Macromolecular Rapid Communications* 37.18 (2016), pp. 1527–1532.

[Giu+18] Anais Giustiniani, Simon Weis, Christophe Poulard, Paul Kamm, Francisco García-Moreno, Matthias Schröter, and Wiebke Drenckhan. "Skinny emulsions take on granular matter". In: *Soft Matter* (2018). ISSN: 1744-6848. DOI: 10.1039/c8sm00830b.

[GO16]   S. Günther and S. Odenbach. "A Method for Image Decomposition and Particle Quantification in Multiphase Systems". In: *Transport in Porous Media* 112.1 (Jan. 2016), pp. 105–116. ISSN: 1573-1634. DOI: 10.1007/s11242-016-0634-x.

[Gör+13] D. Göring, M. A. Klatt, C. Stegmann, and K. Mecke. "Morphometric analysis in gamma-ray astronomy using Minkowski functionals". In: *Astronomy and Astrophysics* 555 (June 2013), A38. ISSN: 1432-0746. DOI: 10.1051/0004-6361/201321136.

[GSB17]   Katalin A. Gillemot, Ellák Somfai, and Tamás Börzsönyi. "Shear-driven segregation of dry granular materials with different friction coefficients". In: *Soft Matter* 13.2 (2017), pp. 415–420. ISSN: 1744-6848. DOI: 10.1039/c6sm01946c.

[GW07]   R. Gonzalez and R. Woods. *Digital Image Processing: Third Edition.* Prentice Hall International, 2007.

[HA10]   A. Hasan and K.A. ALSHIBLI. "Experimental assessment of 3D particle-to-particle interaction within sheared sand using synchrotron microtomography". In: *Géotechnique* 60.5 (May 2010), pp. 369–379. ISSN: 1751-7656. DOI: 10.1680/geot.2010.60.5.369.

[Had57]   H. Hadwiger. *Vorlesungen über Inhalt, Oberfläche und Isoperimetrie.* Springer, 1957.

[Hag12]   Willi H. Hager. "Wilfrid Noel Bond and the Bond number". In: *Journal of Hydraulic Research* 50.1 (Feb. 2012), pp. 3–9. ISSN: 1814-2079. DOI: 10.1080/00221686.2011.649839.

[Hal+10] S.A. Hall, M. Bornert, J. Desrues, Y. Pannier, N. Lenoir, G. Viggiani, and P. Bésuelle. "Discrete and continuum analysis of localised deformation in sand using X-ray mu CT and volumetric digital image correlation". In: *Géotechnique* 60.5 (May 2010), pp. 315–322. ISSN: 1751-7656. DOI: 10.1680/geot.2010.60.5.315.

[Hal05]   Thomas C. Hales. "A Proof of the Kepler Conjecture". In: *Annals of Mathematics* 162.3 (2005), pp. 1065–1185. ISSN: 0003486X. URL: http://www.jstor.org/stable/20159940.
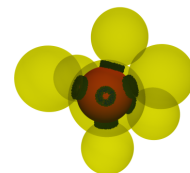
[Hal27]   Stephen Hales. *Vegetable Staticks: or, an account of some statical experiments on the Sap in Vegetables...Also, a specimen of an attempt to analyse the Air.* W. and J. Innys, 1727.

[Han+15]   M. Hanifpour, N. Francois, V. Robins, A. Kingston, S. M. Vaez Allaei, and M. Saadatfar. "Structural and mechanical features of the order-disorder transition in experimental hard-sphere packings". In: *Physical Review E* 91.6 (June 2015).

[Har57]   W.R. Harper. "The generation of static charge". In: *Advances in Physics* 6.24 (Oct. 1957), pp. 365–417. ISSN: 1460-6976. DOI: 10.1080/00018735700101396.

[HBS08]   Stephan Herminghaus, Martin Brinkmann, and Ralf Seemann. "Wetting and Dewetting of Complex Surface Geometries". In: *Annual Review of Materials Research* 38.1 (Aug. 2008), pp. 101–121. ISSN: 1545-4118. DOI: 10.1146/annurev.matsci.38.060407.130335.

[HBV99]   Daniel Howell, R. P. Behringer, and Christian Veje. "Stress Fluctuations in a 2D Granular Couette Experiment: A Continuous Transition". In: *Physical Review Letters* 82.26 (July 1999), pp. 5241–5244. ISSN: 1079-7114. DOI: 10.1103/physrevlett.82.5241.

[HC17]   Reinhard Höhler and Sylvie Cohen-Addad. "Many-body interactions in soft jammed materials". In: *Soft Matter* 13.7 (2017), pp. 1371–1383. ISSN: 1744-6848. DOI: 10.1039/c6sm01567k.

[HCO09]   Stephen T. Hyde, Liliana de Campo, and Christophe Oguey. "Tricontinuous mesophases of balanced three-arm "star polyphiles"". In: *Soft Matter* 5.14 (2009), p. 2782. ISSN: 1744-6848. DOI: 10.1039/b822814k.

[Hec09]   M. van Hecke. "Jamming of soft particles: geometry, mechanics, scaling and isostaticity". In: *J. Phys.: Condens. Matter* 22.3 (Dec. 2009), p. 033101. ISSN: 1361-648X. DOI: 10.1088/0953-8984/22/3/033101.

[Hei+15]   K Heim, GS Vinod-Kumar, F Garcia-Moreno, A Rack, and J Banhart. "Stabilisation of aluminium foams and films by the joint action of dispersed particles and oxide films". In: *Acta Materialia* 99 (2015), pp. 313–324.

[Her00]   S. Herminghaus. "Roughness-induced non-wetting". In: *EPL (Europhysics Letters)* 52.2 (2000), p. 165.

[Her13]   Stephan Herminghaus. *Wet Granular Matter: A Truly Complex Fluid (Series in Soft Condensed Matter).* World Scientific Publishing Company, 2013. ISBN: 9814417696.

[Her80]   Gabor T Herman. "Image Reconstruction from Projections: The Fundamentals of Computerized Tomography (Computer Science Applied Mathematics)". In: *image* 10 (1980), p. 03.

[HHS10]   S. Henkes, M. van Hecke, and W. van Saarloos. "Critical jamming of frictional grains in the generalized isostaticity picture". In: *EPL (Europhysics Letters)* 90.1 (Apr. 2010), p. 14003. ISSN: 1286-4854. DOI: 10.1209/0295-5075/90/14003.
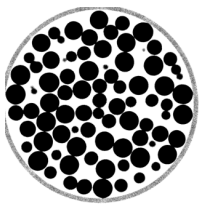
[Hie15]   J. Hielscher. "Circular Dichroism of Distorted Structure-Photonic Materials". In: *Master thesis, FAU Erlangen* (2015).

[HK04]   Suman K. Hajra and D. V. Khakhar. "Sensitivity of granular segregation of mixtures in quasi-two-dimensional fluidized layers". In: *Physical Review E* 69.3 (Mar. 2004). ISSN: 1550-2376. DOI: 10.1103/physreve.69.031304.

[HK76]   J. Hoshen and R. Kopelman. "Percolation and cluster distribution. I. Cluster multiple labeling technique and critical concentration algorithm". In: *Phys. Rev. B* 14.8 (Oct. 1976), pp. 3438–3445. ISSN: 0556-2805. DOI: 10.1103/physrevb.14.3438.

[HL97]   Thomas C. Halsey and Alex J. Levine. "How Sandcastles Fall". In: *Physical Review Letters* 80.14 (Apr. 1997), pp. 3141–3144. ISSN: 1079-7114. DOI: 10.1103/physrevlett.80.3141.

[HM06]   Jean-Pierre Hansen and I.R. McDonald. *Theory of Simple Liquids, Third Edition.* Academic Press, 2006. ISBN: 0123705355.

[Hop+11] Adam B. Hopkins, Yang Jiao, Frank H. Stillinger, and Salvatore Torquato. "Phase Diagram and Structural Diversity of the Densest Binary Sphere Packings". In: *Physical Review Letters* 107.12 (Sept. 2011). ISSN: 1079-7114. DOI: 10.1103/physrevlett.107.125501.

[Hör+14] Julia Hörrmann, Daniel Hug, Michael Andreas Klatt, and Klaus Mecke. "Minkowski tensor density formulas for Boolean models". In: *Advances in Applied Mathematics* 55 (Apr. 2014), pp. 48–85. ISSN: 0196-8858. DOI: 10.1016/j.aam.2014.01.001.

[Hor+97] DJ Hornbaker, Réka Albert, István Albert, Albert-Lázló Barabási, and Peter Schiffer. "What keeps sandcastles standing?" In: *Nature* 387.6635 (1997), p. 765.

[Hou+18] Zibing Hou, Dongwei Guo, Jianghai Cao, and Yi Chang. "A method based on the centroid of segregation points: A Voronoi polygon application to solidification of alloys". In: *Journal of Alloys and Compounds* 762 (Sept. 2018), pp. 508–519. ISSN: 0925-8388. DOI: 10.1016/j.jallcom.2018.05.160.

[HSP09]   R. Holtzman, D. B. Silin, and T. W. Patzek. "Frictional granular mechanics: A variational approach". In: *International Journal for Numerical Methods in Engineering* (2009), n/a–n/a. ISSN: 1097-0207. DOI: 10.1002/nme.2727.

[HSS08a] D. Hug, R. Schneider, and R. Schuster. "Integral geometry of tensor valuations". In: *Adv. in Appl. Math.* 41 (2008), pp. 482–509.

[HSS08b] D. Hug, R. Schneider, and R. Schuster. "The space of isometry covariant tensor valuations". In: *St. Petersburg Math. J.* 19 (2008), pp. 137–158.

[Hur+14] Ryan Hurley, Eloïse 3teau, Guruswami Ravichandran, and José E. Andrade. "Extracting inter-particle forces in opaque granular materials: Beyond photoelasticity". In: *Journal of the Mechanics and Physics of Solids* 63 (Feb. 2014), pp. 154–166. ISSN: 0022-5096. DOI: 10.1016/j.jmps.2013.09.013.
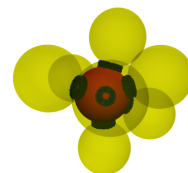
[Hur+16]   R. C. Hurley, S. A. Hall, J. E. Andrade, and J. Wright. "Quantifying Interparticle Forces and Heterogeneity in 3D Granular Materials". In: *Physical Review Letters* 117.9 (Aug. 2016). ISSN: 1079-7114. DOI: 10.1103/physrevlett.117.098005.

[Huy09]   Johnny Huynh. "Separating axis theorem for oriented bounding boxes". In: *URL: jkh. me/files/tutorials/Separating% 20Axis% 20Theorem% 20for% 20Oriented% 20Bounding% 20Boxes. pdf* (2009).

[HW04]   H. Hinrichsen and E. Wolf. *The Physics of Granular Media.* Wiley-VCH, 2004. ISBN: 3527403736.

[HXZ12]   W. Hu, L. Xie, and X. Zheng. "Contact charging of silica glass particles in a single collision". In: *Applied Physics Letters* 101.11 (Sept. 2012), p. 114107. ISSN: 1077-3118. DOI: 10.1063/1.4752458.

[HZ86]   John Harer and Don Zagier. "The Euler characteristic of the moduli space of curves". In: *Inventiones mathematicae* 85.3 (1986), pp. 457–485.

[Ipp+95]   Irene Ippolito, Chrystèle Annic, Jacques Lemaître, Luc Oger, and Daniel Bideau. "Granular temperature: Experimental analysis". In: *Physical Review E* 52.2 (Aug. 1995), pp. 2072–2075. ISSN: 1095-3787. DOI: 10.1103/physreve.52.2072.

[Ive+01]   Simon M. Iveson, James D. Litster, Karen Hapgood, and Bryan J. Ennis. "Nucleation, growth and breakage phenomena in agitated wet granulation processes: a review". In: *Powder Technology* 117.1-2 (June 2001), pp. 3–39. ISSN: 0032-5910. DOI: 10.1016/s0032-5910(01)00313-8.

[Jer+08]   Melissa Jerkins, Matthias Schröter, Harry L. Swinney, Tim J. Senden, Mohammad Saadatfar, and Tomaso Aste. "Onset of Mechanical Stability in Random Packings of Frictional Spheres". In: *Physical Review Letters* 101.1 (June 2008). ISSN: 1079-7114. DOI: 10.1103/physrevlett.101.018301.

[Jia+03]   Wen Jiang, Matthew L Baker, Qiu Wu, Chandrajit Bajaj, and Wah Chiu. "Applications of a bilateral denoising filter in biological electron microscopy". In: *Journal of Structural Biology* 144.1-2 (Oct. 2003), pp. 114–122. ISSN: 1047-8477. DOI: 10.1016/j.jsb.2003.09.028.

[JLN89]   H. M. Jaeger, Chu-heng Liu, and Sidney R. Nagel. "Relaxation at the Angle of Repose". In: *Physical Review Letters* 62.1 (Jan. 1989), pp. 40–43. ISSN: 0031-9007. DOI: 10.1103/physrevlett.62.40.

[JN92]   H. M. Jaeger and S. R. Nagel. "Physics of the Granular State". In: *Science* 255.5051 (Mar. 1992), pp. 1523–1531. ISSN: 1095-9203. DOI: 10.1126/science.255.5051.1523.

[Joh06]   Steven Johnson. *The Ghost Map: The Story of London's Most Terrifying Epidemic–and How It Changed Science,Cities, and the Modern World.* Riverhead Books, 2006.

[Jon02]   Richard A. L. Jones. *Soft Condensed Matter (Oxford Master Series in Condensed Matter Physics, Vol. 6).* Oxford University Press, 2002. ISBN: 0198505892.
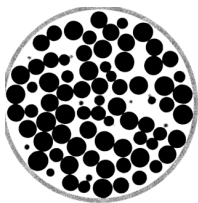
[Jor+11]   I. Jorjadze, L.-L. Pontani, K. A. Newhall, and J. Brujic. "Attractive emulsion droplets probe the phase diagram of jammed granular matter". In: *Proceedings of the National Academy of Sciences* 108.11 (Feb. 2011), pp. 4286–4291. ISSN: 1091-6490. DOI: 10.1073/pnas.1017716108.

[Jos+00]   Christophe Josserand, Alexei V. Tkachenko, Daniel M. Mueth, and Heinrich M. Jaeger. "Memory Effects in Granular Materials". In: *Physical Review Letters* 85.17 (Oct. 2000), pp. 3632–3635. ISSN: 1079-7114. DOI: 10.1103/physrevlett.85.3632.

[Jos17]   R.P. Behringer Joshua Dijksman N. Brodu. "Refractive index matched scanning and detection of soft particles". In: *Review of Scientific Instruments* (2017). https://arxiv.org/abs/1703.02816.

[JST11]   Yang Jiao, Frank H. Stillinger, and Salvatore Torquato. "Nonuniversality of density and disorder in jammed sphere packings". In: *Journal of Applied Physics* 109.1 (Jan. 2011), p. 013508. ISSN: 1089-7550. DOI: 10.1063/1.3524489.

[JT85]   W. S. Jodrey and E. M. Tory. "Computer simulation of close random packing of equal spheres". In: *Physical Review A* 32.4 (Oct. 1985), pp. 2347–2351. ISSN: 0556-2791. DOI: 10.1103/physreva.32.2347.

[Kal06]   W.A. Kalender. *Computertomographie*. Wiley, 2006. ISBN: 9783895782152. URL: https://books.google.de/books?id=ptLsmgEACAAJ.

[Kan81]   Ken-ichi Kanatani. "The use of entropy in the description of granular materials". In: *Powder Technology* 30.2 (Nov. 1981), pp. 217–223. ISSN: 0032-5910. DOI: 10.1016/0032-5910(81)80015-0.

[Kap+10]   S C Kapfer, W Mickel, Fabian Schaller, M Spanner, C Goll, T Nogawa, N Ito, K Mecke, and Gerd. E Schröder-Turk. "Local anisotropy of fluids using Minkowski tensors". In: *Journal of Statistical Mechanics: Theory and Experiment* 2010.11 (Nov. 2010), P11010. ISSN: 1742-5468. DOI: 10.1088/1742-5468/2010/11/p11010.

[Kap+12]   S. Kapfer, W. Mickel, K. Mecke, and Gerd E. Schröder-Turk. "Jammed spheres: Minkowski tensors reveal onset of local crystallinity". In: *Phys. Rev. E* 85.3 (Mar. 2012). ISSN: 1550-2376. DOI: 10.1103/physreve.85.030301.

[Kap11]   Sebastian Kapfer. "Morphometry and Physics of Particulate and Porous Media". In: *PhD thesis, FAU Erlangen* (2011).

[Kar+17]   Sadegh Karimpouli, Pejman Tahmasebi, Hamed Lamei Ramandi, Peyman Mostaghimi, and Mohammad Saadatfar. "Stochastic modeling of coal fracture network by direct use of micro-computed tomography images". In: *International Journal of Coal Geology* 179 (June 2017), pp. 153–163. ISSN: 0166-5162. DOI: 10.1016/j.coal.2017.06.002.

[Kar+18]   Z. Karatza, E. Andò, S.-A. Papanicolopulos, J. Y. Ooi, and G. Viggiani. "Evolution of deformation and breakage in sand studied using X-ray tomogra-

phy". In: *Géotechnique* 68.2 (Feb. 2018), pp. 107–117. ISSN: 1751-7656. DOI: 10.1680/jgeot.16.p.208.
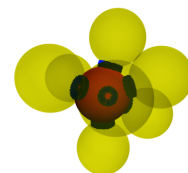
[Kár+98] A. Károlyi, J. Kertész, S. Havlin, H. Makse, and H. Stanley. "Filling a silo with a mixture of grains: Friction-induced segregation". In: *EPL (Europhysics Letters)* 44.3 (1998), p. 386. URL: http://stacks.iop.org/0295-5075/44/i=3/a=386.

[KHH08] Jonathan K. Kummerfeld, Toby S. Hudson, and Peter Harrowell. "The Densest Packing of AB Binary Hard-Sphere Homogeneous Compounds across all Size Ratios". In: *The Journal of Physical Chemistry B* 112.35 (Sept. 2008), pp. 10773–10776. ISSN: 1520-5207. DOI: 10.1021/jp804953r.

[Kit17] Charles Kittel. *Einführung in die Festkörperphysik (German Edition)*. Oldenbourg Wissenschaftsverlag, 2017. ISBN: 3486272195.

[KL07] Randall D. Kamien and Andrea J. Liu. "Why is Random Close Packing Reproducible?" In: *Physical Review Letters* 99.15 (Oct. 2007). ISSN: 1079-7114. DOI: 10.1103/physrevlett.99.155501.

[KL09] Jasper F. Kok and Daniel J. Lacks. "Electrification of granular systems of identical insulators". In: *Physical Review E* 79.5 (May 2009). ISSN: 1550-2376. DOI: 10.1103/physreve.79.051304.

[Kla+17] M. Klatt, G. Last, K. Mecke, C. Redenbach, Fabian Schaller, and Gerd E. Schröder-Turk. "Cell Shape Analysis of Random Tessellations Based on Minkowski Tensors". In: *Lecture Notes in Mathematics* 2177 (2017). Ed. by Eva B. Vedel Jensen and Markus Kiderlen, pp. 385–421.

[Kle99] Christoph Kleinschmidt. "Analytical considerations of beam hardening in medical accelerator photon spectra". In: *Medical Physics* 26.9 (Sept. 1999), pp. 1995–1999. ISSN: 0094-2405. DOI: 10.1118/1.598704.

[KMS01] M. Kerscher, K. Mecke, and P. Schücker. "Non-Gaussian morphology of galaxy cluster distribution: Minkowski functionals of the REFLEX catalogue". In: *Tracing Cosmic Evolution with Galaxy Clusters*. Ed. by M. Mezzetti S. Borgani and R. Valdarnini. Astron. Soc. Pacific Conference Ser. San Francisco, California, 2001, pp. 60–62.

[Kni+95] James B. Knight, Christopher G. Fandrich, Chun Ning Lau, Heinrich M. Jaeger, and Sidney R. Nagel. "Density relaxation in a vibrated granular material". In: *Physical Review E* 51.5 (May 1995), pp. 3957–3963. ISSN: 1095-3787. DOI: 10.1103/physreve.51.3957.

[Koh+04] Mika M. Kohonen, Dimitrios Geromichalos, 3io Scheel, Christof Schier, and Stephan Herminghaus. "On capillary bridges in wet granular materials". In: *Physica A: Statistical Mechanics and its Applications* 339.1-2 (Aug. 2004), pp. 7–15. ISSN: 0378-4371. DOI: 10.1016/j.physa.2004.03.047.

[Kol+16] Jari Kolehmainen, Ali Ozel, Christopher M. Boyce, and Sankaran Sundaresan. "Triboelectric charging of monodisperse particles in fluidized beds". In: *AIChE*
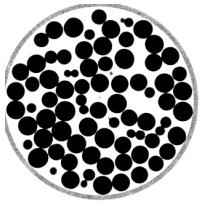
Journal 63.6 (Nov. 2016), pp. 1872–1891. ISSN: 0001-1541. DOI: `10.1002/aic.15541`.

[KRS03]   Andrew M. Kraynik, Douglas A. Reinelt, and Frank van Swol. "Structure of random monodisperse foam". In: *Physical Review E* 67.3 (Mar. 2003). ISSN: 1095-3787. DOI: `10.1103/physreve.67.031403`.

[KSM17a]   M. Klatt, Gerd E. Schröder-Turk, and K. Mecke. "Anisotropy in finite continuum percolation: threshold estimation by Minkowski functionals". In: *Journal of Statistical Mechanics: Theory and Experiment* 2017.2 (2017), p. 023302.

[KSM17b]   M. Klatt, Gerd E.. Schröder-Turk, and K. Mecke. "Mean-intercept anisotropy analysis of porous tissue and microstructures. I and II". In: *Medical Physics* 44 (2017), pp. 3650–3675.

[KT14]   Michael A. Klatt and Salvatore Torquato. "Characterization of maximally random jammed sphere packings: Voronoi correlation functions". In: *Physical Review E* 90.5 (Nov. 2014). ISSN: 1550-2376. DOI: `10.1103/physreve.90.052120`.

[KTH13]   Gijs Katgert, Brian P. Tighe, and Martin van Hecke. "The jamming perspective on wet foams". In: *Soft Matter* 9.41 (2013), p. 9739. ISSN: 1744-6848. DOI: `10.1039/c3sm51543e`.

[Kud04]   Arshad Kudrolli. "Size separation in vibrated granular matter". In: *Reports on Progress in Physics* 67.3 (Feb. 2004), pp. 209–247. ISSN: 1361-6633. DOI: `10.1088/0034-4885/67/3/r01`.

[Kum+16]   Nishant Kumar, Vanessa Magnanimo, 3co Ramaioli, and Stefan Luding. "Tuning the bulk properties of bidisperse granular mixtures by small amount of fines". In: *Powder Technology* 293 (May 2016), pp. 94–112. ISSN: 0032-5910. DOI: `10.1016/j.powtec.2015.11.042`.

[Lav32]   F. Laves. "Zur Klassifikation der Silikate. Geometrische Untersuchungen möglicher Silicium-Sauerstoff- Verbände als Verknüpfungsmöglichkeiten regulärer Tetraeder". In: *Zeitschrift für Kristallographie - Crystalline Materials* 82.1-6 (Jan. 1932), pp. 1–14. ISSN: 2194-4946. DOI: `10.1524/zkri.1932.82.1.1`.

[Lec+06]   F Lechenault, F da Cruz, O Dauchot, and E Bertin. "Free volume distributions and compactivity measurement in a bidimensional granular packing". In: *Journal of Statistical Mechanics: Theory and Experiment* 2006.07 (July 2006), P07009–P07009. ISSN: 1742-5468. DOI: `10.1088/1742-5468/2006/07/p07009`.

[Lee+15]   Victor Lee, Scott R. Waitukaitis, 3c Z. Miskin, and Heinrich M. Jaeger. "Direct observation of particle interactions and clustering in charged granular streams". In: *Nature Physics* 11.9 (June 2015), pp. 733–737. ISSN: 1745-2481. DOI: `10.1038/nphys3396`.

[Lee81]   S. Lee. *Optical Information Processing: Fundamentals (Topics in Applied Physics).* Springer, 1981. ISBN: 3540105220.
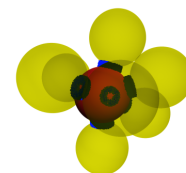
[LHW14]   Chun-Chung Liao, Shu-San Hsiau, and Chi-Sou Wu. "Combined effects of internal friction and bed height on the Brazil-nut problem in a shaker". In: *Powder Technology* 253 (Feb. 2014), pp. 561–567. ISSN: 0032-5910. DOI: `10.1016/j.powtec.2013.12.031`.

[Liu+13]   Ruihao Liu, Xianzhen Yin, Haiyan Li, Qun Shao, Peter York, You He, Tiqiao Xiao, and Jiwen Zhang. "Visualization and quantitative profiling of mixing and segregation of granules using synchrotron radiation X-ray microtomography and three dimensional reconstruction". In: *International Journal of Pharmaceutics* 445.1-2 (Mar. 2013), pp. 125–133. ISSN: 0378-5173. DOI: `10.1016/j.ijpharm.2013.02.010`.

[LM11]   Daniel J Lacks and R Mohan Sankaran. "Contact electrification of insulating materials". In: *Journal of Physics D: Applied Physics* 44.45 (Oct. 2011), p. 453001. ISSN: 1361-6463. DOI: `10.1088/0022-3727/44/45/453001`.

[LMW95]   C. N. Likos, K. R. Mecke, and H. Wagner. "Statistical morphology of random interfaces in microemulsions". In: *The Journal of Chemical Physics* 102.23 (June 1995), pp. 9350–9361. ISSN: 1089-7690. URL: `http://dx.doi.org/10.1063/1.468802`.

[LN01]   A. Liu and S. Nagel. *Jamming and Rheology: Constrained Dynamics on Microscopic and Macroscopic Scales*. CRC Press, 2001. ISBN: 0748408797.

[LN98]   A. Liu and S. Nagel. "Jamming is not just cool any more". In: *Nature* 396.6706 (Nov. 1998), pp. 21–22. ISSN: 0028-0836. DOI: `10.1038/23819`.

[LT86a]   J Lowell and WS Truscott. "Triboelectrification of identical insulators. I. An experimental investigation". In: *Journal of physics D: Applied physics* 19.7 (1986), p. 1273.

[LT86b]   J Lowell and WS Truscott. "Triboelectrification of identical insulators. II. Theory and further experiments". In: *Journal of Physics D: Applied Physics* 19.7 (1986), p. 1281.

[Luc+99]   V. Luchnikov, N. Medvedev, L. Oger, and J. Troadec. "Voronoi-Delaunay analysis of voids in systems of nonspherical particles". In: *Phys. Rev. E* 59.6 (June 1999), pp. 7205–7212. ISSN: 1095-3787. DOI: `10.1103/physreve.59.7205`.

[LYY11]   P. Y. Liu, R. Y. Yang, and A. B. Yu. "Dynamics of wet particles in rotating drums: Effect of liquid surface tension". In: *Physics of Fluids* 23.1 (Jan. 2011), p. 013304. ISSN: 1089-7666. DOI: `10.1063/1.3543916`.

[MA05]   Klaus Mecke and C H Arns. "Fluids in porous media: a morphometric approach". In: *Journal of Physics: Condensed Matter* 17.9 (Feb. 2005), S503–S534. ISSN: 1361-648X. URL: `http://dx.doi.org/10.1088/0953-8984/17/9/014`.

[Mae+13]   Armando Maestro, Wiebke Drenckhan, Emmanuelle Rio, and Reinhard Höhler. "Liquid dispersions under gravity: volume fraction profile and osmotic
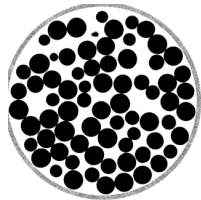
pressure". In: *Soft Matter* 9.8 (2013), p. 2531. ISSN: 1744-6848. DOI: 10.1039/c2sm27668b.

[Mak13] H. Makse. *Software and Data: Research on hard sphere packings.* 2013. URL: http://lev.ccny.cuny.edu/~hmakse/soft_data.html.

[MAr29] Neil M'Arthur. "Principal radii of curvature at a point on an ellipsoid". In: *Mathematical Notes* 24 (Jan. 1929), pp. xvi–xvii. ISSN: 1757-7489. DOI: 10.1017/s1757748900001961.

[Mas+99] T. G. Mason, A. J. Levine, D. Ertaş, and T. C. Halsey. "Critical angle of wet sandpiles". In: *Physical Review E* 60.5 (Nov. 1999), R5044–R5047. ISSN: 1095-3787. DOI: 10.1103/physreve.60.r5044.

[Mat+10] S. Matsusaka, H. 3uyama, T. Matsuyama, and M. Ghadiri. "Triboelectric charging of powders: A review". In: *Chemical Engineering Science* 65.22 (Nov. 2010), pp. 5781–5807. ISSN: 0009-2509. DOI: 10.1016/j.ces.2010.07.005.

[MB05] T. S. Majmudar and R. P. Behringer. "Contact force measurements and stress-induced anisotropy in granular materials". In: *Nature* 435.7045 (June 2005), pp. 1079–1082. ISSN: 1476-4687. DOI: 10.1038/nature03805.

[MBW94] K. Mecke, T. Buchert, and H. Wagner. "Robust Morphological Measures for Large-scale Structure in the Universe". In: *Astronomy and Astrophysics* 288.3 (Aug. 1994), pp. 697–704.

[MDS09] K. Michielsen, H. De Raedt, and D. G. Stavenga. "Reflectivity of the gyroid biophotonic crystals in the ventral wing scales of the Green Hairstreak butterfly, Callophrys rubi". In: *Journal of The Royal Society Interface* 7.46 (Oct. 2009), pp. 765–771. ISSN: 1742-5662. DOI: 10.1098/rsif.2009.0352.

[ME89] Anita Mehta and S.F. Edwards. "Statistical mechanics of powder mixtures". In: *Physica A: Statistical Mechanics and its Applications* 157.3 (June 1989), pp. 1091–1100. ISSN: 0378-4371. DOI: 10.1016/0378-4371(89)90035-6.

[Mec00] K. Mecke. "Additivity, Convexity, and Beyond: Applications of Minkowski Functionals in Statistical Physics". In: *Lecture Notes in Physics* (2000), pp. 111–184. DOI: 10.1007/3-540-45043-2_6.

[Mec96] K. R. Mecke. "Morphological characterization of patterns in reaction-diffusion systems". In: *Physical Review E* 53.5 (May 1996), pp. 4794–4800. ISSN: 1095-3787. URL: http://dx.doi.org/10.1103/PhysRevE.53.4794.

[Mec98] K.R. Mecke. "Morphological thermodynamics of composite media". In: *Fluid Phase Equilibria* 150-151 (Sept. 1998), pp. 591–598. ISSN: 0378-3812. URL: http://dx.doi.org/10.1016/S0378-3812(98)00306-9.

[Mel11] H.J. Melosh. *Planetary Surface Processes.* Cambridge Planetary Science. Cambridge University Press, 2011. ISBN: 9781139498302. URL: https://books.google.de/books?id=3bQD1DJgliIC.
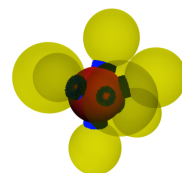
[MGG06]   M. Micoulaut, Y. Guissani, and B. Guillot. "Simulated structural and thermal properties of glassy and liquid germania". In: *Physical Review E* 73.3 (Mar. 2006). ISSN: 1550-2376. DOI: 10.1103/physreve.73.031504.

[Mic+08]   Walter Mickel, Stefan Münster, Louise M. Jawerth, David A. Vader, David A. Weitz, Adrian P. Sheppard, Klaus Mecke, Ben Fabry, and Gerd E. Schröder-Turk. "Robust Pore Size Analysis of Filamentous Networks from Three-Dimensional Confocal Microscopy". In: *Biophysical Journal* 95.12 (Dec. 2008), pp. 6072–6080. ISSN: 0006-3495. DOI: 10.1529/biophysj.108.135939.

[Mic+13]   W. Mickel, S. Kapfer, Schröder-Turk Gerd E., and K. Mecke. "Shortcomings of the bond orientational order parameters for the analysis of disordered particulate matter". In: *The Journal of Chemical Physics* 138.4 (2013), p. 044501. ISSN: 0021-9606. DOI: 10.1063/1.4774084.

[Mik+18]   Gerd Mikolajczyk, Li Huang, Michaela Wilhelm, Wolfgang Dreher, and Stefan Odenbach. "Colloid deposition in monolithic porous media – Experimental investigations using X-ray computed microtomography and magnetic resonance velocimetry". In: *Chemical Engineering Science* 175 (Jan. 2018), pp. 257–266. ISSN: 0009-2509. DOI: 10.1016/j.ces.2017.09.054.

[MJM08]   H. Mantz, K. Jacobs, and K. Mecke. "Utilising Minkowski Functionals for Image Analysis". In: *Journal of Statistical Mechanics: Theory and Experiment* (2008), P12015. URL: http://www.iop.org/EJ/abstract/1742-5468/2008/12/P12015.

[MJN98]   Daniel M. Mueth, Heinrich M. Jaeger, and Sidney R. Nagel. "Force distribution in a granular medium". In: *Physical Review E* 57.3 (Mar. 1998), pp. 3164–3169. ISSN: 1095-3787. DOI: 10.1103/physreve.57.3164.

[ML03]   Anita Mehta and JM Luck. "Why shape matters in granular compaction". In: *Journal of Physics A: Mathematical and General* 36.23 (2003), p. L365.

[MMS07]   Amit Mehrotra, Fernando J. Muzzio, and Troy Shinbrot. "Spontaneous Separation of Charged Grains". In: *Physical Review Letters* 99.5 (June 2007). ISSN: 1079-7114. DOI: 10.1103/physrevlett.99.058001.

[Mou98]   Cristian F. Moukarzel. "Isostatic Phase Transition and Instability in Stiff Granular Materials". In: *Physical Review Letters* 81.8 (Aug. 1998), pp. 1634–1637. ISSN: 1079-7114. DOI: 10.1103/physrevlett.81.1634.

[MS05]   K. R. Mecke and D. Stoyan. "Morphological Characterization of Point Patterns". In: *Biometrical Journal* 47.4 (Aug. 2005), pp. 473–488. ISSN: 1521-4036. URL: http://dx.doi.org/10.1002/bimj.200310137.

[MS97]   Klaus R. Mecke and Victor Sofonea. "Morphology of spinodal decomposition". In: *Physical Review E* 56.4 (Oct. 1997), R3761–R3764. ISSN: 1095-3787. URL: http://dx.doi.org/10.1103/PhysRevE.56.R3761.
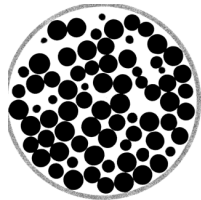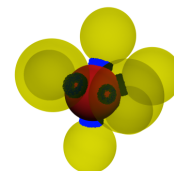
[MSM12]   W. Mickel, G. E. Schroder-Turk, and K. Mecke. "Tensorial Minkowski functionals of triply periodic minimal surfaces". In: *Interface Focus* 2.5 (June 2012), pp. 623–633. ISSN: 2042-8901. URL: http://dx.doi.org/10.1098/rsfs.2012.0007.

[Mur+15] Julie Murison, Robabeh Moosavi, Michael Schulz, Burkhard Schillinger, and Matthias Schröter. "Neutron Tomography as a Tool To Study Immiscible Fluids in Porous Media without Chemical Dopants". In: *Energy and Fuels* 29.10 (Sept. 2015), pp. 6271–6276. ISSN: 1520-5029. DOI: 10.1021/acs.energyfuels.5b01403.

[MV15]   Stefano Mancuso and Alessandra Viola. *Die Intelligenz der Pflanzen.* Antje Kunstmann, 2015.

[MW08]   Logan S. McCarty and George M. Whitesides. "Electrostatic Charging Due to Separation of Ions at Interfaces: Contact Electrification of Ionic Electrets". In: *Angewandte Chemie International Edition* 47.12 (Mar. 2008), pp. 2188–2207. ISSN: 1521-3773. DOI: 10.1002/anie.200701812.

[MW91]   K. R. Mecke and H. Wagner. "Euler characteristic and related measures for random geometric sets". In: *Journal of Statistical Physics* 64.3-4 (Aug. 1991), pp. 843–850. ISSN: 1572-9613. URL: http://dx.doi.org/10.1007/BF01048319.

[Nac+11] S. Nachtrab, S. Kapfer, C. Arns, M. Madadi, K. Mecke, and Gerd E. Schröder-Turk. "Morphology and Linear-Elastic Moduli of Random Network Solids". In: *Advanced Materials* 23.22-23 (2011), pp. 2633–2637. DOI: 10.1002/adma.201004094. URL: http://dx.doi.org/10.1002/adma.201004094.

[Nat86]   F. Natterer. *The Mathematics of Computerized Tomography.* Classics in Applied Mathematics. Society for Industrial and Applied Mathematics (SIAM, 3600 Market Street, Floor 6, Philadelphia, PA 19104), 1986. ISBN: 9780898719284. URL: https://books.google.de/books?id=07s8HIGWvB8C.

[NDP00]   M. Nicolas, P. Duru, and O. Pouliquen. "Compaction of a granular material under cyclic shear". In: *The European Physical Journal E* 3.4 (Dec. 2000), pp. 309–314. ISSN: 1292-8941. DOI: 10.1007/s101890070001.

[Neu+13] Max Neudecker, Stephan Ulrich, Stephan Herminghaus, and Matthias Schröter. "Jammed Frictional Tetrahedra are Hyperstatic". In: *Physical Review Letters* 111.2 (July 2013). ISSN: 1079-7114. DOI: 10.1103/physrevlett.111.028001.

[New+11] Katherine A. Newhall, Ivane Jorjadze, Eric Vanden-Eijnden, and Jasna Brujic. "A statistical mechanics framework captures the packing of monodisperse particles". In: *Soft Matter* 7.24 (2011), p. 11518. ISSN: 1744-6848. DOI: 10.1039/c1sm06243c.

[NIS18]   website NIST. *https://www.nist.gov/pml/x-ray-mass-attenuation-coefficients.* 2018.
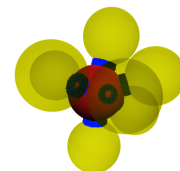
[NMW08]   R. Neher, K. Mecke, and H. Wagner. "Topological estimation of percolation thresholds". In: *Journal of Statistical Mechanics: Theory and Experiment* 2008.01 (Jan. 2008), P01011. ISSN: 1742-5468. DOI: `10.1088/1742-5468/2008/01/p01011`.

[Nye57]   J.F. Nye. *Physical Properties of Crystals: Their Representation by Tensors and Matrices*. Oxford University Press, 1957.

[Oge+96]   L. Oger, A. Gervois, J. P. Troadec, and N. Rivier. "Voronoi tessellation of packings of spheres: Topological correlation and statistics". In: *Philosophical Magazine B* 74.2 (Aug. 1996), pp. 177–197. ISSN: 1463-6417. URL: `http://dx.doi.org/10.1080/01418639608240335`.

[OH04]   Alexander Otten and Stephan Herminghaus. "How Plants Keep Dry: A Physicist's Point of View". In: *Langmuir* 20.6 (Mar. 2004), pp. 2405–2408. ISSN: 1520-5827. DOI: `10.1021/la034961d`.

[OHe+01]   Corey S. O'Hern, Stephen A. Langer, Andrea J. Liu, and Sidney R. Nagel. "Force Distributions near Jamming and Glass Transitions". In: *Physical Review Letters* 86.1 (Jan. 2001), pp. 111–114. ISSN: 1079-7114. DOI: `10.1103/physrevlett.86.111`.

[OHe+02]   Corey S. O'Hern, Stephen A. Langer, Andrea J. Liu, and Sidney R. Nagel. "Random Packings of Frictionless Particles". In: *Physical Review Letters* 88.7 (Jan. 2002). ISSN: 1079-7114. DOI: `10.1103/physrevlett.88.075507`.

[OHe+03]   Corey S. O'Hern, Leonardo E. Silbert, Andrea J. Liu, and Sidney R. Nagel. "Jamming at zero temperature and zero applied stress: The epitome of disorder". In: *Physical Review E* 68.1 (July 2003). ISSN: 1095-3787. DOI: `10.1103/physreve.68.011306`.

[Oka+00]   Atsuyuki Okabe, Barry Boots, Kokichi Sugihara, and Sung Nok Chiu. *Spatial Tessellations: Concepts and Applications of Voronoi Diagrams*. Wiley, 2000. ISBN: 0471986356.

[OL90]   George Y. Onoda and Eric G. Liniger. "Random loose packings of uniform spheres and the dilatancy onset". In: *Physical Review Letters* 64.22 (May 1990), pp. 2727–2730. ISSN: 0031-9007. DOI: `10.1103/physrevlett.64.2727`.

[OS88]   Stanley Osher and James A Sethian. "Fronts propagating with curvature-dependent speed: Algorithms based on Hamilton-Jacobi formulations". In: *Journal of Computational Physics* 79.1 (Nov. 1988), pp. 12–49. ISSN: 0021-9991. DOI: `10.1016/0021-9991(88)90002-2`.

[Ots75]   Nobuyuki Otsu. "A threshold selection method from gray-level histograms". In: *Automatica* 11.285-296 (1975), pp. 23–27.

[OTT04]   M Oda, T. Takemura, and M. Takahashi. In: *Geotechnique* 54.8 (2004), pp. 539–542.
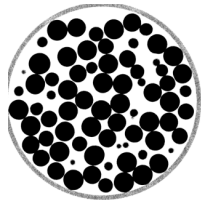
[Our72]   Our Molecular Physics Correspondent. "What is Random Packing?" In: *Nature* 239.5374 (Oct. 1972), pp. 488–489. ISSN: 0028-0836. DOI: 10.1038/239488a0.

[Pal+13]   M. Palombo, A. Gabrielli, V. D. P. Servedio, G. Ruocco, and S. Capuani. "Structural disorder and anomalous diffusion in random packing of spheres". In: *Scientific Reports* 3.1 (Sept. 2013). ISSN: 2045-2322. DOI: 10.1038/srep02631.

[Pap+16]   Lia Papadopoulos, James G. Puckett, Karen E. Daniels, and Danielle S. Bassett. "Evolution of network architecture in a granular material under compression". In: *Physical Review E* 94.3 (Sept. 2016). ISSN: 2470-0053. DOI: 10.1103/physreve. 94.032908.

[Par10]   Jim R Parker. *Algorithms for image processing and computer vision.* John Wiley and Sons, 2010.

[Paw06]   J Pawley. *Handbook of Biological Confocal Microscopy.* Springer, 2006. ISBN: 038725921X.

[PD06]   Sylvain Paris and Frédo Durand. "A Fast Approximation of the Bilateral Filter Using a Signal Processing Approach". In: *Lecture Notes in Computer Science* (2006), pp. 568–580. ISSN: 1611-3349. DOI: 10.1007/11744085_44.

[PD13]   James G. Puckett and Karen E. Daniels. "Equilibrating Temperaturelike Variables in Jammed Granular Subsystems". In: *Physical Review Letters* 110.5 (Jan. 2013). ISSN: 1079-7114. DOI: 10.1103/physrevlett.110.058001.

[Pet09]   Catherine A. Peters. "Accessibilities of reactive minerals in consolidated sedimentary rock: An imaging study of three sandstones". In: *Chemical Geology* 265.1-2 (July 2009), pp. 198–208. ISSN: 0009-2541. DOI: 10.1016/j.chemgeo. 2008.11.014.

[PG87]   Jim Piper and Erik Granum. "Computing distance transformations in convex and non-convex domains". In: *Pattern Recognition* 20.6 (1987), pp. 599–615. ISSN: 0031-3203. URL: http://dx.doi.org/10.1016/0031-3203(87)90030-6.

[PH07]   S. Pudasaini and K Hutter. *AvalanchDynamics.* Springer, 2007.

[Pin+98]   D Pinson, R P Zou, A B Yu, P Zulli, and M J McCarthy. "Coordination number of binary mixtures of spheres". In: *Journal of Physics D: Applied Physics* 31.4 (Feb. 1998), pp. 457–462. ISSN: 1361-6463. DOI: 10.1088/0022-3727/31/4/016.

[Pit99]   N. Pitet. "Dynamical percolation through the Voronoi tessellations". In: *Journal of Physics A* 32.4611 (1999).

[Pla+06]   G Plantard, H Saadaoui, P Snabre, and B Pouligny. "Surface-roughness–driven segregation in a granular slurry under shear". In: *Europhysics Letters (EPL)* 75.2 (July 2006), pp. 335–341. ISSN: 1286-4854. DOI: 10.1209/epl/i2006-10088-6.

[Poh+06]   N. Pohlman, B. Severson, J. Ottino, and R. Lueptow. "Surface roughness effects in granular matter: Influence on angle of repose and the absence of segregation". In: *Phys. Rev. E* 73.3 (Mar. 2006). ISSN: 1550-2376. DOI: 10.1103/ physreve.73.031304.

[pol18]   github polyrender. *https://github.com/spatialfruitsalad/polyRender*. 2018.

[pom18a]   github pomelo. *https://github.com/spatialfruitsalad/pomelo*. 2018.

[pom18b]   theo1 pomelo. *http://theorie1.physik.fau.de/research/pomelo/index.html*. 2018.

[pom18c]   github pomelotools. *https://github.com/spatialfruitsalad/pomeloTools*. 2018.

[pov18]   website povray. *http://www.povray.org/*. 2018.

[Pra78]   William K. Pratt. *Digital Image Processing*. John Wiley and Sons Inc, 1978. ISBN: 0471018880.

[Pre92]   E. Preteux. "Watershed and skeleton by influence zones: A distance-based approach". In: *Journal of Mathematical Imaging and Vision* 1.3 (Sept. 1992), pp. 239–255. ISSN: 1573-7683. DOI: 10.1007/bf00129878.

[Pug+10]   Luis A. Pugnaloni, Iván Sánchez, Paula A. Gago, José Damas, Iker Zuriguel, and Diego Maza. "Towards a relevant set of state variables to describe static granular packings". In: *Physical Review E* 82.5 (Nov. 2010). ISSN: 1550-2376. DOI: 10.1103/physreve.82.050301.

[Pug+11]   Luis Ariel Pugnaloni, José Damas, Iker Zuriguel, and Diego Maza. "Master curves for the stress tensor invariants in stationary states of static granular beds. Implications for the thermodynamic phase space". In: *Papers in Physics* 3.0 (Aug. 2011). ISSN: 1852-4249. DOI: 10.4279/pip.030004.

[Qin+16]   Jian Qin, Jiyuan Li, Victor Lee, Heinrich Jaeger, Juan J. de Pablo, and Karl F. Freed. "A theory of interactions between polarizable dielectric spheres". In: *Journal of Colloid and Interface Science* 469 (May 2016), pp. 237–241. ISSN: 0021-9797. DOI: 10.1016/j.jcis.2016.02.033.

[Rad86]   J. Radon. "On the determination of functions from their integral values along certain manifolds". In: *IEEE Trans. Med. Imaging* 5.4 (Dec. 1986), pp. 170–176. ISSN: 1558-254X. DOI: 10.1109/tmi.1986.4307775.

[Rag92]   I. Ragnemalm. "Fast erosion and dilation by contour processing and thresholding of distance maps". In: *Pattern Recognition Letters* 13.3 (1992), pp. 161–166. ISSN: 0167-8655. DOI: http://dx.doi.org/10.1016/0167-8655(92)90055-5. URL: http://www.sciencedirect.com/science/article/pii/0167865592900555.

[Rah66]   Aneesur Rahman. "Liquid Structure and Self-Diffusion". In: *The Journal of Chemical Physics* 45.7 (Oct. 1966), pp. 2585–2592. ISSN: 1089-7690. DOI: 10.1063/1.1727978.

[Rap04]   D. C. Rapaport. *The Art of Molecular Dynamics Simulation*. Cambridge University Press, 2004. ISBN: 0521825687.
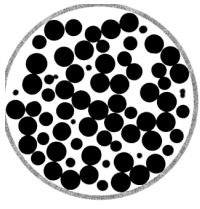
[RD76]   A Rosenfeld and S. Dwyer. *Digital Picture Analysis (Topics in Applied Physics)*. Springer, 1976. ISBN: 3540075798.

[Rib+05]   Ph. Ribière, P. Richard, D. Bideau, and R. Delannay. "Experimental compaction of anisotropic granular media". In: *The European Physical Journal E* 16.4 (Mar. 2005), pp. 415–420. ISSN: 1292-895X. DOI: `10.1140/epje/i2004-10096-x`.

[Rib+07]   Ph. Ribière, P. Richard, P. Philippe, D. Bideau, and R. Delannay. "On the existence of stationary states during granular compaction". In: *The European Physical Journal E* 22.3 (Mar. 2007), pp. 249–253. ISSN: 1292-895X. DOI: `10.1140/epje/e2007-00017-x`.

[Ric+03]   Patrick Richard, Pierre Philippe, Fabrice Barbe, Stéphane Bourlès, Xavier Thibault, and Daniel Bideau. "Analysis by x-ray microtomography of a granular packing undergoing compaction". In: *Physical Review E* 68.2 (Aug. 2003). ISSN: 1095-3787. DOI: `10.1103/physreve.68.020301`.

[Ric+99]   Patrick Richard, Luc Oger, Jean-Paul Troadec, and Annie Gervois. "Geometrical characterization of hard-sphere systems". In: *Physical Review E* 60.4 (Oct. 1999), pp. 4551–4558. ISSN: 1095-3787. DOI: `10.1103/physreve.60.4551`.

[Ric44]   O. Rice. "On the Statistical Mechanics of Liquids, and the Gas of Hard Elastic Spheres". In: *The Journal of Chemical Physics* 12.1 (1944), p. 1. ISSN: 0021-9606. DOI: `10.1063/1.1723874`.

[Rie+18]   Frank Rietz, Charles Radin, Harry L. Swinney, and Matthias Schröter. "Nucleation in Sheared Granular Matter". In: *Physical Review Letters* 120.5 (Feb. 2018). ISSN: 1079-7114. DOI: `10.1103/physrevlett.120.055701`.

[Rio+14]   Emmanuelle Rio, Wiebke Drenckhan, Anniina Salonen, and Dominique Langevin. "Unusually stable liquid foams". In: *Advances in Colloid and Interface Science* 205 (Mar. 2014), pp. 74–86. ISSN: 0001-8686. DOI: `10.1016/j.cis.2013.10.023`.

[RMM08]   S. Rehse, K. Mecke, and R. Magerle. "Characterization of the dynamics of block copolymer microdomains with local morphological measures". In: *Physical Review E* 77.5 (May 2008). ISSN: 1550-2376. DOI: `10.1103/physreve.77.051805`.

[Rob+16]   Vanessa Robins, Mohammad Saadatfar, Olaf Delgado-Friedrichs, and Adrian P. Sheppard. "Percolating length scales from topological persistence analysis of micro-CT images of porous materials". In: *Water Resources Research* 52.1 (Jan. 2016), pp. 315–329. ISSN: 0043-1397. DOI: `10.1002/2015wr017937`.

[Rön98]   Wilhelm Conrad Röntgen. "Ueber eine neue Art von Strahlen". In: *Annalen der Physik* 300.1 (1898), pp. 1–11.

[RT98]   M. D. Rintoul and S. Torquato. "Hard-sphere statistics along the metastable amorphous branch". In: *Physical Review E* 58.1 (July 1998), pp. 532–537. ISSN: 1095-3787. DOI: `10.1103/physreve.58.532`.

[rtk18]   website rtk. `https://www.openrtk.org/`. 2018.
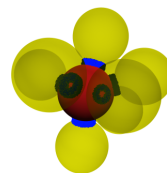
[Rub+15]   S. M. Rubio-Largo, A. Janda, D. Maza, I. Zuriguel, and R. C. Hidalgo. "Disentangling the Free-Fall Arch Paradox in Silo Discharge". In: *Physical Review Letters* 114.23 (June 2015). ISSN: 1079-7114. DOI: 10.1103/physrevlett.114.238002.

[Rut62]   R. Rutgers. "Packing of Spheres". In: *Nature* 193.4814 (Feb. 1962), pp. 465–466. ISSN: 0028-0836. DOI: 10.1038/193465a0.

[Ryc+06]   Chris H. Rycroft, Gary S. Grest, James W. Landry, and Martin Z. Bazant. "Analysis of granular flow in a pebble-bed nuclear reactor". In: *Physical Review E* 74.2 (Aug. 2006). ISSN: 1550-2376. DOI: 10.1103/physreve.74.021306.

[Ryc09]   Chris H. Rycroft. "Voro++: A three-dimensional Voronoi cell library in C++". In: *Chaos* 19.041111 (2009). URL: %5Curl%7Bhttps://escholarship.org/uc/item/8sf4t5x8%7D.

[Saa+12]   Mohammad Saadatfar, Adrian P. Sheppard, Tim J. Senden, and Alexandre J. Kabla. "Mapping forces in a 3D elastic assembly of grains". In: *Journal of the Mechanics and Physics of Solids* 60.1 (Jan. 2012), pp. 55–66. ISSN: 0022-5096. DOI: 10.1016/j.jmps.2011.10.001.

[Saa+13]   Mohammad Saadatfar, Nicolas Francois, Alon Arad, Mahyar Madadi, Adrian Sheppard, Tim Senden, and Mark Knackstedt. "Grain-based characterisation and acoustic wave propagation in a sand packing subject to triaxial compression". In: (2013). DOI: 10.1063/1.4811995.

[SAM12]   O. Sharma, F. Anton, and D. Mioc. "Level Sets and Voronoi based Feature Extraction from any Imagery". In: *GEOProcessing* (2012).

[San04]   L. Santalo. *Integral geometry and geometric probability*. Cambridge university press, 2004.

[Sch+06]   Matthias Schröter, Stephan Ulrich, Jennifer Kreft, Jack B. Swift, and Harry L. Swinney. "Mechanisms in the size segregation of a binary granular mixture". In: *Physical Review E* 74.1 (June 2006). ISSN: 1550-2376. DOI: 10.1103/physreve.74.011307.

[Sch+08]   M. Scheel, R. Seemann, M. Brinkmann, M. Di Michiel, A. Sheppard, B. Breidenbach, and S. Herminghaus. "Morphological clues to wet granular pile stability". In: *Nature Materials* 7.3 (Feb. 2008), pp. 189–193. ISSN: 1476-4660. DOI: 10.1038/nmat2117.

[Sch+10a]   Gerd E. Schröder-Turk, S. Kapfer, B. Breidenbach, C. Beisbart, and K. Mecke. "Tensorial Minkowski functionals and anisotropy measures for planar patterns". In: *Journal of Microscopy* 238.1 (Apr. 2010), pp. 57–74. ISSN: 1365-2818. DOI: 10.1111/j.1365-2818.2009.03331.x.

[Sch+10b]   Gerd E. Schröder-Turk, W. Mickel, M. Schröter, G. Delaney, M. Saadatfar, T. Senden, K. Mecke, and T. Aste. "Disordered spherical bead packs are anisotropic". In: *EPL (Europhysics Letters)* 90.3 (May 2010), p. 34001. ISSN: 1286-4854. URL: %5Curl%7Bhttp://dx.doi.org/10.1209/0295-5075/90/34001%7D.
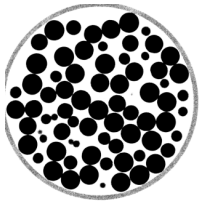
[Sch+11] Gerd E. Schröder-Turk, W. Mickel, S. Kapfer, M. Klatt, Fabian Schaller, M. Hoffmann, N. Kleppmann, P. Armstrong, A. Inayat, D. Hug, and et al. "Minkowski Tensor Shape Analysis of Cellular, Granular and Porous Structures". In: *Advanced Materials* 23.22-23 (June 2011), pp. 2535–2553. ISSN: 0935-9648. DOI: 10.1002/adma.201100562.

[Sch+12] Christian Scholz, Frank Wirner, Jan Götz, Ulrich Rüde, Gerd E. Schröder-Turk, Klaus Mecke, and Clemens Bechinger. "Permeability of Porous Materials Determined from the Euler Characteristic". In: *Physical Review Letters* 109.26 (Dec. 2012). ISSN: 1079-7114. DOI: 10.1103/physrevlett.109.264504.

[Sch+13a] Fabian Schaller, S. Kapfer, M. Evans, M. Hoffmann, T. Aste, M. Saadatfar, K. Mecke, G. Delaney, and Gerd E. Schröder-Turk. "Set Voronoi diagrams of 3D assemblies of aspherical particles". In: *Philosophical Magazine* 93.31-33 (Sept. 2013), pp. 3993–4017. ISSN: 1478-6443. DOI: 10.1080/14786435.2013.834389.

[Sch+13b] Fabian Schaller, M. Neudecker, M. Saadatfar, G. Delaney, K. Mecke, Gerd E. Schröder-Turk, and M. Schröter. "Tomographic analysis of jammed ellipsoid packings". In: *AIP Conference Proceedings* (2013). DOI: 10.1063/1.4811946.

[Sch+13c] Gerd E. Schröder-Turk, W. Mickel, S. Kapfer, Fabian Schaller, B. Breidenbach, D. Hug, and K. Mecke. "Minkowski tensors of anisotropic spatial structure". In: *New Journal of Physics* 15.8 (Aug. 2013), p. 083028. ISSN: 1367-2630. DOI: 10.1088/1367-2630/15/8/083028.

[Sch+13d] Gerd E. Schröder-Turk, R. Schielein, S. Kapfer, Fabian Schaller, G. Delaney, T. Senden, M. Saadatfar, T. Aste, and K. Mecke. "Minkowski tensors and local structure metrics: Amorphous and crystalline sphere packings". In: *AIP Conference Proceedings* 1542.1 (2013), pp. 349–352. DOI: 10.1063/1.4811939. URL: http://link.aip.org/link/?APC/1542/349/1.

[Sch+15a] Fabian Schaller, Sebastian C. Kapfer, James E. Hilton, Paul W. Cleary, Klaus Mecke, Cristiano De Michele, Tanja Schilling, Mohammad Saadatfar, Matthias Schröter, Gary W. Delaney, and et al. "Non-universal Voronoi cell shapes in amorphous ellipsoid packs". In: *EPL (Europhysics Letters)* 111.2 (July 2015), p. 24002. ISSN: 1286-4854. DOI: 10.1209/0295-5075/111/24002.

[Sch+15b] Fabian Schaller, Max Neudecker, Mohammad Saadatfar, Gary W. Delaney, Gerd E. Schröder-Turk, and Matthias Schröter. "Local Origin of Global Contact Numbers in Frictional Ellipsoid Packings". In: *Physical Review Letters* 114.15 (Apr. 2015). ISSN: 1079-7114. DOI: 10.1103/physrevlett.114.158001.

[Sch+17a] Fabian Schaller, Horst Punzmann, Gerd E. Schröder-Turk, and Mohammad Saadatfar. "Towards minimal models for realistic granular materials: Tomographic analysis of bidispersed assemblies of ellipsoids". In: *EPJ Web of Conferences* 140 (2017). Ed. by F. Radjai, S. Nezamabadi, S. Luding, and J.Y.Editors Delenne,
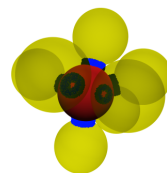
p. 06030. ISSN: 2100-014X. URL: http://dx.doi.org/10.1051/epjconf/201714006030.

[Sch+17b] Philipp W. A. Schönhöfer, Laurence J. Ellison, Matthieu 3echal, Douglas J. Cleaver, and Gerd E. Schröder-Turk. "Purely entropic self-assembly of the bicontinuous Ia3d gyroid phase in equilibrium hard-pear systems". In: *Interface Focus* 7.4 (June 2017), p. 20160161. ISSN: 2042-8901. DOI: 10.1098/rsfs.2016.0161.

[Sch05a] Peter Schiffer. "A bridge to sandpile stability". In: *Nature Physics* 1.1 (Oct. 2005), pp. 21–22. ISSN: 1745-2481. DOI: 10.1038/nphys129.

[Sch05b] Gerd E. Schröder-Turk. "Skeletons in the labyrinth". In: *PhD Thesis, The Australian National University* (2005).

[Sch09] M. Scheel. "Experimente zur Untersuchung mechanischer Eigenschaften feuchter Granulate". In: *Dissertation, Uni Göttingen* (2009).

[Sch12] Fabian Schaller. "The Structure of Random Ellipsoid Packings". In: *Diploma thesis, FAU Erlangen* (2012).

[Sch14] M. Schröter. "Statistical mechanics of static granular media". In: *Unpublished habilitation thesis, Uni Göttingen* (2014).

[SCH16] Li-Tsung Sheng, Wei-Ching Chang, and Shu-San Hsiau. "Influence of particle surface roughness on creeping granular motion". In: *Physical Review E* 94.1 (July 2016). ISSN: 2470-0053. DOI: 10.1103/physreve.94.012903.

[Sch16] G.K. von Schulthess. *Röntgen, Computertomografie und Co.: Wie funktioniert medizinische Bildgebung?* Springer Berlin Heidelberg, 2016. ISBN: 9783662539316. URL: https://books.google.de/books?id=zba8DQAAQBAJ.

[Sch17] Matthias Schröter. "A local view on the role of friction and shape". In: *EPJ Web of Conferences* 140 (2017), p. 01008. DOI: 10.1051/epjconf/201714001008.

[Sch70] Alan H. Schoen. "Infinite periodic minimal surfaces without self-intersections." In: *Technical Note D-5441.* (1970). URL: %5Curl%7Bhttp://ntrs.nasa.gov/archive/nasa/casi.ntrs.nasa.gov/19700020472.pdf%7D.

[Sch78] R. Schneider. "Curvature measures of convex bodies". In: *Ann. Math. Pura Appl.* 11 (1978), pp. 101–134.

[Sch93] R. Schneider. *Convex Bodies: The Brunn-Minkowski Theory.* Cambridge University Press, 1993.

[SCO60] G. DAVID SCOTT. "Packing of Spheres: Packing of Equal Spheres". In: *Nature* 188.4754 (Dec. 1960), pp. 908–909. ISSN: 1476-4687. DOI: 10.1038/188908a0.

[SDP02] M. Scott Shell, Pablo G. Debenedetti, and Athanassios Z. Panagiotopoulos. "Molecular structural order and anomalies in liquid silica". In: *Physical Review E* 66.1 (July 2002). ISSN: 1095-3787. DOI: 10.1103/physreve.66.011202.
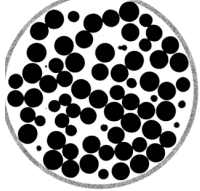
[Sei+00]   G. T. Seidler, G. 3tinez, L. H. Seeley, K. H. Kim, E. A. Behne, S. Zaranek, B. D. Chapman, S. M. Heald, and D. L. Brewe. "Granule-by-granule reconstruction of a sandpile from x-ray microtomography data". In: *Physical Review E* 62.6 (Dec. 2000), pp. 8175–8181. ISSN: 1095-3787. DOI: 10.1103/physreve.62.8175.

[Ser83]   J. Serra. *Image analysis and mathematical morphology*. Academic Press, 1983.

[Set85]   J. A. Sethian. "Curvature and the evolution of fronts". In: *Communications in Mathematical Physics* 101.4 (Dec. 1985), pp. 487–499. ISSN: 1432-0916. DOI: 10.1007/bf01210742.

[Set99]   J. Sethian. *Level Set Methods and Fast Marching Methods: Evolving Interfaces in Computational Geometry, Fluid Mechanics, Computer Vision, and Materials Science … and Computational Mathematics*. Cambridge University Press, 1999.

[SFB29]   W. O. Smith, Paul D. Foote, and P. F. Busang. "Packing of Homogeneous Spheres". In: *Physical Review* 34.9 (Nov. 1929), pp. 1271–1274. ISSN: 0031-899X. DOI: 10.1103/physrev.34.1271.

[SGH04]   Mario Scheel, Dimitrios Geromichalos, and Stephan Herminghaus. "Wet granular matter under vertical agitation". In: *Journal of Physics: Condensed Matter* 16.38 (Sept. 2004), S4213–S4218. ISSN: 1361-648X. DOI: 10.1088/0953-8984/16/38/033.

[Sha80]   M. Shahinpoor. "Statistical mechanical considerations on the random packing of granular materials". In: *Powder Technology* 25.2 (Mar. 1980), pp. 163–176. ISSN: 0032-5910. DOI: 10.1016/0032-5910(80)87027-6.

[SHB14]   M. Sonka, V. Hlavac, and R. Boyle. *Image processing, analysis, and machine vision*. Cengage Learning, 2014.

[SHS07]   Kostya Shundyak, Martin van Hecke, and Wim van Saarloos. "Force mobilization and generalized isostaticity in jammed packings of frictional grains". In: *Physical Review E* 75.1 (Jan. 2007). ISSN: 1550-2376. DOI: 10.1103/physreve.75.010301.

[SHS17]   André Schella, Stephan Herminghaus, and Matthias Schröter. "Influence of humidity on tribo-electric charging and segregation in shaken granular media". In: *Soft Matter* 13.2 (2017), pp. 394–401. ISSN: 1744-6848. DOI: 10.1039/c6sm02041k.

[Sie18]   website SiemensOEM. *https://www.oem-xray-components.siemens.com/x-ray-spectra-simulation*. 2018.

[Sil+02]   L. Silbert, D. Ertaş, G. Grest, T. Halsey, and D. Levine. "Geometry of frictionless and frictional sphere packings". In: *Phys. Rev. E* 65.3 (Feb. 2002). ISSN: 1095-3787. DOI: 10.1103/physreve.65.031304.

[Sil10]   L. Silbert. "Jamming of frictional spheres and random loose packing". In: *Soft Matter* 6.13 (2010), p. 2918. ISSN: 1744-6848. DOI: 10.1039/c001973a.
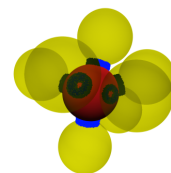
[SK05]   V. Senthil Kumar and V. Kumaran. "Voronoi cell volume distribution and configurational entropy of hard-spheres". In: *The Journal of Chemical Physics* 123.11 (Sept. 2005), p. 114501. ISSN: 1089-7690. DOI: 10.1063/1.2011390.

[SK69]   G. Scott and D. Kilgour. "The density of random close packing of spheres". In: *J. Phys. D: Appl. Phys.* 2.6 (June 1969), pp. 863–866. ISSN: 0022-3727. DOI: 10.1088/0022-3727/2/6/311.

[SKZ08]   T. Shinbrot, T. S. Komatsu, and Q. Zhao. "Spontaneous tribocharging of similar materials". In: *EPL (Europhysics Letters)* 83.2 (July 2008), p. 24004. ISSN: 1286-4854. DOI: 10.1209/0295-5075/83/24004.

[Som+07]   Ellák Somfai, Martin van Hecke, Wouter G. Ellenbroek, Kostya Shundyak, and Wim van Saarloos. "Critical and noncritical jamming of frictional grains". In: *Physical Review E* 75.2 (Feb. 2007). ISSN: 1550-2376. DOI: 10.1103/physreve.75.020301.

[SP08]   K. Siddiq and S. Pizer. *Medial Representations.* Springer, 2008. ISBN: 9781402086588.

[Spe05]   Matthias Sperl. "Experiments on corn pressure in silo cells – translation and comment of Janssen's paper from 1895". In: *Granular Matter* 8.2 (Dec. 2005), pp. 59–65. ISSN: 1434-7636. DOI: 10.1007/s10035-005-0224-z.

[SS11]   Yuqing Song and Lianshuan Shi. "License Plate Location by Level Set Transform and Voronoi Diagram". In: *2011 4th International Conference on Intelligent Networks and Intelligent Systems* (Nov. 2011). DOI: 10.1109/icinis.2011.25.

[Sta+02]   F. Starr, S. Sastry, J. Douglas, and S. Glotzer. "What Do We Learn from the Local Geometry of Glass-Forming Liquids?" In: *Phys. Rev. Lett.* 89 (12 Aug. 2002), p. 125501. DOI: 10.1103/PhysRevLett.89.125501. URL: http://link.aps.org/doi/10.1103/PhysRevLett.89.125501.

[Sta17]   Ralf Stannarius. "Magnetic resonance imaging of granular materials". In: *Review of Scientific Instruments* 88.5 (May 2017), p. 051806. ISSN: 1089-7623. DOI: 10.1063/1.4983135.

[SW08]   R. Schneider and W. Weil. *Stochastic and Integral Geometry (Probability and Its Applications).* Springer, 2008.

[SW62]   Z. W. Salsburg and W. W. Wood. "Equation of State of Classical Hard Spheres at High Density". In: *The Journal of Chemical Physics* 37.4 (Aug. 1962), pp. 798–804. ISSN: 1089-7690. DOI: 10.1063/1.1733163.

[SWK16]   Fabian Schaller, R. Weigel, and S. Kapfer. "Densest Local Structures of Uniaxial Ellipsoids". In: *Physical Review X* 6.4 (Nov. 2016). ISSN: 2160-3308. DOI: 10.1103/physrevx.6.041032.

[SWM08]   Ch. Song, P. Wang, and H. Makse. "A phase diagram for jammed matter". In: *Nature* 453.7195 (May 2008), pp. 629–632. ISSN: 1476-4687. DOI: 10.1038/nature06981.
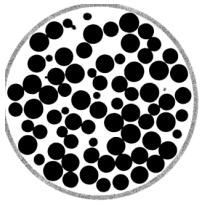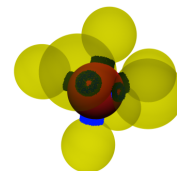
[SWS17]   André Schella, Simon Weis, and Matthias Schröter. "Charging changes contact composition in binary sphere packings". In: *Physical Review E* 95.6 (June 2017). ISSN: 2470-0053. DOI: `10.1103/physreve.95.062903`.

[Tad+13]   Shin-ichi Tadaki, Macoto Kikuchi, Minoru Fukui, Akihiro Nakayama, Katsuhiro Nishinari, Akihiro Shibata, Yuki Sugiyama, Taturu Yosida, and Satoshi Yukawa. "Phase transition in traffic jam experiment on a circuit". In: *New Journal of Physics* 15.10 (Oct. 2013), p. 103034. ISSN: 1367-2630. DOI: `10.1088/1367-2630/15/10/103034`.

[TB16]   Junyao Tang and R. P. Behringer. "Orientation, flow, and clogging in a two-dimensional hopper: Ellipses vs. disks". In: *EPL (Europhysics Letters)* 114.3 (May 2016), p. 34002. ISSN: 1286-4854. DOI: `10.1209/0295-5075/114/34002`.

[TB17]   Stephanie Taylor and Emily E. Brodsky. "Granular temperature measured experimentally in a shear flow by acoustic energy". In: *Physical Review E* 96.3 (Sept. 2017). ISSN: 2470-0053. DOI: `10.1103/physreve.96.032913`.

[TD15]   C. C. Thomas and D. J. Durian. "Fraction of Clogging Configurations Sampled by Granular Hopper Flow". In: *Physical Review Letters* 114.17 (Apr. 2015). ISSN: 1079-7114. DOI: `10.1103/physrevlett.114.178001`.

[TG91]   Peter A. Thompson and Gary S. Grest. "Granular flow: Friction and the dilatancy transition". In: *Physical Review Letters* 67.13 (Sept. 1991), pp. 1751–1754. ISSN: 0031-9007. DOI: `10.1103/physrevlett.67.1751`.

[Thy+18]   N. Thyagu, M. Neudecker, Simon Weis, Fabian Schaller, and Matthias Schröter. "Local analysis of the history dependence in tetrahedra packings". In: *Physical Review E. (in review)* (2018). URL: `http://arxiv.org/abs/1501.04472`.

[TJ10]   S. Torquato and Y. Jiao. "Robust algorithm to generate a diverse class of dense disordered and ordered sphere packings via linear programming". In: *Physical Review E* 82.6 (Dec. 2010). ISSN: 1550-2376. URL: `http://dx.doi.org/10.1103/PhysRevE.82.061302`.

[TM15]   Paul A. Tipler and Gene Mosca. *Physik: für Wissenschaftler und Ingenieure (German Edition)*. Springer Spektrum, 2015. ISBN: 3642541658.

[TM98]   Carlo Tomasi and Roberto Manduchi. "Bilateral filtering for gray and color images". In: *Computer Vision, 1998. Sixth International Conference on*. IEEE. 1998, pp. 839–846.

[TS10]   S. Torquato and F. Stillinger. "Jammed hard-particle packings: From Kepler to Bernal and beyond". In: *Rev. Mod. Phys.* 82.3 (Sept. 2010), pp. 2633–2672. ISSN: 1539-0756. DOI: `10.1103/revmodphys.82.2633`.

[Tso94]   Haim Tsoar. "Bagnold, RA 1941: The physics of blown sand and desert dunes. London: Methuen". In: *Progress in physical geography* 18.1 (1994), pp. 91–96.
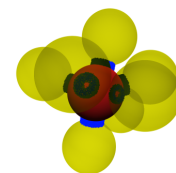
[TTD00]   S. Torquato, T. M. Truskett, and P. G. Debenedetti. "Is Random Close Packing of Spheres Well Defined?" In: *Phys. Rev. Lett.* 84 (2000), p. 2064. DOI: `10.1103/PhysRevLett.84.2064`.

[Tuf01]   Edward R. Tufte. *The Visual Display of Quantitative Information.* Graphics Pr, 2001. ISBN: 0961392142.

[USS07]   Stephan Ulrich, Matthias Schröter, and Harry L. Swinney. "Influence of friction on granular segregation". In: *Physical Review E* 76.4 (Oct. 2007). ISSN: 1550-2376. DOI: `10.1103/physreve.76.042301`.

[Ute+11] S. Utermann, Ph. Aurin, M. Benderoth, C. Fischer, and M. Schröter. "Tailoring the frictional properties of granular media". In: *Phys. Rev. E* 84.3 (Sept. 2011). ISSN: 1550-2376. DOI: `10.1103/physreve.84.031306`.

[Utt12]   S. Uttermann. "Friction and diffusive light transport in a granular medium". PhD thesis. Georg-8ust-Universität Göttingen, 2012.

[Van+12] N. Vandewalle, G. Lumay, F. Ludewig, and J. E. Fiscina. "How relative humidity affects random packing experiments". In: *Phys. Rev. E* 85.3 (Mar. 2012). ISSN: 1550-2376. DOI: `10.1103/physreve.85.031309`.

[Van+99] Loic Vanel, Daniel Howell, D. Clark, R. P. Behringer, and Eric Clément. "Memories in sand: Experimental tests of construction history on stress distributions under sandpiles". In: *Physical Review E* 60.5 (Nov. 1999), R5040–R5043. ISSN: 1095-3787. DOI: `10.1103/physreve.60.r5040`.

[VC06]   J. M Valverde and A Castellanos. "Random loose packing of cohesive granular materials". In: *Europhysics Letters (EPL)* 75.6 (Sept. 2006), pp. 985–991. ISSN: 1286-4854. DOI: `10.1209/epl/i2006-10208-4`.

[Vor09]   G. Voronoi. "Nouvelles applications des paramètres continus à théorie des formes quadratiques. Deuxième Mémoire. Recherches sur les paralléloèdres primitifs." In: *Journal für die reine und angewandte Mathematik* 136 (1909).

[Vor18]   link VoronoiRendering. *Video of Voronoi diagram for spheres:* `https://goo.gl/8L1Qog`; *Video of Set-Voronoi diagram for ellipsoids:* `https://goo.gl/uUsvGG`. 2018.

[VV88]   Lucas J. van Vliet and Ben J.H. Verwer. "A contour processing method for fast binary neighbourhood operations". In: *Pattern Recognition Letters* 7.1 (Jan. 1988), pp. 27–36. ISSN: 0167-8655. URL: `http://dx.doi.org/10.1016/0167-8655(88)90041-4`.

[WA08]   Denis Weaire and Tomaso Aste. *The Pursuit of Perfect Packing, Second Edition.* CRC Press, 2008. ISBN: 1420068172.

[Wai+14] Scott R. Waitukaitis, Victor Lee, James M. Pierson, Steven L. Forman, and Heinrich M. Jaeger. "Size-Dependent Same-Material Tribocharging in Insulating Grains". In: *Physical Review Letters* 112.21 (May 2014). ISSN: 1079-7114. DOI: `10.1103/physrevlett.112.218001`.
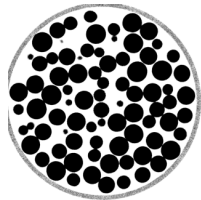
[Wak50]   Takao Wakabayashi. "Photo-elastic Method for Determination of Stress in Powdered Mass". In: *Journal of the Physical Society of Japan* 5.5 (Sept. 1950), pp. 383–385. ISSN: 1347-4073. DOI: `10.1143/jpsj.5.383`.

[Wan+10]   Ping Wang, Chaoming Song, Yuliang Jin, Kun Wang, and Hernán A Makse. "Distribution of volumes and coordination numbers in jammed matter: mesoscopic ensemble". In: *Journal of Statistical Mechanics: Theory and Experiment* 2010.12 (Dec. 2010), P12005. ISSN: 1742-5468. DOI: `10.1088/1742-5468/2010/12/p12005`.

[Wea+07]   Denis Weaire, Vincent Langlois, Mohammad Saadatfar, and Stefan Hutzler. "Foam as granular matter". In: *Granular and Complex Materials* (Oct. 2007), pp. 1–26. ISSN: 1793-1037. DOI: `10.1142/9789812771995_0001`.

[Wei+17]   Simon Weis, Philipp W. A. Schönhöfer, Fabian Schaller, Matthias Schröter, and Gerd E. Schröder-Turk. "Pomelo, a tool for computing Generic Set Voronoi Diagrams of Aspherical Particles of Arbitrary Shape". In: *EPJ Web of Conferences* 140 (2017), p. 06007. DOI: `10.1051/epjconf/201714006007`.

[Wei15]   Simon Weis. "Einfluss der Reibung auf strukturelle und mechanische Eigenschaften von Kugel- und Ellipsoidpackungen". In: *Master thesis Materialphysik, FAU Erlangen* (2015).

[WH30]   A. E. R. Westman and H. R. Hugill. "THE PACKING OF PARTICLES1". In: *Journal of the American Ceramic Society* 13.10 (Oct. 1930), pp. 767–779. ISSN: 1551-2916. DOI: `10.1111/j.1151-2916.1930.tb16222.x`.

[WH99]   D Weaire and S Hutzler. "The Physics of Foams". In: *Oxford University Press, New York* (1999).

[wika]   website off wikipedia. `https://en.wikipedia.org/wiki/OFF_(file_format)`, *year=2018*.

[wikb]   website poly wikipedia. `https://de.wikipedia.org/wiki/Polygon_File_Format`, *year=2018*.

[wik18]   wikimedia.org. `http://commons.wikimedia.org`. 2018.

[WK17]   T. Williams and C. Kelley. *gnuplot Version 4.6 patchlevel 0* `http://www.gnuplot.info`. 2017.

[WK82]   N. Wakao and S. Kaguei. NY: Gordon and Breach, 1982.

[Wor94]   K. J Worsley. "Local maxima and the expected Euler characteristic of excursion sets of χ 2, F and t fields". In: *Advances in Applied Probability* 26.1 (1994), pp. 13–42.

[WS17]   Simon Weis and Matthias Schröter. "Analyzing X-ray tomographies of granular packings". In: *Review of Scientific Instruments* 88.5 (May 2017), p. 051809. ISSN: 1089-7623. DOI: `10.1063/1.4983051`.

[WSS18] Simon Weis, Gerd E. Schröder-Turk, and Matthias Schröter. "Structural similarity between dry and wet sphere packings". In: *(In preparation for peer review)* XX (Aug. 2018). URL: https://arxiv.org/abs/1808.04342.

[WW02] Eric R. Weeks and D. A. Weitz. "Properties of Cage Rearrangements Observed near the Colloidal Glass Transition". In: *Physical Review Letters* 89.9 (Aug. 2002). ISSN: 1079-7114. DOI: 10.1103/physrevlett.89.095704.

[Xie+13] L. Xie, G. Li, N. Bao, and Jùn Zhou. "Contact electrification by collision of homogenous particles". In: *Journal of Applied Physics* 113.18 (May 2013), p. 184908. ISSN: 1089-7550. DOI: 10.1063/1.4804331.

[Yar+73] J. L. Yarnell, M. J. Katz, R. G. Wenzel, and S. H. Koenig. "Structure Factor and Radial Distribution Function for Liquid Argon at 85 °K". In: *Physical Review A* 7.6 (June 1973), pp. 2130–2144. ISSN: 0556-2791. DOI: 10.1103/physreva.7.2130.

[Yos+16] R. Yoshimatsu, N. A. M. Araújo, T. Shinbrot, and H. J. Herrmann. "Field driven charging dynamics of a fluidized granular bed". In: *Soft Matter* 12.29 (2016), pp. 6261–6267. ISSN: 1744-6848. DOI: 10.1039/c6sm00357e.

[Yos+17] R. Yoshimatsu, N. A. M. Araújo, G. Wurm, H. J. Herrmann, and T. Shinbrot. "Self-charging of identical grains in the absence of an external field". In: *Scientific Reports* 7 (Jan. 2017), p. 39996. ISSN: 2045-2322. DOI: 10.1038/srep39996.

[You+81] Ian T. Young, Ricardo L. Peverini, Piet W. Verbeek, and Peter J. van Otterloo. "A new implementation for the binary and Minkowski operators". In: *Computer Graphics and Image Processing* 17.3 (Nov. 1981), pp. 189–210. ISSN: 0146-664X. URL: http://dx.doi.org/10.1016/0146-664X(81)90001-0.

[ZEZ18] Shiwei Zhao, T. Matthew Evans, and Xiaowen Zhou. "Three-dimensional Voronoi analysis of monodisperse ellipsoids during triaxial shear". In: *Powder Technology* 323 (Jan. 2018), pp. 323–336. ISSN: 0032-5910. DOI: 10.1016/j.powtec.2017.10.023.

[Zha+12] Song-Chuan Zhao, Stacy Sidle, Harry L. Swinney, and M Schröter. "Correlation between Voronoi volumes in disc packings". In: *Europhys. Lett.* 97 (2012), p. 34004.

[Zha14] Song-Chuan Zhao. *Length Scales in Granular Matter, PhD thesis GAU Göttingen*. 2014.

[ZM05] H. P. Zhang and H. A. Makse. "Jamming transition in emulsions and granular materials". In: *Physical Review E* 72.1 (June 2005). ISSN: 1550-2376. DOI: 10.1103/physreve.72.011301.

[Zol17] D. Zoller. "Röntgentomographische Charakterisierung von Wurzelwachstum in granularer Materie". In: *Master thesis, FAU Erlangen* (Oct. 2017).
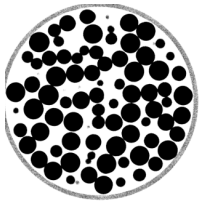
[ZS14]   Song-Chuan Zhao and Matthias Schröter. "Measuring the configurational temperature of a binary disc packing". In: *Soft Matter* 10.23 (2014), p. 4208. ISSN: 1744-6848. DOI: 10.1039/c3sm53176g.

[Zur+05]   Iker Zuriguel, Angel Garcimartín, Diego Maza, Luis A. Pugnaloni, and J. M. Pastor. "Jamming during the discharge of granular matter from a silo". In: *Physical Review E* 71.5 (May 2005). ISSN: 1550-2376. DOI: 10.1103/physreve.71.051303.